DYNAMIC
ELASTIC
MODULUS
MEASUREMENTS
IN MATERIALS

ALAN WOLFENDEN, EDITOR

STP 1045

ASTM

STP 1045

Dynamic Elastic Modulus Measurements in Materials

Alan Wolfenden, editor

ASTM
1916 Race Street
Philadelphia, PA 19103

Library of Congress Cataloging-in-Publication Data

Dynamic elastic modulus measurements in materials/Alan Wolfenden, editor.
(STP; 1045)
"ASTM publication code number (PCN) 04-010450-23"—T.p. verso.
Papers presented at the Symposium on Dynamic Modulus Measurements, held in Kansas City, Mo., May 25–26, 1989, sponsored by the ASTM Committee E-28 on Mechanical Properties and its Task Group E28.03.05 on Dynamic Modulus Measurements.
Includes bibliographical references.
ISBN 0-8031-1291-2
1. Elasticity—Congresses. 2. Materials—Testing—Congresses. I. Wolfenden, Alan, 1940- . II. Symposium on Dynamic Modulus Measurements (1988: Kansas City, Mo.) III. ASTM Committee E-28 on Mechanical Properties. IV. ASTM Committee E-26 on Mechanical Properties. Task Group E28.03.05 on Dynamic Modulus Measurements. V. Series: ASTM special technical publication; 1045.
TA418.D9 1990
620.1'1232—dc20 90-31702
CIP

Peer Review Policy

Each paper published in this volume was evaluated by three peer reviewers. The authors addressed all of the reviewers' comments to the satisfaction of both the technical editor(s) and the ASTM Committee on Publications.

The quality of the papers in this publication reflects not only the obvious efforts of the authors and the technical editor(s), but also the work of these peer reviewers. The ASTM Committee on Publications acknowledges with appreciation their dedication and contribution of time and effort on behalf of ASTM.

Printed in Ann Arbor, MI
May 1990

Foreword

This publication, *Dynamic Elastic Modulus Measurements in Materials*, contains papers presented at the Symposium on Dynamic Modulus Measurements, which was held in Kansas City, Missouri, 25-26 May 1989. The symposium was sponsored by ASTM Committee E-28 on Mechanical Properties and its task group E28.03.05 on Dynamic Modulus Measurements. Alan Wolfenden, Texas A & M, presided as symposium chairman and was editor of this publication.

Contents

Overview

This symposium was organized for the purpose of documenting theoretical and experimental techniques that are used for predicting, analyzing or measuring dynamic elastic moduli in solid materials.

The volume is comprised of fifteen papers which cover the spectrum of pertinent aspects from fundamental research to technological application. The invited overview paper by Berry illustrates the power of precise elastic modulus measurements in understanding the influence of microstructural defects at the atomic level on the mechanical properties of materials, including the new superconductors with high critical temperatures. The other fourteen papers address various aspects of elastic modulus measurements, predictions and analyses. Examples of experimental data from high frequency (MHz) measurements are presented by Kinra and Dayal, and Blessing, and from low frequency (< 1 kHz) measurements by Wren and Kinra. The influence of temperature on dynamic elastic modulus is documented in the papers by Cook, Wolfenden and Ludtka, and Lemmens. Measurements and analyses of dynamic elastic moduli in composite materials are covered in the contributions by Heyliger, Ledbetter and Austin, Wolla and Wolfenden, and Datta and Ledbetter. The theory and modeling of elastic constants are studied in the papers by Ledbetter, and Datta and Ledbetter. Elegant technological use of dynamic elastic modulus measurements is displayed in the papers on crack monitoring by Carpenter, on bonded joints by Dickstein, Sinclair, Spelt, Segal, and Segal, and on cemented soils by Lovelady and Picornell. A comparison of three measurement techniques (including the well-known static technique) is presented by Wyrick, Poole, and Smith for mechanically alloyed materials. The use of computer interfacing for data processing of dynamic elastic modulus results forms the basis of the paper by Fowler. Lemmens shows in his paper that measurements can be made as rapidly as one per second. The volume has some details of the varied instrumentation necessary for dynamic elastic modulus measurements and the papers are well referenced.

This volume offers guidance in the selection of appropriate methods of measuring dynamic elastic modulus where temperature, frequency and strain amplitude are of concern. It will be useful to materials scientists and engineers who are concerned with fundamental or practical aspects of dynamic elastic contants, including the effects of cracks. Some papers in the volume will be of interest to NDE and QC practitioners.

Many existing (and future) problems in engineering and science are connected with the precise determination of dynamic elastic modulus. This book is therefore relevant in areas such as load-deflection, thermoelastic stresses, buckling, elastic instability, creep, fracture mechanics, interatomic potentials, thermodynamic equations of state, lattice defects and free energy. Knowledge of the dynamic elastic modulus of materials is of prime importance in the design of high-speed turbines and components for the planned hypersonic vehicles.

As a major conclusion from this group of contributors. it can be seen that measurements of dynamic elastic modulus (and its complex counterpart damping) will provide both fundamental and technological information on the elastic (and anelastic) behaviour of solid materials. The measurements are particularly useful if they are carried out under the appropriate service conditions of frequency, temperature and strain amplitude. Although a wide range of frequencies (typically 50 Hz to 15 MHz), temperatures (approximately 78 to 1800 K) and strain amplitudes (10^{-8} to 10^{-4}) has been explored by the authors in this volume, there are obvious gaps remaining for future research.

Alan Wolfenden
CSIRO
Division of Materials Science
and Technology
Locked Bag 33
Clayton, Vic 3168
AUSTRALIA

on leave from

Mechanical Engineering Department
Texas A & M University
College Station, TX 77843-3123
USA

Brian S. Berry

DYNAMIC MODULUS MEASUREMENTS AND MATERIALS RESEARCH

REFERENCE: Berry, B. S., "Dynamic Modulus Measurements and Materials Research", Dynamic Elastic Modulus Measurements in Materials, ASTM STP 1045, Alan Wolfenden, editor, American Society for Testing and Materials, Philadelphia 1990.

ABSTRACT: Dynamic modulus measurements are of interest in materials research not only as a source of data on elastic behavior, but also for the insight they provide into structure-property relationships in general. A description is given of a vibrating-reed apparatus which has proved highly adaptable for studies of the elastic and damping behavior of thin-film and other thin-layer electronic materials. Results are reported for amorphous and crystalline ferromagnetic materials, for the high-T_c superconducting oxide $Y_1Ba_2Cu_3O_{7-x}$, and for thin films of aluminum and silicon monoxide, to illustrate the important role which the dynamic modulus can play as a tool in materials research.

KEYWORDS: elastic modulus, vibrating reed, internal friction, ferromagnetic materials, metallic glasses, superconductors, dielectrics.

INTRODUCTION

In addition to their basic significance in the description of mechanical stress-strain behavior, the elastic moduli are important in materials science because they are intimately linked to the internal structure of solids at both the atomic and microstructural levels. For this reason, interest in elastic behavior is not confined to structural materials, but encompasses materials of all types. In the present paper, we shall consider the application of dynamic modulus measurements to amorphous and crystalline ferromagnetic materials, to a superconducting ceramic oxide, and to thin films. In some cases, we will see that the most useful information is obtained when the modulus measurements are combined with those of the complementary mechanical loss or internal friction, and are studied over a wide range of temperature or frequency for the detection of relaxation, transformation, or other phenomena caused by specific structural or defect rearrangements.

Dr. Berry is a Research Staff Member at the IBM Research Division, T.J. Watson Research Center, P.O. Box 218, Yorktown Heights, New York, 10598.

With only minor variations in technique, all of the measurements reported below have been made with a vibrating-reed apparatus developed initially for the investigation of thin films of microelectronic materials supported by a high-Q substrate [1]. This apparatus has since proved adaptable to a wide variety of investigations, and the examples we shall consider below include the use of single and multilayer sample geometries.

EXPERIMENTAL METHOD

A simplified layout of the vibrating-reed apparatus is shown in Fig. 1. Each sample is secured, either by a mechanical clamp or some type of bond, to an individual pedestal base which in turn is clamped to the frame which carries the drive and detection electrodes. The electrodes are positioned around the sample with a typical gap distance of 0.5 mm to 1 mm, and are used in pairs to provide push-pull electrostatic drive and condenser microphone detection [1]. An electrostatic screen is placed between the two pairs of electrodes to minimize pickup of the drive signal. To avoid nodal positions, the drive electrodes are located at the free end of the sample, and the detection electrodes at about one-third of the sample length from the fixed end. This enables the frequency and damping measurements to be made in both the fundamental cantilever mode and a number of higher overtones. The measurements are performed in vacuum primarily to avoid atmospheric damping and to protect the sample

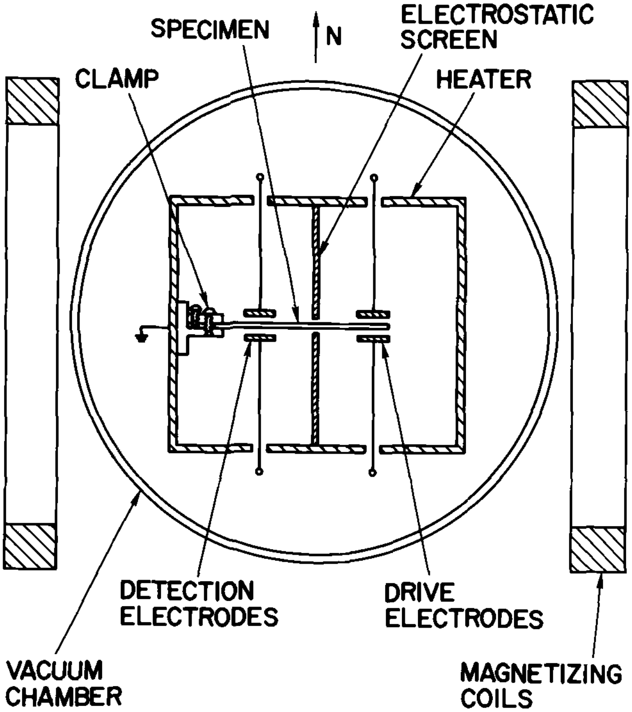

FIG. 1 Schematic layout of the vibrating-reed apparatus.

at elevated temperatures. The heater enables operation to 800K; with the provision of a conduction cooling arrangement measurements have also been made down to 40K. For measurements in a longitudinal magnetic field, the vacuum chamber (which has an external diameter of 15 cm) may be surrounded either by a pair of Helmholtz coils or by an electromagnet. A transverse field may also be obtained without reorienting the internal arrangement by placing coils concentrically around the vacuum chamber.

For the study of supported thin films, it is necessary to employ a thin-reed substrate chosen for its intrinsically high-Q behavior, and to avoid the relatively lossy mechanical clamp in favor of an integral bond. Suitable pedestal-mounted reed substrates of 50μm thickness and with Q's approaching 10^6 can be prepared from fused silica and from single-crystal silicon. These and other experimental details have recently been reviewed elsewhere [2]. Because of differences in the manner of handling the data from single-layer and multilayer samples, it is convenient to divide the presentation of results into two sections. We begin with the simpler geometry, where the test sample is wholly comprised of the material of interest.

RESULTS FOR SINGLE-LAYER SAMPLES

The dynamic Young's modulus E of a uniform reed of thickness a, length ℓ and density ρ can be calculated from the resonant frequencies f_n using the relation

$$f_n = (C_n a/\ell^2)(E/\rho)^{1/2}, \tag{1}$$

where C_n is a mode parameter whose values are listed in standard texts [3]. Furthermore, to the extent that external losses are negligible, the internal friction of the material is represented by the measured damping. This may be conveniently expressed either by the logarithmic decrement of free decay, δ, or by the inverse Q value. For small damping, these quantities are interrelated by the expression $Q^{-1} = \delta/\pi$.

The ΔE-effect in Ferromagnetic Materials

The ΔE-effect (the dependence of E on magnetization M) is one of several interrelated magnetoelastic effects that can occur in ferromagnetic materials due to the tendency of an applied stress to induce changes in the domain structure [4]. Because these changes are accompanied by a nonelastic (magnetostrictive) strain that adds to the normal elastic strain, the ΔE-effect corresponds to a reduction of the modulus to a value below that observed at saturation, E_s, where the aligned domains are held fixed by the applied field. We may thus write

$$\Delta E/E = (E_s - E)/E = (E^{-1} - E_s^{-1})/E_s^{-1}, \tag{2}$$

where the last expression is included because it is frequently more useful to think of the ΔE-effect in terms of changes in the compliance or reciprocal modulus E^{-1} rather than in terms of E itself [5, 6].

In recent years, an improved understanding of the ΔE-effect has emerged from studies of a relatively new class of materials, namely the ferromagnetic metallic glasses produced by

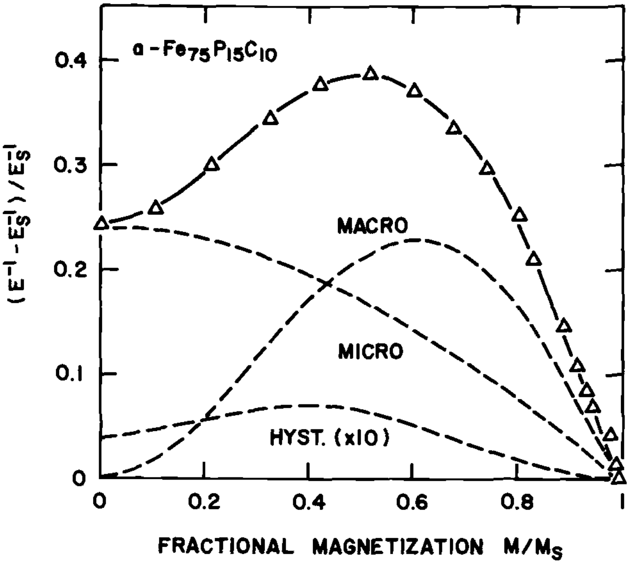

FIG. 2 The ΔE-effect shown by a strip of stress-relieved amorphous $Fe_{75}P_{15}C_{10}$ of 0.003 cm thickness, as determined by vibrating-reed measurements at approximately 400 Hz. The broken lines show the estimated contributions that, at higher frequencies, become rate-limited by macroscopic eddy-currents, microscopic eddy-currents, and hysteric domain movements. From reference [5].

rapid-solidification methods. Two factors have contributed to these advances. First, the magnitude of the ΔE-effect is frequently impressively large in these materials. For example, the magnitude of $\Delta E/E$ shown in Fig. 2 for the stress-relieved a - $Fe_{75}P_{15}C_{10}$ alloy is two orders of magnitude larger than for crystalline Fe, or for the same sample after a crystallization anneal. The second important factor relates to the small sample thicknesses (typically $\leq$ 50μm) with which most metallic glasses are produced. For such thin samples, and for the relatively low vibration frequencies realized experimentally, the eddy-current skin depth is much greater than the sample thickness. The vibrating-reed experiments are thus not subject to the shielding which tends to inhibit a macroscopic stress-induced change in the bulk magnetization. As a consequence, vibrating-reed experiments permit the observation of a total, equilibrium, or fully-relaxed ΔE-effect which includes an important "macroscopic" contribution (Fig. 2) that is typically excluded from resonant-rod measurements on thicker samples. This exclusion is clearly demonstrated in Fig. 3 which shows, for a nickel reed of intermediate thickness, a progressive reduction in the ΔE-effect as the measurement frequency is raised by the use of the fundamental mode and a series of overtones. Before leaving Figs. 2 and 3, we may note that the macroscopic ΔE-effect characteristically vanishes for both the demagnetized and saturated conditions, and passes through a maximum value at $M/M_s \simeq 0.5$. As a consequence, the low-frequency dynamic modulus of magnetically soft materials can be expected to exhibit a characteristic "modulus minimum" at intermediate magnetizations. Such minima have indeed been observed for a number of common magnetic materials [5].

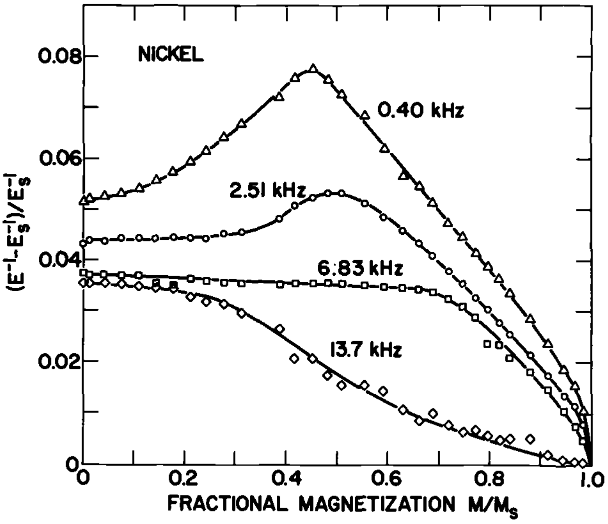

FIG. 3 The ΔE-effect shown by a strip of polycrystalline nickel of 0.152 cm thickness, as measured at four different frequencies. The changes observed are due primarily to the exclusion of the macroscopic ΔE-effect. From reference [7].

One of the earliest and most striking observations concerning the ΔE-effect is the pronounced maximum observed for nickel near 450K. This was first observed by Siegel and Quimby [8] more than 50 years ago, using an early form of the composite oscillator technique. We have reinvestigated this behavior using the vibrating-reed method and annealed high-purity samples, and have observed a ΔE-effect three times larger than that reported by Siegel and Quimby. These results are shown in Fig. 4, together with literature values for the saturation magnetostriction λ_s and a term K_c representing the magnetocrystalline anisotropy energy difference between the hard <100> and the easy <111> directions. From the behavior shown, we conclude that the rapid rise in $\Delta E/E$ on heating above room temperature is primarily associated with the decline in K_c, which enhances the contribution to $\Delta E/E$ from stress-induced domain rotation. At higher temperatures, where K_c effectively vanishes, we may postulate a switch-over to a regime in which $\Delta E/E$ is controlled by a residual internal stress σ_i, and where the decline in $\Delta E/E$ is essentially controlled by the decrease in λ_s that accompanies the approach to the Curie point. Combining earlier expressions [4] for these different regimes, we may express $\Delta E/E$ in the form

$$\Delta E/E = E_s\left\{\frac{K_c}{k_1\lambda_s^2} + \frac{\sigma_i}{k_2\lambda_s}\right\}^{-1}, \tag{3}$$

where k_1 and k_2 are constants that may be evaluated by pinning Eq. 3 to the data at two chosen temperatures (300K and 540K). As shown in Fig. 4, the calculated curve obtained by this procedure is an excellent fit to the experimental data.

To conclude our discussion of magnetic materials, it is worth recalling that the most significant use of the ΔE-effect in recent years relates to the discovery of a reversible magnetic

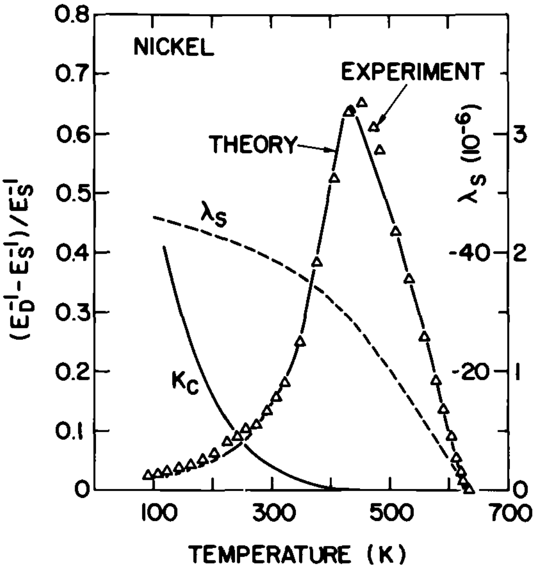

FIG. 4 Temperature dependence of the ΔE-effect in a demagnetized reed of annealed high-purity nickel, compared with the curve calculated from Eq. 3 using the magnetostriction and anisotropy parameters included above.

annealing response in metallic glasses [9-11]. Magnetic annealing (i.e. annealing in a magnetic field) provides a means of developing a uniaxial magnetic anisotropy in an amorphous alloy through the development of a state of directional short-range order. The technological importance of magnetic annealing is that it can produce improved magnetic properties along certain selected directions, and can thus enhance the performance of transformers and other non-rotating devices. Finally, we note that the ΔE-effect has also been applied in a novel manner to investigate the kinetics of the magnetic annealing process [10].

Anelastic Relaxation Behavior of a High-T_c Superconducting Oxide

Long before the discovery of high-temperature superconductivity in ceramics such as the now-famous "1-2-3" compound $Y_1Ba_2Cu_3O_{7-x}$, dynamic modulus and damping measurements had already proved useful for the study of conventional metallic superconductors such as elemental tin [12] or the A15 intermetallic compounds [13]. It is therefore not surprising that similar measurements have been promptly applied to the new high-T_c materials that are currently under intense worldwide investigation [14]. Rather than attempt a survey of this rapidly-moving field, we shall focus on one result which illustrates a quite general point; namely the importance that can sometimes attach to the joint measurement of both the modulus and the damping behavior. Figure 5 shows some of our internal friction results obtained by the vibrating-reed method on a thin strip of the 1-2-3 material. This sample was prepared from a polycrystalline sintered disc which had been annealed in oxygen to achieve a T_c near 90K. The data of Fig. 5 clearly indicate a strong damping effect in the vicinity of T_c, which immediately raises the possibility that the mechanism involved may relate directly

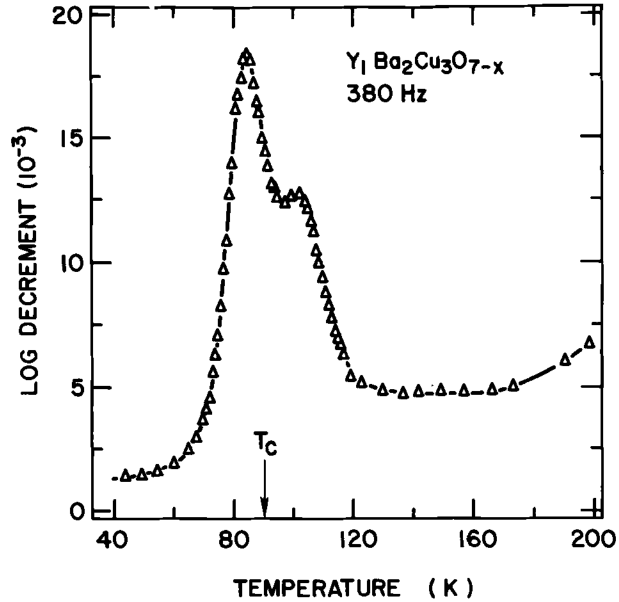

FIG. 5 The overlapping internal friction peaks exhibited in the vicinity of T_c by a polycrystalline sintered strip of the oxygen-annealed "1-2-3" superconductor, tested at a nominal frequency of 380 Hz.

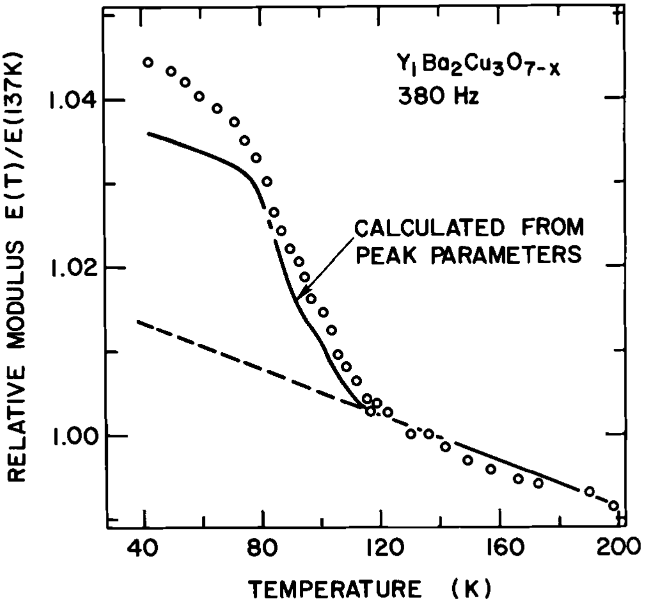

FIG. 6 Behavior of Young's modulus for the sample of Fig. 5, compared with that calculated from the peak parameters assuming thermally-activated relaxation behavior.

to the superconducting transition. On the other hand, a careful analysis of these results reveals that they can be fitted remarkably well by two overlapping and slightly broadened Debye peaks. Peaks of this shape are not usually associated with critical point phenomena, but instead are characteristic of a thermally-activated relaxation process involving the stress-induced ordering of asymmetric structural groups or defect centers [3, 15]. The basic question posed by Fig. 5 is therefore the following: Does the damping near T_c correspond to an instability associated with a phase transition, or is it due to a relaxation process which by coincidence happens to be near T_c ? To answer this question, we may consider first the evidence available from resonant frequency measurements that provide information on the complementary behavior of the dynamic modulus. Whereas phase transitions are typically associated with a dip or cusp in the modulus at T_c, relaxation produces a monotonic variation in the modulus from a larger unrelaxed value on the low-temperature side of the peak to a lower relaxed value on the high-temperature side. Furthermore, the magnitude of the relaxation strength given by the size of this change should agree with that computed independently from the shape and size of the internal friction peak. As shown by Fig. 6, such a comparison clearly indicates that we are dealing with a relaxation process. This conclusion has also been confirmed by experiments in which the peak has been observed to shift to higher temperatures as the frequency of measurement is raised by the use of overtones. The activation energies so obtained for the component peaks of Fig. 5 are 17kJ/mol and 21kJ/mol, in good agreement with the values estimated directly from the peak temperatures with the assumption of an attempt frequency of normal magnitude. Based on a systematic study involving progressive changes in the oxygen stoichiometry, an update of earlier conclusions [16] concerning the relaxation behavior of the 1-2-3 superconductor can be summarized as follows:

(i) The doublet peak of the type shown in Fig. 5 appears to be a characteristic of the fully-oxygenated material, and indicates that the 1-2-3-7 stoichiometric compound contains intrinsic disorder involving two similar but distinct defects or structural groups of low symmetry. These are capable of reorientation with such low activation energies (~ 19kJ/mol) that they are in motion at temperatures well below T_c. It seems very unlikely that such low activation energies correspond to jumps producing long-range atomic motion, and they are believed instead to indicate the presence of localized crankshaft motions of "off-center" atoms, moving over distances corresponding to only a fraction of an interatomic spacing.

(ii) The peaks of Fig. 5 undergo a well-defined sequence of changes in response to a progressive reduction in the oxygen content, and are ultimately replaced by a third strong peak at a lower temperature and with an activation energy of only 13kJ/mol. During these changes, the component peaks appear simply to change in magnitude while maintaining an approximately constant shape and location. The impression conveyed by this behavior is that deviations from stoichiometry are accommodated by changes in the relative proportions of a few distinct defect configurations which retain their basic identity over appreciable ranges of composition.

(iii) Finally, while the family of low-temperature peaks referred to above appears to represent the most intriguing aspect of the internal friction behavior, it should also be noted that another prominent peak occurs well above room temperature, in the region of 600K. This peak has an activation energy of about 125kJ/mol, which readily identifies it with the diffusive motion of oxygen atoms in the basal plane of the 1-2-3 structure, and also exhibits an interesting sequence of changes in position and strength as the oxygen deficit is varied.

RESULTS FOR SUPPORTED FILMS

The use of a composite reed, prepared by deposition of the material of interest on one or both sides of a suitably chosen substrate, has found considerable application for the dynamic mechanical analysis of thin-layer microelectronic materials [2]. Although developed independently and with widely different geometries and applications in mind, it is of interest to note a close parallel to standard testing methods that utilize an Oberst test bar [17]. For reasons of analytical simplicity and experimental convenience, the preferred configuration is that of a symmetrical trilayer, in which layers of equal thickness a_L are added to each side of a substrate of thickness a_S. For this configuration, a given mode frequency of the composite reed f_C , is related to that of the blank substrate, f_S , by the relation [2]

$$(f_C / f_S)^2 = (1 + \gamma_{ST}) / (1 + \chi_{ST}), \tag{4}$$

$$\text{where } \gamma_{ST} \equiv \{ [1 + (2a_L/a_S)]^3 - 1 \} E_L / E_S \tag{5}$$

$$\text{and } \chi_{ST} \equiv \mu_L / \mu_S = 2a_L \rho_L / a_S \rho_S. \tag{6}$$

Here, E_L, μ_L and ρ_L denote the modulus, mass/unit length and density of the added layers, and E_S, μ_S and ρ_S are the corresponding quantities for the substrate. The damping of the composite reed, δ_C is given by

$$\delta_C = \left(\frac{1}{1 + \gamma_{ST}} \right) \delta_S + \left(\frac{\gamma_{ST}}{1 + \gamma_{ST}} \right) \delta_L , \tag{7}$$

where δ_S and δ_L denote the logarithmic decrements which would be exhibited by the substrate and layers, respectively, if tested individually under otherwise identical conditions. For the important special case $a_L \ll a_S$ which represents the "thin-film limit", Eq. 5 simplifies to

$$\gamma_{ST} = 6a_L E_L / a_S E_S , \tag{8}$$

and Eqs. 4 and 7 can be put in this form

$$(f_C / f_S)^2 - 1 = n_L \left(\frac{3E_L}{E_S} - \frac{\rho_L}{\rho_S} \right) \frac{a_L}{a_S} \tag{9}$$

and

$$\delta_C - \delta_S = 3n_L \left(\frac{a_L E_L}{a_S E_S} \right) \delta_L , \tag{10}$$

where the coefficient n_L is set equal to 2 for the situation in which both sides of the substrate carry a layer a_L. For the thin-film limit, Eqs. 9 and 10 also apply, with $n_L = 1$, to the case of a layer a_L on only one side of the substrate.

It is evident from Eq. 10 that, provided a substrate of sufficiently low damping is available, the observed damping of the composite will be dominated by the behavior of δ_L. On the other hand, the determination of the modulus E_L by the use of Eq. 9 can present greater difficulty. One reason is that the difference between f_C and f_S is usually quite small. Secondly, it is evident from Eq. 9 that this difference involves two factors; a positive contribution from the stiffness term E_L/E_S and a negative contribution from the inertia term ρ_L/ρ_S. In favorable circumstances, such as those discussed below, the stiffness term is the dominant effect. However, this is not the case for films of the heavy metals, such as gold or lead.

Measurements on Aluminum Films

Because of its low density and a near absence of elastic anisotropy, aluminum provides a favorable material with which to test Eqs. 4 or 9. The results of Fig. 7 were obtained with high-purity evaporated aluminum films deposited in the symmetrical trilayer configuration on calibrated fused silica reeds of 50μm thickness. The increase observed in the reed frequencies is seen to agree satisfactorily with the behavior calculated with assumption that the films possess normal (bulk) values of density and Young's modulus. The lower calculated line in Fig. 7 is included to show the magnitude of the inertia loading term in relation to the stiffening effect provided by the modulus.

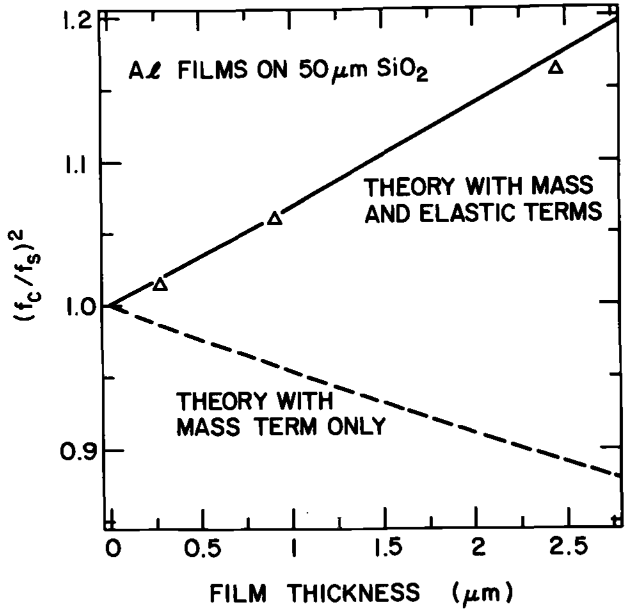

FIG. 7 A test of Eq. 4 for the symmetrical trilayer configuration obtained by evaporating aluminum films of equal thickness on both sides of a thin reed substrate of fused-silica.

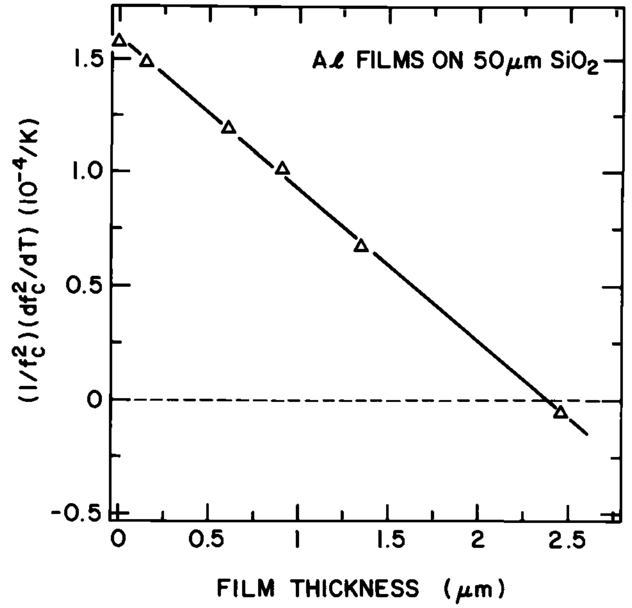

FIG. 8 The temperature coefficient of f_c^2 for symmetrical trilayer samples of aluminum on fused silica, demonstrating the null obtained near a film thickness of 2.5 μm.

In an extension of these measurements, we have found that it is possible to fabricate a composite reed oscillator of remarkable temperature stability, as may be of interest for some electromechanical applications. This temperature-compensated condition is achieved with a reed geometry that leads to a cancellation of the opposing effects of temperature on the moduli of the fused silica substrate and the deposited films. Figure 8 shows that the compensated condition for 50 μm reeds of fused silica is obtained with aluminum films of approximately 2.5 μm thickness on each face of the reed.

Elasticity and Structural Relaxation of Silicon Monoxide Films

As discussed earlier in this section, a determination of the Young's modulus of a thin film by the composite vibrating-reed method requires measurement of the reed frequencies before and after deposition of the film. Although fused silica is often a desirable choice for a substrate, its electrically insulating character means that blank reeds cannot be measured by the normal electrostatic excitation and detection methods applied to conducting samples. Our initial approach to this problem was to excite the blank reed mechanically (simply by tapping the vacuum chamber), and to determine the frequency stroboscopically. A major limitation of this approach is its restriction to the fundamental mode. Fortunately, this difficulty has been resolved by the discovery of a conditioning or activation treatment that produces frozen-in charges on the blank reed. This enables measurements to be made in a sequence of modes using essentially the same procedure as that employed for conducting samples [18]. An important additional advantage of this procedure is that it provides a means for the study of dielectric films, as in the work of Lacombe and Greenblatt on various polymeric materials [19]. We shall consider here the inorganic thin-film dielectric silicon monoxide. Unlike its better known relative SiO_2, the vapor pressure of the monoxide SiO is high enough for films to be prepared in vacuum from a sublimation source. The measurements of Fig. 9 were made possible by the activation procedure mentioned above, and were obtained at the third overtone of the sample before and after deposition of the films. The increase in the frequency of the blank reed with temperature is a direct indication of the unusual temperature dependence shown by the Young's modulus of fused silica. This behavior is also exhibited by the composite reed, due to the dominant effect of the substrate. Deposition of the films is seen to produce an increase of over 5% in the reed frequency, indicating that the stiffness term in Eq. 9 exceeds the inertia term. For the as-deposited condition, the modulus of SiO is found to be 92 GPa, which is significantly higher than that of fused silica (73 GPa). The temperature coefficient $(1/E)\ dE/dT$ is also of considerable interest in view of the unusual positive coefficient ($+\ 1.7 \times 10^{-4}$ /K) exhibited by fused silica. It appears from the present measurements that SiO is almost at the crossover point to more normal behavior, with a small but negative coefficient of about -2×10^{-5} /K.

The upper two curves of Fig. 9 illustrate that subsequent annealing treatments produced a significant increase in the modulus of the as-deposited films. Results for a sequence of isochronal anneals up to 1073K are shown in Fig. 10. It can be seen that the modulus increased by 17% in a smooth sigmoidal manner to a final value of 108 GPa. At the same time, large complementary changes occurred in the internal friction behavior [2]. Together, these changes are clear indicators of a structural relaxation to a denser and stiffer configuration

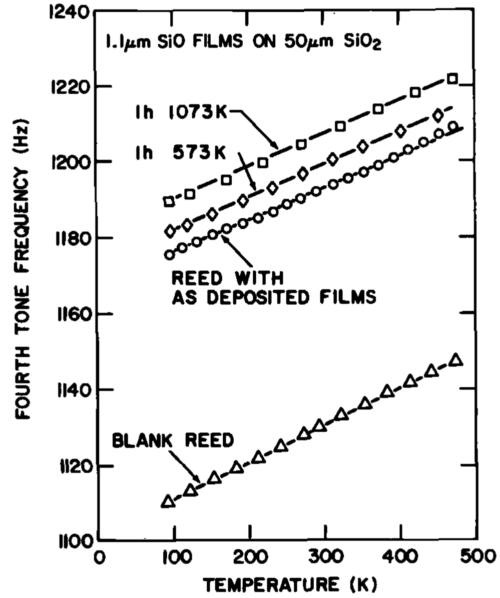

FIG. 9 Vibrating-reed data for SiO films deposited in the symmetrical trilayer configuration on a blank substrate of fused silica. The frequency increase produced by the post-deposition anneals reflects an increase in the film modulus due to structural relaxation.

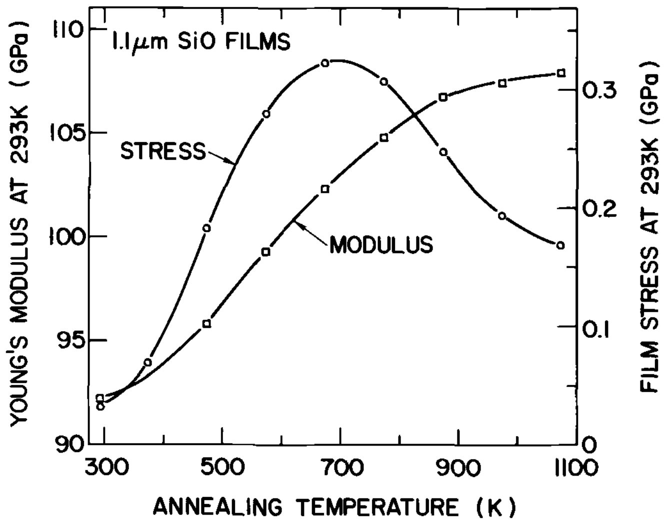

FIG. 10 Comparison of the effect of 1-hour isochronal anneals on the room-temperature modulus and internal stress of SiO films deposited on fused silica substrates.

containing less free volume. To verify that densification occurred, sister samples have been studied by the bending-bilayer method to observe the effect of annealing on the film stress. As shown in Fig. 10, the tensile stress in the SiO films was found to increase by almost an order of magnitude before passing through a pronounced maximum near 673K due to the onset of stress relaxation by viscous flow. The increase of stress observed at lower temperatures is a direct indication of densification with elastic accommodation of the shrinkage strain. The density change calculated from the maximum increase of stress in Fig. 10 is 0.7%; from this we may estimate that the total increase of 17% in the modulus is associated with a density increase of about 1.5%.

CONCLUDING REMARKS

The purpose of this article has been to show by the use of a few examples that the dynamic modulus, particularly when combined with the dynamic loss or internal friction, is an important tool in materials research. The examples chosen have been taken from the author's work primarily on the grounds of familiarity; without doubt other writers would have made an entirely different selection for much the same reason. The collective proceedings of this Symposium will therefore provide the reader with a broader and more balanced perspective of the field as a whole than has been attempted here.

ACKNOWLEDGEMENT

It is a pleasure to acknowledge the participation of my colleague W. C. Pritchet in much of the work described in this article.

REFERENCES

[1] Berry, B. S. and Pritchet, W. C., "Vibrating Reed Internal Friction Apparatus for Films and Foils", IBM Journal of Research and Development , Vol. 19, 1975, pp. 334-343.

[2] Berry, B. S. "Anelastic Relaxation and Diffusion in Thin-Layer Materials", in Diffusion Phenomena in Thin Films and Microelectronic Materials , edited by D. Gupta and P. S. Ho, Noyes Publications, Park Ridge, New Jersey, 1988, pp. 73-145.

[3] Nowick, A. S. and Berry, B. S., Anelastic Relaxation in Crystalline Solids , Academic Press, New York, 1972.

[4] Bozorth, R. M., Ferromagnetism , Van Nostrand, Princeton, New Jersey, 1951, pp. 684-712.

[5] Berry, B. S. and Pritchet, W. C., "Magnetoelasticity and Internal Friction of an Amorphous Ferromagnetic Alloy", Journal of Applied Physics , Vol. 47, 1976, pp. 3295-3301.

[6] Berry, B.S., "Elastic and Anelastic Behavior", in Metallic Glasses , edited by J. J. Gilman and H. J. Leamy, American Society for Metals, Metals Park, Ohio, 1978, pp. 161-189.

[7] Berry, B. S. and Pritchet, W. C., "ΔE-Effect and Macroeddy-Current Damping in Nickel", Journal of Applied Physics , Vol. 49, No. 3, 1978, pp. 1983-1985.

[8] Siegel, S. and Quimby, S. L., "Variation of Young's Modulus with Magnetization and Temperature in Nickel", Physical Review , Vol. 49, 1936, pp. 663-670.

[9] Berry, B. S. and Pritchet, W. C., "Magnetic Annealing and Directional Ordering of an Amorphous Ferromagnetic Alloy", Physical Review Letters , Vol. 34, 1975, pp. 1022-1025.

[10] Berry, B. S. and Pritchet, W. C., "Magnetoelastic Phenomena in Amorphous Alloys", American Institute of Physics Conference Proceedings No. 34 , edited by J. J. Becker and G. H. Lander, American Institute of Physics, New York, 1976, pp. 292-297.

[11] Berry, B. S. and Pritchet, W. C., U.S. Patent 3,820,040, June 25, 1974 and U.S. Patent 4,033,795, July 5, 1977.

[12] Mason, W. P. and Bömmel, H. E., "Ultrasonic Attenuation at Low Temperatures for Metals in the Normal and Superconducting States", Journal of the Acoustical Society of America , Vol. 28, 1956, pp. 930-943.

[13] Testardi, L. R., "Structural Instability of A-15 Superconductors", in Physical Acoustics edited by W. P. Mason and R. N. Thurston, Academic Press, New York, 1977, Vol. 13, pp.29-47.

[14] Ledbetter, H., "Elastic Properties of Metal-Oxide Superconductors", Journal of Metals , Vol. 40, No. 1, 1988, pp. 24-30.

[15] For an elementary introduction, see Berry, B. S., "Atomic Diffusion and the Breakdown of Hooke's Law", The Physics Teacher , Vol. 21, No. 7, 1983, pp. 435-440.

[16] Berry, B. S., "Defect-Related Anelastic Behavior of Superconducting Oxides", Bulletin of the American Physical Society , Vol. 33, No. 3, 1988, p. 512.

[17] "Standard Method for Measuring Vibration-Damping Properties of Materials", ASTM Standard, Designation E756-83, American Society for Testing and Materials, Philadelphia, 1983, pp. 1-10.

[18] Berry, B. S. and Pritchet, W. C., "Extended Capabilities of a Vibrating Reed Internal Friction Apparatus", Review of Scientific Instruments , Vol. 54, No. 2, 1983, pp. 254-256.

[19] Lacombe, R. and Greenblatt, J., "Mechanical Properties of Thin Polyimide Films", in Polyimides , edited by K. L. Mittal, Plenum, New York, 1984, Vol. 2, pp. 647-670.

Vikram K. Kinra and Vinay Dayal

MEASUREMENT OF THE MODULUS OF DYNAMIC ELASTICITY OF EXTREMELY THIN (SUB-WAVELENGTH) SPECIMENS

REFERENCE: Kinra, V.K. and Dayal, V., "Measurement of the Modulus of Dynamic Elasticity of Extremely Thin (Sub-Wavelength) Specimens," Dynamic Elastic Modulus Measurements in Materials, ASTM STP 1045, Alan Wolfenden, editor, American Society for Testing and Materials, Philadelphia, 1990.

ABSTRACT: The current methods of ultrasonic modulus measurement make, implicitly or explicitly, the following key assumption: The front-surface and the back-surface reflections of an incident pulse are separable in the time-domain, i.e., the plate is several wavelengths thick. By combining standard ultrasonic methods with the theory of Fourier Transforms, a new technique has been developed which removes the preceding restriction. The theoretical and the experimental procedures are described in detail. The efficacy of the method is demonstrated for three disparate materials: (1) non-attenuative, non-dispersive; (2) weakly attenuative, non-dispersive; and (3) highly attenuative, highly dispersive.

KEYWORDS: thin specimens, sub-wavelength, sub-millimeter, ultrasonic, dispersion, attenuation, Fourier transform, frequency dependence, dynamic versus static modulus

---

Dr. V.K. Kinra is Associate Professor, Department of Aerospace Engineering, Texas A&M University, College Station, Texas 77843, (409) 845-1667.
Dr. V. Dayal is Assistant Professor, Department of Aerospace Engineering, Iowa State University, Ames, IA 50011.

Nomenclature

$F^*(\omega)$	Fourier transform of $f(t)$
$G^*(\omega)$	Fourier transform of $g(t)$
M	modulus of a complex number
N	number of digitizing points
R_{ij}	Reflection coefficient in medium i from medium j
T_{ij}	Transmission coefficient for a wave incident in medium i and transmitted into medium j
T	sampling interval in time domain, ns
T_0	signal length, μs
a	a characteristic length of the microstructure, mm
c,	longitudinal phase velocity in specimen, mm/μs
c_1, c_2	longitudinal and shear phase velocity in specimen, mm/μs
c_0	longitudinal phase velocity of wave in water mm/μs
c_g	group velocity in specimen, mm/μs
f	frequency, MHz
f_c	cut-off frequency, MHz
Δf	frequency resolution, MHz
h	plate thickness, mm
i	$\sqrt{-1}$
k	complex wavenumber, $k_1 + ik_2$, mm^{-1}
k_1	ω/c, real part of wavenumber in specimen, mm^{-1}
k_2	attenuation coefficient, nepers/mm
k_0	wavenumber in water, real, mm^{-1}
m	integer number of complete round trips taken by the wave across the plate thickness
t	time, μs
u	particle displacement
x	distance
$\bar{\sigma}$	standard deviation of a data sample
Ω	normalized frequency, $\omega a/c_1$
λ	wavelength, mm
ξ	normalized wavenumber, $\omega a/\langle c_1\rangle$
ρ	density of specimen, g/ml
ρ_0	density of water, g/ml
ϕ	phase of a complex number
ω	circular frequency, rad/μs
$\langle\ \rangle$	aggregate property of a composite

INTRODUCTION

The elastic moduli of an isotropic material can be obtained by measuring the speed of longitudinal and shear waves, and density. The measurement of two wavespeeds is equivalent to measuring the two elastic moduli. The classical method of measuring the speed of sound in non-dispersive media is the time-of-flight method, see Reference [1] for example. We note that in a non-dispersive isotropic medium the phase velocity and the group velocity are identical [2]. When the material is either dispersive (wavespeed depends upon frequency) or exhibits frequency - dependent attenuation this method breaks down and a suitable method then is the so-called toneburst method. Here, a burst of pure tone, typically about ten cycles in duration is used; this places a constraint on the specimen thickness. It must be thick enough so that the toneburst reflections from the two faces of the specimen can be clearly separated in time-domain i.e. it should be roughly five-wavelength thick. For example, in steel at, say, one MHz frequency, the required minimum thickness would be about 30 mm. There are many situations of practical importance where one must conduct an ultrasonic examination of specimens which are considerably thinner than 30 mm or five wavelengths. For example, aircraft and aerospace structures using graphite/epoxy or metal-matrix composites employ panels as thin as one mm. By combining standard FFT methods with conventional ultrasonics we have developed a method by which one can measure the dynamic modulus of thin specimens (sub-millimeter or sub-wavelength in thickness). A detailed description of this technique is the central objective of this paper. We will illustrate the use of this technique on three distinctly disparate materials: an aluminum, an epoxy, and a particulate composite. It will be demonstrated that this technique works equally well for thin or thick specimens, and for dispersive as well as non-dispersive media.

THEORY

Consider an infinite elastic plate (whose dynamic modulus needs to be measured) immersed in an elastic fluid (water). A Lagrangian diagram indicating the space-time location of a wavefront which occupied the position x=0 at time t=0 is shown in Fig. 1. A plane-fronted, finite-duration pulse, ray 1, is normally incident on the plate. This results in an infinite series of reflected and transmitted pulses. The expressions for the reflection and transmission coefficients of a displacement wave for perfectly elastic media may be found in Achenbach's book [3]. Let the displacement in the incident field be given by

$$u^{inc} = f_o(\omega t - k_o x) \qquad (1)$$

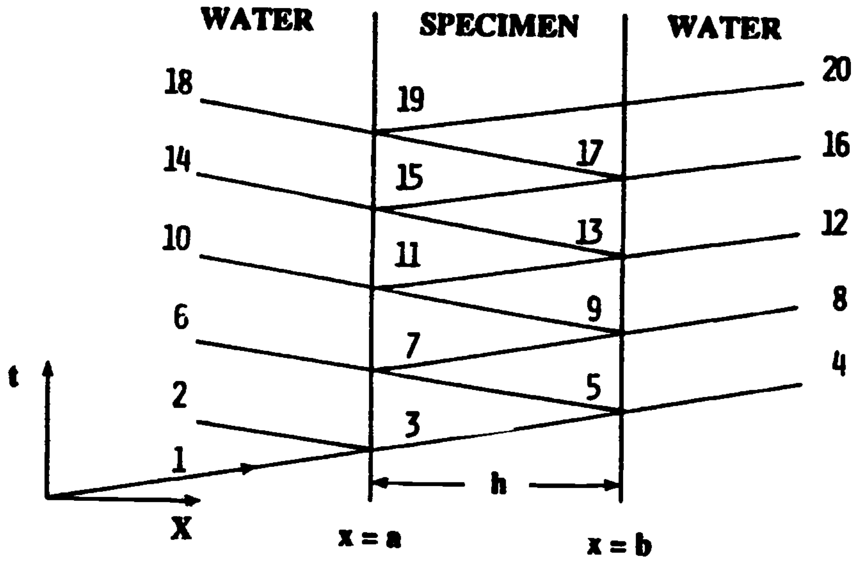

FIG. 1 -- Various reflections and transmissions from a plate immersed in water.

where $f_o(s) \equiv 0$ for $s<0$. Here ω is the circular frequency and k_o is the wavenumber of a monochromatic harmonic wave in water; $c_o = \omega/k_o$. The displacement field along the various reflected rays may be written as

$$u_2 = R_{12} f_o(s-s_2);\ s_2 = 2k_o a$$

$$u_6 = T_{12} R_{21} T_{21} f_o(s-s_6);\ s_6 = 2k_o a + 2kh \qquad (2)$$

$$u_{10} = T_{12} R_{21}^2 T_{21} f_o(s-s_{10});\ s_{10} = 2k_o a + 4kh$$

$$\vdots$$

$$u_\infty$$

Here, $s = \omega t + k_o x$, $h = b-a$ is the plate thickness, R_{ij} is the reflection coefficient in medium i from medium j, T_{ij} is the transmission coefficient for a wave incident in medium i and transmitted into medium j, $k=\omega/c$, c is the phase velocity in the plate, and

$$R_{12} = \frac{\rho_o c_o - \rho c}{\rho_o c_o + \rho c} = -R_{21},$$

$$T_{12} = \frac{2\rho_o c_o}{\rho_o c_o + \rho c} = 2 - T_{21}, \qquad (3)$$

where ρ_o and ρ are, respectively, the density of water and the plate material. The entire reflected field, $u^r = u_2 + u_6 + u_{10} + \ldots u_\infty$, may be written as

$$u^r = R_{12} f_o(s-s_2) + T_{12} R_{21} T_{21} \sum_{m=1}^{\infty} R_{21}^{m-1} f_o(s-s_m), \qquad (4)$$

$$s_m = 2\ k_o a + m\ 2kh.$$

In an exactly analogous manner, one can write down the expressions for the transmitted pulses. With $s = \omega t - k_o x$

$$u_4 = T_{12} T_{21} f_o(s-s_4);\ s_4 = h(k-k_o)$$

$$u_8 = T_{12}\ R_{21}^2\ T_{21}\ f_o(s-s_8);\ s_8 = h(3k-k_o) \qquad (5)$$

$$u_{12} = T_{12}\ R_{21}^4\ T_{21}\ f_o(s-s_{12});\ s_{12} = h(5k-k_o)$$

$$\vdots$$

$$u_\infty$$

The total transmitted field may be written as

$$u^t = T_{12}\, T_{21} \sum_{m=0} R_{21}^{2m}\; f_o(s-s_m),$$

$$s_m = h\,[(2m+1)\; k-k_o] \qquad (6)$$

In eqs (4) and (6) m is the number of <u>complete round trips</u> taken by the wave across the plate thickness h.

The Fourier transform of a function f(t) is defined as

$$F^*(\omega) = \frac{1}{\sqrt{2\pi}} \int_{-\infty}^{\infty} f(t)\; \bar{e}^{i\omega t} dt, \; - \infty<\omega<\infty \qquad (7a)$$

with the associated inverse transform given by,

$$f(t) = \frac{1}{\sqrt{2\pi}} \int_{-\infty}^{\infty} F^*(\omega)\; e^{i\omega t} d\omega, \; - \infty < t < \infty \qquad (7b)$$

Analysis for Thick Specimens

We first consider the case of a relatively thick specimen such that various pulses in Fig. 1 can be clearly separated from each other in the time-domain. Let f(t) be the signal corresponding to ray 2 and g(t) be the signal corresponding to rays 2 and 6 combined sensed by a transducer at x=0. (This is the so-called pulse-echo mode). Then

$$f(t) = R_{12}\; f_o(\omega t - 2k_o a), \qquad (8)$$

and

$$g(t) = T_{12}R_{21}T_{21}f_o(\omega t - 2k_o a - 2kh) + f(t). \qquad (9)$$

Let $F^*(\omega)$, $G^*(\omega)$ and $F_o^*(\omega)$ be the Fourier transforms of f(t), g(t) and $f_o(t)$, respectively. Then, a straightforward application of the shifting theorem for Fourier transforms yield

$$F^*(\omega) = R_{12}\; e^{-i2k_o a} F_o^*\,(\omega) \qquad (10)$$

$$G^*(\omega) = R_{12}F_o^*(\omega)\; e^{-i2k_o a}\,[1 - T_{12}T_{21}\bar{e}^{i2kh}] \qquad (11)$$

and $$\frac{G^*(\omega)}{F^*(\omega)} = 1 - T_{12}T_{21}e^{-i2kh} \tag{12}$$

It is emphasized that in the foregoing it is assumed that the plate behaves in a perfectly elastic manner i.e. the wavenumber k is real and $c=\omega/k$ is a constant. The key term in eqs (11) and (12) is e^{-i2kh} or $e^{-i2h\omega/c}$. Thus, in eq (11) if one plots $|G^*(\omega)|$ vs ω it will be characterized by a series of resonance peaks whose spacing is given by $\Delta(2h\omega/c) = 2\pi$, or in view of $\omega = 2\pi f$, by

$$c = 2h\,\Delta f \tag{13}$$

Measurement of the longitudinal wavespeed c in aluminum using eq (13) is illustrated in Fig. 2. Here $F(\omega) = |F^*(\omega)|$ and $G(\omega) = |G^*(\omega)|$.

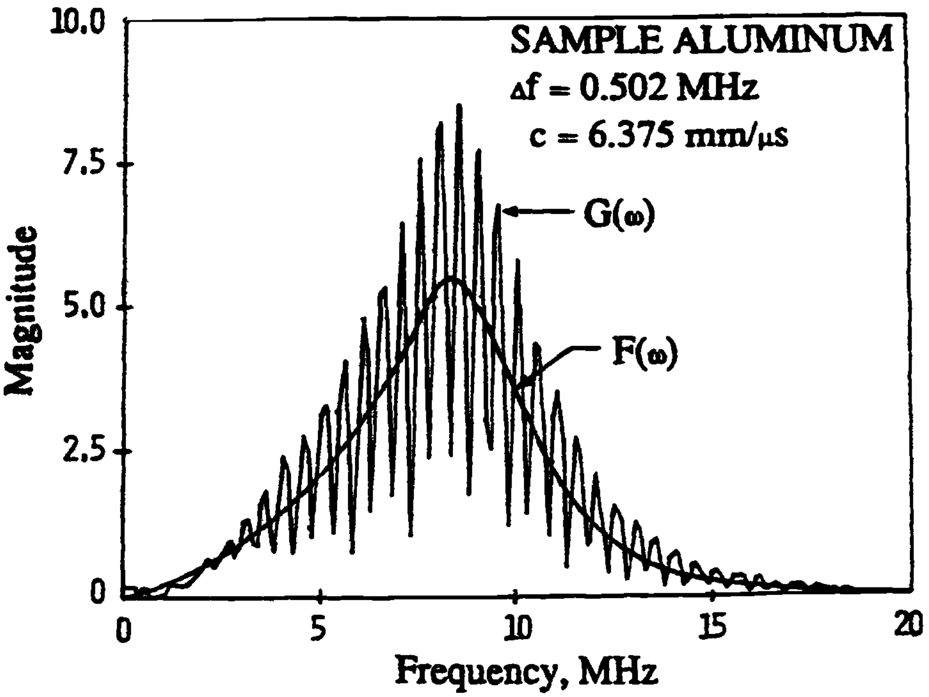

FIG. 2 -- Magnitudes of fourier transforms of f(t) and g(t) when pulses can be separated.

Note that $G(\omega)$ consists of the transducer response, $F(\omega)$, superimposed by an oscillation due to $e^{-i2h\omega/c}$ term.

A further improvement in the measurement method can be achieved by plotting $(G^*(\omega)/F^*(\omega) - 1)$, eq (12). This is illustrated in Fig. 3. By taking out the shape of the transducer response we are left with oscillations due to the constructive and destructive interference between the front-surface (ray 2) and back-surface reflections (ray 6).

Even though eq (12) is derived for an elastic material, by a straightforward application of the Correspondence Principle of the theory of Linear Viscoelasticity, it may be shown that it is rigorously valid for a linear viscoelastic material provided the damping is small i.e. in $k=k_1+ik_2$, $k_2/k_1<<1$ [13]. We rewrite eq (12) as

$$\bar{e}^{i2kh} = - (G^*(\omega)/F^*(\omega) - 1)/T_{12}T_{21} = Me^{i\phi} \quad (14a)$$

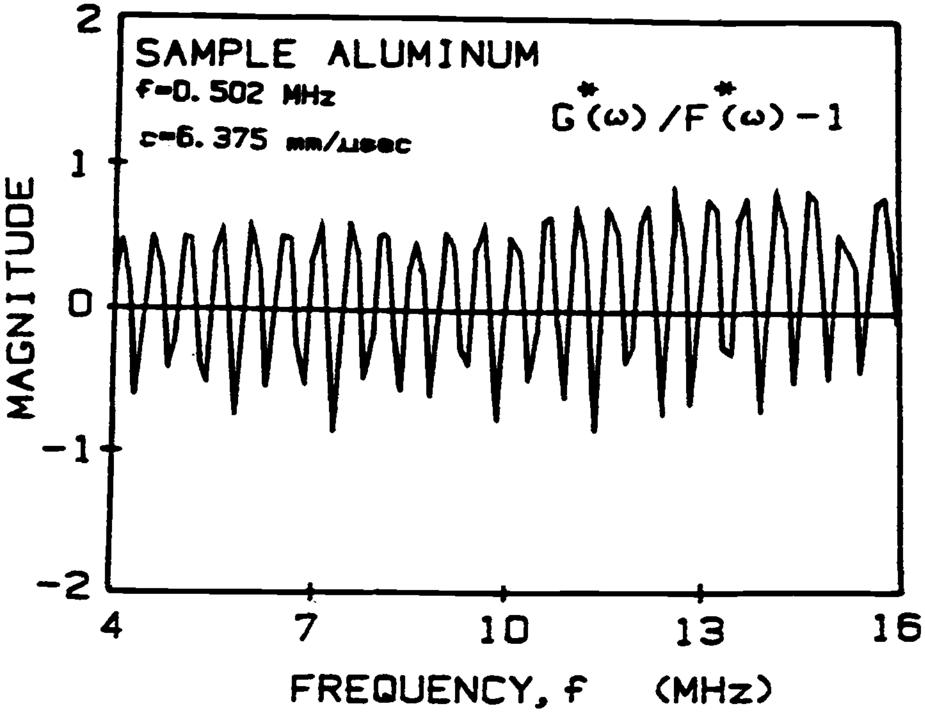

FIG. 3 -- Magnitude of $(G^*-F^*)/F^*$ from fig. 2 i.e. fourier transform after deconvolution. Resonance spacing can be measured more accurately from the zero line crossing.

Then, by equating real and imaginary parts

$$k_1(\omega) = -\phi/2h$$

and $$k_2(\omega) = (\ln M)/2h, \qquad (14b)$$

where $M = |[(G^*(\omega)/F^*(\omega)) - 1]/T_{12}T_{21}|$

Since $k_1(\omega) = \omega/c$ and $\omega = 2\pi f$

$$c(\omega) = \frac{4\pi h}{(-\phi/f)}, \qquad (15a)$$

and $$k_2(\omega) = (\ln M)/2h. \qquad (15b)$$

These are the desired equations for calculating the phase velocity and the attenuation.

Now consider the transmitted field for a thick specimen. Two measurements are made. In the first, the specimen is removed from the water path i.e. the wave travels solely through water. Let the receiving transducer be located at some $x = l > b$. Then $u^{inc}(l,t) \equiv f(t) = f_o(\omega t - k_o l)$ The specimen is now inserted in the wavepath and the signal due to ray 4 alone is recorded. Thus, $u^4(l,t) \equiv g(t) = T_{12}T_{21}f_o(\omega t - k_o l - 2k_o a - kh)$. Then,

$$\frac{G^*(\omega)}{F^*(\omega)} = T_{12}T_{21}e^{-i(kh+k_o h)} \qquad (16)$$

If $\dfrac{G^*(\omega)e^{ik_o h}}{F^*(\omega)T_{12}T_{21}}$ is set equal to $Me^{i\phi}$ then

$$k_1(\omega) = -\phi/h \qquad (17a)$$

and $$k_2(\omega) = (\ln M)/h \qquad (17b)$$

where $M = \left|\dfrac{G^*(\omega)}{F^*(\omega)}\right|/T_{12}T_{21}$.

Substituting $k_1 = 2\pi f/c$, we get

$$c = \frac{2\pi h}{(-\phi/f)} \qquad (18a)$$

and $$k_2(\omega) = (1/h)\ \ell nM \qquad (18b)$$

In the foregoing, since two independent measurements are necessary, the random errors are doubled. In the following, we propose a variation on this theme wherein $k_1+i\ k_2$ can be deduced from a single experiment, resulting in an improved accuracy.

With reference to eqns. (3) and (5), when the acoustic impedance of the plate is comparable to that of water the first transmitted signal (Ray 4) is very large but the successive transmissions (Ray 8, etc) are small and one is forced to use the method described above. Note that $u^8/u^4 = R_{21}^2$. If $\rho c >> \rho_o c_o$ then R_{21}^2 is a significant fraction of unity and u^8 remains comparable to u^4. (For example, for the case of aluminum in water, $\rho c/\rho_o c_o = 11.43$, $R_{21} = 0.83$ and $R_{21}^2 = 0.69$). Under such circumstances u^4 may be viewed as the incident field and the following approach yields more accurate results. Let f(t) and g(t) be, respectively, the signals corresponding to rays 4 and 8, let $F^*(\omega)$ and $G^*(\omega)$ be their Fourier transforms, then

$$\frac{G^*(\omega)}{F^*(\omega)} = R_{21}^2\ \bar{e}^{i2kh} \qquad (19)$$

As before, if we set $G^*(\omega)/F^*(\omega)\ R_{21}^2 = Me^{i\phi}$ then, Eq. (15) can be used to calculate the wavespeed and attenuation. In the following for brevity, these methods will be referred to as Separable Pulse Method (SP).

We note that this method is equally effective for dispersive media. From eq (14) one plots k_1 vs. ω. A secant to the curve yields inverse of the phase velocity (phase slowness). For dispersive media a quantity of interest is the group velocity. This is the speed with which energy propagates in a medium, $c_g = \partial\omega/\partial k_1$; this too can be computed from the phase plot, and eq (14b) yields frequency dependent attenuation. Finally, we introduce a normalized attenuation $k_2\lambda$. This is the attenuation of a wave over one wavelength. The motivation for this particular normalization is that for most engineering materials, such as epoxies and plastics, $k_2\lambda$ is independent of frequency.

Analysis for Thin Specimens

In this paper the qualifiers "thick" and "thin" are used in the following sense. When various reflections or transmissions corresponding to a short duration pulse can be separated in the time-domain, the specimen is considered thick. However, the duration (or length) of the pulse depends on the center-frequency of the transducer. Hence, with reference to the absolute dimensions of the specimen the use of the word "thick" is quite arbitrary. On the other hand, the word "thick" is not arbitrary with respect to the wavelength: a specimen is considered thick if $h>3\lambda$.

The total reflected field comprising rays 2, 6, 10, 14 ..... ∞ at x=0 is given by eq (12) as

$$u^r(o,t) \equiv g(t) = R_{12} f_o(\omega t-2k_o a) +$$

$$T_{12}R_{21}T_{21}\sum_{m=1}^{\infty} R_{21}^{2(m-1)} f_o(\omega t-2k_o a-m2kh) \qquad (20)$$

Note that ray 2 cannot be used as the reference signal because it cannot be separated from the subsequent rays. One has to conduct a separate experiment as follows: the thin coupon is replaced by a thick coupon with the front surface precisely at x=a. Let the front surface reflection be labeled f(t), then

$$f(t) = R_{12} f_o(\omega t-2k_o a)$$

$$F^*(\omega) = R_{12} e^{-i2k_o a} F_o^*(\omega)$$

$$G^*(\omega) = F^*(\omega) + T_{12}R_{21}T_{21}\sum_{m=1}^{\infty} R_{21}^{2(m-1)} F_o^*(\omega)\, e^{i[2k_o a+m\,2kh|} \qquad (21)$$

Let $$Z = R_{21}^2\, \bar{e}^{i2kh},\ |Z|<1, \qquad (22)$$

Then, $$\frac{G^*}{F^*} - 1 = \frac{T_{12}T_{21}}{R_{12}R_{21}} \sum_{m=1}^{\infty} Z^m$$

Observing that for $|Z| < 1$, $(1-Z)^{-1} = 1+Z+Z^2 + \ldots\infty$, and defining

$$\beta = \frac{R_{12}R_{21}}{T_{12}T_{21}}\left(\frac{G^*(\omega)}{F^*(\omega)} -1\right)$$

we get $$Z = \frac{\beta}{1+\beta} \qquad (23)$$

From Z one can readily calculate the complex-valued wavenumber k(ω).

For completeness we include here a variation of this method. Suppose a thick coupon to obtain a reference signal is not available. One can then use a thick specimen of some other material, for example, aluminum. Let the acoustic impedance of this material be $\rho_1 c_1$. Let the front-surface reflection be $f(t)=Rf_0(\omega t-2k_0 a)$ where the reflection coefficient $R = (\rho_0 c_0 - \rho_1 c_1)/(\rho_0 c_0 + \rho_1 c_1)$, and g(t) is still given by eq (18). As before with

$$\beta = \frac{R_{12}R_{21}}{T_{12}T_{21}}\left[\frac{R}{R_{12}}\;\frac{G^*(\omega)}{F^*(\omega)} -1\right], \tag{24}$$

$$Z = R_{21}^2\, e^{-ikh} = \beta/(1+\beta). \tag{25}$$

In the following, for brevity, these methods will be referred to as Non-Separable Pulse Method (NSP).

We now consider the transmitted field. Here a second transducer is used as a receiver at some $x = l>b$. To obtain a reference signal the specimen is removed and the signal through water is recorded.

$$f(t) = u^{inc}(l,t) = f_0(\omega t-k_0 l)$$

Let g(t) be the total transmitted field, rays 4, 8, 12, ...∞ then from eq (6)

$$g(t) = T_{12}T_{21}\sum_{m=0}^{\infty} R_{21}^{2m}\, f_0[\omega t-k_0 l-h\{(2m+1)k-k_0\}], \tag{26}$$

and

$$\frac{G^*(\omega)}{F^*(\omega)} = \frac{T_{12}T_{21}e^{-ih(k-k_0)}}{1-R_{21}^2\, e^{-i2kh}}\;. \tag{27}$$

We note one major difference between eqs (23) and (27). Unlike eq (23), eq (27) is a quadratic in Z = exp(-ikh). This presents some additional numerical problems. Equation (27) may be rewritten as

$$Z^2 + ZY - D_o = 0,$$

where
$$Y = \frac{T_{12}T_{21}}{R_{21}Z_o}\,\frac{F^*(\omega)}{G^*(\omega)}, \qquad (28)$$

$$Z_o = \exp(-ihk_o),$$

$$D_o = 1/R_{21}^2,$$

and k_0 is the wavenumber in water. Since the phase velocity in water is known, Z_0 is known a priori. If the acoustic impedance of the plate, ρc, was known, one could calculate T_{ij} and R_{ij}. However, c is precisely the unknown we are seeking to measure. This problem could be solved by a simple iteration procedure. An approximate phase velocity was initially used in the algorithm to estimate T_{ij} and R_{ij}. The quadratic equation (28) is solved and two roots of Z are obtained. The correct root is chosen based on the fact that the phase of Z decreases as frequency increases (for the other root, the converse is true). This velocity is used for the next iteration cycle. This procedure converges very rapidly. When we purposely supplied an initial phase velocity with a very large error (30%), the convergence was found to occur in about five iterations. More realistically, the wavespeed can be estimated to within five percent. Here convergence to within 0.01 percent occurs within three or four iterations. When the value of c obtained by this procedure was substituted back into eq (28) to calculate attenuation, $k_2\lambda$ was found to be an oscillatory function of frequency for a linear viscoelastic material, namely, an epoxy. Now, it is well-known that for such a material $k_2\lambda$ is a constant. The oscillating nature of $k_2\lambda$ could, however, be readily explained as follows. A detailed numerical examination of eq (28) revealed that the calculation of $k_2\lambda$ is very sensitive to small variation in the phase velocity c. The oscillations were due to the fact that the measured velocity was different from the true velocity. This problem could be resolved in the following manner. If one takes the absolute value of both sides, eq (25) can be re-written as follows:

$$\cos\frac{4\pi hf}{c} + \frac{1}{2}\left(\frac{T_{12}T_{21}}{R_{21}}\right)^2\left|\frac{F^*(\omega)}{G^*(\omega)}\right| = \frac{1}{2}\left[R_{21}^2e^{qf} + \frac{1}{R_{21}^2e^{qf}}\right] \qquad (29)$$

where $q = 2h\, k_2\lambda/c$.
The terms in eq (29) have been separated judiciously as follows. The left hand side (LHS) is a function of wavespeed only while the right hand side (RHS) depends on both, the wavespeed as well as the attenuation. The RHS is a sum of two exponentials and, therefore, is not an oscillatory function of frequency f. On the other hand, the LHS is the sum of a cosine function of frequency and the experimentally determined $F^*(\omega)/G^*(\omega)$ which was found to be oscillatory. Now if the correct value of c is not used in eq (29) the periods of the two terms do not match exactly and the oscillatory parts do not cancel each other as they would for the correct value of c. With this in mind, the RHS is viewed as the reference curve and a numerical search is made around the value of c obtained by the iterative procedure described earlier, to minimize the root-sum-square of the LHS. This fixes c. Now we view the LHS as the reference curve and conduct a numerical search over a range of $k_2\lambda$ so as to minimize the root-sum-square between the LHS and the RHS. This fixes k_2.

Finally, it is noted that the theoretical procedures developed in this section are equally valid for, and have been used for, both the longitudinal as well as the shear waves with a slight change in detail: For shear disturbances, water is replaced by polystyrene. For longitudinal waves $c=c_1$ and for shear waves $c=c_2$ in the foregoing.

EXPERIMENTAL PROCEDURES

A schematic of the apparatus is shown in Fig. 4. The heart of the system is a pair of accurately-matched, broad-band, water-immersion, piezoelectric transducers. An experiment is initiated at time t=0 by a triggering pulse produced by a pulser/receiver; the pulse is used to trigger a digitizing oscilloscope; simultaneously the pulser/receiver produces a short-duration (about 100 ns) large-amplitude (about 200 volts) spike which is applied to the transmitting transducer. In the reflection mode it also acts as a receiver. The received signal is post-amplified (to about one volt) and then digitized with maximum sampling rate of 100 MHz (or 10 nanoseconds per point). To reduce the ubiquitous random errors, each measurement is averaged over a sample size of 64 (or 256).

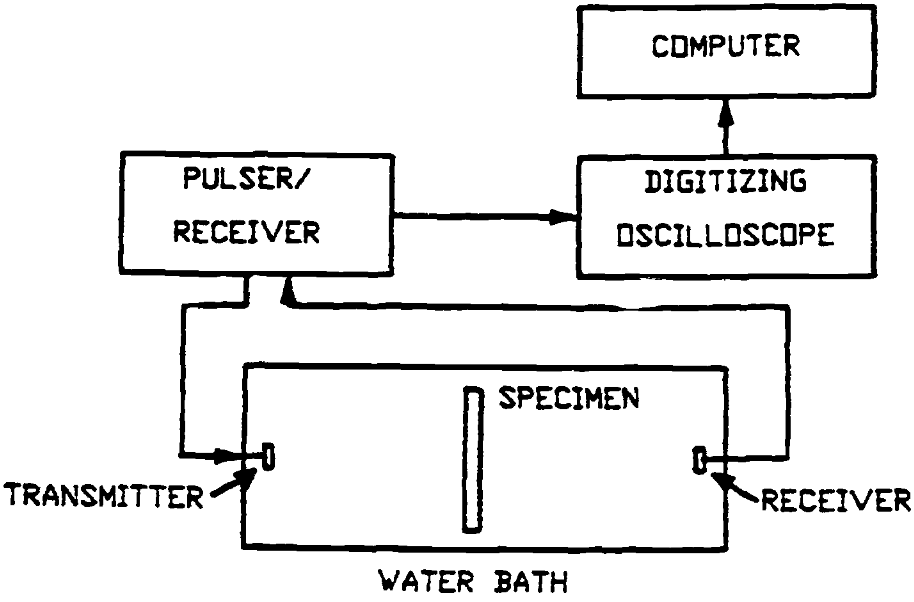

FIG. 4 -- Block diagram of the experimental set up.

Consequently the precision in measuring time is ±1 ns (or better). A laboratory computer controls all operations of the digital oscilloscope through an IEEE bus. The built-in signal processor of the oscilloscope performs FFT on the acquired signals and the relevant parts of the data are then transferred to the computer for further analysis. The measurement process is fully-automated; the final values of wavespeed and attenuation are computed without human intervention.

RESULTS AND DISCUSSIONS

From the measurement of the longitudinal wavespeed, c_1, the shear wavespeed, c_2, and the density, ρ, any desired pair of elastic constants can be calculated by the equations given below.

Young's Modulus $E = \rho\, c_2^2(3\, c_1^2 - 4\, c_2^2)/(c_1^2 - c_2^2)$

Poisson's Ratio $\nu = (c_1^2 - 2\, c_2^2)/2(c_1^2 - c_2^2)$ (30a)

Lame' Constants $\lambda = \rho(c_1^2 - 2\, c_2^2)$ (30b)

$\mu = \rho\, c_2^2$

Bulk Modulus $K = \rho\, (c_1^2 - 4\, c_2^2/3)$

Shear Modulus $G(\text{or}\mu) = \rho\, c_2^2$ (30c)

The experimental procedures reported in this work were used to measure the elastic moduli of three rather disparate materials:

1. Non-dispersive, non-attenuative (elastic)
2. Non-dispersive, weakly-attenuative (viscoelastic)
3. Highly-dispersive, highly attenuative

The results are presented in the following.

Dynamic Modulus of a Non-Dispersive, Non-attenuative Medium

Aluminum is neither dispersive nor attenuative (within the error bounds of the present measurement). A "thick" 6061-T6 aluminum plate (2.807 ± 0.025 mm) was first tested using conventional toneburst method [8-10]. Then the thickness was gradually machined down to 0.258 mm (about 10 mil, a very thin foil) in five steps. In non-dimensional terms the thickness was reduced from about 4.4 to 0.4 wavelengths; a frequency of 10 MHz was used. At each step c was measured. We could have used five different samples. Instead we adopted the foregoing elaborate procedure in order to ensure that we are always testing exactly the same material. The density was measured by the Archimedes principle to an accuracy of ± 0.015%. The error analysis is given in the Appendix. The results are presented in Table 1. Here, $\bar{\sigma}$ is standard deviation of c. The first measurement was made using the conventional toneburst method [4,5].

TABLE 1 -- Test results for an aluminum sample.

Material: Aluminum
Wave Type: Longitudinal
Mode: Transmission
Frequency: 10 MHz
Density: 2.8177 ± 0.0004 g/ml (±0.015%)

h mm	h/λ	c mm/μs	σ/c %	Method	Reference Figure
2.807	4.4	6.3572		Toneburst	5a
2.807	4.4	6.3239	0.013	Separable Pulse	5b
2.807	4.4	6.3275	0.010	Non-Separable Pulse	5b
1.686	2.7	6.3461	0.040	Non-Separable Pulse	5c
0.613	0.96	6.3594	0.130	Non-Separable Pulse	5e
0.258	0.4	6.3231	0.140	Non-Separable Pulse	5f

The time-domain signal is shown in Fig. 5(a). A particular peak (say the fourth peak) near the center of the toneburst is selected as the reference peak. The twice-transit-time, 2h/c could be measured to an accuracy of 1 ns. The thickness varied by ± 0.001 in (± 0.0254 mm). The thickness variation is the major source of error in c. This explains a monotonic increase in error as thickness decreases (one-standard deviation, $\bar{\sigma}/c$, column 4). In the second measurement the toneburst was reduced to about one cycle; see Fig. 5(b). Note that the pulses can be clearly separated. The Separable-Pulse Method, eq (15), was used to analyze this data. Since only the first two pulses are needed for data analysis, the remaining pulses are electronically gated out or nulled. In the third measurement, the data analysed remains the same i.e. Fig. 5(b). However, the Non-Separable Pulse Method, eq (27), is used. In other words, g(t) is now viewed as the sum of all transmissions. For the remaining measurements the specimen was gradually machined down. Non-Separable Pulse Method was used to analyze the data. The pulses for h=1.686 mm are shown in Fig. 5(c). Note that the conventional toneburst method can no longer be used. Although both methods developed in this work can be used, we used the Non-Separable Pulse Method. The pulse for

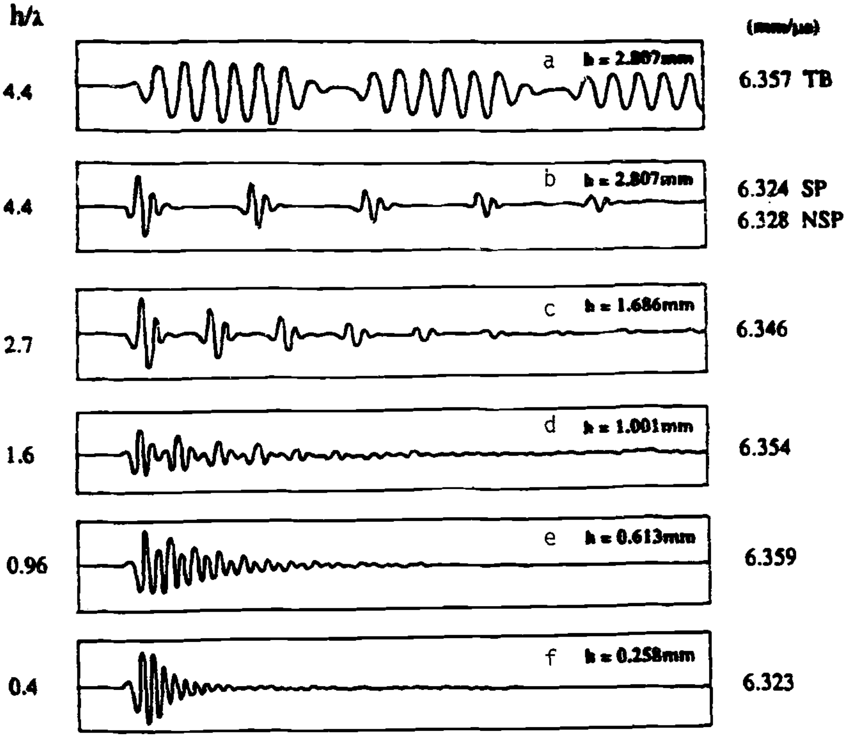

FIG. 5 -- 10 MHz signal through aluminum plates of different thickness. (a) is for toneburst. Others are for a single pulse. Plate thickness given on each signal.

the next three thicknesses, h=1.001, 0.613 and 0.258 mm are shown in Figs. 5d, 5e, 5f, respectively. Because of the reduced thickness the pulses cannot be separated in the time domain. Therefore, even the Separable-Pulse Method cannot be used; here we have to use the Non-Separable Pulse Method. For the thinnest specimen the round trip time is only 82 nS; the pulse duration is roughly 200 ns. With reference to Table 1, the average of all the measurements is 6.342 mm/μsec ± 0.25%. We conclude that the Non-Separable Pulse Method developed for ultra-thin (sub-wavelength) specimens and the Separable-Pulse Method for moderately thin (about one wavelength) specimens yield results which agree to 0.25% with the conventional toneburst method. (We hesitate to make absolute claims on accuracy because, for the given piece of aluminum, we do not know the true value of the phase velocity).

The ideal method for "calibrating" a new experimental technique is to use it to measure a quantity which is known with a ten times better accuracy. Unfortunately, the National Institute of Standards and Technology has not yet developed a standard for dynamic elastic moduli. Our laboratory did, however, participate in a six-laboratory ASTM round-robin led by Dr. Alan Wolfenden (Department of Mechanical Engineering, Texas A&M University, College Station, Texas 77843, (409) 845-4835). This allowed us an opportunity to compare our error-estimates with those of the others using different experimental procedures [7]. The material tested were two nickel-based alloys, see Table 2. Since these specimens are very "thick" (several wavelengths), the Separable Pulse Method, eq (15), was used. Furthermore, shear velocity also was measured. Here a shear (or Y cut) transducer was directly cemented onto the metal specimen using a shear couplant. Ignoring the "main bang," the remaining reflected signal was collected. From the measurements of the longitudinal and shear velocity, c_1 and c_2, and density ρ, the elastic constants E and ν can be readily calculated; the associated error analysis is presented in the Appendix. The results of the round-robin test are presented in Tables 2 and 3. Reasonably good agreement (within 1.5%) is observed amongst the independent results obtained in six different laboratories using different techniques.

Dynamic Modulus of a Non-Dispersive, Weakly-Attenuative Medium

Next, we tested our experimental method on a medium which is non-dispersive (velocity independent of frequency) and slightly attenuative. An epoxy (EPON 828Z) was selected for this purpose. The results are presented in Table 4. Note that three frequencies, spanning nearly a decade, were used. The phase velocity measured by the toneburst method on a thick specimen is 2.915 mm/μsec and agrees very well with that measured with the Non-Separable Method.

Highly-Attenuative, Highly-Dispersive Medium

Finally, we applied the new technique to a material which is highly dispersive as well as highly attenuative. We tested a random particulate composite consisting of lead spheres in an epoxy matrix. These composites have been described in [8,9]. Transducers with 0.25 MHz center-frequency were employed. Separable Pulse Method in through-transmission mode, eq (16), was used.

TABLE 2 -- Results of ASTM round-robin tests of Ni based alloys*.

Sample 1 :	INCONEL ALLOY 600
Composition:	Ni 37.46, C 0.01, Co 14.38, Nb 4.71, Ti 1.46, Fe 41.98
Geometry:	25.280 dia x 6.263 mm (Specimen ID = A2, 1.2) 12.098 dia x 6.3649 mm (Specimen ID = Physics, 1.4)
Frequency:	5.0 MHz
Mode:	Reflection

Sample 2 :	INCOLOY ALLOY 907
Composition:	Ni 74.91, Cr 15.48, C 0.08, Fe 9.53
Geometry:	50.952 x 50.952 x 18. 848 mm (Specimen ID = B2, 2.1)
Frequency:	5.0 MHz
Mode:	Reflection

SAMPLE ID	h	ρ	c_1	c_2	E	ν
	mm	g/ml	mm/μs	mm/μs	GN/m^2	
A2, 1.2**	6.263	8.371	5.872 ± 0.025%	3.161 ± 0.167%	216.9 ± 0.14%	0.2960 ± 0.20%
Physics, 1.4	6.365	8.373	5.877 ± 0.05%	3.163 ± 0.05%	216.6 ± 0.15%	0.2960 ± 0.20%
B2, 2.1	18.848	8.267	5.273 ± 0.05%	2.7308 ± 0.064%	163.0 ± 0.26%	0.3153 + 0.18%

---

* All error estimates are based on one standard deviation of a sample size of at least 10 and at most 20.

** The first digit (1 or 2) refers to the alloy while the second digit (1-4) is merely to identify different physical specimens.

TABLE 3 -- Comparison of ASTM round robin for the Young's Modulus, E (GN/m^2).

SAMPLE LAB	1.1**	1.2	1.3	1.4	2.1	2.2	2.3
1	218.0 218.0 218.1	216.9	218.5	-	161.5	159.9	157.2
2	210.5	209.2	-	-	164.1	-	155.7
3	218.8	216.0	217.5 217.0 216.2 217.3	-	162.0 161.8 160.8	- -	158.4
4	212.0	-	205.0	-	156.0	-	172.0
5	215.6	-	214.2	-	156.0	-	162.0
6	-	216.9	-	216.6	163.0	-	-
7	203.0	-	210.3	-	156.8	-	155.8 158.0

Techniques:	LAB. 1, 2, 7	Free-Free Beam
	LAB. 3	Impulse Fourier Transform
	LAB. 4	Pulse-Echo-Overlap Ultrasonic
	LAB. 5	Piezoelectric Ultrasonic Composite Oscillator Technique (PUCOT)
	LAB. 6	Ultrasonic Fourier Transform (this work)

** The first digit (1 or 2) refers to the alloy while the second digit (1-4) is merely to identify different physical specimens.

TABLE 4 -- Test results on Epon 828-Z Epoxy.

Material: Epon 828-Z epoxy
Wave Type: Longitudinal
Mode: Transmission
Thickness: 1.869 ± 0.0025 mm
Density: 1.2069 ± 0.0004 g/ml

Frequency MHz	Wavespeed mm/μs	σ/c percent	$k_2\lambda$	σ	Method
1.0	2.874	0.1	0.1340	1.4	Non-Separable
5.0	2.884	0.14	0.0924	1.5	Non-Separable
10.0	2.915	0.08	0.0975	1.0	Non-Separable
10.0	2.915	0.24	0.0979	2.2	Toneburst

Kinra [9] has shown that the wave propagation in these composites occurs along two separate branches: (1) The low-frequency, slower, acoustical branch along which the particle motion is essentially in phase with the excitation and; (2) The high-frequency, faster, optical branch along which the particle motion is essentially out of phase with the excitation. The two are separated by a cut-off frequency which corresponds to the excitation of the rigid-body-translational resonance of the heavy inclusions; this occurs when $k_1a = O(1)$, where a is the inclusion radius. Around the cut-off frequency both the phase velocity and the attenuation change dramatically with frequency. This is what makes this composite such an interesting material to study using our technique which was developed especially for dispersive media.

The experimental results are presented in Figures 6 and 7. Here the normalized frequency $\Omega = k_1a = \omega a/c_1$, $<c_1>$ is the longitudinal wavespeed in the composite, and $\tilde{c}$ is the volume fraction of spherical inclusions. In the past, each point on the curve had to be measured separately [8-10]. Thus each true value was shifted up or down by the random error; this affects the experimentally obtained shape of the dispersion curve. The present technique is tremendously faster; the entire dispersion curve is obtained in a single experiment. Further, the entire curve may be shifted up or down by the random errors but these errors cannot alter the shape of the dispersion curve. Thus the true shape becomes accessible. The dispersion curve is shown in Fig. 6. The arrow labeled HASHIN is the velocity calculated from the static modulii calculated by Hashin and Strikman [11]. Intuitively, as frequency goes to zero, the dynamic modulus should asymptotically approach the static modulus; this is borne out by the experiments. As frequency increases, first the velocity decreases i.e. the dynamic modulus decreases. Then the phase velocity increases very sharply. This phenomenon corresponds to the cut-off frequency of the individual lead spheres, Ω_c. A heuristic explanation is offered now. Consider a single sphere in an unbounded matrix. The sphere is displaced from its equilibrium position and let go. It will undergo damped oscillations like a mass on a viscoelastic spring. The "inertia" term is due to the density of lead being very large compared to that of the matrix. The "spring" term is due to the restorative force applied by the matrix on the

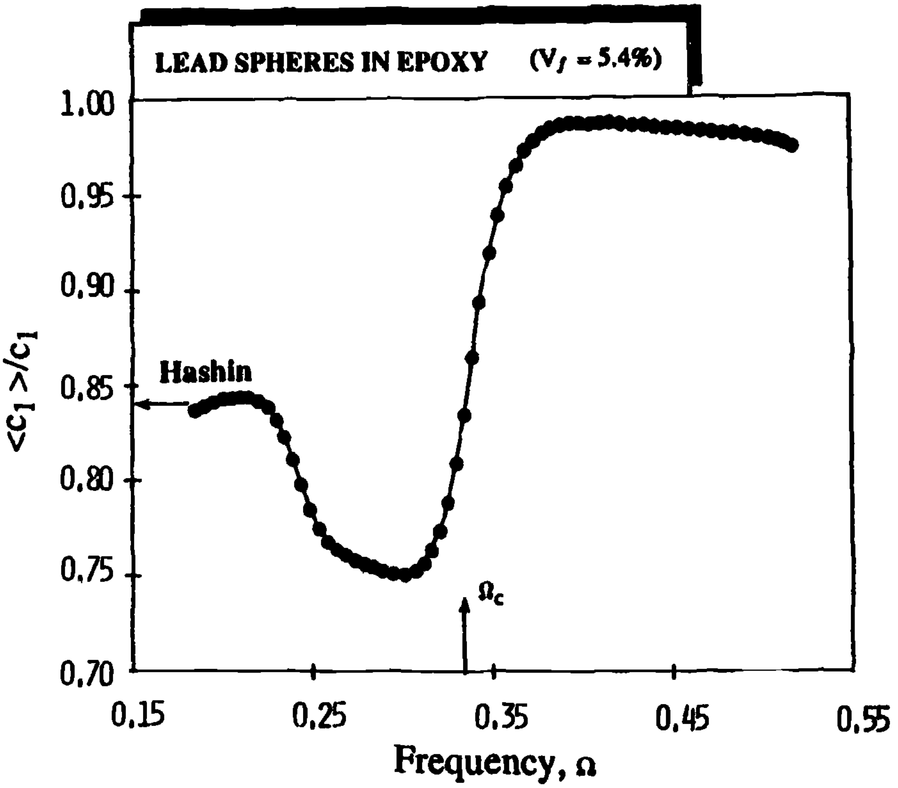

FIG. 6 -- Normalized phase velocity versus frequency curve for the dispersive lead/epoxy specimen.

inclusion. The "dashpot" term is due to radiation of waves carrying mechanical energy away from the sphere out to infinity. When the excitation frequency coincides with the resonant frequency, the particle undergoes large-amplitude vibrations thus scattering maximum amount of energy. This is borne out in Fig. 7 where attenuation, $k_2\lambda$, is plotted. Note that attenuation reaches maximum very near the calculated value of Ω_c = 0.33 [8]. (A second smaller peak to the left of the main peak is most probably due to some artifact of the measurement system. The low end of the useful frequency range of the 0.25 MHz transducer had previously been established to be about 0.17 MHz [8]. Properly, the data below 0.17 MHz should not be reported, but it is included here for completeness and to cover the possibility that the reader may offer another plausible explanation).

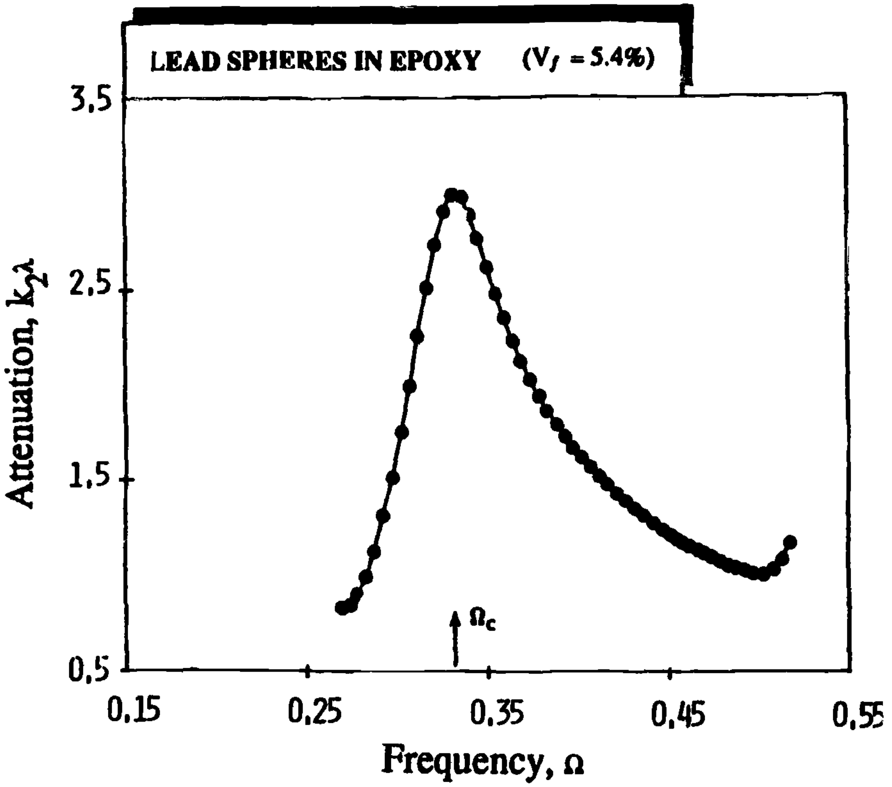

FIG. 7 -- Normalized attenuation versus frequency curve. Note a very high attenuation (large energy absorption) due to resonant scattering at the cut-off frequency, Ω_c.

Finally, returning to Fig. 6, the highest modulus is 100% larger than the lowest modulus. This is for the lowest volume fraction, $\tilde{c}$ = 5.4%. Similar measurement have been carried out for $\tilde{c}$ = 15, 25, 35, 45 and 53 percent (nominal). At the high volume fractions the difference between the minimum and the maximum modulus is even more dramatic, namely, 250 percent. <u>For materials with microstructure, therefore, the concept of a single constant serving as "the dynamic elastic modulus" completely breaks down</u>. For more details see Ref. [12].

CONCLUSIONS

From the measurement of two wavespeeds one can calculate a pair of dynamic elastic moduli. All the techniques reported in the literature in the past suffer from one limitation: the specimen thickness must exceed (roughly) five wavelengths. By the use of Fourier transforms we have devised a new technique which removes this restriction. The new technique has been demonstrated to produce accurate results down to a thickness which is about one order of magnitude smaller than the wavelength (experiments are now underway where we are trying to extend the range to $h/\lambda = 0\ (10^{-2})$).

For most engineering materials (isotropic, homogeneous, elastic or slightly viscoelastic) the difference between the static and the dynamic modulus of elasticity is generally very small. By considering a material with microstructure, and by varying the wavelength across the characteristic dimension of the microstructure, we have demonstrated that here the dynamic modulus of elasticity may differ from its true static value by as much as 100 percent. Consequently, for materials with microstructure, we have established that the static modulus of elasticity and the dynamic modulus of elasticity are altogether different entitites.

ACKNOWLEDGEMENT

This research was supported by the Air Force Office of Scientific Research Contract No. AFOSR-84-0066 to Texas A&M University, College Station, Texas 77843. Thanks are due to Connie Rice for a careful preparation of the manuscript.

REFERENCES

[1] Tauchert, T.R., and Guzelsu, A.M., "An Experimental Study of Dispersion of Stress Waves in a Fiber-Reinforced Composite," ASME Journal of Applied Mechanics, Vol. 39, pp. 98-102, 1972.
[2] Kolsky, H., "Stress Waves in Solids," Dover, 1953.
[3] Achenbach, J.D., "Wave Propagation in Elastic Solids," North-Holland Publishing Company, 1973.
[4] Kinra, V.K., Petraites, M.S., and Datta S.K., "Ultrasonic Wave Propagation in a Random Particulate Composite," International Journal of Solids and Structures, Vol. 16, pp. 301-312, 1980.

[5] Kinra, V.K. and Anand, A., "Wave Propagation in a Random Particulate Composite at Long and Short Wavelength," International Journal of Solids and Structures, Vol. 18(5), pp. 367-380, 1982.

[6] Kinra, V.K. and Ker, E.L., "Effective Elastic Moduli of a Thin-Walled Glass Microsphere/PMMA Composite," Journal of Composite Materials, Vol. 16, pp. 117-188, March 1982.

[7] Wolfenden, A., Harmouche, M.R., Blessing, G.V., Chen, Y.T., Terranova, P., Kinra, V.K., Dayal, V., Lemmens, J.W., Phillips, R.R., Smith, J.S., Mahmoodi, P. and Wann, R.J., "Dynamic Young's Modulus Measurements in Metallic Materials: Results of an Interlaboratory Testing Program," ASTM Journal of Testing and Evaluation, Vol. 17, No. 1, pp. 1-13, 1989.

[8] Kinra, V.K. and Li, P.N., "Resonant Scattering of Elastic Waves by a Random Distribution of Inclusions," International Journal of Solids and Structures, Vol. 22(1), pp. 1-11, 1986.

[9] Kinra, V.K., "Dispersive Wave Propagation in Random Particulate Composites," Recent Advances in Composites in the United States and Japan, ASTM STP 864, J.R. Vinson and M. Taya, Eds., pp. 309-325, 1985.

[10] Kinra V.K. and Rousseau, C.Q., "Acoustical and Optical Branches of Wave Propagation: Some Additional Results," Journal of Wave-Material Interaction, Vol. 2, No. 2, pp. 141-152, 1987.

[11] Hashin, Z. and Strikman, S., "A Variational Approach to the Theory of The Elastic Behavior of Multiphase Materials," Journal of Mechanics and Physics of Solids, Vol. 11, pp. 127-140, 1963.

[12] Kinra, V.K. and Dayal, V., "Will the Real Youngs Modulus Please Stand Up?" Manual on Experimental Methods for Mechanical Testing of Composites," Society for Experimental Mechanics (to appear).

[13] Schapery, R.A., "Viscoelastic Behavior and Analysis of Composite Materials," Composite Materials, Vol. 2, ed. G. Sendeckji, Academic Press, New York, 1974.

APPENDIX

PROPAGATION OF ERRORS

Wavespeed Measurements

Let c be either c_1 or c_2. With reference to Figs. 5(a) and 5(b)

$$c = 2h/(t_2-t_1)$$

where t_1 and t_2 are arrival times of a point of constant phase in two successive arrivals of the toneburst, $(t_2-t_1) > 0$, and

$$\frac{dc}{c} = \frac{dh}{h} - \frac{dt_2 - dt_1}{(t_2 - t_1)}.$$

We identify dc, dh, dt_1, and dt_2 with <u>absolute errors</u> in measuring the corresponding quantities. Furthermore, $dt_1 = dt_2 = dt$. In going from calculus to error analysis one must take <u>absolute</u> value of all coefficients of independent variables on the right hand side (component errors always add, they never cancel each other out). Defining normalized error

$$e_c = dc/c,\ e_h = dh/h, \text{ and } e_t = dt/t,$$

$$e_c = e_h + 2\ e_t. \qquad \text{(A1)}$$

As a typical example of thick specimens, $dh = 0.0254$ mm, $h = 10$ mm, $dt = 1$ ns, $t = 3.165$ μs, $e_h = 2.54 \times 10^{-3}$, $e_t = 3.2 \times 10^{-4}$, then

$$e_c = 2.54 \times 10^{-3} + 0.64 \times 10^{-3}$$

or

$$e_c = 3.18 \times 10^{-3}$$

Note that the thickness was revealed as the major source of error. For measurements involving only one specimen, the precision is one-order-of-magnitude higher, namely $e_c = 3 \times 10^{-4}$.

Density Measurements

The density was measured by the time-honored Archimedes Principle. First, a suspension wire is weighed in air (M_w). Next, the specimen and the suspension wire together are weighed in air (M_1), and then in water (M_2). Let ρ, ρ_o be the density of specimen and water, respectively, and V be the volume of the specimen then

$$M_1 = \rho V + M_w,$$

$$M_2 = (\rho - \rho_o)\ V + M_w,$$

and

$$\rho = \rho_o (M_1 - M_w)/(M_1 - M_2).$$

Now,

$$d\rho = \frac{\partial\rho}{\partial\rho_o} + \frac{\partial\rho}{\partial M_1}\,dM_1 + \frac{\partial\rho}{\partial M_2}\,dM_2 + \frac{\partial\rho}{\partial M_w}\,dM_w,$$

$$\frac{d\rho}{\rho} = \frac{1}{\rho}\frac{\partial\rho}{\partial\rho_o}\,d\rho_o + \frac{1}{\rho}\frac{\partial\rho}{\partial M_1}\,dM_1 + \frac{1}{\rho}\frac{\partial\rho}{\partial M_2}\,dM_2 + \frac{1}{\rho}\frac{\partial\rho}{\partial M_w}\,dM_w,$$

$$\frac{d\rho}{\rho} = \frac{d\rho_o}{\rho_o} + \frac{M_2}{M_1 - M_2}\left(\frac{dM_1}{M_1} + \frac{dM_2}{M_2}\right) - \frac{1}{M_1 - M_w}\,dM_w,$$

and

$$e_\rho = e_{\rho_o} + \frac{M_2}{M_1 - M_2}\,(e_{M_1} + e_{M_2}) + \frac{M_w}{M_1 - M_w}\,e_{M_w}. \qquad \text{(A2)}$$

As an example consider specimen A2, 1.2, Table 2.

$M_1 = 26.2409$ g, $d_{M_1} = 10^{-4}$ g, $e_{M_1} = 3.8 \times 10^{-6}$

$M_2 = 23.1134$ g, $d_{M_2} = 10^{-4}$ g, $e_{M_2} = 4.3 \times 10^{-6}$

$M_w = 0.1718$ g, $d_{M_w} = 10^{-4}$ g. $e_{M_w} = 5.8 \times 10^{-4}$

For the high accuracies desired here the temperature dependence of the density of water must be taken into account. Room temperature was 23°C. At 20°C, $\rho_o = 0.99862$; at 25°C, $\rho_o = 0.99707$. Therefore, by interpolation, at 23°C, $\rho_o = 0.99769$. Since temperature was measured to the nearest °C, $d\rho_o = 3.1 \times 10^{-4}$. Substituting into eq (A2)

$$e_\rho = 3.1 \times 10^{-4} + 0.6 \times 10^{-4} + 0.04 \times 10^{-4}$$

$$e_\rho = 3.74 \times 10^{-4}$$

It is interesting to note that a majority of the total error is due to the uncertainty in the water temperature and not in the weighing process. This is the value of such error analysis. It indicates clearly that if further improvements in accuracy are desired, one must turn to more accurate measurements of water temperature. It also reveals the inherent aesthetics of the Archimedes' Principle and explains its survival for two thousand years.

Modulus Measurement

In this section we will derive the equations for calculating the "resultant" errors in E, ν, λ, μ(=G) and K from "component" errors in c_1, c_2, and ρ. Recall

$$E = \rho\, c_2^2(3\, c_1^2 - 4\, c_2^2)/(c_1^2 - c_2^2).$$

$$dE = \frac{\partial E}{\partial \rho}\, d\rho + \frac{\partial E}{\partial c_1}\, dc_1 + \frac{\partial E}{\partial c_2}\, dc_2,$$

$$\frac{dE}{E} = \frac{d\rho}{\rho} + 2\left[\frac{c_1^2 c_2^2}{(c_1^2 - c_2^2)\,(3\, c_1^2 - 4\, c_2^2)}\right]\frac{dc_1}{c_1} +$$

$$2\left[1 - \frac{c_1^2\, c_2^2}{(c_1^2 - c_2^2)(3c_1^2 - c_2^2)}\right]\frac{dc_2}{c_2}$$

For materials of interest here, the coefficients of $d\rho/\rho$, dc_1/c_1 and dc_2/c_2 are positive (if they are negative one takes their absolute value). Let e_E e_ρ e_1, and e_2 be, respectively, the normalized errors in E, ρ, c_1, and c_2 respectively, then

$$e_E = e_\rho + 2\left[\frac{c_1^2 c_2^2}{(c_1^2 - c_2^2)\,(3c_1^2 - 4c_2^2)}\right] e_1 +$$

$$2\left[1 - \frac{c_1^2 c_2^2}{(c_1^2 - c_2^2)(3c_1^2 - c_2^2)}\right]\frac{dc_2}{c_2} \qquad \text{(A3)}$$

Next, we present similar calculations for other quantities.

Poisson's Ratio

$$\nu = (c_1^2 - 2\,c_2^2)/2\,(c_1^2 - c_2^2),$$

$$e_\nu = \frac{2\,c_1^2 c_2^2}{(c_1^2 - c_2^2)\,(c_1^2 - 2\,c_2^2)}\,(e_1 + e_2). \qquad \text{(A4)}$$

Lame' Constants $\lambda = \rho\,(c_1^2 - 2\,c_2^2),$ (A5)

$$e_\lambda = e_\rho + \frac{2\,c_1^2}{(c_1^2 - 2\,c_2^2)}\,e_1 + \frac{4\,c_2^2}{c_1^2 - 2\,c_2^2}\,e_2.$$

Shear Modulus μ or $G = \rho\,c_2^2,$

$$e_\mu \text{ or } e_G = e_\rho + 2\,e_2 \qquad \text{(A6)}$$

Bulk Modulus $K = \rho\,(c_1^2 - (4/3)\,c_2^2)$

$$e_K = e_\rho + \frac{6\,c_1^2}{(3\,c_1^2 - 4\,c_2^2)}\,e_1 + \frac{8\,c_2^2}{(3\,c_1^2 - 4\,c_2^2)}\,e_2 \qquad \text{(A7)}$$

As an example, we compute the resultant errors for one particular case, namely, Sample 1.4 in Table 2. For a (statistical) population size N=13,

$c_1 = 5.8723 \pm 0.0029$ mm/μs (one standard deviation)

$$e_1 = \pm\,4.94\text{x}10^{-4}$$

$c_2 = 3.1615 \pm 0.0017$ mm/μs (one standard deviation)

$$e_2 = \pm\,5.28\text{x}10^{-4}$$

$\rho = 8.371 \pm 2.846\text{x}10^{-3}$ g/mℓ (one standard deviation)

$$e_\rho = \pm\,3.4\text{x}10^{-4}$$

From eq(A3)

$$e_E = e_\rho + 0.444\,e_1 + 1.557\,e_2$$

It is instructive to note that the resultant error in E is almost four times more sensitive to error in the shear wavespeed compared to that in the longitudinal wavespeed. Finally,

$$e_E = 1.4 \times 10^{-3} \text{ or } 0.14\%$$

G. V. Blessing

THE PULSED ULTRASONIC VELOCITY METHOD FOR DETERMINING MATERIAL DYNAMIC ELASTIC MODULI

REFERENCE: Blessing, G.V., "The Pulsed Ultrasonic Velocity Method for Determining Material Dynamic Elastic Moduli," Dynamic Elastic Modulus Measurements in Materials, ASTM STP 1045, A. Wolfenden, Ed., American Society for Testing and Materials, Philadelphia, PA 1990.

ABSTRACT: Material dynamic elastic moduli can be readily obtained from a knowledge of the material's sound velocity(s) and density. One well-established ultrasonic technique for making the velocity measurements is the pulsed-wave transit-time technique. It is a versatile and potentially very accurate technique that can also assess the material elastic homogeneity and anisotropy. Here the many measurement and material factors affecting the precision of the method are addressed. A specific example of the effect of grain size on measurements in steel is presented in some detail.

KEYWORDS: ultrasonic moduli, ultrasonic velocity, elastic moduli, material dynamic elasticity

INTRODUCTION

The dynamic elastic moduli of a material can be determined from a knowledge of the material's sound velocity(s) and density. Both pulsed-wave transit-time and resonant frequency techniques have been extensively applied to the quantitative measurement of material sound velocities and moduli for many years. See, for example, texts by McMaster [1] and by Truell, Elbaum and Chick [2], and the ASTM document of standard practice [3]. In this paper the discussion will be on the ultrasonic pulsed technique, where the sound velocity is obtained from the

Dr. G.V. Blessing is a physicist in the Ultrasonic Standards Group at the National Institute of Standards and Technology,

ratio of the ultrasonic path length to the pulse transit time in the material. Furthermore, this paper is not meant to be a comprehensive review of even that restricted methodology, but rather an introductory overview of both the capability and limitation of the technique. It can be applied to a wide variety of material types ranging from the homogeneous and isotropic, to the inhomogeneous and highly anisotropic as for many reinforced composites. Here, the focus will be on relatively homogeneous and isotropic materials such as common structural metals.

Some particular attention will be given to the frequent assumption that a randomly oriented grain structure, i.e., zero texture, in metals necessarily leads to ultrasonic elastic homogeneity. It is pointed out that this presumes a large number of grains in the ultrasonic path, a condition that may not apply for thin samples or large grains. In such cases, a statistical limitation applies to our knowledge of the material modulus based on a velocity measured at one position. An example of this limitation observed in stainless steel will be presented.

It is noted that all dynamic elasticity measurement techniques require a knowledge of both the sample dimension(s) and the density [1-3]. The transit time or resonant frequency is only one of at least four (mass, volume, length, and time or frequency) independent measurands that are required in order to determine the material moduli. Thus the propagation of errors in the calculation of the modulus must be recognized.

ULTRASONIC PULSE TECHNIQUE

The ultrasonic pulsed-wave transit-time technique is a well-established method for measuring the sound velocity in materials, as demonstrated by the existent ASTM E-494 "Standard Practice for Measuring Ultrasonic Velocity in Materials" [3]. As the name implies, it involves the transit-time measurement of short wave pulses (by necessity less than sample propagation times) travelling over a known path through the bulk of the sample. The ratio of the path length to the transit time yields the velocity. Figure 1 outlines the system components. The technique actually measures an average of the velocity over the path length taken by the pulse. Pulse durations on the order of or less than microseconds with megahertz carrier frequencies are typical. High rate repetitive pulse techniques on the order of kilohertz allow for both rapid and accurate transit-time measurements using time-averaging techniques.

One particularly powerful transit-time technique that is relatively simple to implement is the pulse-echo-overlap technique reviewed by Papadakis [4]. Lateral beam dimensions emanating from the transducer nominally range from millimeters to centimeters. As a result of the finite beam size and wave directivity, the technique also acts as a useful tool for assessing material inhomogeneity and anisotropy. Depending on the accuracy desired, the specific size and shape of samples need not be critical, although flat and parallel sample faces for the wave pulse to echo between are necessary. (This requirement may be at least partially relaxed by point excitation/reception techniques described elsewhere in these conference proceedings by Hsu and Eitzen [5].)

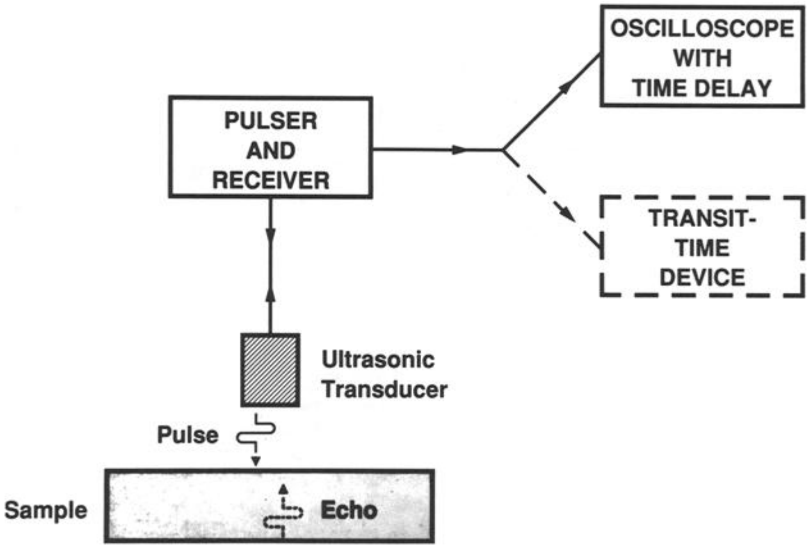

FIG. 1 -- Basic experimental arrangement for the ultrasonic pulsed-wave transit-time technique. A liquid coupling medium between the transducer and sample is assumed.

Moduli Relationships

For short duration wave pulses with wavelengths much less than the sample dimensions, two normal modes of bulk wave propagation pertain to extended isotropic media as described in [3] and by Kolsky [6]. They are the longitudinal and shear modes with respective velocities V_L and V_S. Longitudinal waves, sometimes referred to as compressional waves, alternately compress and dilate the material lattice (i.e., generate compressive and tensile strains) as they pass by. The resulting particle motion of the material is parallel to the direction of wave propagation. Shear waves, on the other hand, generate particle displacements perpendicular to the propagation direction, causing the material lattice to shear as the waves pass by. From these two wave speeds and the density (ρ), all the elastic parameters of an isotropic material can be calculated: the Young's, bulk, and shear moduli, and Poisson's ratio. Their relationships are:

$$\text{Young's modulus} = \rho V_S^2(3V_L^2 - 4V_S^2)/(V_L^2 - V_S^2) \quad (1)$$

$$\text{Bulk modulus} = \rho(V_L^2 - (4/3)\ V_S^2) \quad (2)$$

$$\text{Shear modulus} = \rho V_S^2 \quad (3)$$

$$\text{Poisson's ratio} = (V_L^2 - 2V_S^2)/(2V_L^2 - 2V_S^2) \quad (4)$$

For anisotropic materials, single crystals and most composites for example, the equations are more complex. The number of independent elastic parameters is greater than two, requiring additional sound speed measurements in specific directions relative to the material symmetry axes. (See, e.g., the review treatise by Green [7] and extensive references therein.)

Measurement Precision

The precision of the velocity measurement, and therefore of the calculated moduli, depends on many factors both intrinsic and extrinsic to the material itself. Many of the intrinsic material factors will be discussed in the next section. Some of the obvious extrinsic factors are the specimen dimensions (especially the path length and end-face parallelism), the transit-time measurement technique, and the ultrasonic coupling between transducer and sample.

Electronic start/stop clock techniques exist, both manual and automated, that may readily provide transit-time precisions of better than 0.1% in a repetitive pulse arrangement. (Precisions that are orders of magnitude greater may be achieved on ideal samples in a laboratory setting [2]). This time precision would typically provide moduli precisions of better than 1% if the density and path length were well known. For example, if the transit time, path length, and density were each known to one part in a thousand, a quadrature addition of the individual uncertainties would result in an uncertainty of 3 to 5 parts per 1000 for the elastic parameters described by eqs. (1) through (4) above. As a result, a 1% precision for the elastic moduli of engineering samples should be realizable, while a 0.1% precision would be difficult.

MATERIAL FACTORS

There are numerous material factors which affect velocity measurements and must be recognized especially for precise measurements. Assuming fully dense materials so that porosity is not a factor, they include texture, grain size, temperature, diffraction, residual stress and frequency dispersion. These will be briefly outlined here, with references cited for additional details.

Polycrystalline Materials

Two principal factors affecting velocity measurements in polycrystalline metal samples are the texture (i.e., grain alignment) and the crystalline grain size. They respectively contribute to sample elastic anisotropy and inhomogeneity. The first arises when there is a non-random ordering of the crystallites in the material due to rolling, extrusion etc. The second arises when the crystallites are large (i.e., comprise a statistically small number for averaging the single-crystal elasticity) relative to the ultrasonic path length. Obviously, both factors can be present simultaneously, but the point to note is that grain size effects can be present even when there is a completely random crystallite structure. A specific example of this with some quantitative details will be given in the next section.

Both factors derive from the single crystal elastic anisotropy and may also affect the velocity measurement in other ways via refraction and diffraction. Much work, especially in recent years by Sayers, et al. [8], Thompson, et al. [9], and Hirao, et al. [10], has been directed toward quantifying and isolating the contribution of texture to the material sound velocity. The statement of its contribution may be expressed in a simplified manner as follows:

$$V^2 = V_o^2 + Cf(W_{\alpha\beta\gamma}) \quad (5)$$

where V_o is the velocity without texture, C is a constant, and the $W_{\alpha\beta\gamma}$ are crystal orientation distribution coefficients which define sample texture in terms of the average crystal orientation. The three independent $W_{\alpha\beta\gamma}$ associated with a unidirectionally deformed aggregate of cubic crystals (the case for aluminum and steel rolled sheet) require the measurement of three wave modes in specific directions relative to the principal material axes. Using this model analysis, an example comparing ultrasonic results with the engineering texture parameter known as the formability may be found in Clark, et.al. [11] for the case of rolled aluminum.

Temperature

The elasticity of materials is usually dependent on temperature [2]. (The thermal expansion, a second-order effect on the transit time relative to that of temperature on the intrinsic elasticity in common metals, should be accounted for by way of the sample dimension corresponding to the ultrasonic path length at the desired temperature.) For small changes of the temperature T, the following first-order linear relationship provides a sufficient description of the effect of temperature on velocity:

$$V(T) = V_o(T_o) + \gamma\Delta T \quad (6)$$

where $\Delta T = T - T_o$ and γ is a material dependent constant. For example, on a set of 304-stainless steel samples described in the next section, γ was measured to be a negative 1.5×10^{-3} mm/μs per °C over a five degree range around room temperature.

Beam Diffraction

Ultrasonic diffraction (or beam spread) occurs in isotropic media and can become quite significant in anisotropic media, as pointed out by Papadakis [12]. The effect of a finite transducer aperture and therefore beam width is to lose, with increasing path length, the side lobe contributions to the integrated wave front phase function. These contributions depend on the transducer aperture, the wavelength, the path length, and the material anisotropy. Assume, by example, a 1 cm aperture and a 0.1 cm longitudinal wavelength generated by a circular transducer exhibiting piston-like behavior. For an echo pair in the first 10 cm of material path, the phase correction may be on the order 0.05% in an isotropic medium and 0.2% in a highly anisotropic medium [12]. The correction is always an addition to the measured transit time, thereby reducing the apparent phase velocity. Diffraction effects may be minimized by working with echoes in the far field (distance > a^2/λ where a is the transducer radius and λ is the wavelength).

Dispersion and Residual Stress

Two factors that are generally of lesser significance, at least in engineering metals for their effect on ultrasonically measured velocity values, are dispersion and residual stress. Here we are addressing material dispersion (as opposed to geometric dispersion due to sample boundaries), wherein the frequency dependence of the velocity is due to the intrinsic properties of the material medium. In this case, a nonlinear relationship between the ultrasonic frequency and the wave number k ($2\pi/\lambda$) causes the phase velocity ω/k to diverge from the group velocity $d\omega/dk$. The term ω equals $2\pi f$ where f is the frequency. The moduli expressions given above in eqs. (1)-(4), representing solutions of the constitutive relationships for elastic wave propagation, are functions of the phase velocities, as is clearly pointed out by Ting and Sachse [13]. Since the pulsed-wave transit-time technique may yield a group velocity, we must be careful of the error that might incur using eqs. (1)-(4). On the other hand, in nondispersive media the phase velocity by definition equals the group velocity, since a linear relationship exists between the wave frequency and the wave number. While dispersion effects can become appreciable in composites and some other materials, structural metals are generally nondispersive at the ultrasonic frequencies of common use.

Residual stress, which may occur due to the nonuniform contraction of molten metal upon cooling, can typically affect the material velocity on the order of parts per ten thousand in structural metals (Green [7] and references therein). However, even if its presence is suspect, it is difficult to assess without a reference standard of like material and is often masked by the material texture. (See the comparison papers by Hsu, Proctor, and Blessing [14], and by Blessing, Hsu, and Proctor [15].) To maximize the accuracy of modulus measurements where the residual stress may be of concern, stress relieving the sample by heat treatment prior to making the ultrasonic measurements may be considered.

FINITE GRAIN SIZE EXAMPLE

As pointed out above, a completely random polycrystalline aggregate does not necessarily yield a homogeneous medium for ultrasonic velocity measurements. Relatively large grains or thin samples will result in a statistically limited number of crystallites in the path of the ultrasonic wave. This effect has been studied in some detail in stainless steel by Blessing et.al. [16], and will be summarized here.

Experimental

Four thin disk samples were sliced from a 75 mm diameter hot-rolled 304-stainless steel bar, to be evaluated for their elastic homogeneity. Two of the 1.5 mm samples were studied as received with ASTM No. 7 [17] grain structure (nominal grain dimensions of 30 μm). The other two samples were heat-treated to form a relatively coarse and varied-grain structure with ASTM No.'s 3 to 5-1/2 (grain dimensions as large as 150 μm).

A pulse-echo water immersion ultrasonic technique was applied for the velocity determination at eight equi-spaced positions across an arbitrarily chosen diameter of each sample. (Previous ultrasonic scattering experiments had shown that the samples' grain structures were circularly symmetric.) A frequency of 10 MHz provided optimum precision for the sample set, corresponding to a wavelength of 0.6 mm in the stainless steel material. The circular aperture of the transducer produced a nominal beam diameter of 2 mm. A pulse-echo-overlap technique utilized the first six sample echoes to provide a precise (better than 0.1 ns) transit-time average through the sample thickness. Thickness measurements were in turn made by Doiron [18] using an interferometer-based contacting comparator system to an accuracy of 0.1 μm. (Thicknesses were constant to about five percent across the sample diameters.) With this transit-time precision and path length accuracy, the velocity precision obtained was better than 0.05%.

Theory

Based on model developments by Mason and McSkimin [19] for longitudinal wave propagation in polycrystalline aggregates, Fisher and Johnson [20] have demonstrated the substantial velocity variations that can be expected due to a finite grain structure in metals. The model is based on the statistical stacking distribution of N randomly oriented crystallites (grains) in the ultrasonic path. It assumes the average aggregate velocity V_o, for an infinite number of randomly oriented crystallites, is equal to the average single crystal velocity measured in all directions. The model may be expressed as follows:

$$V = V_o \pm \Delta V(N), \qquad (7)$$

where ΔV is the measured velocities' statistical fluctuation which decreases as N increases.

Applying the central limit theorem in statistics which states that for sufficiently large N, the velocity (as a function of position in the aggregate) is a random variable whose variance S^2

is proportional to the single crystal variance S_o^2 and inversely proportional to N:

$$S^2 = S_o^2/N. \tag{8}$$

For crystals of cubic structure the standard deviation for longitudinal waves, normalized to the average aggregate velocity, may be expressed in terms of the single crystal elastic coefficients C_{ij} as [19]:

$$S_o = \frac{2}{5\sqrt{21}} \frac{\mu}{C_{12} + 2C_{44} - 2\mu/5} \tag{9}$$

where $\mu = (C_{11} - C_{12} - 2C_{44})$ is the single crystal anisotropy. (A similar relationship has been obtained for shear waves by Stanke [21].) It is seen that a lesser crystalline anistropy or smaller crystallites reduces the variance in a sample of given thickness.

Results

The variation in the velocity as a function of position was, in fact, observed to increase with increasing grain size. The four experimental points taken from the four disks are plotted as a function of grain size in Fig. 2, together with the finite-grain-

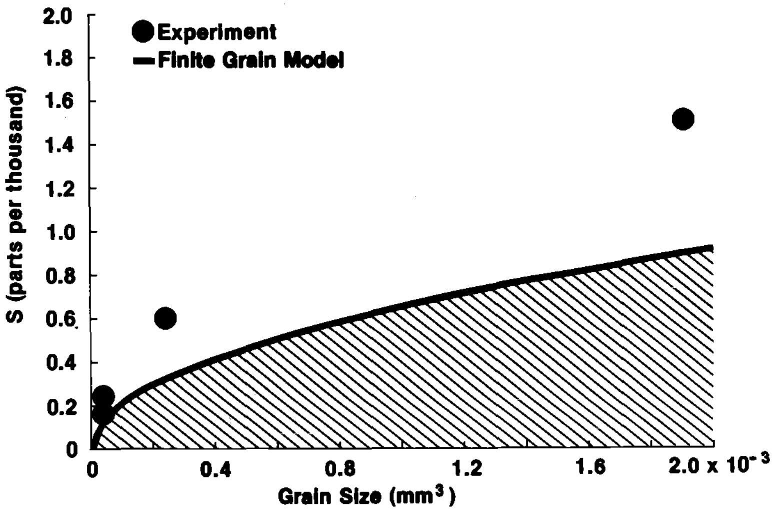

FIG. 2 -- Noramlized statistical longitudinal velocity variations experimentally observed (solid circles) on four samples, versus grain size; and model calculations (bold line) for the expected contribution of finite grain size to the velocity variation.

size model's contribution which is indicated by the solid boundary line proportional to $1/\sqrt{N}$. For the experimental points, the standard deviation of each sample disk's velocities taken across a diameter was calculated and normalized to the average velocity V_0 of all disks.

The model contribution was obtained using eqs. (8) and (9), with 304-stainless steel C_{ij} values taken from Ledbetter [22]. The intrinsic limitation to velocity homogeneity for the largest grain structure plotted is shown to be a quite significant 0.1%. The greater values experimentally observed for S may be attributed to other ultrasonic material variables. These include scattering as a function of grain size, density variations, texture, and residual stress. The increasing divergence with grain size of the experimental from the model values might be specific ally attributed to large grain scattering. As a result, the solid boundary may be considered the lower limit of velocity variation that may be expected in practice, and the shaded region to represent a dimensional accuracy regime inaccessible to the ultrasonic measurements.

CONCLUSIONS

The ultrasonic pulsed-wave transit-time technique is a powerful method for measuring not only a material's dynamic modulus, but also its anisotropy and in homogeneity. It is capable of great precision, exceeding 0.1% under certain conditions. For such precision, however, both the material and the ultrasonic path length must be well known, and the many factors affecting the precise measurement of the transit time recognized.

A specific example of the intrinsic limitation of finite grain size on polycrystalline homogeneity and therefore sound velocity is demonstrated on a set of stainless steel specimens. It is shown that, even assuming a random crystal orientation, the inhomogeneity problem can become acute for relatively thin samples where there may be a statistically limited number of grains in the ultrasonic path length.

ACKNOWLEDGEMENTS

Recognition is made of the many vendor inquiries/requests to the National Institute of Standards and Technology for precise material velocity measurements, thereby providing the inducement for this research. Thanks are extended to Professor A. Wolfenden, Texas A&M University, for his leadership in this area of work as chairman of the ASTM subcommittee E28.03.05.

REFERENCES

[1] McMaster, R.C., Ed., Nondestructive Testing Handbook, Vol. II, Sec. 43, Ronald Press Co., NY, 1959.

[2] Truell, R., Elbaum, C., and Chick, B.B., Ultrasonic Methods in Solid State Physics, Academic Press, NY, 1969.

[3] Anon., ASTM E494-75, "Practice for Measuring Ultrasonic Velocity in Materials," Vol. 03.03, 1985 Annual Book of ASTM Standards, ASTM, Philadelphia, PA 1985, pp 112-149.

[4] Papadakis, E.P., "Ultrasonic Velocity and Attenuation: Measurement Methods with Scientific and Industrial Applications," Physical Acoustics Principles and Methods XII (Eds., Mason, W.P. and Thurston, R.N.) Academic Press, NY, 1976, pp 277-374.

[5] Hsu, N.N. and Eitzen, D.G., "Point Source/Point Receiver Dynamic Moduli Measurements," Dynamic Modulus Measurements in Materials, ASTM STP 1045, Ed., A. Wolfenden, ASTM, Philadelphia, 1989.

[6] Kolsky, H., Stress Waves in Solids, Dover Publications, NY, 1963.

[7] Green, R.E., Jr., Ultrasonic Investigation of Mechanical Properties, Vol 3 of Treatise on Materials Science and Technology, Academic Press, NY, 1973.

[8] Sayers, C.M., Allen, D.R., Haines, G.E., and Proudfoot, G.G., "Texture and Stress Determination in Metals Using Ultrasonic Rayleigh Waves and Neutron Diffraction," Phil. Trans. R. Soc. Lond., A320, 1986, pp 187-200.

[9] Thompson, R.B., Lee, S.S., and Smith, J.G., "Angular Dependence of Ultrasonic Wave Propagation in a Stressed, Orthorhombic Continuum: Theory and Application to the Measurement of Stress and Texture," J. Acoust. Soc. Am. 80(3), Sept. 1986, pp 921-931.

[10] Hirao, M., Aoki, K., and Fukuoka, H., "Texture of Polycrystalline Metals Characterized by Ultrasonic Velocity Measurements," J. Acoust. Soc. Am. 81(5), May 1987, pp 1434-1440.

[11] Clark, A.V., Blessing, G.V., Thompson, R.B., and Smith, J.F., "Ultrasonic Methods of Texture Monitoring for Characterization of Formability of Rolled Aluminum Sheet," Rev. Progr. Quant. NDE, 7B, (Eds., Thompson, D.O. and Chimenti, D.E.) Plenum Press, NY, 1988, pp 1265-1373.

[12] Papadakis, E.P., "Ultrasonic Phase Velocity by the Pulse-Echo-Overlap Method Incorporating Diffraction Phase Corrections," J. Acoust. Soc. Am. 42(5), 1967, pp 1045-1051.

[13] Ting, C.S. and Sachse, W., "Measurement of Ultrasonic Dispersion by Phase Comparison of Continuous Harmonic Waves," J. Acoust. Soc. Am. 64(3), Sept. 1978, pp 852-857.

[14] Hsu, N.N., Proctor, T.M., and Blessing, G.V., "An Analytical Approach to Reference Samples for Ultrasonic Residual Stress Measurement," J. of Test. and Eval. 10(5), Sept. 1982, pp 230-234.

[15] Blessing, G.V., Hsu, N.N., and Proctor, T.M., "Ultrasonic-Shear-Wave Measurement of Known Residual Stress in Aluminum," Exper. Mech. 24(3), Sept. 1984, pp 218-221.

[16] Blessing, G.V., Eitzen, D.G., Henning, J.F., Clark, A.V., Jr., and Schramm, R.E., "Precision Ultrasonic Thickness Measurements of Thin Steel Disks," Rev. Progr. Quant. NDE, 7B (Eds., Thompson, D.O. and Chimenti, D.E.) Plenum Press, NY, 1988, pp 1563-1572.

[17] Anon., "Standard Methods for Determining Average Grain Size," 1985 Annual Book of ASTM Standards, 03.03, ASTM, PA, 1985, pp 112-149.

[18] Doiron, T.D. (private communication) National Instutute of Standards and Technology, Gaithersburg, MD, 1986.

[19] Mason, W.P. and McSkimin, H.J., "Attenuation and Scattering of High Frequency Sound Waves in Metals and Glasses," J. Acoust. Soc. Am. 19(3), 1947, pp 464-473.

[20] Fisher, M.J. and Johnson, G.C., "Acoustic Velocity Variations Due to Finite Grain Size in Polycrystalline Materials," Rev. Progr. in Quant. NDE, 3B (Eds., Thompson, D.O. and Chimenti, D.E.) Plenum Press, NY, 1984, pp 1119-1128.

[21] Stanke, F.E., "Unified Theory and Measurements of Elastic Waves in Polycrystalline Materials," Ph.D dissertation, Stanford University, 1983.

[22] Ledbetter, H.M., "Predicted Monocrystal Elastic Constants of 304-Type Stainless Steel," Physica 128B, 1985, pp 1-4.

Graeme G. Wren and Vikram K. Kinra

AN EXPERIMENTAL STUDY OF THE COMPLEX DYNAMIC MODULUS

REFERENCE: Wren, G.G., and Kinra, V.K., "An Experimental Study of the Complex Dynamic Modulus," Dynamic Elastic Modulus Measurements in Materials, ASTM STP 1045, Alan Wolfenden, editor, American Society for Testing and Materials, Philadelphia, 1990.

ABSTRACT: An overview of an experimental program for determining the dynamic flexural constitution of materials is presented. This program entails the development of a fully-automated flexural apparatus, its calibration, and studies of structural damping and dynamic flexural modulus of a variety of materials. Furthermore, graphite/aluminum laminates, $[\pm\theta]_s$, with θ ranging from zero to ninety degrees in fifteen degree increments, were tested. Classical laminate theory and the work of Ni and Adams was found to adequately predict both the modulus and the damping. It is demonstrated that the attachment of an end-mass (to vary the resonant frequency) does not contribute to the measured damping.

KEYWORDS: Damping, modulus, composite material, flexural, structural, dynamic, experimental, logarithmic decrement, vacuum.

SYMBOLS USED

A = cross sectional area of beam, amplitude
C_p = specific heat per unit mass at constant pressure
D_{ij} = components of the flexural modulus matrix for a laminate
E = Young's modulus
f = frequency (cycles/second)
h = beam thickness
I = second moment of area of beam
k_t = transverse thermal conductivity (in thickness direction)
L = beam length

Flight Lieutenant Wren is a graduate student at Texas A&M University studying under the auspices of the Royal Australian Air Force. Dr Kinra is Associate Professor of Aerospace Engineering at Texas A&M University, College Station, Texas, 77843.

m = end-mass, cosine of ply (fiber) orientation
n = sine of ply (fiber) orientation
T = absolute temperature
t = time
w = beam width
W = maximum elastic energy stored during a cycle
ΔW = mechanical energy dissipated per cycle
x = coordinate along the length of the beam
y = amplitude of transverse vibration
α = linear coefficient of thermal expansion, eigenvalue
β = eigenvalue
δ = logarithmic decrement
ϵ_ψ = accuracy of experimental damping measurement
$\zeta = \xi$ = damping ratio
η = loss factor
λ = eigenvalue
ρ = density per unit volume of beam material
τ = relaxation time
ϕ = phase angle by which the applied stress leads the resulting strain
ω = frequency (radians/second), $2\pi f$
ω_0 = resonant frequency of beam without an end-mass
ψ = damping = $\Delta W/W$
$()'$ = real part of a complex quantity ()
$()''$ = imaginary part of a complex quantity ()

INTRODUCTION

The design of any structure requires the quantitative knowledge of many parameters pertaining to the material of which the structure is built. Two parameters of importance in the analysis of structures subject to dynamic loads are the dynamic modulus and damping capacity. The measure of these entities, particularly damping, depends on the type of dynamic loading applied. Intrinsic, or material damping, is defined herein as the dissipation of energy within a material through the excitation of internal defect phenomena by the application of a homogeneous strain field. Structural damping on the other hand is composed of both intrinsic (material) and extrinsic (structural) components, and is defined to be the dissipation of energy produced by the application of a non-homogeneous strain field which is determined by specimen shape and structural application. Hence, a specimen subject to uniaxial tensile or compressive loading deforms and dissipates energy under a homogeneous strain field and therefore yields a measurement of intrinsic material damping. However, the strain field in a beam of the same material subject to flexural oscillations varies in the thickness direction and with position along the beam, this variation depending on boundary conditions. Therefore, energy dissipation within the beam will also be a function of thickness and position along the length of the beam, and will give a measure of structural damping. An example of such damping is the transport of thermal currents across the thickness dimension of a beam (Zener or thermoelastic relaxation).

Many experimental techniques have been proposed and developed to measure the dynamic constitution of materials. The technique described herein determines the dynamic properties in flexure with speed, automation, and measures of accuracy and precision. The experimental apparatus consists of a beam specimen mounted under cantilevered boundary conditions and vibrated in first-mode flexural resonance. Data acquisition and reduction techniques entail accurate determination of the resonant frequency, and a measure of the rate of decay in free-vibrational amplitude using a logarithmic decrement method for ascertaining the dynamic flexural modulus and structural damping, respectively [1].

Results pertaining to the flexural modulus and structural damping of 6061 aluminum and a symmetric four-ply metal-matrix composite composed of pitch-55 graphite fibers in a 6061 aluminum matrix are presented. These results are compared with those predicted by Euler-Bernoulli, Zener (thermoelastic), and laminate theories and show good agreement. End-masses were used to vary the resonant frequency of the test specimens [2]. A brief overview of the end-massed beam analysis and experimental results is presented to show that the addition of an end-mass only alters the resonant frequency of the specimen and does not contribute to the measure of damping. Damping results are presented in the form $\psi=\Delta W/W$, where ΔW is the energy dissipated during each loading cycle and W is the maximum energy stored. Calibration of the cantilevered configuration for apparatus losses was carried out in two steps. First, the damping of fused quartz, a material possessing negligible damping, was measured in a free-free apparatus [1]. This yielded a determination of the free-free apparatus losses. Second, flexural damping data for annealed 6061 aluminum obtained from both free-free and cantilevered configurations were compared. Results showed that, within the range of experimental scatter, both configurations provided the same measure of damping. This agreement of the data justified equating the cantilevered apparatus losses to those of the free-free configuration. Accuracy of the experimental dynamic flexural modulus values was dependent upon the measurement of the resonant frequency and specimen parameters. An estimate of accuracy was obtained by comparing the results of the present study with those of an experimental study using ultrasonic wave propagation [3]. These procedures determined accuracy of the modulus and damping values to be 0.1 percent and $\epsilon_\psi=3.0\text{x}10^{-4}$, respectively. It is noted that ϵ_ψ is a systematic error and $\epsilon_\psi>0$. Statistical analysis of all experimental data ascertained the precision to be 0.1 percent and $5\text{x}10^{-4}$ (one standard deviation), for modulus and damping, respectively.

SPECIMENS

A variety of specimens were tested including annealed 6061 and 6061T6 aluminum alloys (6061Al), magnesium-0.6% zirconium alloy (Mg-0.6%Zr), magnesium-1% manganese alloy (Mg-1.0%Mn), leaded and lead-free brass, fused quartz, and three metal-matrix composite laminates comprising continuous pitch-55 graphite fibers (P55Gr) in a matrix of 6061 aluminum (P55Gr/6061Al), P55Gr fibers in a matrix of magnesium with 0.6 percent zirconium (P55Gr/Mg-0.6%Zr), and P55Gr fibers in a matrix of magnesium with one percent manganese (P55Gr/Mg-1%Mn). The P55Gr/6061Al specimens were cut from a four-ply, balanced, symmetric, laminated plate at angles ranging from zero to ninety degrees in fifteen degree increments; in a zero degree specimen, the fibers are aligned along the length dimension of the beam. The P55Gr/Mg-0.6%Zr and P55Gr/Mg-1%Mn specimens were cut from a zero-degree, eight-ply laminate.

The P55Gr/6061Al diffusion bonded laminated composite beam specimens were constructed of four orthotropic, unidirectional lamina oriented at specific angles to the longitudinal beam axis and symmetrically disposed to the midplane of the laminate. During the fabrication process Gr/Al precursor tows each containing 2000, 10 μm diameter fibers were consolidated between 0.089 mm thick 6061 aluminum face sheets at the angles appropriate to the particular laminate layup. The laminate was processed at 588°C and 24.1 MPa for 20 minutes, yielding a composite plate of 50% fiber volume. Two specimens of each laminate orientation were tested. The dimensions, density, flexural modulus, and flexural damping of the 6061 aluminum and metal-matrix laminate specimens tested are given in Table 1.

TABLE 1 - SPECIMEN PARAMETERS

Specimen Type	L m $\times 10^2$	w m $\times 10^2$	h m $\times 10^2$	ρ kg/m^3 $\times 10^3$	E_L GPa	Ψ $\Delta W/W$ $\times 10^2$
6061Al	Table 2	1.270	0.162	2.70	68.92	Figure 6
P55Gr/6061Al:						
$[0_4]_T$	13.10	1.214	0.211	2.41	157.90	0.35
$[0_4]_T$	13.08	1.212	0.208	2.41	160.65	0.40
$[\pm 15]_s$	13.18	1.089	0.208	2.43	124.38	1.03
$[\pm 15]_s$	13.23	1.146	0.203	2.41	125.48	0.90
$[\pm 30]_s$	13.03	0.955	0.208	2.43	74.39	2.00
$[\pm 30]_s$	13.20	1.143	0.211	2.41	72.81	1.80
$[\pm 45]_s$	15.21	1.217	0.208	2.41	47.09	2.35
$[\pm 45]_s$	15.24	1.212	0.208	2.38	45.78	2.10
$[\pm 60]_s$	13.13	0.957	0.211	2.41	36.13	2.60
$[\pm 60]_s$	13.51	0.955	0.211	2.41	35.51	2.70
$[\pm 75]_s$	15.47	1.212	0.203	2.43	37.37	2.25
$[\pm 75]_s$	13.59	1.214	0.203	2.43	36.82	2.35
$[90_4]_T$	13.18	1.146	0.203	2.43	36.68	1.60
$[90_4]_T$	13.30	1.140	0.203	2.43	36.47	1.55

EXPERIMENTAL APPARATUS

A schematic diagram of the experimental apparatus utilized in this research is presented in Figure 1. This equipment determines the dynamic properties in flexure with speed, automation and measures of accuracy and precision. The apparatus consists of a beam specimen supported under cantilevered boundary conditions and vibrated in first-mode flexural resonance, a Wavetek Model 164 frequency generator, a Bruel and Kjaer electromagnetic transducer, a power amplifier for increasing the signal received by the transducer, a Micro-Measurements BAM-1 strain bridge, a Data Precision Model 6000/611 waveform analyzer, and a Hewlett Packard 9000/217 computer connected to the Data 6000 by an IEEE 488 interface. To isolate the system from the effects of air damping, the specimen was mounted in a vacuum chamber connected to a Cenco Hypervac 25 vacuum pump capable of drawing a hard vacuum of 0.013 Pa.

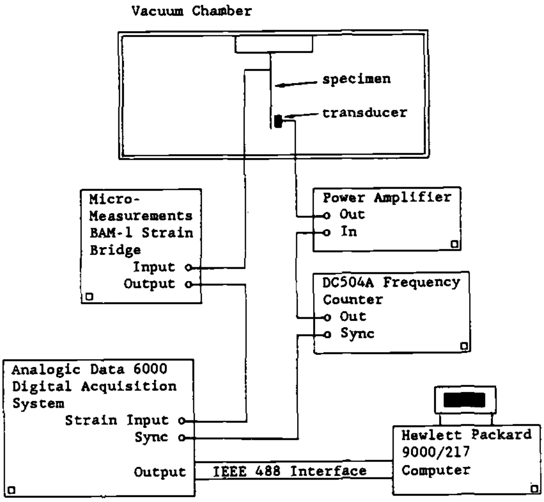

Figure 1 - Experimental Configuration

THEORETICAL BACKGROUND

To preserve the succinct nature of the paper only the final results of the Euler-Bernoulli, logarithmic decrement, thermoelastic, and laminate theories entailed in these studies will be given here.

Dynamic Flexural Modulus

Let ω' be the frequency of a cantilevered beam made of an isotropic anelastic material, and E' be the real part of the Young's modulus. By the use of the Correspondence Principle of linear viscoelasticity [4], and the Euler-Bernoulli theory of flexure, the relationship between E' and ω' is given by:

$$\omega' = \frac{\alpha^2}{L^2}\sqrt{\frac{E'I}{\rho A}} \qquad (1)$$

where ()' denotes the real part of a complex quantity, α is the eigenvalue, which for the fundamental mode of a cantilevered beam has a value of 1.875, E is the Young's modulus, I is the second moment of area, ρ is the density per unit volume, and A is the cross-sectional area. This analysis assumes that the free vibrations of low-loss viscoelastic materials are approximately harmonic [5].

Logarithmic Decrement

The logarithmic decrement technique entails measuring the rate at which the free-vibration amplitude decays with time. An expression for the damping is given by:

$$\psi = \frac{\Delta W}{W} = \frac{4\pi \ln[A(t_1)/A(t_2)]}{\omega_r[t_2-t_1]} \qquad (2)$$

where ω_r is the resonant frequency, and $A(t_1)$ and $A(t_2)$ are the peak displacements at times t_1 and t_2, respectively. In accordance with equation (2), $\ln[A(t_1)/A(t_2)]$ was plotted against (t_2-t_1), the least squares method was used to fit a straight line, and from the slope, m, of the straight line, the damping was calculated from:

$$\psi = 4\pi m/\omega_r \qquad (3)$$

Several other definitions of damping currently appear in the literature. For the convenience of the reader, their inter-relationship is documented here:

$$\psi = 2\pi\tan\phi = 2\pi\eta = 4\pi\zeta = 4\pi\xi = 2\pi Q^{-1} = 2\pi E''/E' = 4\pi\omega''/\omega' = 2\delta$$

Thermoelastic (Zener) Damping

The variation of damping with frequency due to the transport of thermal currents as determined from Zener theory [6] is given by:

$$\psi = \psi_o \left[\frac{\omega\tau}{1+\omega^2\tau^2}\right] \qquad (4)$$

where $\psi_o = \frac{2\pi\alpha^2 ET}{\rho C_p}$ and $\tau = \frac{h^2\rho C_p}{\pi^2 k_t}$

Equation (4) describes the damping in a beam produced from the transport of thermal currents across the thickness dimension. This form of energy dissipation is dependent on the structural configuration and is produced by a non-homogeneous strain field. It is therefore a form of structural damping. This equation has been used in calculating the curves in Figures 4, 6 and 7.

Laminate Theory

The following expressions for flexural modulus and damping for a balanced, symmetric, laminated composite beam were derived using general plate theory of laminated composites [7] and the studies of Ni and Adams [8], respectively. It is noted that this laminate theory is based on the theory of linear elasticity and does not include thermoelastic effects. The coordinate system of the lamina (on-axis, principal, [1,2,3]) and laminate (off-axis, [x,y,z]), and the laminate ply counting sequence are shown in Figures 2 and 3, respectively. The effective flexural modulus in free-flexure, where bending-twisting coupling is not constrained, is given by:

$$E_f = \frac{12}{h^3 D'_{11}} \tag{5}$$

Although it is obvious that the boundary conditions used do not constrain bending-twisting coupling (except at the clamped-end), this constraint was investigated for confirmation and completeness. The constrained flexural modulus, termed

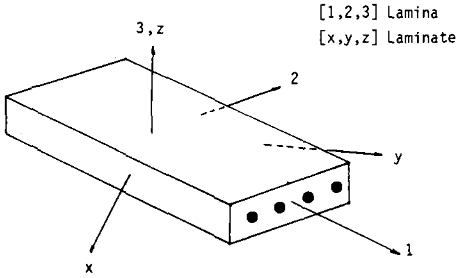

Figure 2 - Laminate Coordinate System

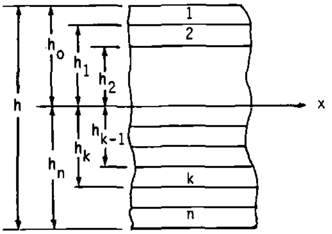

Figure 3 - Ply Counting Sequence

pure-flexure, is given by:

$$E_p = \frac{12D'_{66}}{h^3[D'_{11}D'_{66} - (D'_{16})^2]} \tag{6}$$

where D_{ij}' are components of the laminate flexural modulus matrix.

The total flexural damping is given by:

$$\psi = \psi_1 + \psi_2 + \psi_{12} \tag{7}$$

where $\psi_1 = \frac{\Delta W_1}{W} \quad \psi_2 = \frac{\Delta W_2}{W} \quad \psi_{12} = \frac{\Delta W_{12}}{W}$

$$\psi_1 = \frac{\psi_L}{3D'_{11}} \sum_{k=1}^{n} m^2(\bar{Q}_{11}D'_{11} + \bar{Q}_{12}D'_{12} + \bar{Q}_{16}D'_{16})(m^2D'_{11} + mnD'_{16})(h^3_k - h^3_{k-1})$$

$$\psi_2 = \frac{\psi_T}{3D'_{11}} \sum_{k=1}^{n} n^2(\bar{Q}_{11}D'_{11} + \bar{Q}_{12}D'_{12} + \bar{Q}_{16}D'_{16})(n^2D'_{11} - mnD'_{16})(h^3_k - h^3_{k-1})$$

$$\psi_{12} = \frac{\psi_{LT}}{3D'_{11}} \sum_{k=1}^{n} mn(\bar{Q}_{11}D'_{11} + \bar{Q}_{12}D'_{12} + \bar{Q}_{16}D'_{16})(2mnD'_{11} - [m^2-n^2]D'_{16})(h^3_k - h^3_{k-1})$$

and $m=\cos\theta_k$ and $n=\sin\theta_k$. The above relations were derived assuming negligible shear deformation and rotary inertia (Euler-Bernoulli beam theory) which holds for length-to-thickness ratios greater than approximately 30 [9]. The length-to-thickness ratio for the composite specimens tested was of the order of 100.

EXPERIMENTAL PROCEDURE

Vibrational motion of the beam specimen was induced using an electromagnetic transducer driven at the resonant frequency of the specimen. As the specimens were non-magnetic, a small, high permeability disc was attached to the end of the specimens to provide coupling with the transducer. The cyclic signal representing the motion of the specimen was obtained via a strain gage attached near the root. This gage was connected to the direct-current strain bridge, whose analog voltage output was passed to the Data 6000 acquisition device. When the specimen reached steady-state, forced vibrational motion, the resonant frequency was recorded by the computer. The current to the excitation transducer was then interrupted and the specimen went into free vibrational decay. The steady-state and the free-decay motion were recorded in digital form by the Data 6000 where the voltage of each positive peak of the waveform was determined and passed via the IEEE 488 bus to the computer.

In order to study the variation of dynamic flexural modulus and structural damping with frequency, an end-mass was attached to the end of the specimen to facilitate the variation of its resonant frequency [2]. The dynamic flexural modulus was calculated using equation (1) and the experimental values of resonant frequency and specimen parameters. Structural damping was determined using equations (2) and (3).

EXPERIMENTAL ERROR

Calibration of the cantilevered configuration for apparatus losses was carried out in two steps. First, the damping of fused quartz, a material possessing negligible damping, was measured in a free-free apparatus [1]. A reported damping value for fused quartz is 1.2×10^{-6} [10]. The value measured using the free-free vibrational apparatus was 3×10^{-4}. As the cited value is negligibly small, 3×10^{-4} is determined to represent apparatus losses, and is denoted ϵ_ψ. Therefore, the measured value of damping of any material using this apparatus can be decomposed into the thermoelastic (Zener) and intrinsic damping of the material plus apparatus losses:

$$\psi_{\text{measured}}^{\text{free-free}} = \psi_{\text{Zener}}^{\text{free-free}} + \psi_{\text{intrinsic}} + \epsilon_\psi^{\text{free-free}} \qquad (8)$$

Because it is impractical to measure the damping of fused quartz using a cantilevered apparatus due to the required clamping pressures and the fragile nature of the material, a comparison between measured damping values for annealed 6061 aluminum in both free-free and cantilevered configurations was carried out. As shown in Figure 4, results displayed a negligible difference in the mean damping values obtained from the two techniques. The standard error for the least squares curve fit of all the data was 5×10^{-4}. In an analogous manner to that used for the free-free apparatus, the measured damping value of a material can again be decomposed according to equation (8):

$$\psi_{\text{measured}}^{\text{cantilever}} = \psi_{\text{Zener}}^{\text{cantilever}} + \psi_{\text{intrinsic}} + \epsilon_\psi^{\text{cantilever}} \qquad (9)$$

As the intrinsic damping of a material is a constitutional property, and comparison of experimental data was made at the same frequency using specimens of the same dimensions, then:

$$\psi_{Zener}^{\text{free-free}} = \psi_{Zener}^{\text{cantilever}} \tag{10}$$

Since the measured values of damping obtained from two different techniques agree over the range of frequencies and strain amplitudes studied, it follows from equations (8), (9) and (10) that:

$$\epsilon_{\psi}^{\text{free-free}} = \epsilon_{\psi}^{\text{cantilever}} \tag{11}$$

Therefore, from equation (11) and the agreement between the experimental results shown in Figure 4, the apparatus losses of the cantilevered configuration can be equated to the measured value of extraneous losses in the free-free apparatus; that is, for both configurations, the accuracy in the measurement of damping, defined by ϵ_{ψ}, is $3.0\text{x}10^{-4}$. An additional point of interest obtained from Figure 4 is that the value of Zener damping, which is strain amplitude independent, lies within the range of intercept of the least squares best-fit straight line and the lines specifying the standard error. This adds credence to the measured data, and also demonstrates that, for the particular material tested where intrinsic damping is very low, an accurate measure of the intrinsic damping cannot be determined from the flexural damping as it lies within the range of experimental scatter. However, one may put bounds on its magnitude; that is $0<\psi_{intrinsic}<5\text{x}10^{-4}$.

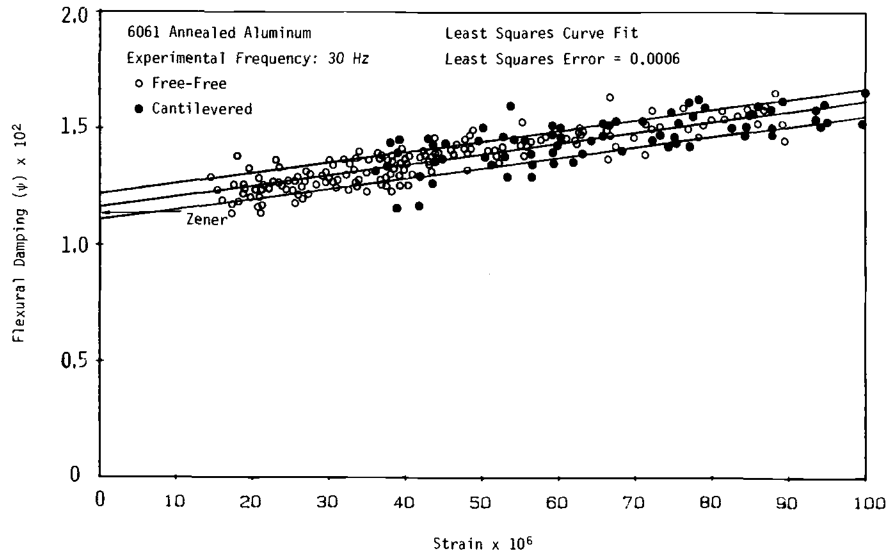

Figure 4 - Comparison of Flexural Damping Data from Free-Free and Cantilevered Configurations

Accuracy of the experimental dynamic flexural modulus values is dependent upon the measurement of the resonant frequency and specimen parameters. A measure of the accuracy and precision of the modulus data was determined by calculating the modulus from thirty independent tests in which the resonant frequency was disturbed by attaching different end-masses to the end of a specimen [2]; this will be discussed further in the next section. Evaluation of the dynamic flexural modulus from the thirty different experimental values of frequency, and the corresponding eigenvalues determined from the end-mass used, resulted in a mean value of 69.376 GPa ± 0.1% (one standard deviation). This agrees within 0.1% with the value of 69.439 GPa ± 0.1% obtained from an independent study using ultrasonic wave propagation [3].

Thus, the accuracy of the measured modulus and damping values presented herein are 0.1 percent and $3.0\text{x}10^{-4}$, respectively. Precision of the experimental data was ascertained to be 0.1 percent and $5\text{x}10^{-4}$ (one standard deviation), for modulus and damping, respectively.

RESULTS AND DISCUSSION

For continuity the essential results pertaining to the attachment of an end-mass to a beam specimen to facilitate the variation of resonant frequency are reproduced from [2]. This technique was used to determine the frequency dependence of dynamic flexural modulus and structural damping for the specimens tested. The data, covering almost two decades of frequency, were obtained using five different beam lengths and six different end-masses. The length, mass and frequency matrix is shown in Table 2.

TABLE 2 -THEORETICAL VALUES OF RESONANT FREQUENCIES FOR DIFFERENT LENGTH/END-MASS COMBINATIONS

beam length (cm)	end-mass (g)					
	m_6 91.17	m_5 40.09	m_4 19.96	m_3 10.34	m_2 4.99	m_1 0.17
L_1 12.70	**11.19**	16.68	23.15	31.10	41.70	78.46
L_2 16.51	7.52	**11.19**	15.44	20.55	27.11	46.90
L_3 20.32	5.49	8.15	**11.19**	14.76	19.20	31.15
L_4 24.13	4.24	6.25	8.55	**11.19**	14.90	22.19
L_5 27.94	3.39	4.99	6.79	8.82	**11.19**	16.96

width=1.27 cm, thickness=0.162 cm

The relationship between the frequency and end-mass is given by equation (1) where now the eigenvalues, α, are the solutions of the transcendental equation [2]:

$$\frac{1 + \cos\alpha\cosh\alpha}{\alpha(\sin\alpha\cosh\alpha - \cos\alpha\sinh\alpha)} = \frac{m}{\rho AL} \qquad (12)$$

Figure 5 shows the normalized frequency as a function of normalized mass for annealed 6061 aluminum and justifies the applicability of Euler-Bernoulli beam theory in the analysis. Further, each experimental data point is an independent measure of the dynamic flexural modulus since the eigenvalues are specified by equation (12) and vibrational frequencies are experimentally determined. Thus, the modulus can be calculated via a rearrangement of equation (1). It is emphasized that each data point provides an independent determination of the modulus as all parameters in equation (1), except the eigenvalues, are experimentally measured. Evaluation of the dynamic flexural modulus from the thirty experimental data points resulted in a mean value of 69.376 GPa ± 0.1% (one standard deviation). This agrees very well with the value of 69.439 GPa ± 0.1% obtained from an independent study [3].

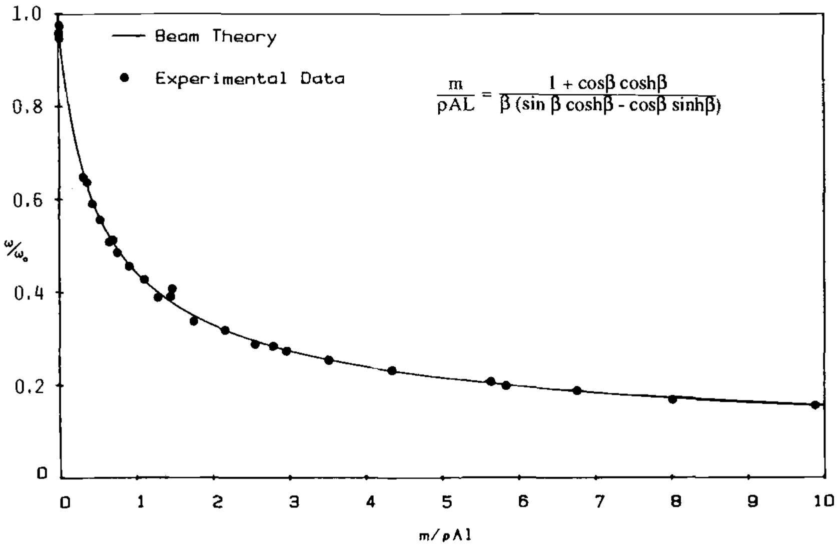

Figure 5 - The Effect of End-Mass on the Resonant Frequency of a Cantilevered Beam

Figure 6 shows the normalized damping as a function of normalized frequency for 6061 aluminum. The vertical arrow points to the frequency common to five of the reference beam length/end-mass combinations (11.19 Hz). These five measurements lie in the range ψ=0.81x10^{-2} ± 0.02x10^{-2} (±2.5%). It is important to note that this observation of precision agrees well with the value of 5×10^{-4} obtained from the independent study of comparative damping values for the free-free and cantilevered configurations. The experimental program was designed to cover a broad range of frequency values on either side of the Zener relaxation frequency $\omega\tau=1$ and, as shown, experimental results follow the Zener curve very well. Figure 7 displays the normalized damping as a function of normalized mass for four nominal frequencies, namely, 8, 11.19, 16, and 20 Hz. Clearly, within the bounds of experimental error, the damping is insensitive to the end-mass.

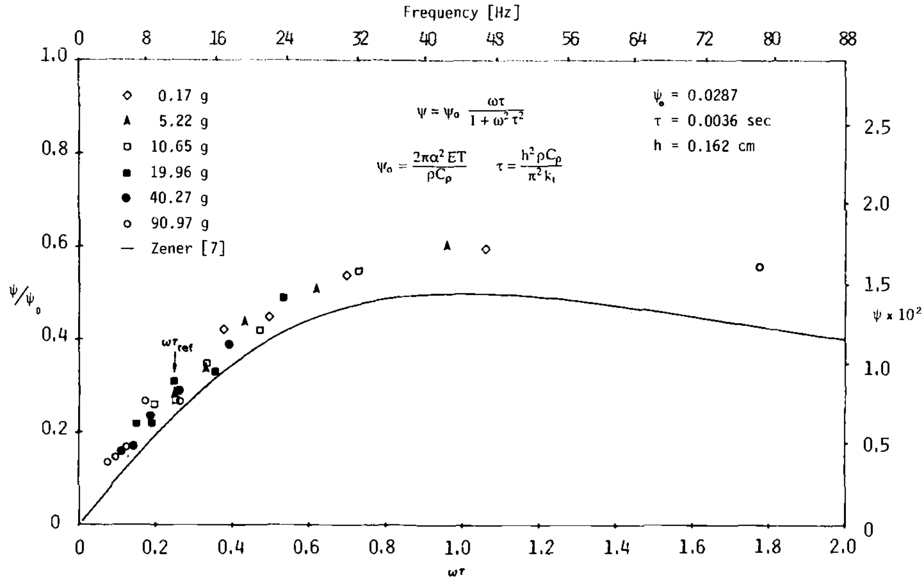

Figure 6 - Normalized Damping vs Normalized Frequency for 6061 Aluminum

Five beam lengths and six end-masses were chosen to produce the same resonant frequency (marked by arrow). Within the errors of measurement, the measured damping does not depend on end-mass.

The variation of flexural modulus and damping with ply-angle for the P55Gr/6061Al metal-matrix composite laminate specimens was investigated at fixed values of frequency (35 Hz) and strain amplitude ($55\mu\epsilon$). Two specimens of each ply-angle were tested. The experimental flexural modulus results and the curves defined by equations (5) and (6) are shown in Figure 8. Locations where only one symbol is shown indicate that agreement of the experimental data was within the size of the graphing symbol. The variation of the unconstrained (free) dynamic flexural modulus with ply-angle, as defined by equation (5), is illustrated as the solid line in Figure 8. This semi-empirical curve was generated using experimental values of the longitudinal and transverse moduli, Poisson's ratio, and the resultant element value of the

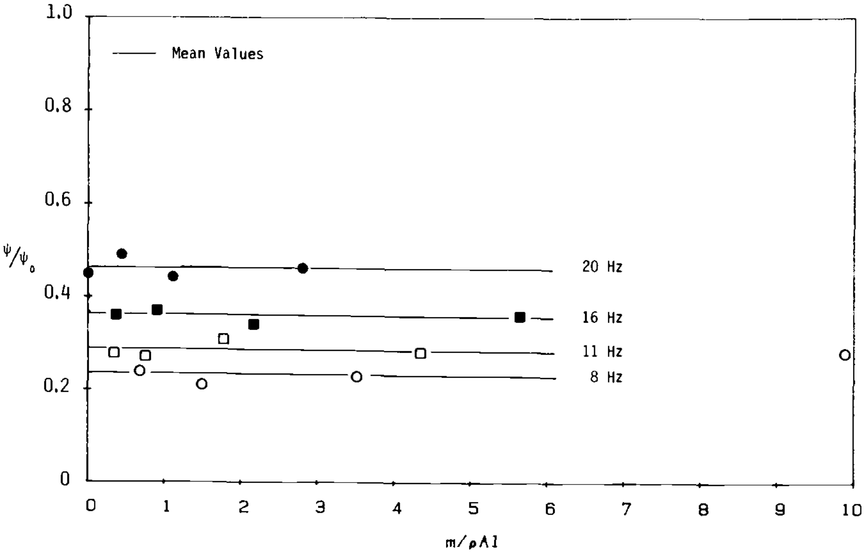

Figure 7 - Damping as a Function of End-mass for Four Nominal Frequencies

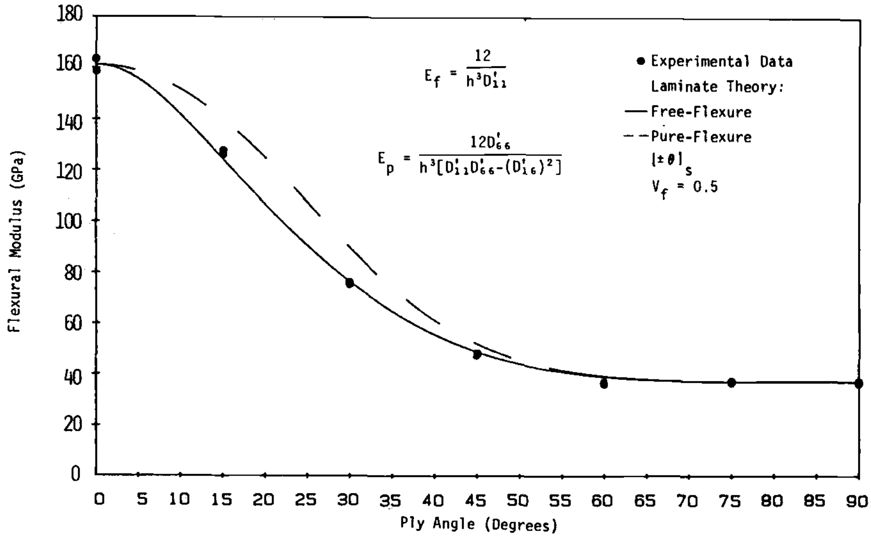

Figure 8 - Flexural Modulus vs Ply-Angle for Symmetric 4-Ply P55Gr/6061Al Composite

Two specimens of each ply angle were tested - the experimental data overlap

laminate flexural modulus matrix, D'_{11}, calculated from a laminate code. As the shear modulus was unavailable, this parameter was varied in the laminate code to give the least-squares best-fit curve through the experimental flexural modulus data. From this routine a longitudinal shear modulus value of 16.5 GPa was obtained. The curve for the constrained (pure) flexural modulus, as defined by equation (6), is shown as the dashed line in Figure 8. Comparison of the two curves indicate that flexure is best modelled by assuming the twisting due to the bending-twisting coupling terms to be unconstrained, as expected.

Prediction of laminate structural damping, as given by equation (7), was calculated from the laminate code using the experimentally determined value for G_{LT} (from the flexural modulus curve-fit), measured values of ψ_L, ψ_T, obtained from flexural damping experiments on zero and 90 degree specimens, and curve-fitting for ψ_{LT}. The theoretical curve and experimental data are shown in Figure 9. The curve shown was generated using an analogous least-squares best-fit routine as that used to determine G_{LT}. This resulted in a value of ψ_{LT}=0.039. Experimental results indicate that within experimental scatter, laminate theory predicts the flexural modulus and damping in graphite-aluminum metal-matrix laminates reasonably well. Tables 3, 4 and 5 provide a summary of the mechanical properties of annealed 6061 aluminum, continuous Pitch 55 graphite fibers, and the P55Gr/6061Al metal-matrix composite specimens tested, respectively.

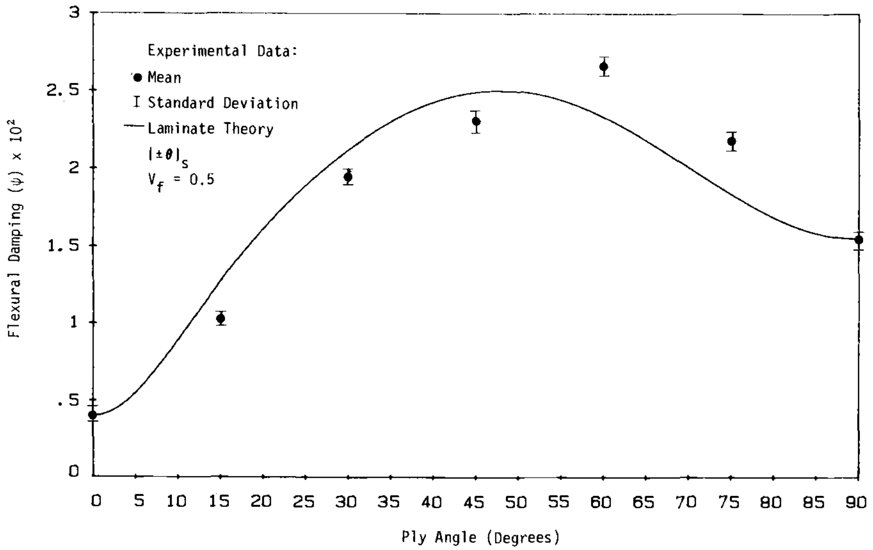

Figure 9 - Flexural Damping vs Ply-Angle for Symmetric 4-Ply P55Gr/6061Al Composite

TABLE 3 - MECHANICAL PROPERTIES OF ANNEALED 6061 ALUMINUM

E GPa	G GPa	ν	ρ kg/m^3 x10^3	α μm/m°K	k J/m°Ks	C_p J/kg°K
68.9	25.9	0.33	2.70	23.0	180.2	895.8

TABLE 4 - MECHANICAL PROPERTIES OF CONTINUOUS PITCH 55 CONTINUOUS GRAPHITE FIBERS

E_L GPa	E_T GPa	G_{LT} GPa	ν_{LT}	ρ kg/m^3 x10^3	α μm/m°K	k J/m°Ks
379.2	3.4	17.2	0.41	1.99	-1.25	120.9

TABLE 5 - EXPERIMENTALLY DETERMINED MECHANICAL PROPERTIES OF P55Gr/6061Al METAL MATRIX COMPOSITE

E_L GPa	E_T GPa	G_{LT} GPa	ν_{LT}	ρ kg/m^3 x10^3	V_f	ψ_L x10^2	ψ_T x10^2	ψ_{LT} x10^2
159.27	36.57	16.5	0.33	2.43	0.5	0.375	1.55	3.9

V_f: volume fraction
ψ: $\Delta W/W$
E_L, E_T, ψ_L, and ψ_T are average values of the specimens tested (from Table 1).
G_{LT} and ψ_{LT} were deduced from experimental results of flexural modulus and damping, respectively.

CONCLUSIONS

The cantilevered flexural resonance apparatus discussed herein facilitates the measurement of the dynamic flexural modulus and structural damping capacity of a material. The attachment of an end-mass does not contribute to measured values of flexural modulus or damping. Experimental values obtained for the flexural modulus and structural damping of annealed 6061 aluminum display good agreement with Euler-Bernoulli and Zener (thermoelastic) theories. Experimental results obtained from specimens cut from a four-ply, balanced, symmetric, P55Gr/6061Al metal-matrix composite laminate at angles ranging from zero to ninety degrees in increments of fifteen degrees indicated that the flexural modulus and structural damping varied with ply angle. The classical laminate theory of Ni and Adams [8] adequately predicts this variation. Accuracy of the modulus and damping values were determined to be 0.1 percent and $\epsilon_{\psi}=3.0\mathrm{x}10^{-4}$, respectively. Statistical analysis of all experimental data ascertained the precision to be 0.1 percent and $5\mathrm{x}10^{-4}$ (one standard deviation), for modulus and damping, respectively.

REFERENCES

[1] Wren, G.G., and Kinra, V.K., "An Experimental Technique for Determining a Measure of Structural Damping," Journal of Testing and Evaluation, Vol. 16, No. 1, January 1988, pp 77-85.

[2] Wren, G.G., and Kinra, V.K., "On The Effect of End-Mass on Damping," to appear in Experimental Mechanics.

[3] Kinra, V.K., Petraitis, M.S., and Datta, S.K., "Ultrasonic Wave Propagation in a Random Particulate Composite," International Journal of Solids and Structures, Vol. 16, 1980, pp 301-312.

[4] Schapery, R.A., "Viscoelastic Behavior and Analysis of Composite Materials," Composite Materials, Vol. 2, G.P. Sendecky editor, Academic Press, New York, 1974.

[5] Read, B.E., and Dean, G.D., The Determination of Dynamic Properties of Polymers and Composites, Adam Hilger, Bristol, England, 1978.

[6] Zener, C.M., Elasticity and Anelasticity of Metals, University of Chicago Press, Chicago, 1948.

[7] Halpin, J.C., Primer on Composite Materials, Technomic Publishing Co., Lancaster, 1984.

[8] Ni, R.G., and Adams, R.D., "The Damping and Dynamic Moduli of Symmetric Laminated Composite Beams - Theoretical and Experimental Results," Journal of Composite Materials, Vol. 18, March 1984, pp 104-121.

[9] Whitney, J.M., Structural Analysis of Laminated Anisotropic Plates, Technomic Publishing Co., Lancaster, 1987.

[10] Kimball, A.L., and Schenectady, N.Y., "Vibration Problems - Part V -Friction and Damping in Vibrations," Journal of Applied Mechanics, September 1941, pp A-135 to A-137.

L. Steven Cook, Alan Wolfenden, and Gerard M. Ludtka

LONGITUDINAL AND FLEXURAL RESONANCE METHODS FOR THE DETERMINATION OF THE VARIATION WITH TEMPERATURE OF DYNAMIC YOUNG'S MODULUS IN 4330V STEEL

REFERENCE: Cook, L. S., Wolfenden, A., and Ludtka, G. M., "Longitudinal and Flexural Resonance Methods for the Determination of the Variation with Temperature of Dynamic Young's Modulus in 4330V Steel," Dynamic Elastic Modulus Measurements in Materials, ASTM STP 1045, A. Wolfenden, Ed., American Society for Testing and Materials, Philadelphia, 1990.

ABSTRACT: The variation with temperature of dynamic Young's modulus in 4330V steel has been characterized using a longitudinal resonance method (the piezoelectric ultrasonic composite oscillator technique - PUCOT) and a flexural resonance method (the impulse excitation technique - IET). The PUCOT yielded an ambient temperature dynamic Young's modulus value of 206.3 GN/m^2 while values obtained from the IET ranged from 197.5-206.8 GN/m^2. Both techniques yielded a dE/dT value of -0.08 GN/(m^2 K). In addition, three numerical methods for the calculation of dynamic Young's modulus from flexural resonance frequencies of prismatic specimens have been evaluated. Experimental uncertainty at ambient temperature has been calculated for the PUCOT and the IET.

KEY WORDS: elastic modulus, Young's modulus, dynamic, elevated temperature, 4330V steel, PUCOT, IET

An understanding of how design parameters such as ultimate tensile strength, yield strength and stiffness vary with temperature is critical to the design of structures intended for service at elevated temperatures. In general, mechanical properties are functions of stress, temperature and time. As a result, strength properties are best characterized by creep or creep-rupture tests where the effects of each independent variable can be more fully understood. At sufficiently high temperatures, the standard tensile test becomes inappropriate for determining stiffness properties as well: Viscous effects associated with the weakening of grain boundaries contribute to test specimen deformation to the extent that the ratio of stress to strain can no longer be considered a true measure of elastic behavior.

Mr. Cook and Dr. Wolfenden are Graduate Research Assistant and Professor, respectively, with the Mechanical Engineering Department, Texas A&M University, College Station, TX 77843; Dr. Ludtka is a Research Metallurgist with the Oak Ridge Y-12 Plant, Oak Ridge TN 37831.

An alternative to the conventional tensile test, wherein the applied stress is both small enough to be well within the elastic range, and applied rapidly enough to minimize time-dependent viscous effects, is required. These requirements are met admirably by dynamic elastic modulus testing techniques. Resonance methods possess the additional advantages of small specimen sizes and the resulting ease of maintaining a constant specimen temperature [1].

ASTM task group E28.03.05 has recently evaluated many of the dynamic elastic modulus testing techniques at ambient temperature [2]. The present study is a comparison of results obtained using two of these techniques (impulse excitation and piezoelectric composite oscillation) to obtain Young's modulus values for a single material in the temperature range 296-873 K. A description of the specimen material and the presentation of theoretical background, experimental details and results, are included. The analysis of results contains an estimation of experimental uncertainty associated with the two techniques and a comparison of three numerical methods used to calculate dynamic elastic modulus values from flexural resonance frequencies obtained with the impulse excitation technique. Conclusions on the relative merits of the two techniques are enumerated.

SPECIMEN MATERIAL

The 4330V alloy steel was chosen for use in this study. Two criteria were used in selecting this material: In the normalized condition, it is metallurgically stable over the temerature range and exposure times encountered by the specimens. Also, it is one of several alloys for which the Oak Ridge Y-12 Plant has need of elevated temperature modulus data. These data are used as input for finite element codes currently being employed in a research and development program concerned with modeling the quenching process. The ultimate goal of the project is the capability to predict the microstructure and residual stresses developed in various alloys upon a quench.

At Oak Ridge, test specimens were machined from a normalized forging blank. Dilatometry was performed at Oak Ridge as well. Results of the dilatometry were reported as linearized coefficients of thermal expansion (CTE) over the temperature ranges 296-473 K (CTE = 11.78×10^{-6} K^{-1}), 473-673 K (CTE = 11.32×10^{-6} K^{-1}), and 673-873 K (CTE = 14.36×10^{-6} K^{-1}). For a given test temperature, a weighted average of the appropriate linearized CTE was used. Dilatometer accuracy is estimated to be about 1%.

At Texas A&M, determination of specimen density was performed using Archimedes' principle. The density of the 4330V specimens was determined to be 7840 ± 50 kg/m^3 (± 0.64%). Mass determinations were performed using an analytic balance with a relatively high degree of accuracy; lack of repeatability (precision) was the dominant contributor to experimental uncertainty.

THEORETICAL BACKGROUND

The mechanical resonance frequencies of a linear elastic, homogeneous, isotropic body are dependent upon the dimensions, density and elastic moduli of the body. This principle is the basis of all resonance methods employed in dynamic modulus measurements. Differences among the various resonance methods include the mode of vibrations excited and the technique used to excite the vibrations.

With respect to resonance methods, Young's modulus E is most often calculated from the resonance frequencies of prismatic specimens. This section discusses the mathematical models typically used to calcuate Young's modulus from data obtained experimentally using the piezoelectric ultrasonic composite oscillator technique (PUCOT) and the impulse excitation technique (IET). The first subsection deals with longitudinal vibrations and applies to the PUCOT; the remaining three subsections concern flexural vibrations and apply to the IET.

Longitudinal Vibrations

The equation of motion for longitudinal resonance behavior in prismatic specimens is the wave equation [3]:

$$\frac{\partial^2 u}{\partial t^2} = c^2 \frac{\partial^2 u}{\partial x^2} \tag{1}$$

where

x = axial direction coordinate
u = displacement along x-axis
t = time
c = a constant.

A "shortcut" solution is obtained by noting that for a linear elastic, homogeneous, isotropic body, the constant c is equal to the bulk wave velocity and related to Young's modulus and density by

$$c = \sqrt{\frac{E}{\rho}} \tag{2}$$

where

E = Young's modulus
ρ = density.

Wave velocity, frequency and wavelength are related by

$$c = f\lambda \tag{3}$$

where

f = resonant frequency
λ = wavelength.

Resonance methods employing longitudinal vibrations most often use specimens one-half wavelength long. Setting specimen length equal to λ/2 and combining Eqs. 2 and 3 yield

$$E = 4\rho l^2 f^2 \tag{4}$$

where

l = specimen length.

Equation 4 is the equation used to calculate Young's modulus from parameters determined experimentally by the PUCOT. It should be noted that Eq. 4 is not an exact solution, but an approximation based on the assumption that cross-sections of the specimen remain plane and that the particles in these sections perform only motion in the axial direction of the specimen. It is general practice to accept this approximation for wavelength-to-diameter ratios of ten-to-one or greater.

Flexural Vibrations

The analysis of flexural resonance of prismatic specimens is not as straightforward as that of longitudinal resonance. Several approaches have been taken.

The Bernoulli-Euler model: The equation of motion for flexural resonance behavior in prismatic specimens is [3]

$$\frac{\partial^2 y}{\partial t^2} + a^2 \frac{\partial^4 y}{\partial x^4} = 0 \tag{5}$$

where

y = lateral direction coordinate
a = a constant.

The constant a has the physical significance

$$a = \sqrt{\frac{EI}{\rho A}} \tag{6}$$

where

I = second moment of the cross-sectional area about the neutral axis
A = cross-sectional area.

This looks similar to the wave equation, but it is not. For nodally supported boundary conditions, Young's modulus may be obtained using [4]

$$E = \frac{64\pi^2 \rho l^4 f_n^2}{m_n^4 d^2} \tag{7}$$

where

f_n = resonant frequency of the nth mode of vibration
d = diamter of specimen
m_n = nth root of $(\cos m)(\cosh m) = 1$.

This model assumes that cross-sections of the specimen remain plane and normal to the neutral axis. The effects of shear deformation and rotatory inertia are neglected.

The Timoshenko Beam model: Lord Rayleigh [5] added a term to the equation of motion to account for the effects of rotatory inertia. Timoshenko [6,7] added a term to the equation to correct for the effects of shear deformation. The resulting equations of motion are:

$$EI\frac{\partial^2\psi}{\partial x^2} + \kappa\left(\frac{\partial y}{\partial x} - \psi\right)AG - I\rho\frac{\partial^2\psi}{\partial t^2} = 0 \tag{8}$$

$$\rho A\frac{\partial^2 y}{\partial t^2} - \kappa\left(\frac{\partial^2 y}{\partial x^2} - \frac{\partial\psi}{\partial x}\right)AG = 0 \tag{9}$$

where

ψ = bending slope
κ = numerical shape factor for cross-section
G = shear modulus.

These equations have been solved for various boundary conditions by Goens [4] and Huang [8].

Huang's solution was chosen for use in this study because of the ease with which an incremental search computer code can be used to find a root to the frequency equation. For the nodally supported case, the frequency equation is

$$2 - 2\cosh(b\alpha)\cos(b\beta) + \frac{b}{(1 - b^2r^2s^2)^{1/2}}[b^2r^2(r^2 - s^2)^2 + 3r^2 - s^2)]\sinh(b\alpha)\sin(b\beta) = 0 \tag{10}$$

where

$$b^2 = \frac{\rho A}{EI}l^4\omega^2 \qquad (\omega = 2\pi f)$$

$$r^2 = \frac{1}{Al^2}$$

$$s^2 = \frac{EI}{\kappa AGl^2}$$

$$\alpha = \left\{\frac{1}{\sqrt{2}} - (r^2 + s^2) + \left[(r^2 + s^2)^2\frac{4}{b^2}\right]^{1/2}\right\}^{1/2}$$

$$\beta = \left\{\frac{1}{\sqrt{2}} + (r^2 + s^2) + \left[(r^2 + s^2)^2\frac{4}{b^2}\right]^{1/2}\right\}^{1/2}$$

The shape factor κ is a constant depending on the shape of the cross-section. Values for several shapes have been tabulated [9]. For a cylinder, Ref. 9 gives κ = 0.847. Equation 10 is utilized by defining the values of all known parameters and substituting various values of E (by computer) until a zero-crossing is reached. The increment of change in E is decreased until a value for E within the desired tolerance is reached.

Exact solutions: Pochhammer [10] and Chree [11] used the three-dimensional theory of elasticity approach to arrive at a general solution for the propagation of elastic waves in cylindrical rods. Bancroft [12] derived the frequency equation appropriate to flexural vibrations and Hudson [13], Pickett [14] and Teft [15] have each arrived at numerical solutions to these equations for the case of cylindrical rods. Using Teft's solution, Young's modulus is obtained by

$$E = K_n \frac{\rho l^4}{d^2} f_n^2 T_n \tag{11}$$

where

K_n = constant, depending on mode number
T_n = constant, depending on mode number and function of (d/l) and G.

Values for the constands K_n and T_n are tabulated in Ref. 15. Similar equations exist for prismatic specimens of rectangular cross-section [16].

EXPERIMENTAL TECHNIQUE

The pertinent mathematical models having been developed, attention can now be focused on the techniques used to excite the vibrations. The PUCOT and the IET are described briefly, and the test procedure is given.

The PUCOT

The PUCOT uses two alpha quartz piezoelectric crystals (drive and gauge) to induce longitudinal ultrasonic resonant stress waves in the specimens to be tested. For room temperature measurements, the three component system (drive, gauge, specimen) is used; the four component system (drive, gauge, specimen, plus a fused quartz spacer rod) is used in order to isolate the piezoelectric crystals from furnace temperatures (Fig. 1). The quartz spacer rod is tuned to resonance and glued between the gauge crystal (with a cyanoacrylate glue) and the specimen (with a ceramic cement).

A closed-loop oscillator is used to drive the system at resonance. The resonant frequency of the three or four component oscillator is measured using an electronic frequency counter with an accuracy of about 0.5 Hz. The resonant frequency of the specimen may be extracted mathematically from the resonant frequency of the composite oscillator [17]. Specimen temperature is measured using a Pt/Pt-Rh thermocouple positioned about 5 mm from the specimen. The three-zone vertical tube furnace used with the PUCOT allows a specimen temperature gradient of 1 K or less to be maintained. Equation 4 is used to calculate dynamic Young's modulus from experimentally determined parameters. Further details of the PUCOT apparatus can be found in Ref. 17.

The IET

The IET uses a small steel impacter to excite flexural resonant vibrations in a nodally-supported specimen. An electronic circuit is used to extract the resonant frequency from the signal provided by an appropriate transducer [2]. Equations 7, 10 or 11 may be used to calculate Young's modulus from the experimentally determined parameters.

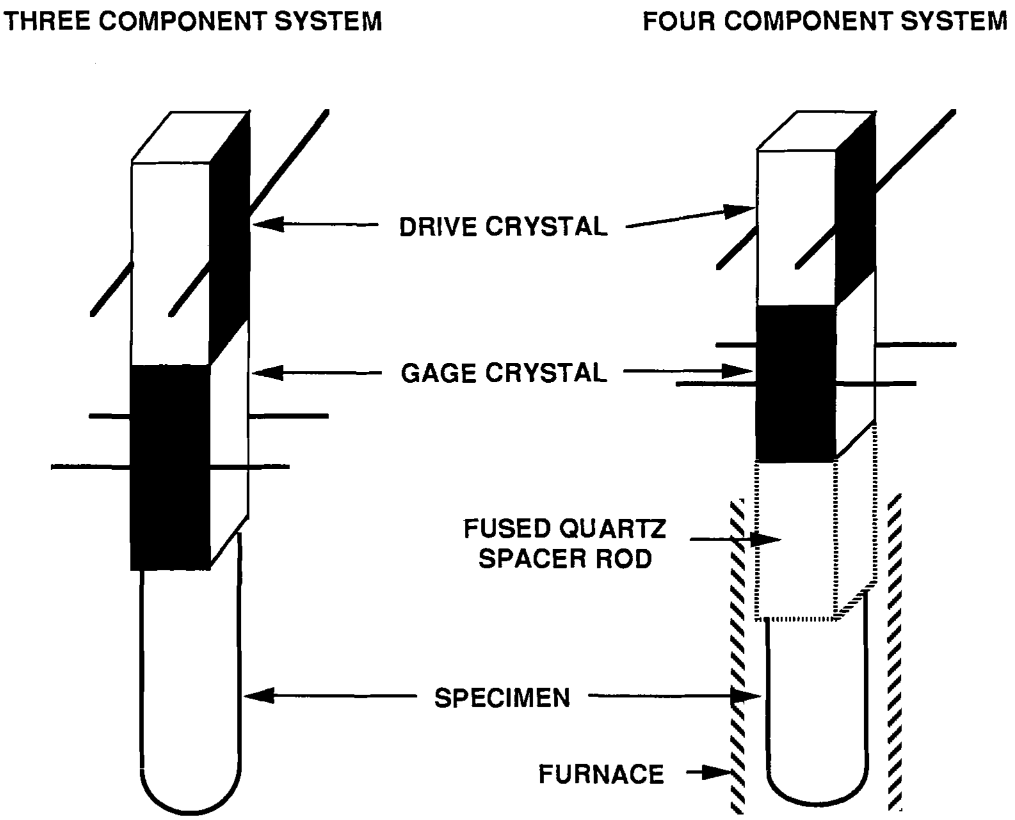

FIG. 1 - Schematic diagram of the PUCOT.

The IET has been modified for elevated temperature use [18] by placing the specimen in a horizontal tube furnace, dropping the impacter from an upper vertical tube, and extracting an audio signal with a microphone placed at the opening of a lower vertical tube (Fig. 2). Specimen temperature is measured using a Chromel/Alumel thermocouple positioned about 5 mm from the specimen. The single-zone horizontal tube furnace used with the IET can show specimen temperature gradients of up to 25 K. In addition, center-of-specimen thermocouple readings can deviate from the controller-selected test temperature by as much as 35 K.

Experimental Procedure

Specimen dimensions were measured with a digital caliper. The accuracy of the caliper is given by the manufacturer as ± 0.03 mm (l ± 0.1% for a typical 30 mm long specimen, d ± 1% for a typical 30 mm long specimen).

Using both the PUCOT and the IET, tests were performed at 296, 423, 573, 723 and 873 K. Experimental variables recorded were: specimen length, specimen diameter (for the IET only), specimen temperature, and resonant frequency of the specimen.

RESULTS AND DISCUSSION

Experimentally determined parameters are recorded in Table 1. Values of dynamic Young's modulus for 4330V steel calculated from these parameters are given in Table 2, and are presented graphically in Figure 3. Several features warrant further evaluation.

Room Temperature Results

The excellent agreement between the PUCOT and the IET - Eq. 11 (about 0.05%) should be noted. The agreement between the PUCOT and the IET - Eq. 10 (about 0.25%) is only slightly less impressive. The values obtained from the IET - Eq. 7 deviate significantly from the other results (nearly 5%). This is due likely to violation by the specimen geometry of the simplifying assumptions of the model. Validity of the Bernoulli-Euler model is generally linked to the use of "long slender specimens" although there is no commonly employed criterion analogous to the previously mentioned "ten-to-one rule" used with the PUCOT.

Experimental uncertainty in the calculated values of dynamic Young's modulus can be related to the uncertainty of the experimentally determined parameters used in the calculation by [19]

$$w_R = \left[\left(\frac{\partial R}{\partial x_1} w_1\right)^2 + \left(\frac{\partial R}{\partial x_2} w_2\right)^2 + \ldots + \left(\frac{\partial R}{\partial x_i} w_i\right)^2\right]^{1/2} \tag{12}$$

where

$R = R(x_1, x_2, \ldots, x_i)$

x_i = independent variables

w_i = uncertainty in the ith variable.

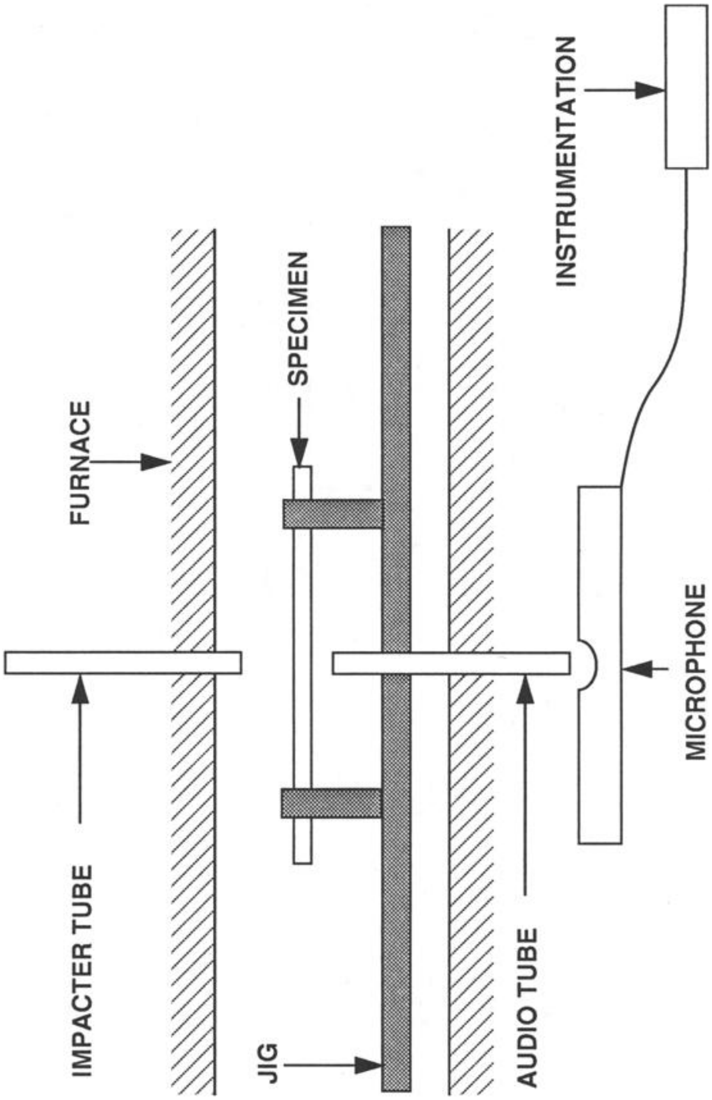

FIG. 2 - Schematic diagram of the IET.

TABLE 1 - Experimentally Determined Parameters

		PUCOT		IET		
T [K]	ρ [kg/m^3]	l [mm]	f [kHz]	l [mm]	d [mm]	f [kHz]
296	7840	32.22	79.6081	76.36	3.00	12.423
423	7805	31.27	79.8351	76.48	3.00	12.216
573	7765	30.48	80.0744	76.61	3.01	11.911
723	7722	29.57	79.8927	76.65	3.02	11.501
873	7674	28.45	79.9324	76.91	3.02	10.961

TABLE 2 - Calculated Dynamic Young's Modulus Values for 4330V Steel

T [K]	PUCOT [GN/m^2]	IET - Eq. 7 [GN/m^2]	IET - Eq. 10 [GN/m^2]	IET - Eq. 11 [GN/m^2]
296	206.3	197.5	206.8	206.2
423	194.6	191.3	200.3	199.1
573	185.0	181.0	189.5	189.0
723	172.4	167.9	175.8	175.9
873	158.8	152.8	160.0	159.4

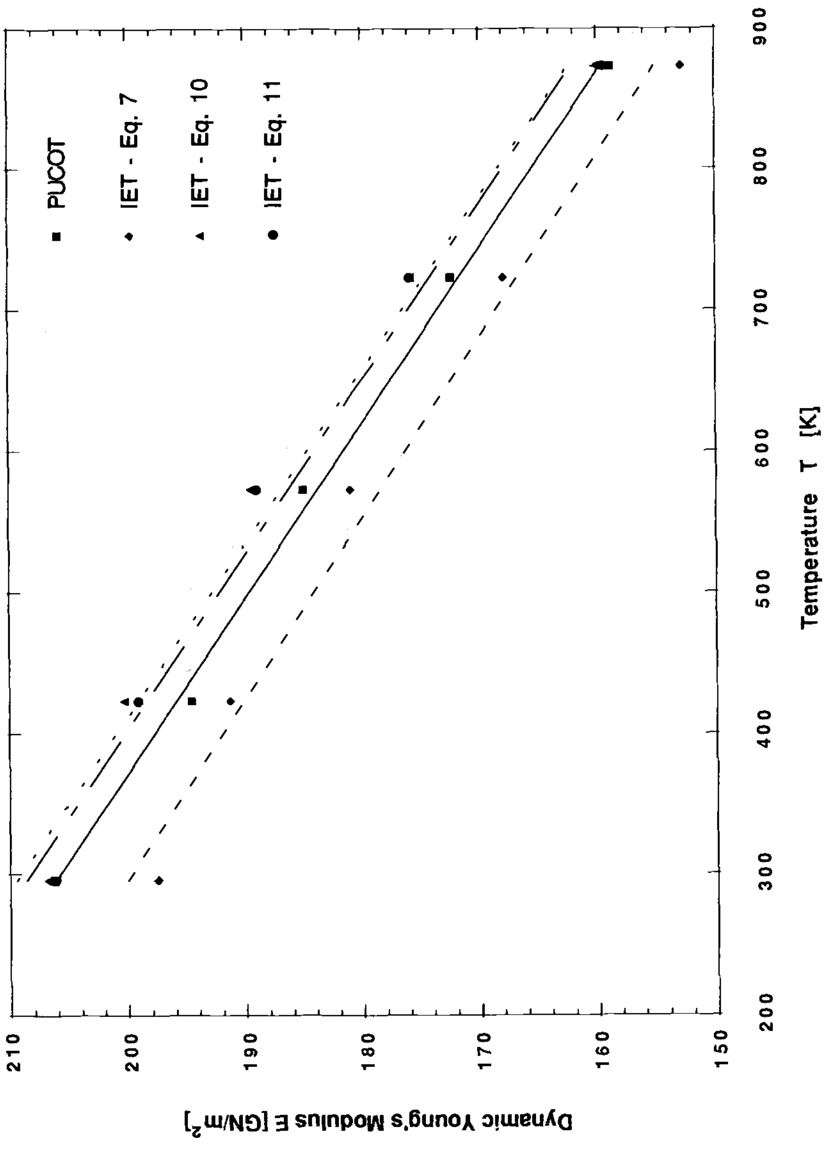

FIG. 3 - Elevated Temperature Dynamic Young's Modulus in 4330V Steel.

Both techniques may be evaluated by performing the indicated partial derivatives on the appropriate equation and substituting the previously stated uncertainties associated with the measurement of the experimentally determined parameters. The PUCOT shows a total experimental uncertainty of about 0.5%, with imprecision in the determination of specimen density accounting for most of the uncertainty. The IET shows a total experimental uncertainty of about 2%, with accuracy of specimen diameter measurement accounting for most of the uncertainty.

It should be mentioned that the difference in uncertainty between the two techniques is not due to any difference in the quality of the associated instrumentation, but instead reflects the inherent simplicity of the mathematics used with longitudinal vibrations in contrast to that used with flexural vibrations. For example, the same caliper is used to measure specimen dimensions for both techniques. However, a higher-order functional dependence of resonant frequency on specimen dimensions magnifies the error of the measurement for the IET.

Elevated Temperature Results

At elevated temperatures, the PUCOT shows a linear dependence of dynamic Young's modulus on temperature. The results from the IET are less linear, which may be explained partially by the previously mentioned problems with temperature control in the single-zone furnace used with the IET. In all cases however, a linear least-squares fit to the data yielded a dE/dT value of about -0.08 GN/(m^2 K).

Another factor worth mentioning is the effect of uncertainty of coefficients of thermal expansion used to correct for changes in dimension with temperature. Such corrections are made for length, diameter, and thus density as well. These parameters are, as previously mentioned, primary sources of error in these types of measurements. The corrections are very small, however, and a dilatometer possessing 1% accuracy or better will give CTE values which may be used without affecting the total experimental uncertainty.

CONCLUSIONS AND RECOMMENDATIONS

Dynamic Young's modulus in 4330V steel is about 206 GN/m^2 at ambient temperature. The dynamic Young's modulus falls in a linear fashion with temperature at the rate of about -0.08 GN/(m^2 K).

Assuming absolute accuracy of the mathematical models, the experimental uncertainty of the PUCOT is about 0.5% while that of the IET is about 2%. The measurement of specimen density is the primary source of imprecision in the PUCOT while the measurement of specimen diameter is the largest contributing factor to imprecision in the IET.

The experimental results suggest that the IET is best used with an exact solution (such as Eq. 11) if possible. If an exact solution does not exist for the specimen geometry used, the Timoshenko Beam model will, with careful choice of shear correction factor κ, yield results of only slightly less quality. The Bernoulli-Euler model should be used with caution, keeping in mind the model's assumptions concerning specimen geometry.

ACKNOWLEDGEMENTS

Two of the authors (S. C. and A. W.) thank Dr. J. Lemmens for the loan of the Grindosonic instrument used with the IET and for his assistance with the development of the apparatus for high temperature use.

REFERENCES

[1] Kingery, W. D., Property Measurements at High Temperatures, Wiley, New York, 1959, pp. 169-174.

[2] Wolfenden, A., Harmouche, M. R., Blessing, G. V., Chen, Y. T., Terranova, P., Kinra, V. K., Dayal, V., Lemmens, J. W., Phillips, R., Smith, J. S., and Wann, R. J., "Dynamic Young's Modulus Measurements in Metallic Materials: Results of an Interlaboratory Testing Program," Journal of Testing and Evaluation, Vol . 17, No. 1, Jan. 1989, pp. 2-13.

[3] Timoshenko, S., Vibration Problems in Engineering, Van Nostrand, New York, 1928, pp. 199-326.

[4] Goens, V. E., Über die Bestimmung des Elastizitätsmoduls von Stäben mit Hilfe von Biegungsschwingungen," Annalen der Physik, 5. Folge, 1931, Band 11, Heft 6.

[5] Rayleigh, The Theory of Sound, Macmillan, London, 1926, pp. 359-360.

[6] Timoshenko, S., On the Correction for Shear of the Differential Equation for Transverse Vibrations of Prismatic Bars," Philosophical Magazine, Vol. XLI - 6th series, 1921, pp. 744-747.

[7] Timoshenko, S., "On the Transverse Vibrations of Bars of Uniform Cross-Section," Philosophical Magazine, Vol. XLIII - 6th series, 1922, pp. 125-131.

[8] Huang, T. C., "The Effect of Rotatory Inertia and of Shear Deformation on the Frequency and Normal Mode Equations of Uniform Beams with Simple End Conditions," Journal of Applied Mechanics, Vol. 28, No. 4, Dec. 1961, pp. 579-584.

[9] Mindlin, R. D. and Deresiewicz, H., "Timoshenko's Shear Coeffficient for Flexural Vibrations of Beams," Proceedings Second National Congress of Applied Mechanics, ASME, 1954.

[10] Pochhammer, L., "Über die Fortpflanzungsgeschwindigkeiten Schwingungen in Einem Isotropen Kreiscylinder," Journal für Mathematik, Vol. 81, 1876, pp. 324-336.

[11] Chree, C., "The Equations of an Isotropic Elastic Solid in Polar and Cylindrical Coordinates, Their Solution and Application," Transactions of the Cambridge Philosophical Society, Vol. 14, 1889, p. 250.

[12] Bancroft, D., "The Velocity of Longitudinal Waves in Cylindrical Bars," Physical Review, Vol. 59, April 1941, pp. 588-593.

[13] Hudson, G. E., "Dispersion of Elastic Waves in Solid Circular Cylinders," Physical Review, Vol. 63, January 1943, pp. 46-51.

[14] Pickett, G., "Flexural Vibration of Unrestrained Cylinders and Discs," Journal of Applied Physics, Vol. 16, No. 12, Dec. 1945, pp. 820-831.

[15] Teft, W. E., "Numerical Solution of the Frequency Equations for the Flexural Vibration of Cylindrical Rods," Journal of Research of the National Bureau of Standards, Vol. 64B, No. 4, 1960. pp. 237-242.

[16] Spinner, S. and Teft, W. E., "A Method for Determining Mechanical Resonance Frequencies and for Calculating Elastic Moduli from These Frequencies," Proceedings ASTM, Vol. 61, 1961pp. 1221-1238.

[17] Robinson, W. H., and Edgar, A., "The Piezoelectric Method of Determining Mechanical Damping at Frequencies of 30 to 200 kKz," IEEE Transactions on Sonics and Ultrasonics, Vol. SU-21, No. 2, April 1974, pp. 98-105.

[18] Heritage, K., Frisby, C., and Wolfenden, A., "The Impulse Excitation Technique for Dynamic Flexural Measurements at Moderate Temperatures," Review of Scientific Instruments, Vol. 59, No. 6, June 1988, pp. 973-974.

[19] Kline, S. J. and McClintock, F. A., "Describing Uncertainties in Single-Sample Experiments," Mechanical Engineering, Vol. 75, No. 1, Jan. 1953, p. 3.

DISCLAIMER AND COPYRIGHT NOTICE

Joseph W. Lemmens

IMPULSE EXCITATION : A TECHNIQUE FOR DYNAMIC MODULUS MEASUREMENT

REFERENCE: Lemmens, J.W., "Impulse Excitation : A Technique for Dynamic Modulus Measurement", Dynamic Elastic Modulus Measurements in Materials, Alan Wolfenden, Editor, American Society for Testing and Materials, Philadelphia, 1990.

ABSTRACT: The impulse excitation technique is a dynamic method of measurement based on the analysis of a transient vibration of the test object resulting from a mechanical impact. The result is a precise indication of the fundamental natural frequency of this vibration. This information may be used as the basis for calculating the elastic moduli of the material under test. The natural frequency reading by itself may be used as a relative measure for the purpose of comparative evaluation. The technique is characterised by the speed and ease of the measurements as well as by the wide range of its application. Because of this, the method is not confined to the laboratory environment but opens new perspectives in industrial quality control and performance improvement.

KEYWORDS: Non-destructive testing, Elastic modulus, Transient vibration, Natural frequency

THE BASIC PRINCIPLE

As the name implies, the pulse excitation technique obtains its information from the analysis of the transient vibration of the test object following a mechanical impact. The energy thus acquired by the sample is dissipated in a vibratory movement, the nature of which is dependent on the geometry of the test piece, as well as on the density and the elastic properties of the material.
It is the purpose of the instrument to capture the mechanical vibration, analyse it and give an accurate measure of the natural frequency. This information, together with the mass and the shape factor of the test object, will permit the calculation of the elastic moduli [1-2-3].

J.W.Lemmens is Managing Director of J.W.Lemmens-Elektronika N.V. Research Park, B-3030 Leuven, Belgium, and President of J.W.Lemmens, Inc. 10801 Pear Tree Lane, St Louis, Missouri 63074.

Generally, the vibration resulting from a mechanical impulse will be very complex in nature, a mixture of fundamental and higher order harmonics (fig. 1).

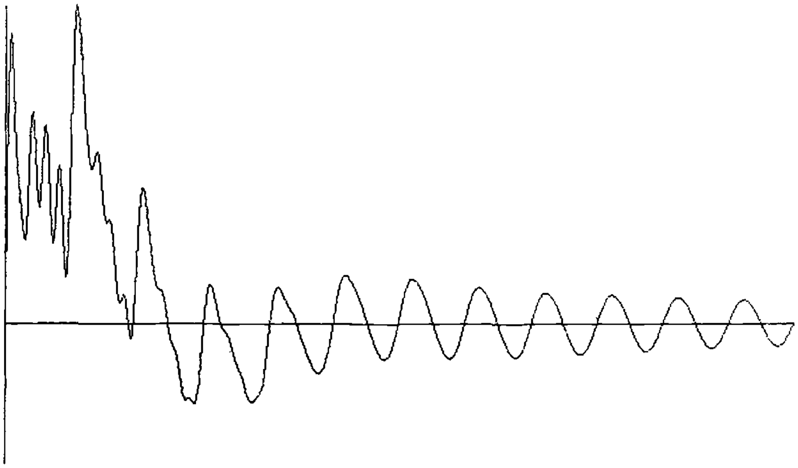

FIG. 1 -- Typical vibratory movement showing harmonic content.

Hence, the instrument is programmed to perform a time analysis on the incoming signal in order to identify the fundamental component of the vibration. Then the zero-crossings are determined as accurately as possible and used as time markers for measuring the period of the vibration against a precise quarz-crystal controlled oscillator. The result is displayed on the front panel in numerical form.

The oscillator serves as a reference element and ensures that the test instrument is inherently calibrated to a high degree of accuracy. Current specifications state a frequency stability of 0.005 percent, inclusive of calibration tolerance at 25 °C., operating temperature range of 0 to 70 °C., input voltage change of plus and minus 10 percent, aging, shock and vibration.

The block diagram of the electronic instrument is shown in Fig. 2. The input signal is first amplified and then fed through two parallel logic channels. One will acknowledge receipt of an incoming signal and initialise the rest of the circuitry for processing. It will eliminate the undesirable effect of test piece movement and only retain the signal coming from its vibration. It will further monitor the decay of the signal and indicate when it is in the linear range of the amplifier and at which moment processing should stop because the signal is about to fade in the background noise, etc.
The other channel will determine the signal zero-crossing points, thus marking off the successive periods clearly. The time measurements are stored in memory and as soon as the minimum usable signal level has been reached, the processor will compute the result, output the data and activate the display. The result is given with a constant 4-digit resolution, in either frequency (Hz - kHz) or period (ms - μs).

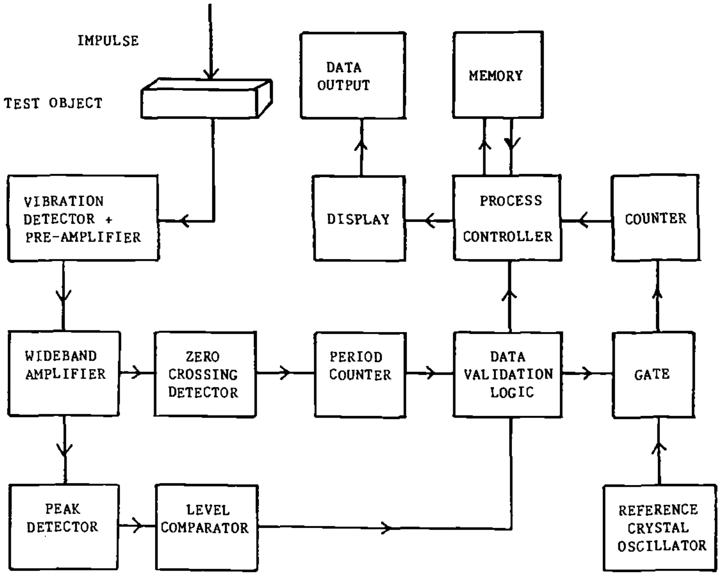

FIG. 2 -- Block diagram of the instrument.

THE MEASUREMENT METHOD

In practice, the entire procedure is extremely simple and essentially consists of the following :

The test object is placed on an appropriate support.
The piezo-electric probe is held in contact with the test object.
A light mechanical impulse is imparted to the test object.
The result of the measurement is read from the front panel.

It will hardly ever require more than a few seconds to perform the test. The result remains visible for 750 milliseconds, after which the display is cleared and the instrument is ready for the next measurement. It is interesting to note that the operator does not take part in the measurement itself. His role is limited to providing the initial energy required for initiating the vibration. From that moment onward, the response of the test object is passed directly on to the instrument for analysis, without any further operator interference.

Vibration modes

Most test pieces can readily be induced to vibrate in several modes, depending primarily upon the choice of the point of impact of the exciting impulse. As an example, elastic moduli are often determined using a prismatic specimen and obtaining the flexural (two directions), torsional and longitudinal resonances. Disc-shaped specimens are also very convenient for obtaining both flexural and torsional modes. Cylinders are often used but it is difficult to force them into their torsional mode of vibration.

Supporting the test object

A dynamic test will obviously require that the test object be allowed to vibrate as freely as possible. It must therefore be isolated from external vibrations and prevented from contacting other solid objects which could induce additional stiffness or cause disturbing contact resonances. Ideally, the test object should be supported in the nodal zones of the desired vibration pattern. Stretched wires or narrow strips of soft rubber can be used as supports. In many instances, it will be entirely satisfactory to simply place the test object on a flat sheet of plastic foam. In practice, the greater the length to thickness ratio of the test object, and the lower the elastic modulus, the more important the positioning of the supports becomes.

Correctly positioning the supports will be helpful in discouraging unwanted vibration modes and avoiding excessive damping of the desired mode.

It is interesting to note that one single set of four supporting points (the intersections of the nodal diameters and the nodal circle) will accommodate both flexural and torsional vibration modes of discs, making disc-shaped specimens a good choice when one wishes to determine both the modulus of elasticity and the shear modulus (Fig. 3).

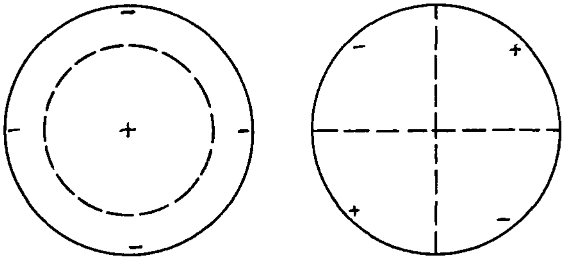

FIG. 3 -- Vibration patterns of a disc-shaped object.

Pulse excitation

The energy of the impulse is converted into the desired vibration mode most effectively when it is given in an antinode of that specific mode. As with all other elements of the measuring technique, the method of excitation is not at all critical: a light and elastic tap is all that is required. Its purpose is to cause a short vibration of the test piece. The measurement is completely independent of the force of the impact but nothing can be gained from tapping violently. This will only make the test piece jump on its support, causing an unnecessarily distorted signal which is more difficult to analyse. Moreover, it is far easier to maintain steady contact between the detector and the test piece with gentle tapping. It is very important, however, that the impulse be elastic and that the impacting body be allowed to bounce away freely after making contact. This will again make sure that the vibrating body will be completely free during the relaxation.

Many common objects can be used for initiating measurements. The most appropriate tapping object is made in the form of a sphere fixed at the end of a thin and flexible stem. Thus the centre of gravity is placed in the point of impact which makes elastic tapping quite easy.

The selection of a smaller or larger tapping hammer, or one made of hard or soft material, will depend on the mass, shape and material of the test object. A variety of simple ball hammers, measuring from 3 to about 25 mm in diameter and ranging from soft-rubber to steel, will be adequate to cover most applications. Generally, a stiff object (one having a low length to thickness ratio and/or a high modulus) will require the use of a hard hammer, and vice versa.

The pulse excitation technique lends itself very well to automation. Electromagnetic and pneumatic devices have been developed for tapping test objects in the required ballistical manner and are installed in industrial measuring stations and in automated laboratory experiments.

Signal capture

Various types of transducers have been used to detect the mechanical vibration of the test object and convert it into an electric signal. Although capacitive, optical and electromagnetic sensing devices proved successful, in practice the greater part of the application range has been covered by a specially designed piezo-electric detector. It will cover a frequency range from about 20 Hertz up to 80 kiloHertz.

An acoustic sensor has also proven quite valuable although precautions are required to prevent perturbation from surrounding noises. Normally it is placed at a distance of a few millimeters from the test piece. Excellent results are obtained when the test object, the microphone and a mechanical tapping device are mounted inside a soundproof enclosure. Measurements have been performed up to about 50 kiloHertz. Using a microphone reduces the loading of the test object significantly. This is quite a help when measuring thin foils (less than 0.3 mm thick).

Measurements in vacuum or at elevated temperatures require some form of waveguide for transmitting the vibration outside of the conditioned chamber and feeding it to one of the above mentioned sensors. Solid waveguides in the form of a wire or rod have proven quite effective in conjunction with the piezo-electric detector. Microphones can best be used with stethoscope-type devices using a length of closed tubing as the coupling element.

Some work is being carried out to investigate the potential of laser interferometric techniques for non-contact vibration sensing. The outlook thus far is quite promising [4].

MEASUREMENT CHARACTERISTICS

Non-destructive

The non-destructive nature of the method allows any number of repeat measurements to be made on a single test piece. Time related- or event related histories can be recorded easily. The example of Fig. 4 shows the room temperature relaxation of a CuZnAl alloy after heat treatment at 750 °C. (15 mins) and salt immersion at 155 °C. (30 mins), measured over a period of two hours. Fig. 5 shows the effect on refractory materials of successive exposures to thermal shock cycling (1200 °C. to 25 °C.).

Non-destructive testing has another advantage, which is of particular interest to industrial users: there is no limit on the number of parts that may be tested. In fact, the pulse excitation method is being used increasingly to perform 100 percent testing of large volume production.

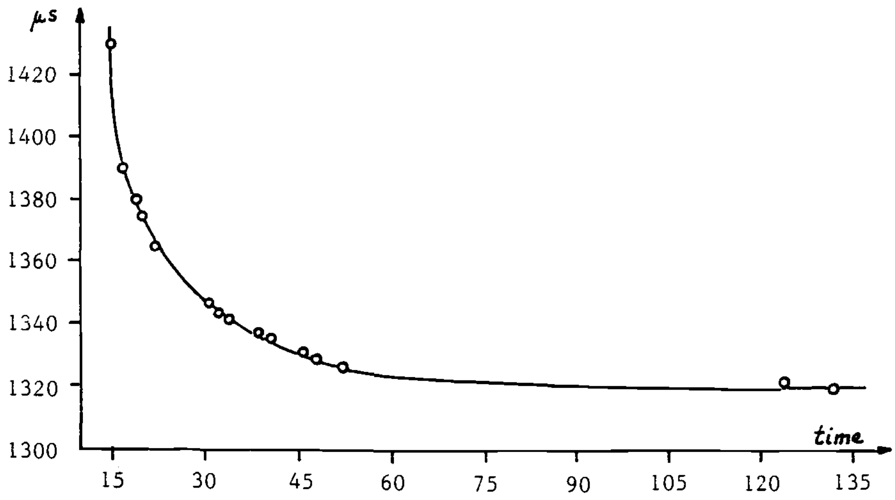

FIG. 4 -- Relaxation of CuZnAl after heat treatment.

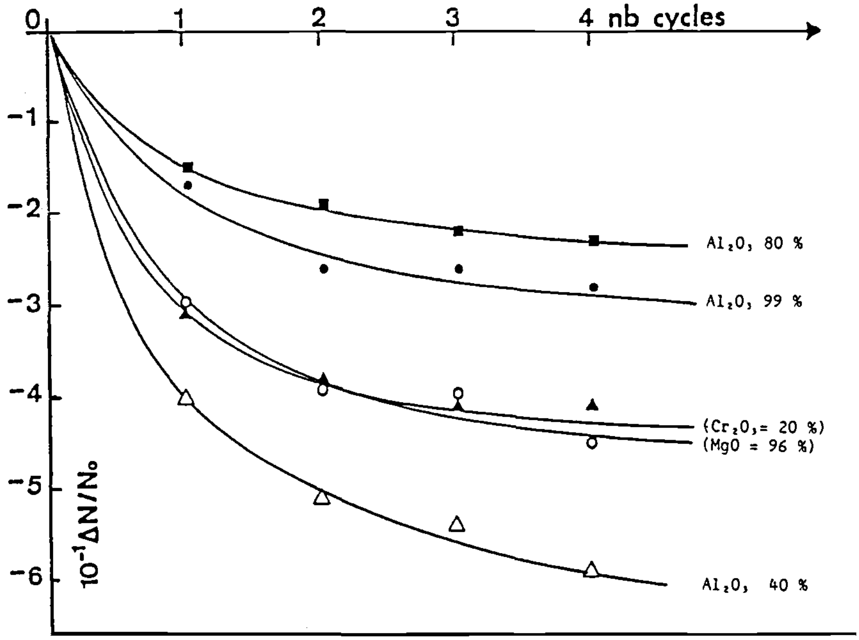

FIG. 5 -- Effect of thermal shock cycling on refractories.

High speed operation

The measurements are of extremely short duration: most will require only a fraction of a second. Visual readout of the result takes about 750 milliseconds, which will generally limit the measuring rate to one per second. If higher rates are required, the display function can be disabled and the results evacuated over the data link to an external recording device.

Range of moduli

The pulse excitation technique is capable of measuring a wide range of elastic materials. As the method is based on the analysis of transient vibrations, the limit is set by the amount of vibrational information provided by the material under test. In practice, at least two or three usable periods should be available for a reliable measurement.
Of course it is impossible to measure critically damped materials with this method, which would exclude rubbers and generally all primarily visco-elastic materials. Nevertheless, materials which can be tested range from ultra-light fibrous insulators with E-modulus values of the order of 50 MPa to synthetic diamond with 750 GPa. This range includes polymers, resins, wood, cement, graphite, concrete, rocks, composites, metals, refractories, ceramics, abrasives, ultra-hard materials, etc.

Range of specimen configurations

Test piece geometries may vary greatly provided that the shape presents some minimum length to thickness ratio of 2 to 1. This means that both cubes and spheres are notable exceptions which cannot, at the present time, be measured by this method.
Absolute values of elastic moduli will generally be determined using specimens with simple shapes: cylinders, prisms and discs are mostly used. Shapes and dimensions are widely uncritical. Cylinders and prisms have been measured from the 2 to 1 aspect ratio, which is a common specimen in concrete testing practice, to more than 100 to 1. Discs constitute very good specimens because of the ease with which both flexural and torsional vibrations can be measured, even in extreme geometries. Discs with diameter to thickness ratios from 2 to 1 to more than 250 to 1 have been measured.
Specimen sizes have ranged from test bars 2 x 2 x 20 mm to concrete beams, 4 meters long and 50 by 20 cm cross section.
Relative measurements, on the other hand, can be performed on an infinity of shapes and sizes as they do occur in industry. Objects as complex as turbine blades or automobile brake-pads or slide-gates and shrouds for the steel industry are measured easily.

Range of temperatures

Measuring at low and elevated temperatures is relatively easy with the pulse excitation technique. Using the devices described in earlier paragraphs, it has been possible to measure concrete specimens at temperatures as low as -180 °C. and ceramic specimens up to a temperature of +1500 °C. In both cases the experiments were limited rather by the capabilities of the equipment than by the measuring technique.
Currently, an experiment is being set up for measuring metal specimens in vacuum, up to 600 °C.

SOME APPLICATIONS

In all areas of materials technology, three levels of interest can be distinguished :

- Materials research and product development
- The process of manufacturing a product
- Utilisation of a manufactured product

The impulse excitation technique is useful in fundamental and applied materials research [5-6-7].

Manufacturers have a twofold interest: quality control of their product and information about their manufacturing process. One hundred percent testing of products and their classification will result in close adherence to specifications, meeting every customer's specific needs and ensuring satisfaction with the highest degree of certainty.
The vast amount of statistical data which is gathered from high volume testing yields valuable information on various parameters of the manufacturing process.

The user of a product has a different point of view. He is primarily interested in the product performance. This is particularly true with critical parts, where the failure to perform may lead to very high consequential losses. Very often, there is no relation between the cost of a product and the economical task which it will be required to perform. Users therefore will test incoming products for confirmation of performance expectation prior to installation. Many will carry out a further classification, thus fine tuning the product application and realising substantial performance improvement.

A first application has developed in the field of abrasive machining, a vital operation in metalworking industry. Pulse excitation is used to determine the elastic modulus of grinding and honing tools. Extensive research has shown that this property is closely related to the cost of abrasive machining and to the integrity of the machined part [8]. Grinding tool manufacturers use the test in product grading, industrial users check the abrasive tools at the manufacturing site.

Refractory products are used in steel manufacturing, cement factories, glass production and oil refineries. They are invariably called to withstand heavy mechanical and thermal loading. The large numbers of parts installed present the usual variations corresponding to today's state of the manufacturing art (Fig. 5). Evidently, the performance of the system is limited by the weakest component [9]. Again, testing, classification and selective use lead to substantial economic savings by extending the service life of the installation significantly.
Another application example has been discovered in the steel industry. Ceramic break rings are critical parts used in continuous steel casting installations. Pulse excitation is used for 100 percent testing and is now reported to have eliminated the breakdowns which previously used to lead to very costly production incidents [10].
It is remarkable that product testing, as practiced by many users, is not a rigorous accept-reject decision, but rather a matter of application refinement. Often the advantages are secured by simple product re-arrangement, constituting homogenous rather than random sets.

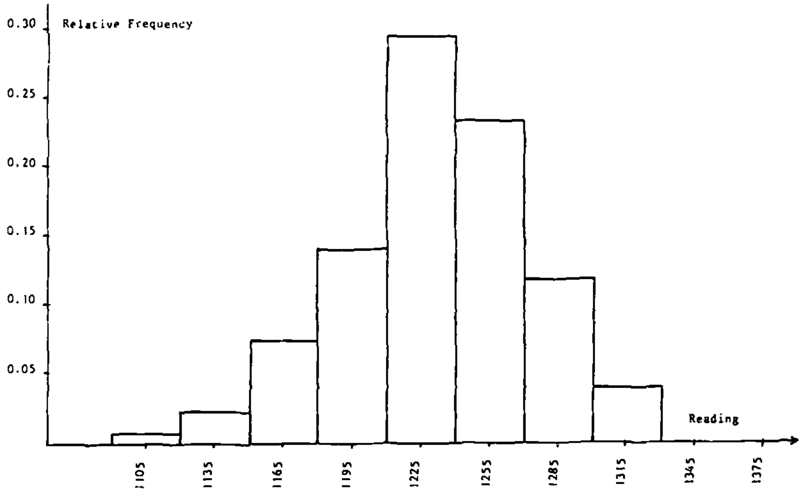

FIG. 5 -- Typical distribution of refractory bricks

Building materials are subject to various influences which cause their strength to degrade progressively: frost damage in cold climates and salt spray in marine environment are two common occurrences. Resistance to these factors are important specifications of roof tiles, bricks, cement and concrete. Pulse excitation is used as a test method in laboratories as well as manufacturing plants to assess damage from frost-thaw cycles. Curves are drawn from the measurement results of 300 successive cycles and excellent correlations have been observed between the instrument readings and the strength of the specimens.

In the design and specification of timber structures is the knowledge of the elastic moduli of prime importance. Until recently, there has not been a recognised and reliable method for their determination. The impulse excitation technique promises to fill this void and has been used for the characterisation and classification of timber [11-12]. Its potential in measuring hardboard products and bonded elements is being investigated by several timber research institutes.

Researchers investigating new isotropic composite materials for dental restoration have found the impulse excitation technique to be very helpful. Using small specimens of 35 x 5 x 1.5 mm they have observed the effects of variable filler fraction, monitored postpolymerisation and measured the influence of water sorption. The result has been the development of a phenomenological model for these composite materials which is used for predictive purposes [13-14].

Compressive strength and porosity of rocks are of interest not only to geologists but also to mining and tunnel building engineers as well as to oil prospecting companies. Pulse excitation can be applied in the field of rock characterisation, monitoring and testing. The physical properties are measured as a function of temperature, weathering, degree of saturation and chemical alteration [15].

SUMMARY

Various methods of dynamic modulus measurement based on mechanical resonance methods have been in use for several decades and they have rendered excellent services. However, the complexity and delicacy of the instrumentation, the need for experienced handling and the rather high cost have prevented their more widespread use.
The development of the impulse excitation technique has been undertaken to widen the potential of dynamic modulus measurement whilst retaining the merits of the earlier methods. The new system has proven to be a powerful research tool at the disposal of materials scientists and to allow industry to gain valuable information and realise substantial performance improvements.

REFERENCES

1 Spinner S. and Tefft W.E., "A method for determining mechanical frequencies and for calculating elastic moduli from these frequencies", Proceedings ASTM Vol 61, 1961.
2 Glandus J.C., "Rupture fragile et résistance aux chocs thermiques de céramiques à usages mécaniques", Thesis, University of Limoges, France, 1981.
3 Adriaenssens D., Aerens R., Peters J., "Generalised Formulae incorporating Martincek's Theory," University of Leuven, Belgium, 1986.
4 Selbach H. and Lewin A., "Laser-interferometrie zur Positions- und Schwingungsmessung," Feinwerktechnik & Messtechnik, 1988.
5 Heritage K., Frisby C. and Wolfenden A. "Impulse excitation technique for dynamic flexural measurements at moderate temperature," Review of Scientific Instruments, June 1988.
6 Van Daele R., "Mechanische eigenschappen van glas," Thesis, University of Leuven, Belgium, 1984.
7 Van Riet C., "Superplasticiteit in één-en meerfazige legeringen," Thesis, University of Leuven, Belgium, 1984.
8 Kőnig W. and Föllinger H., "Elasticity modulus of grinding wheels and its impact on their in-process behavior," Ceramic Forum International 6/7 1987.
9 Aly F. and Semler C.E., "Prediction of refractory strength using nondestructive sonic measurements," American Ceramic Society Bull. vol. 64, no 12 (1985).
10 Engel R., "Non-destructive testing of boron nitride," Research & Technology, Armco Inc., Middletown OH 45043.
11 Görlacher R., "Ein neues Messverfahren zur Bestimmung des Elastizitätsmoduls von Holz," Holz als Roh-und Werkstoff 42(1984) 219-222.
12 Coppens H., "Karakterisatie en sterktesortering van inlands vurenhout," Thesis, University of Gent, Belgium, 1984.
13 Braem M., Lambrechts P., Van Doren V. and Vanherle G., "The impact of composite structure on its elastic response," Journal of Dental Research, May 1986.
14 Braem M., Lambrechts P., Van Doren V. and Vanherle G., "Determination of Young's modulus of dental composites: a phenomenological model," Journal of Materials Science 22(1987) 2037-2042.
15 Allison R.J., "Non-destructive determination of Young's modulus and its relationship with compressive strength, porosity and density," Geological Society Special Publication No.29, pp 63-69.

Paul Heyliger, Hassel Ledbetter, and Mark Austin

RESONATING-ORTHOTROPIC-CUBE METHOD FOR ELASTIC CONSTANTS

REFERENCE: Heyliger, Paul, Ledbetter, Hassel, and Austin, Mark, "Resonating-Orthotropic-Cube Method for Elastic Constants," in Dynamic Elastic Modulus Measurements in Materials, ASTM STP 1045, Alan Wolfenden, editor, American Society for Testing and Materials, Philadelphia, 1990.

ABSTRACT: Following studies by Demarest (1969) and by Ohno (1976), we describe measurements and analysis that yield, from a single cube-shape specimen, in a single measurement, the complete set of anisotropic elastic-stiffness constants, the C_{ij}. Experimentally, we place a cubic specimen between two piezoelectric transducers, which excite and detect the cube's macroscopic free-vibration (fundamental-mode) frequencies, up to 10 MHz. From the specimen's shape, size, and mass, and from the measured resonance-frequency spectrum, we analyze for the C_{ij} within a given tolerance ϵ_i:

$$\lambda_i(C_{ij}) - \overline{\lambda}_i = \epsilon_i. \qquad \text{(No sum on i.)}$$

Here $\overline{\lambda}_i$ relates to the measured resonance frequencies, and λ_i represents eigenvalues calculated by a Rayleigh–Ritz method using Legendre-polynomial approximating functions. Legendre-polynomial orthogonality ensures a diagonal mass matrix [m], which simplifies the resulting eigenvalue problem:

$$([k] - \lambda[m])\ \{x\} = \{0\}.$$

For materials with certain symmetries, the coefficient matrix [k] reduces to a block-diagonal matrix, which reduces computational effort and simplifies vibration-mode identification.

KEYWORDS: anisotropic media; elastic constants; Rayleigh–Ritz method; resonating-cube method; vibrational modes.

Dr. Heyliger is assistant professor in the Civil Engineering Department, Colorado State University, Fort Collins, Colorado 80523. Dr. Ledbetter is a research metallurgist and Mr. Austin is a materials research engineer at NIST (formerly NBS), Boulder, Colorado 80303.

INTRODUCTION

The present approach to elastic-constant measurements depends on exciting and detecting the natural-vibration frequencies of simple-geometry solids. This concept traces back at least to Lamb [1], who in 1882 analyzed the vibrations of an elastic sphere.

Here, we focus not on spheres but on cubes and their natural generalization, a rectangular parallelepiped. For expressive brevity, we say cube. A cube with orthotropic elastic symmetry is equivalent to a rectangular parallelepiped.

Over conventional resonance and pulse methods, the vibrating-parallelepiped method offers many advantages:

1. Simple specimen geometry: sphere, cylinder, cube, parallelepiped, others
2. One specimen (instead of four* or more)
3. Small specimen: down to 1 mm or less
4. One measurement (instead of nine* or more)
5. Simultaneous elastic-constant and internal-friction measurements
6. No transducer-coupling correction
7. Shorter measurement time
8. For temperature measurements, one run (instead of nine); eliminates artifacts arising from temperature-measurement errors among various temperature runs; especially important or studying phase transitions
9. Possible simultaneous frequency-dependence study
10. For relative values of principal elastic constants (versus temperature or pressure) no specimen-geometry requirement
11. For small specimen-to-specimen differences, possible complete automation
12. Especially valuable for monocrystals: no need to cut and prepare various orientations.

(* This number assumes orthotropic symmetry, or nine independent elastic constants.)

NUMERICAL ANALYSIS

To estimate the natural-vibration frequencies of orthotropic cubes, we follow a method originally applied to isotropic materials by Demarest [2] and extended to anisotropic materials by Ohno [3]. First, we consider a cube with dimensions $2L_x$, $2L_y$, $2L_z$ as shown in Fig. 1 with an anisotropic constitutive relationship being represented by the elastic stiffness components C_{ij}.

Hamilton's principle provides the starting point for obtaining the variational form of the equations of motion. This can be expressed as (Reddy [4])

$$0 = \int_{t_1}^{t_2} \delta\ (K-U)\ dt$$

$$= \tfrac{1}{2}\delta \int_{t_1}^{t_2} \int_V (\rho\dot{u}^2 + \rho\dot{v}^2 + \rho\dot{w}^2 - \sigma_{ij}\epsilon_{ij})dVdt.$$

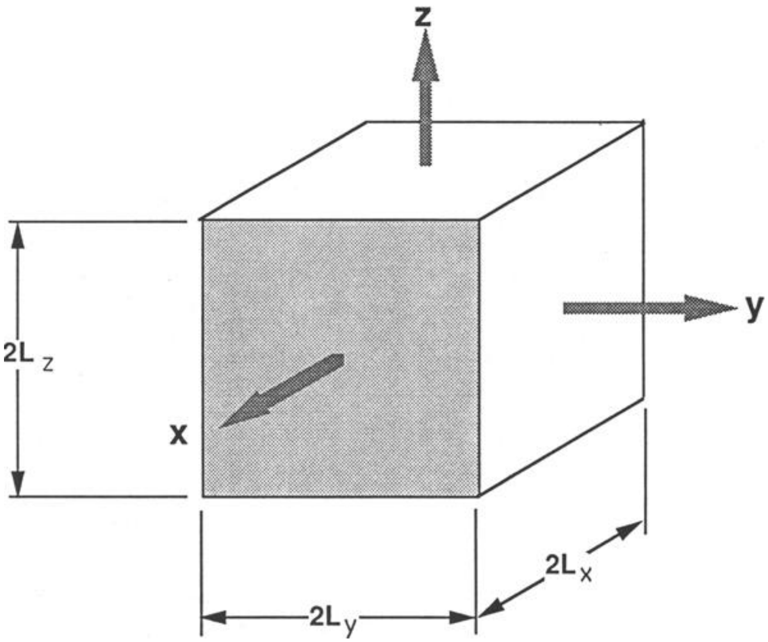

FIG. 1 — Orthotropic-cube geometry.

Here, K and U represent kinetic and potential energy; δ the variational operator; ρ the mass density; u, v, and w displacements in the x, y, and z directions; • partial differentiation with respect to time; σ_{ij} and ϵ_{ij} components of the stress and linear-strain tensors; and V cube volume. Our objective is to find the natural-vibration frequencies of the cube under periodic motion. We assume that the three displacement components behave as

$$\Delta_i\ (x,y,z,t) = \Delta_i\ (x,y,z)\ e^{i\omega t}\ . \tag{1}$$

Here, ω denotes the vibration frequency. Then we can write

$$0 = \tfrac{1}{2}\delta\int_V \{\rho\omega^2[u^2+v^2+w^2] - \sigma_{ij}\epsilon_{ij}\}dV.$$

Substituting in the appropriate expressions for the stress and strain components and using the constitutive relation yields

$$\begin{aligned} 0 = \tfrac{1}{2}\delta\int_V \{&\rho\omega^2[u^2+v^2+w^2] \\ &- C_{11}\left(\frac{\partial u}{\partial x}\right)^2 - 2C_{12}\frac{\partial v}{\partial y}\frac{\partial u}{\partial x} - 2C_{13}\frac{\partial w}{\partial z}\frac{\partial u}{\partial x} \\ &- C_{22}\left(\frac{\partial v}{\partial y}\right)^2 - 2C_{23}\frac{\partial w}{\partial z}\frac{\partial v}{\partial y} - C_{33}\left(\frac{\partial w}{\partial t}\right)^2 \\ &- C_{44}\left[\left(\frac{\partial v}{\partial z}\right)^2 + \left(\frac{\partial w}{\partial y}\right)^2 + 2\frac{\partial w}{\partial y}\frac{\partial v}{\partial z}\right] \end{aligned} \tag{2}$$

$$- C_{55}\left[\left(\frac{\partial u}{\partial z}\right) + \left(\frac{\partial w}{\partial x}\right)^2 + 2\,\frac{\partial u}{\partial z}\,\frac{\partial w}{\partial x} \right]$$

$$- C_{66}\left[\left(\frac{\partial u}{\partial y}\right)^2 + \left(\frac{\partial v}{\partial x}\right)^2 + 2\,\frac{\partial u}{\partial y}\,\frac{\partial v}{\partial x} \right] \Bigg\} dV.$$

Next, we select approximations for the three displacement components. These must be continuous, satisfy the homogeneous form of the essential boundary conditions, and be linearly independent and complete. These approximations take the form

$$u(x,y,z) = \sum_{i=1}^{n} a_i\ \Phi_i^x\ (x,y,z)$$

$$v(x,y,z) = \sum_{i=1}^{n} b_i\ \Phi_i^y\ (x,y,z) \qquad (3)$$

$$w(x,y,z) = \sum_{i=1}^{n} d_i\ \Phi_i^z\ (x,y,z).$$

Here, a_i, b_i, and d_i denote constants and Φ_i functions that meet the appropriate requirements. At this point, it is useful to transform the domain of interest to a unit cube to simplify the necessary integration. To do this, we use the following transformations:

$$X = \frac{x}{L_x},\ Y = \frac{y}{L_y},\ Z = \frac{z}{L_z} \qquad (4)$$

$$\frac{\partial}{\partial x} = \frac{1}{L_x}\frac{\partial}{\partial x},\ \frac{\partial}{\partial y} = \frac{1}{L_y}\frac{\partial}{\partial y},\ \frac{\partial}{\partial z} = \frac{1}{L_z}\frac{\partial}{\partial z} \qquad (5)$$

$$dV = dxdydz = L_xL_yL_z dXdYdZ. \qquad (6)$$

For convenience, we assume that these transformations have been made but we drop the upper-case nomenclature for the transformed coordinates.

For the approximation functions in Eq 3, we select

$$\Phi_i\ (x,y,z) = \frac{1}{\sqrt{L_xL_yL_z}}\ \bar{p}_\xi(x)\bar{p}_\eta(y)\bar{p}_\zeta(z). \qquad (7)$$

Here $\bar{p}_a$ denotes the a^{th} normalized Legendre polynomial. As noted by Demarest, use of the normalized Legendre polynomials implies that

$$\bar{P}_n(x) = P_n(x)\sqrt{\frac{2n+1}{2}} \qquad (8)$$

and

$$\int_{-1}^{1} \bar{P}_n^2(x)\ dx = 1. \qquad (9)$$

Since the Legendre polynomials are orthogonal, use of these terms results in a diagonal mass matrix.

After substitution of the approximation functions from Eqs 3 and 4 into Eq 2, we can take the first variation of the result with respect to the constants a, b, and d. Performing these operations and collecting like terms allows us to express the result in matrix form:

$$\begin{bmatrix} [K^{11}] & [K^{12}] & [K^{13}] \\ [K^{21}] & [K^{22}] & [K^{23}] \\ [K^{31}] & [K^{32}] & [K^{33}] \end{bmatrix} \begin{Bmatrix} \{a\} \\ \{b\} \\ \{d\} \end{Bmatrix} - \rho\omega^2 \begin{bmatrix} [I] & [0] & [0] \\ [0] & [I] & [0] \\ [0] & [0] & [I] \end{bmatrix} \begin{Bmatrix} \{a\} \\ \{b\} \\ \{d\} \end{Bmatrix} = \begin{Bmatrix} \{0\} \\ \{0\} \\ \{0\} \end{Bmatrix} \qquad (10)$$

or

$$([K] - \rho\omega^2[I])\{x\} = \{0\}. \qquad (11)$$

Terms in Eq 10 are defined in the Appendix.

Solving the eigenvalue problem, Eq 11, allows us to calculate the frequencies ω of the cube. It is possible to increase the efficiency of solution of this equation and add some physical insight into the type of vibrational mode associated with a given frequency by grouping the terms in the Legendre polynomials according to known mode shapes. Although we included this procedure in our analysis, we omit the details.

A discussion of this procedure occurs in Ohno [3]. For the analyses reported here, Legendre polynomials up to third order were assumed in the displacement approximations. Hence n = 4 in Eq 3.

INVERSE PROBLEM

The numerical technique discussed in the previous section provides a useful way to approximate the natural-vibration frequencies of anisotropic cubes. Quantities required to calculate these values are the cube dimensions and the material's elastic constants. Using these quantities in combination with the described numerical technique, frequencies for isotropic cubes are obtained that compare well with both analytical and numerical results.

A more important, but more difficult, application of this numerical technique is to calculate the elastic constants of a material using measured natural frequencies. This strategy, typically called an inverse problem, involves specifying the natural frequencies and dimensions of the cube as the problem input, and the elastic stiffnesses as output. As an example, we consider determining the elastic constants C_1 and C_2 for an isotropic material such that

$$\lambda_1(C_1,C_2) = \omega_1$$

$$\lambda_2(C_1,C_2) = \omega_2. \qquad (12)$$

Here, λ_i (i=1,2) denote the numerically determined frequencies and ω_i (i=1,2) the measured frequencies. This system of equations can then be solved for C_1 and C_2 using one of a number of existing routines (for example, see [5]). Ideally, we would expect accurate values for these constants if both the numerical and experimental techniques perform with equivalent accuracy. For example, consider calculating the frequencies for a cube with the following characteristics:

mass = 0.0519 g
$L_x=L_y=L_z$ = 0.2744 cm
C_{11} = 324 GPa
C_{12} = 130 GPa.

This yields the first two distinct frequencies as

ω_1 = 1.0359 MHz
ω_2 = 1.4313 MHz.

Using these values as input along with the cube dimensions, we then attempt to calculate C_{11} and C_{12} using the logic of Eq 1 and the numerical technique in [5]. Using initial guesses of C_{11}^I = 260 GPa and C_{12}^I = 160 GPa, the solution quickly converges to the original values.

Unfortunately, the physical application of this method is less straightforward than the above example. Highly accurate measurements are required to determine the cube's natural-vibration frequencies because of the difficulty of identically satisfying Eq 1. Small perturbations in the experimental frequencies can lead to difficulties in solving Eq 1. Hence, a less restrictive approach for the general case of n elastic constants is to form the residual functions, R_i:

$$\begin{aligned} \lambda_1(C_1,C_2,\ldots,C_n) - \omega_1 &= R_1 \\ \lambda_2(C_1,C_2,\ldots,C_n) - \omega_2 &= R_2 \\ &\vdots \\ \lambda_m(C_1,C_2,\ldots,C_n) - \omega_m &= R_m. \end{aligned} \tag{13}$$

Here, m denotes the number of measured frequencies, and $m \geq n$. The problem becomes one of minimizing the combined residuals to calculate accurate values of C_i. Preliminary results have been obtained using the nonlinear least-squares algorithm in [6] and will be reported elsewhere. We hope to extend this method to shapes other than parallelepipeds.

MEASUREMENTS

Figure 2 shows a block diagram of the measurement electronics. We stepped the synthesizer under computer control between 50 kHz and 3 MHz in 50-kHz steps. At each step, we allowed the lock-in amplifier to settle, and we read by multimeter its in-phase and quadrature outputs.

The 4-MHz PZT transducers contacted the cube-specimen corners as shown schematically in Fig. 3. To minimize leakage, we placed aluminum foil over each transducer. Below 100 kHz, we observed some highly damped resonances, which we attributed to the apparatus, and ignored.

Although we did not measure the clamping force, it is critical to the measurements. A low force fails to reveal all the resonances. A high force shifts the resonance frequencies.

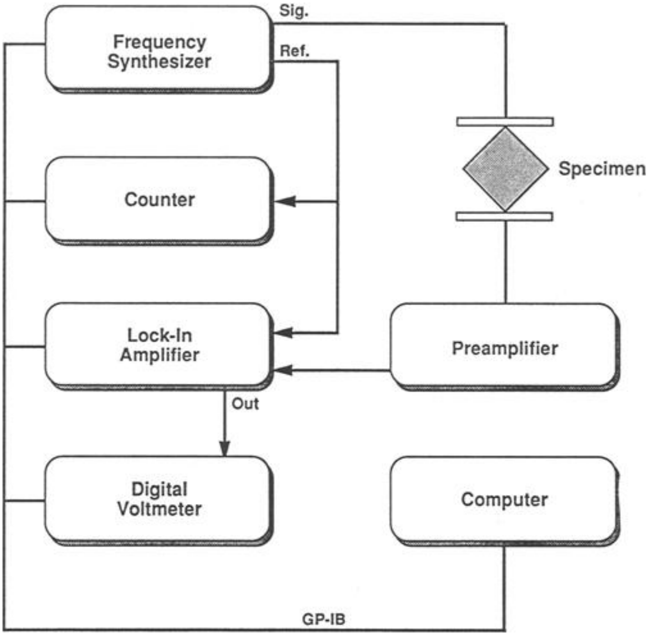

FIG. 2 — Block diagram of measurement electronics.

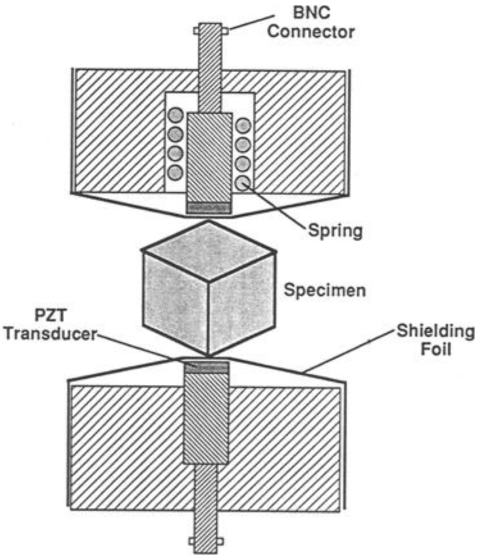

FIG. 3 — Schematic of specimen holder.

RESULTS AND DISCUSSION

For an aluminum-alloy cube, Fig. 4 shows a graph of measured and predicted vibration frequencies. Table 1 gives the numerical comparisons. Predicted frequencies near 140 kHz were not observed.

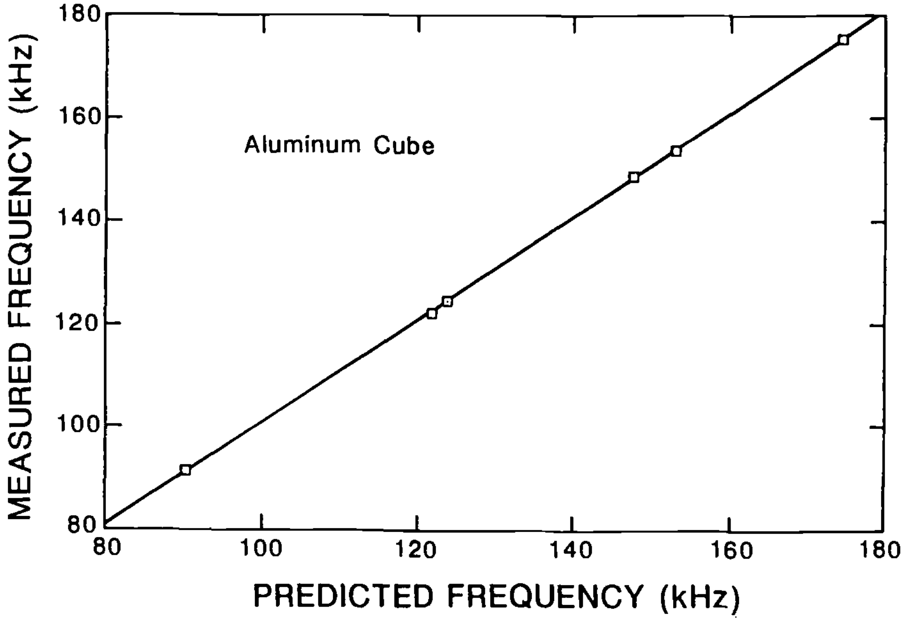

FIG. 4 — Comparison of measured and predicted vibration frequencies.

TABLE 1 — Predicted and measured vibration frequencies, in kHz

Predicted	Measured
90.2	91.1
90.3	91.4
90.3	91.7
121.8	122.3
121.9	122.3
121.9	122.6
123.7	124.6
123.7	124.6
123.7	124.9
140.3	-
140.4	-
140.4	-
147.5	148.8
147.6	148.8
147.7	148.8
152.9	153.5
152.9	153.9
153.0	154.4
174.6	175.2
174.7	175.7

In Fig. 4, each point contains three frequencies that arise from noncubicity and perhaps nonisotropic elastic constants. By a standard pulse-echo method, we measured the aluminum-alloy elastic constants. Table 2 shows these results together with those deduced from a vibrating-cube measurement. The cube weighed approximately 11 g and measured approximately 1.57 cm.

TABLE 2 — Isotropic aluminum-alloy elastic constants determined by two methods.

Method	Bulk Modulus, GPa	Shear Modulus, GPa	Young Modulus, GPa	Poisson Ratio
pulse-echo	75.0	27.6	73.8	0.336
resonant-cube	75.4	27.9	74.6	0.335

The good agreement, obtained for the aluminum alloy, failed to emerge when we measured some practical nonisotropic materials: an SiC_p/Al composite and a graphite-fiber/Mg composite. The latter shows especially strong elastic anisotropy. We continue to study why these materials defy exact analysis by the resonating-cube method. Our future studies will use blocks that depart from cubes. Noncubic blocks provide two advantages. First, a block with three lengths produces three-fold resonance frequencies, thus two extra measurements. Second, the cubic degeneracy produces errors that interfere with the frequencies-to-moduli inversion process.

CONCLUSIONS

1. For an aluminum alloy, using the resonating-cube method, we obtained almost the same elastic constants measured by a standard pulse-echo method.
2. The resonating-cube method presents some formidable but solvable problems. First, getting an accurate, complete, nonspurious resonance spectrum. Second, handling the inverse problem, especially for the anisotropic case.
3. Despite these obstacles, the resonant-cube method offers many advantages.
4. The high promise of the resonating-cube method suggests several further studies:
    a. C_{ij} temperature dependence
    b. C_{ij} pressure dependence
    c. other specimen shapes: cylinders, discs, rods
    d. inverse problem (determine C_{ij} from frequencies)
    e. internal friction (resonance-peak width).

REFERENCES

[1] Lamb, H., "On the vibrations of an elastic sphere," *Proceedings of the London Mathematical Society*, Vol. 13, 1882, pp. 189–2112.

[2] Demarest, H.H., "Cube-resonance method to determine the elastic constants of solids," *Journal of the Acoustical Society of America*, Vol. 49, 1969, pp. 768–775.

[3] Ohno, I., "Free vibration of a rectangular parallelepiped crystal and its application to determination of elastic constants of orthorhombic crystals," *Journal of the Physics of the Earth*, Vol. 24, 1976, pp. 355–379.

[4] Reddy, J.N., *Variational and Energy Methods in Applied Mechanics*, Wiley, New York, 1984.

[5] Dennis, J.E., Gay, G.M., and Welsch, R.E., "Algorithm 573 NL2SOL — An adaptive nonlinear least-squares algorithm, *TOMS*, Vol. 7, 1981, pp. 365–383.

[6] Powell, M.J.D., "A hybrid method for nonlinear algebraic equations," in *Numerical Methods for Nonlinear Algebra*, Gordon and Breach, London, 1970, pp. 87–114.

APPENDIX

We can write the submatrices in Eq 10 in more explicit form:

$$K_{ij}^{11} = \int_V \left(\frac{C_{11}}{L_x^2} \frac{\partial \Phi_i^x}{\partial x} \frac{\partial \Phi_j^x}{\partial x} + \frac{C_{55}}{L_z^2} \frac{\partial \Phi_i^x}{\partial z} \frac{\partial \Phi_j^x}{\partial z} + \frac{C_{66}}{L_y^2} \frac{\partial \Phi_i^x}{\partial y} \frac{\partial \Phi_j^x}{\partial y} \right) dV$$

$$K_{ij}^{12} = \int_V \left(\frac{C_{12}}{L_x L_y} \frac{\partial \Phi_i^x}{\partial x} \frac{\partial \Phi_j^y}{\partial y} + \frac{C_{66}}{L_x L_y} \frac{\partial \Phi_i^x}{\partial y} \frac{\partial \Phi_j^y}{\partial x} \right) dV = K_{ji}^{21}$$

$$K_{ij}^{13} = \int_V \left(\frac{C_{13}}{L_x L_z} \frac{\partial \Phi_i^x}{\partial x} \frac{\partial \Phi_j^z}{\partial z} + \frac{C_{55}}{L_x L_z} \frac{\partial \Phi_i^x}{\partial z} \frac{\partial \Phi_j^z}{\partial x} \right) dV = K_{ji}^{31}$$

$$K_{ij}^{22} = \int_V \left(\frac{C_{22}}{L_y^2} \frac{\partial \Phi_i^y}{\partial y} \frac{\partial \Phi_j^y}{\partial y} + \frac{C_{44}}{L_z^2} \frac{\partial \Phi_i^y}{\partial z} \frac{\partial \Phi_j^y}{\partial z} + \frac{C_{66}}{L_x^2} \frac{\partial \Phi_i^y}{\partial x} \frac{\partial \Phi_j^y}{\partial x} \right) dV$$

$$K_{ij}^{23} = \int_V \left(\frac{C_{23}}{L_y L_z} \frac{\partial \Phi_i^y}{\partial y} \frac{\partial \Phi_j^z}{\partial z} + \frac{C_{44}}{L_y L_z} \frac{\partial \Phi_i^y}{\partial z} \frac{\partial \Phi_j^z}{\partial y} \right) dV = K_{ji}^{32}$$

$$K_{ij}^{33} = \int_V \left(\frac{C_{33}}{L_z^2} \frac{\partial \Phi_i^z}{\partial z} \frac{\partial \Phi_j^z}{\partial z} + \frac{C_{44}}{L_y^2} \frac{\partial \Phi_i^z}{\partial y} \frac{\partial \Phi_j^z}{\partial y} + \frac{C_{55}}{L_x^2} \frac{\partial \Phi_i^z}{\partial x} \frac{\partial \Phi_j^z}{\partial x} \right) dV.$$

Jeffrey M. Wolla and Alan Wolfenden

MEASUREMENT AND ANALYSIS OF DYNAMIC MODULUS IN Al/SiC COMPOSITES

REFERENCE: Wolla, J. M. and Wolfenden, A., "Measurement and Analysis of Dynamic Modulus in Al/SiC Composites," Dynamic Elastic Modulus Measurements in Materials, ASTM STP 1045, A. Wolfenden, Ed., American Society for Testing and Materials, Philadelphia, 1990.

ABSTRACT: This study addresses the need for dynamic mechanical properties of advanced materials which are available only in small quantities by evaluating the ability of the Piezoelectric Ultrasonic Composite Oscillator Technique (PUCOT) to measure the dynamic modulus of small specimens of fibrous and particulate metal matrix composites. This is accomplished by measuring the dynamic modulus of several small rod or bar-shaped specimens of 6061 aluminum reinforced with silicon carbide fibers or particles (Al/SiC) at room temperature with the PUCOT. The fiber or particle volume fractions of the Al/SiC specimens vary from 8 to 56 percent and void volume fractions range from zero to 15 percent. The results are examined in terms of the dynamic modulus and specific dynamic modulus as a function of reinforcement volume fraction. Experimental results show that the modulus versus volume fraction for the fiber-reinforced composites deviates from the linear rule-of-mixtures due to the presence of voids and fiber damage. For the particulate composites, the modulus values fall within the bounds predicted by variational principles. A "strength of materials" approximation based on the assumption of cubic particles has limited success in predicting the particulate composite data. The results demonstrate the ability of the PUCOT to measure accurately the dynamic modulus of small specimens with minimal specimen preparation.

KEY WORDS: dynamic modulus, resonance techniques, PUCOT, metal matrix composites, aluminum/silicon carbide composites

The performance requirements of advanced structures are continually placing new demands on materials scientists to develop materials that are not only stronger, stiffer, and more resistant to extreme environments, but also lighter. As the new materials are being developed in the laboratory, a critical need arises for accurate characterization of the material properties in order to determine the capabilities of the new material and guide further development. In these situations, one is often dealing with small amounts

---

Mr. Wolla is a materials research engineer at the Naval Research Laboratory (Code 6372), Washington, DC 20375; Professor Wolfenden is a professor in the Mechanical Engineering Department, Texas A&M University, College Station, TX 77843.

of material and short deadlines. Therefore, accurate and reliable characterization techniques which can utilize small specimens and require little or no specimen machining, as these materials are often very hard to machine, will be highly desirable. For dynamic structural applications, the dynamic modulus (E) of the material will be of particular importance. In addition, verification of theoretical models requires large numbers of data points to adequately determine the ability of the models to predict material behavior. Again, small specimens will be advantageous in this regard as they will allow more data to be obtained from a given amount of material. This study addresses these concerns by evaluating the ability of the Piezoelectric Ultrasonic Composite Oscillator Technique (PUCOT) to measure accurately the dynamic modulus of small specimens of an advanced material; in this case, a metal matrix composite (MMC), 6061 aluminum reinforced with either silicon carbide fibers or particles (Al/SiC).

The PUCOT is a technique where a small specimen is set into ultrasonic, resonant vibration by piezoelectric crystals in such a way that the dynamic modulus and mechanical damping of the specimen at a known strain amplitude are measured. The theory and technique for the PUCOT were first described by Marx [1] and later refined by Robinson and Edgar [2]. The technique was extended to the torsional case by Robinson, et. al, [3] for determination of dynamic shear modulus, shear strain, and torsional mechanical damping of small specimens. The advantage of the PUCOT in the longitudinal vibration case is its ability to use small specimens with non-uniform cross-sections. The length of the specimen is critical but machining of the lateral sides to some standard configuration is not required. This allows the testing of rod, thin strip, or bar specimens.

This paper will describe the details of the PUCOT and present results that examine the applicability of the PUCOT to testing of MMCs. In addition, the dependence of the dynamic modulus of Al/SiC on the volume fraction of the SiC reinforcement will be analyzed and compared to some theoretical predictions.

PUCOT

General Technique

The PUCOT measures the resonant period of vibration in a specimen. The basic setup for room temperature measurements, shown in Fig. 1, consists of two piezoelectric quartz crystals, known as the drive (D) and the gage (G) crystals, and the specimen (S), glued in series. The drive crystal is excited with a suitable alternating voltage, and, when the specimen has been cut to the appropriate length for resonance, longitudinal, resonant, ultrasonic stress waves are produced in the specimen. The gage crystal acts as a strain gage in the system and outputs an alternating voltage that is proportional to the maximum strain in the system. The length of the matched pair of crystals determines the frequency of vibration. It is emphasized that the resulting stress waves are standing waves and the technique is not to be confused with the well known pulse-echo technique. Also, the wavelength is long compared to microstructural features and dimensions of the test specimen so significant dispersion and attenuation associated with material property discontinuities such as interfaces and voids will not occur. This is particularly important when composite materials, with their inherent material discontinuities, are considered. The discontinuities do not scatter the wave, but, however, they are oscillated by the wave and will, as a result, affect the bulk properties of the material that are measured.

Additional details for the PUCOT experimental setup are shown in Fig. 2. The wires that carry the input and output signals also serve as the crystal supports. The crystals are placed between the wires with the wires contacting the midpoint of the crystal, a vibration node, and held in place with a small amount of conductive silver paint. As shown in Fig. 3, the system is driven at resonance by a closed loop oscillator which controls the input drive voltage while maintaining a constant (user selectable) gage crystal voltage, and hence, a known constant maximum strain (or stress) amplitude in the specimen. Note that the ends of the specimen and the crystals are strain nodes where maximum displacement occurs while their midpoints are displacement nodes where maximum strain occurs. A phase shifter is used to locate and maximize the resonant vibration. The resonant period of vibration for the system, crystals alone (DG) or with specimen attached (DGS), is measured by a frequency counter. During typical tests, the values of the crystal voltages, and the resonant period are measured. These measured values, along with other system constants, such as crystal and specimen masses (m) and the specimen length (L), permit the calculation of the dynamic Young's modulus, mechanical damping, and maximum strain amplitude from standard PUCOT equations [2].

Test Procedure

The test procedure involves an initial determination of the specimen density and estimation of the dynamic modulus of the specimen. The density may be determined by

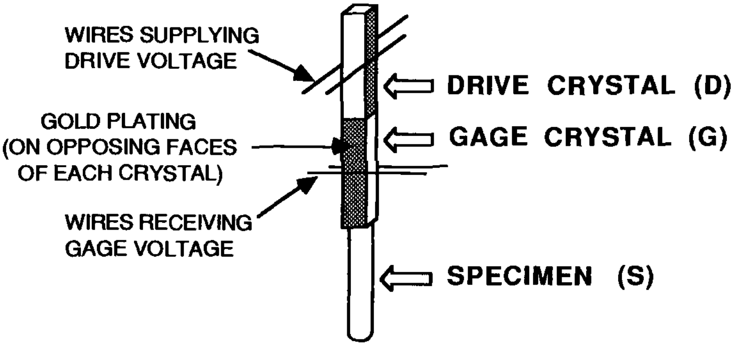

FIG. 1 -- Schematic of crystal and specimen arrangement for room temperature measurements with the PUCOT. Longitudinal crystals are shown.

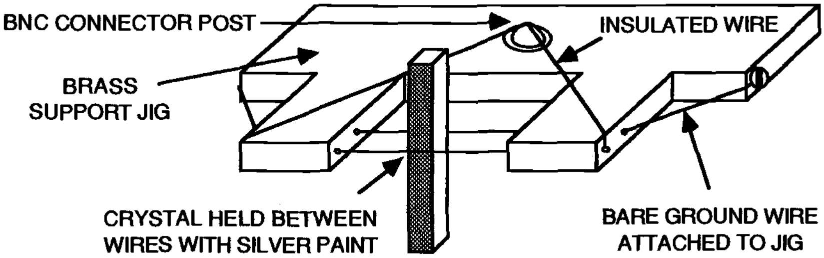

FIG. 2. -- Support fixture and wire connections for longitudinal crystals.

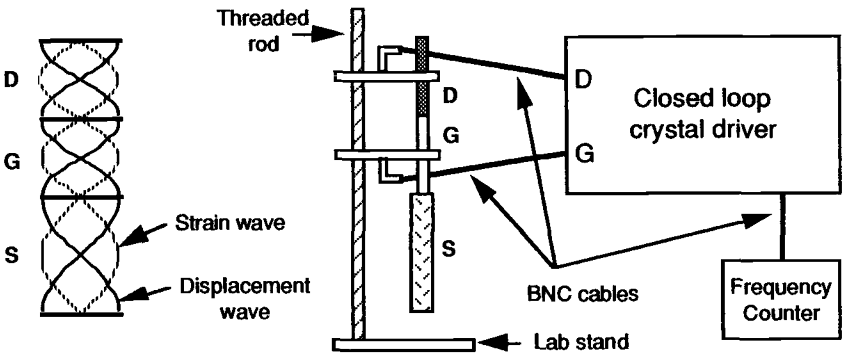

FIG. 3 -- Schematic of experimental setup for room temperature testing with the PUCOT. Displacement and strain (differential of displacement with respect to distance) waves in crystals and specimen are also shown.

suitable means, but accuracy is important as the density measurement will be a significant source of error in the final value obtained for E. Using the estimated value for dynamic modulus, the proper specimen length for the vibrational frequency is obtained from

$$L = (1/2f)\sqrt{(E/\rho)} = \lambda/2 \qquad (1)$$

where

L = specimen length,
f = vibrational frequency,
ρ = specimen density, and
λ = wavelength.

Note that at resonance the specimen will be one-half a wavelength long. This is shown in Fig. 3. If the available specimen material is too short, then a higher frequency (shorter quartz crystals) may be used. As mentioned previously, the cross section of the specimen need not be uniform along its length, but the ratio of the length to the maximum cross-sectional dimension should be greater than five. The masses of the joined crystals and the specimen are measured.

Next, the crystals are placed in the jig assembly and the resonant period is measured. The specimen is then glued to the crystals and the new resonant period is measured. Also, the crystal voltages are recorded if damping and strain amplitude results are desired. With this information, the resonant period in the specimen is determined by

$$\tau_S = \sqrt{m_S}\,\tau_{DG}\,\tau_{DGS}/A \qquad (2)$$

where

τ_i = resonant period in component or system i,
m_i = mass of component or system i
i = S, DG, or DGS, and
$A = \sqrt{\tau_{DG}^2\, m_{DGS} - \tau_{DGS}^2\, m_{DG}}$

Previous studies have shown that this result is considered valid if τ_S is within five percent of τ_{DG}, or

$$0.95 < R = \frac{\tau_S}{\tau_{DG}} < 1.05. \tag{3}$$

where R is the ratio τ_S/τ_{DG}. If Eq 3 is not satisfied, the length of the specimen must be changed and the test repeated. The new specimen length needs to be shorter if R is greater than 1.05 or longer if R is less than 0.95. It is advantageous, initially, to slightly overestimate the modulus of the specimen so that if Eq 3 is not satisfied, it will be due to the specimen being too long and the repeat test may be performed with the same specimen after it has been shortened. If the specimen is too short (modulus underestimated) a new specimen needs to be cut which may not be possible if the material is in short supply. Another alternative is to use a higher frequency (shorter crystals and specimen).

Finally, once a valid result for τ_S has been obtained, Eq 4 is used to determine the specific dynamic modulus (E/ρ). This value may be multiplied by the density to yield the dynamic modulus of the material. Note that the specific dynamic modulus value is not affected by errors in the density measurement.

$$E/\rho = 4L^2/\tau_S^2 \tag{4}$$

Additional Capabilities

As mentioned previously, the PUCOT also measures mechanical damping and strain amplitude in the specimen (simultaneously with modulus measurement). Strain amplitude scans are performed by taking crystal voltage readings at several gage voltages (recall that gage voltage is proportional to the maximum strain in the specimen). The possible range of strain amplitudes is 10^{-8} to 10^{-3}. Frequencies from 20 to 200 kHz can be obtained by using different lengths of quartz crystals (in matched pairs). Also, by using a fused quartz spacer rod between the crystals and the specimen, all the above measurements can be made while the specimen is suspended in a controlled thermal environment.

MATERIAL

The MMCs tested in this study consisted of 6061 aluminum reinforced with silicon carbide in the form of either continuous fibers (fibrous composite) or particles (particulate composite). The fibrous composites were unidirectionally reinforced cylindrical rods while the particulate composites were either cylindrical or rectangular in cross-section. All but one of the fibrous specimens contained 103 μm diameter fibers (SiC deposited on tungsten core) with a reported [4] fiber dynamic modulus of 419 GPa and a density of 3.38 g/cm³. The remaining fibrous composite had 140 μm diameter fibers (SiC on carbon core) with 427 GPa and 3.3 g/cm³ for the fiber modulus and fiber density, respectively [5]. The particles in the particulate composites were assumed to be distributed uniformly throughout the material and were assigned the properties of bulk β-SiC [6]: 450 GPa for the modulus and 3.21 g/cm³ for the density. Handbook values of

TABLE 1 -- Description of Al/SiC test specimens.

Type	Cross-section dimensions (mm)	Reinforcement Volume Fraction	Void Volume Fraction
Particulate	12.8 dia. rod[a]	0.078	0
	6.47 x 5.04 bar	0.245	0.007
	5.29 x 4.37 bar	0.239	0.003
	4.40 x 3.25 bar	0.239	0.007
Fibrous	10.4 dia. rod	0.200	0.019
	10.4 dia. rod	0.284	0.119
	8.00 dia. rod	0.449	0.027
	8.08 dia. rod[b]	0.422	0.023
	10.3 dia. rod	0.441	0.153
	10.3 dia. rod	0.560	0.059

[a] Specimen tested at 40 kHz due to large diameter. All others tested at 80 kHz.

[b] 140 µm diameter fibers. All other fibrous composites had 103 µm diameter fibers.

68.9 GPa and 2.7 g/cm^3 were used for the 6061 aluminum. The specimen dimensions and corresponding volume fractions are listed in Table 1.

Note the small specimen sizes relative to those needed for other techniques such as mechanical testing in a universal testing machine. The cross-sectional dimensions for these specimens are actually larger than necessary and could be reduced by an order of magnitude and still work with the PUCOT. The simple specimen machining process consisted of cutting the specimen to length and sanding the ends with 600 grit paper.

The reinforcement and void volume fractions were determined through a matrix removal process. First, the specimen mass and volume were measured. Then a 10% sodium hydroxide solution at 60°C to 70°C was used to dissolve the matrix and the mass of the fibers or particles was measured. These measurements, along with the fiber and matrix properties then were used to calculate the void fraction [7]. The void fraction was then used in determining the reinforcement volume fraction [8]. This procedure does not establish the void and reinforcement fractions independently as the Schoutens [8] technique would, but it provides excellent estimates of the volume fractions and is a significant improvement over the manufacturer's stated volume fractions.

RESULTS AND DISCUSSION

The results will be examined in terms of the dynamic modulus and specific dynamic modulus as a function of reinforcement volume fraction. Figure 4 shows that the dynamic modulus values measured by the PUCOT agreed very well with rule-of-mixture (ROM) predictions when void fraction is taken into account. The larger disagreement between measured and predicted values for the two cases near 0.45 fiber volume fraction can be attributed to significant fiber damage found in these two specimens. The fiber fragments collected when determining the fiber volume fraction were treated as if they were undamaged fibers in the ROM analysis. In actuality, these fragments will not contribute the full stiffness of continuous fibers and, therefore, the composite stiffness will be reduced relative to the ROM prediction. ROM predictions, assuming no voids, serve as an upper bound on the dynamic modulus for these materials.

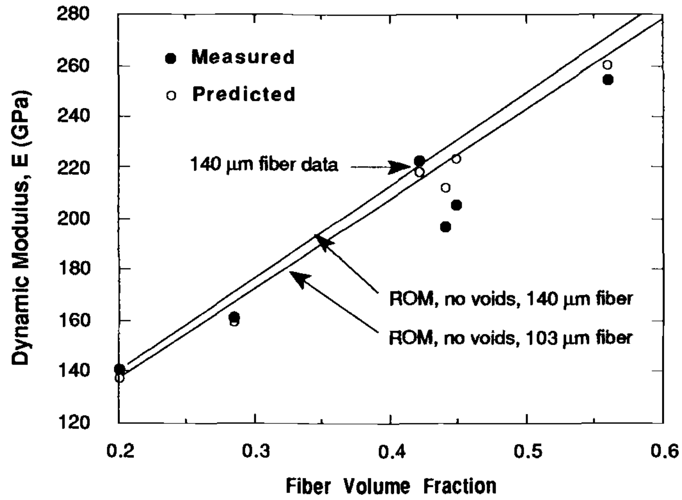

FIG. 4 -- Plot of the dynamic modulus versus fiber volume fraction for the fibrous composites. Values measured by the PUCOT are shown along with values predicted by the rule-of-mixtures (ROM) with void fraction considered. The solid lines are ROM predictions for void-free composites.

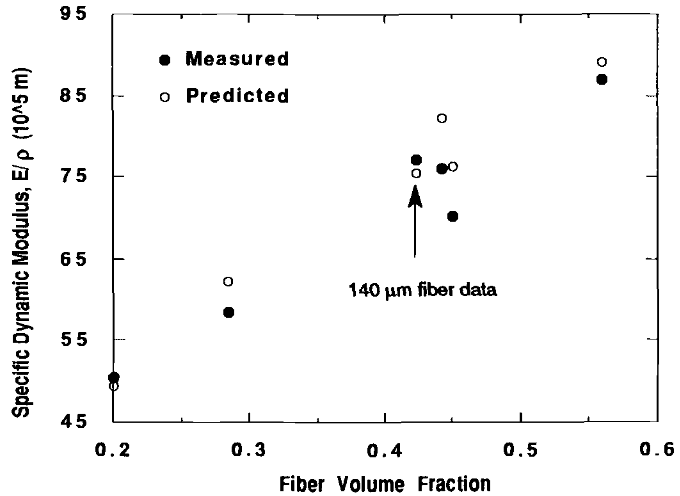

FIG. 5 -- Plot of the specific dynamic modulus versus fiber volume fraction for the fibrous composites. Values measured by the PUCOT are shown along with values predicted by the rule-of-mixtures (ROM) with void fraction considered.

The specific dynamic modulus of the fibrous composites is presented in Fig. 5. The deviations of the measured values from the predicted values appear larger than those for the dynamic modulus (Fig. 4), but the percentage deviations of the measured values from the predicted values are nearly equal. The uncertainty of the specific dynamic modulus is less than the uncertainty of the dynamic modulus (the dynamic modulus has the additional uncertainty associated with the specimen density measurement), yet the results are not significantly better for the specific dynamic modulus. This indicates that the simple density measurements performed in this study (mass and volume measurements or buoyancy technique) are sufficiently accurate. In turn, the degree of confidence in the modulus measurements is not noticeably reduced by the density measurement.

For the particulate composite case (Fig. 6), the measured values of the dynamic modulus fell within the bounds predicted by variational principles (Hashin and Shtrikman [9]). A "strength of materials" approximation based on a cubic inclusion assumption (Paul [10]) has limited success in predicting the dynamic modulus. As with the fibrous composites, the specific dynamic modulus measurements are not noticeably better than the dynamic modulus measurements (see Fig. 7). The measured void fractions were very low for the particulate composites and the modulus measurements were repeatable and accurate. Therefore, the disagreements between the measured and predicted values are attributed partly to incorrect assumptions of the mechanical properties of the particles and partly to the cubic particle assumption not being a true representation of the actual particle shape. The potential for improved agreement exists by comparing the measured dynamic modulus values to predictions from a model due to Ledbetter and Datta [12, 13] which permits a better description of the particle shape and non-homogeneous particle distribution. This comparison has yet to be attempted.

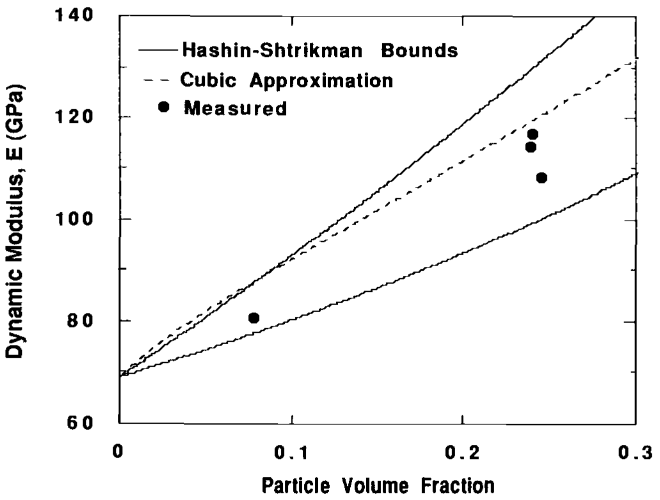

FIG. 6 -- Plot of the dynamic modulus versus particle volume fraction for the particulate composites. Values measured by the PUCOT are shown along with the prediction of an approximate solution based on a cubic inclusion assumption [10] and the Hashin-Shtrikman bounds [9].

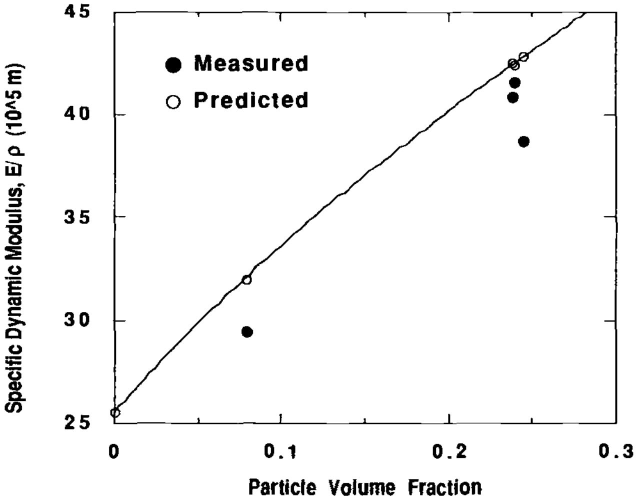

FIG. 7 -- Plot of the specific dynamic modulus versus particle volume fraction for the particulate composites. Values measured by the PUCOT are shown along with values predicted by an approximate solution based on a cubic inclusion assumption [10].

SUMMARY

The PUCOT is capable of measuring the dynamic modulus of small specimens, both accurately and quickly. A detailed uncertainty analysis of the PUCOT yields values of less than two percent uncertainty for the technique. It is a sensitive technique and detects small modulus changes caused by voids or fiber damage. Due to the long, resonant wavelength used in this technique, scattering, attenuation and dispersion effects are negligible and bulk properties can be measured on a variety of specimen shapes. The ability to work with small specimens with varying shapes should prove invaluable in analyzing the progress of material development programs and provide significant data for use in verification of theoretical models of material properties.

REFERENCES

[1] Marx, J., "Use of the Piezoelectric Gauge for Internal Friction Measurements," The Review of Scientific Instruments, Vol. 22, No. 7, July 1951, pp. 503-509.

[2] Robinson, W. H. and Edgar, A., "The Piezoelectric Method of Determining Mechanical Damping at Frequencies of 30 to 200 kHz," IEEE Transactions on Sonics and Ultrasonics, Vol. SU-21, No. 2, April 1984, pp. 98-105.

[3] Robinson, W. H., Carpenter, S. H., and Tallon, J. L., "Piezoelectric Method of Determining Torsional Mechanical Damping Between 40 and 120 kHz," Journal of Applied Physics, Vol. 45, No. 5, May 1974, pp. 1975-1981.

[4] DiCarlo, J.A. and Williams, W., "Dynamic Modulus and Damping of Boron, Silicon Carbide, and Alumina Fibers," Ceramic and Engineering Science Proceedings, Vol. 1, No. 7-8(B), July-August 1980, pp. 671-692.

[5] World-wide Carbon Fibre Directory, 2nd Edition, Pamington, D., Editor, Pammac Directories Limited, Slough, England, 1982, p. 271.

[6] Andersson, C-H and Warren, R., "Silicon Carbide Fibers and Their Potential for Use in Composite Materials. Part 1." Composites, Vol. 15, No. 1, January 1984, pp. 16-24.

[7] Tsai, S.W. and Hahn, H.T., Introduction to Composite Materials, Technomic Publishing Co., Westport, CT, 1980, p. 382.

[8] Schoutens, J.E., "Simple and Precise Measurements of Fibre Volume and Void Fractions in Metal Matrix Composite Materials," Journal of Materials Science, Vol. 19, No. 3, March 1984, pp. 957-964.

[9] Hashin, Z. and Shtrikman, S., "A Variational Approach to the Theory of the Elastic Behaviour of Multiphase Materials," Journal of Mechanics and Physics of Solids, Vol. 11, pp. 127-140.

[10] Paul, B., "Prediction of Elastic Constants of Multiphase Materials," Transactions of the Metallurgical Society of AIME, Vol. 218, No. 1, February 1960, pp. 36-41.

[11] Ledbetter, H.M. and Datta, S.K., "Young's Modulus and the Internal Friction of an SiC-particle-reinforced Aluminum Composite," Materials Science and Engineering, Vol. 67, 1984, pp. 25-30.

[12] Ledbetter, H.M. and Datta, S.K., "Effective wave speeds in an SiC-particle-reinforced Al composite," Journal of the Acoustical Society of America, Vol. 79, No. 2, February 1986, pp. 239-248.

S. K. Datta and H. M. Ledbetter

FIBER-REINFORCED COMPOSITES: MODELS FOR MACROSCOPIC ELASTIC CONSTANTS

REFERENCE: Datta, S. K. and Ledbetter, H. M., "Fiber-Reinforced Composites: Models for Macroscopic Elastic Constants," in Dynamic Elastic Modulus Measurements in Materials, ASTM STP 1045, Alan Wolfenden, editor, American Society for Testing and Materials, Philadelphia, 1990.

ABSTRACT: Considering uniaxial-fiber-reinforced composites, we review selected models for calculating macroscopic elastic constants from the constituent elastic constants (fiber and matrix) and the phase geometry. Especially, we focus on the transverse-isotropic case with five independent elastic-stiffness constants, C_{ij}. Also, we focus on wave-scattering ensemble-average methods developed by Bose and Mal (1974) and by Datta and Ledbetter (1983, 1984). We compare the model results with measurements made by pulse-echo dynamic (MHz) methods. As examples, we consider B/Al and Gr/Mg; the latter fibers possess high elastic anisotropy.

KEYWORDS: composites, elastic constants, fiber-reinforced composites, physical properties, sound velocities, theoretical models, ultrasonic-velocity method.

In recent years, both theory and observation of fiber-reinforced composites have advanced considerably. Reviews of this subject include those on theory by Hashin [1], Sendeckyj [3], Walpole [4], and Bert [5]. In an earlier study, Datta et al [6] also presented a review of the various model studies of aligned continuous fiber-reinforced composites. They also presented a multiple-scattering approach to obtain dispersion relationships for wave propagation perpendicular to the fibers. Such an approach was taken earlier by Bose and Mal [7, 8]. It was shown that three effective static anisotropic elastic constants (in-plane bulk and shear moduli and longitudinal shear modulus) can be obtained by this method in the limit of long

Professor Datta is with the Department of Mechanical Engineering and CIRES, University of Colorado, Boulder, Colorado 80309. Dr. Ledbetter is a research metallurgist at NIST (formerly NBS), Boulder, Colorado 80303.

wavelength. The other two effective elastic constants, longitudinal Young's modulus, E_L, and the Poisson's ratio, ν_{LT}, can then be found (see Datta et al [6], and Datta and Ledbetter [9]) by using Hill's relation [10]. Thus, five effective elastic constants characterizing the transverse isotropy of the composite can be found using this approach.

In this paper, we present the model equations that were derived in [6, 10], and apply them to predict the effective properties of a boron/aluminum, two graphite/magnesium and two graphite/aluminum composites. For boron/aluminum, we also compare the predictions with those obtained by two periodic models: a square array (Achenbach [11]) and a hexagonal array (Hlavacek [12]). Comparison of model results with measurements is also presented.

MATERIAL

The studied boron/aluminum composite consisted of 0.14-mm-diameter boron fibers in 6061-aluminum-alloy-matrix. The alloy was in F-tempered condition. The composite, containing 48% fibers by volume, was fabricated as a 10x10x1.1-cm plate containing about seventy plies. Mass density of this material, measured hydrostatically, was 2.534 g/cm^3. Figure 1 shows the microstructure of the material.

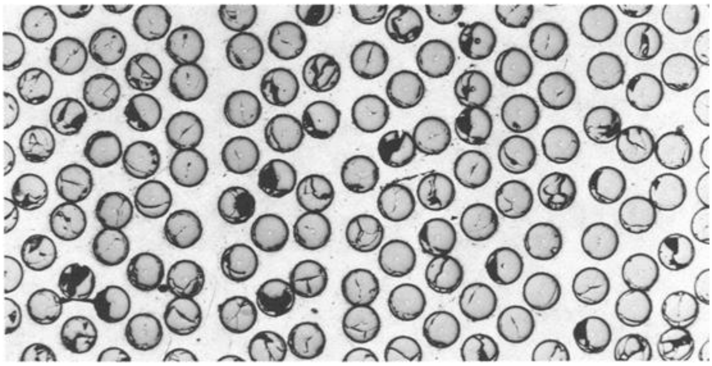

FIG. 1 -- Optical photomicrograph showing distribution of 0.14-mm-diam boron filaments in aluminum matrix. Plane of photo is perpendicular to fibers, which are parallel to x_3 axis. Fiber volume fraction equals 0.48.

We studied two graphite/magnesium and two graphite/aluminum materials produced from commercial fibers and alloys. The two fibers are categorized as high-strength/low-modulus and low-strength/high-modulus. The two matrices consisted of pure magnesium and 5056 aluminum alloy. For the fibers, the manufacturer reported Young moduli of 235 and 392 GPa and mass densities of 1.76 and 1.81 g/cm^3, respectively.

Composites were produced by a squeeze-casting method, where molten matrix metal infiltrates carbon-fiber bundles under high pressure. Carbon fibers were preformed with a polymer fugitive binder. Placed in a mold, the preform was heated to slightly below the matrix-metal melting temperature. The binder was burned away and the carbon fibers were preheated. Molten matrix metal was poured into the mold and pressed at 98 MPa before solidification. This pressure caused the molten metal to infiltrate the fiber bundles. After solidification, the composite was removed from the mold. Further fabrication details occur elsewhere [13].

Figure 2 shows a typical microstructure. Focusing, for the moment, on the low-modulus magnesium-matrix material, by Archimedes's method, we found a mass density of 1.771 g/cm^3. For a fiber volume fraction of 0.70, using 1.738 for magnesium, and 2.269 for graphite, we predict a mass density of 2.110 g/cm^3. Probably, the discrepancy arises from nonperfectly graphitized fibers. Indeed, the manufacturer's reported fiber density, 1.76, leads to a prediction of 1.753, within 1 percent of observed. If we assume a void-and-crack-free matrix, our results predict a fiber density of 1.79 g/cm^3, corresponding to a fiber-void fraction of 0.21.

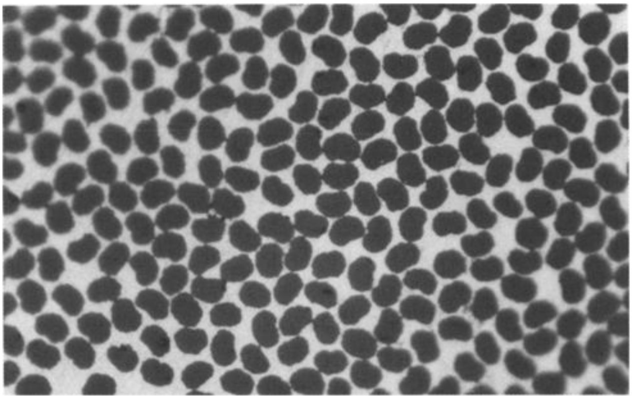

FIG. 2 -- Optical photomicrograph of transverse section of graphite-fiber-reinforced magnesium-matrix composite. The fibers, 7 μm in diameter, occupy 70 volume percent of the composite.

For the magnesium-matrix material, a sample was prepared as described above. For the matrix material, we found an Archimedes-method mass density of 1.738 g/cm^3, close to the accepted value for pure magnesium: 1.737. Similarly, for the aluminum-alloy matrix materials, we found the mass densities to be 2.701 g/cm^3 and 2.652 g/cm^3 for 6061 aluminum and 5056 aluminum alloys, respectively. Table 1 shows the measured elastic constants for these matrix materials. The notation is E = Young's modulus, G = shear modulus, B = bulk modulus, and ν = Poisson's ratio.

TABLE 1 -- Elastic constants of matrix materials.

	E (GPa)	G (GPa)	B (GPa)	ν
Mg	45.34	17.72	34.26	0.279
6061 aluminum	71.5	26.7	75.1	0.341
5056 aluminum	70.39	26.22	74.45	0.342

MEASUREMENTS

We determined the nine C_{ij} by measuring eighteen sound velocities on four specimen geometries described previously [14]. For brevity, we omit further description, except for a few salient details: bond—phenyl salicylate; transducers—quartz, x-cut and ac-cut; frequencies—5 to 6 MHz; specimen size—16-mm cube, or smaller depending on specimen geometry. Previously, we reported details of the measurement method [15]. Figure 3 shows an oscilloscope display.

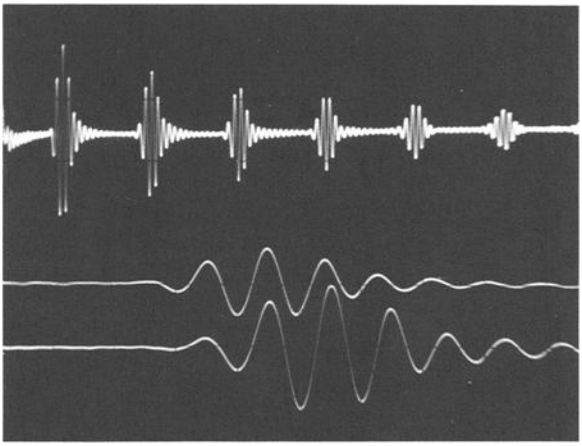

FIG. 3 -- Oscilloscope display of a pulse-echo pattern (top), expanded first echo (center), and expanded second echo (bottom). We measure transit time by superimposing the first nondistorted cycle of the first and second echoes. This example represents a longitudinal wave traveling parallel to the fibers.

Results for boron-aluminum

Results of theoretical calculations and observations for the boron-aluminum composite are shown in Table 3. Experimentally determined nine C_{ij}'s are based on a least-squares fit to eighteen separate wave-velocity directions and polarizations. For details, see [14]. Elastic constants of boron are shown in Table 2. It is found by comparison with theory and measurement that boron is nearly isotropic.

TABLE 2 -- Properties of boron fibers.

	ρ (g/cm^3)	E (10^{11}N/m^2)	G (10^{11}N/m^2)	B (10^{11}N/m^2)	ν
Boron	2.352	3.979	1.763	1.785	0.129

TABLE 3 -- Observed and predicted C_{ij} elastic stiffnesses of a boron-aluminum unidirectionally fiber-reinforced composite, in units of 10^{11}N/m^2.

ij	Observed	Square Model[a]	Hexagonal Model[b]	Random Model[c]	Full Random Model
11	1.852	1.856	1.872	1.790	1.790
22	1.797	1.856	1.872	1.790	1.790
33	2.450	2.480	2.551	---	2.560
44	0.566	0.451	0.561	0.559	0.559
55	0.569	0.451	0.561	0.559	0.559
66	0.526	---	0.606	0.523	0.523
12	0.779	---	0.661	---	0.745
13	0.606	---	0.578	---	0.583
23	0.604	---	0.578	---	0.583

[a] After Achenbach [11].
[b] After Hlavacek [12].
[c] After Bose and Mal [8].

Results for graphite-magnesium and graphite-aluminum

Table 4 shows principal results for another material: low-modulus fiber, magnesium matrix. Column 1 lists various elastic constants described in the previous section. Column 2 gives a set of graphite-fiber elastic constants [16]. We chose these because E_3 agrees closely with the E_3 for the present fiber. Column 3 gives elastic constants predicted by a theoretical model using the column-2

Table 4. Measured and calculated elastic constants for graphite-magnesium composite and calculated elastic constants for graphite fiber. Except for dimensionless ν_{ij}, units are GPa.

	Fiber[a]	Composite, Calculated	Composite, Measured	Fiber, Calc.	Composite, Recalc.	Ratio, Recalc./ Meas.
C_{11}	20.02	27.28	28.19	20.99	28.19	1.00
C_{22}	20.02	27.28	27.08	20.99	28.19	1.04
C_{33}	234.77	180.63	174.68	225.17	174.30	1.00
C_{44}	24.00	21.90	17.91	17.99	17.91	1.00
C_{55}	24.00	21.90	17.70	17.99	17.91	1.00
C_{66}	5.02	7.38	8.76	6.51	8.76	1.00
C_{12}	9.98	12.52	10.66	7.98	10.67	1.00
C_{13}	6.45	9.56	12.41	9.77	12.20	0.98
C_{23}	6.45	9.56	12.41	9.77	12.20	0.98
E_1	15.00	21.38	23.65	17.79	23.81	1.01
E_2	15.00	21.38	22.70	17.79	23.81	1.05
E_3	232.00	176.04	166.64	218.58	166.64	1.00
ν_{12}	0.494	0.449	0.374	0.367	0.359	0.96
ν_{13}	0.014	0.029	0.045	0.027	0.045	1.00
ν_{23}	0.014	0.029	0.046	0.027	0.045	0.98
ν_{21}	0.494	0.449	0.358	0.367	0.359	1.00
ν_{31}	0.215	0.240	0.314	0.337	0.314	1.00
ν_{32}	0.215	0.240	0.335	0.337	0.314	0.94

[a] Ref. 16.

graphite-fiber elastic constants and the measured magnesium elastic constants.

Column 4 shows measured results: the nine orthotropic-symmetry C_{ij}, the principal Young moduli E_i, and the principal Poisson ratios ν_{ij}.

From the measured results and the above model, we calculated the graphite-fiber elastic constants, shown in column 5. We used the calculational sequence: C^f_{44}, C^f_{66}, $C^f_{11} - C^f_{66}$, ν^f_{31}, and E^f_3.

Column 6 shows the composite C_{ij} recalculated using the deduced C^f_{ij}. Finally, column 7 shows the ratio of column 6 to column 4, the ratio of recalculated to measured.

To calculate the predicted composite elastic constants shown in column 3, we used the model described in [6, 9].

Table 5 shows the deduced graphite-fiber elastic constants for all four cases. Table 5 also includes elastic constants for two useful reference cases: an aggregate of randomly oriented graphite crystals and a fiber where all the crystallite basal planes contain the fiber axis. For this latter case, we know only C_{33} and E_3 because the appropriate averaging problem remains unsolved.

The estimate of the quasiisotropic-aggregate elastic constants in the final column of Table 5 deserves some description. These unpublished calculations were done with Dr. B. Gairola of the University of Stuttgart. They represent the first self-consistent-model calculations for such a highly anisotropic material. For usual materials, the upper and lower bounds usually converge within a few percent at either the second-order (Hashin–Shtrikman) or third-order (Kröner) bounds. However, graphite's extraordinary elastic anisotropy prevents such convergence. For graphite, for the shear modules, the upper and lower third-order bounds are 108.2 and 12.9 GPa, respectively!

After carrying the problem to approximately the thirtieth bound, we found convergence and the values shown in Table 5. We see that the quasiisotropic Young modulus equals approximately one-eighth of the maximum-possible value, 1020 GPa. (The average overall direction favors the lower values.) The predicted Poisson ratio, 0.26, indicates a typical material, and fails to show any symptoms of graphite's extreme elastic anisotropy. The Poisson ratios predicted for the fibers do manifest such anisotropy, ranging from 0.008 to 0.613, well beyond the range observed for usual materials.

Table 5. Deduced graphite-fiber elastic constants. Except for dimensionless ν_{ij}, units are GPa.

	Fiber 1		Fiber 2		Perfect Basal-plane Alignment	Quasi-isotropic Aggregate
	Al	Mg	Al	Mg		
C_{11}	19.09	20.99	11.24	12.58	-	160
C_{22}	19.09	20.99	11.24	12.58	-	160
C_{33}	234.99	225.17	348.89	361.45	1060	160
C_{44}	19.94	17.99	14.80	14.54	-	52
C_{55}	19.94	17.99	14.80	14.54	-	52
C_{66}	5.60	6.51	2.53	3.10	-	52
C_{12}	7.89	7.98	6.19	6.39	-	57
C_{13}	10.34	9.77	6.36	11.62	-	57
C_{23}	10.34	9.77	6.36	11.62	-	57
E_1	15.66	17.79	7.81	9.25	-	130
E_2	15.66	17.79	7.81	9.25	-	130
E_3	227.07	218.58	344.25	347.22	1020	130
ν_{12}	0.399	0.367	0.546	0.493	-	0.26
ν_{13}	0.026	0.027	0.008	0.016	-	0.26
ν_{23}	0.026	0.027	0.008	0.016	-	0.26
ν_{21}	0.399	0.367	0.546	0.493	-	0.26
ν_{31}	0.383	0.337	0.365	0.613	-	0.26
ν_{32}	0.383	0.337	0.365	0.613	-	0.26

THEORY

In Table 3, the experimental results are compared with results of four theories:

1. that for a periodic square-lattice array of long, parallel, circular fibers derived by Achenbach [11] using a homogeneous continuum model that predicts three elastic constants;
2. similar to Achenbach's model, a hexagonal-array model derived by Hlavacek [10] that provides five elastic constants;
3. a random-distribution model due to Bose and Mal [7, 8], who derived expressions for three independent elastic constants;
4. a full-random-distribution model derived here by combining the results of [7, 8] with those of Hill [10]. This latter, present model predicts all five independent elastic constants of a matrix reinforced with long, parallel fibers distributed randomly in the transverse plane. The Achenbach, Hlavacek, and Bose-Mal models were described in [9]. The present model is described below.

Here, we show that combining the Bose-Mal relationships with previously derived relationships for other elastic constants leads to a full set of five independent elastic constants for the random-distribution case. For this, a new notation [3] is useful, which will be described as it is introduced.

Hashin and Rosen [17] derived relationships for the effective moduli of a continuous-fiber-reinforced composite where the fibers are distributed randomly and homogeneously. Hashin [18] gave these relationships in essentially the form

$$k_T = k_m - \frac{c(k_f - k_m)(k_m + \mu_m)}{k_f + \mu_m - c(k_f - k_m)} \tag{1}$$

and

$$\mu_{LT} = \mu_m + \frac{2c(\mu_f - \mu_m)\mu_m}{\mu_f + \mu_m - c(\mu_m - \mu_m)} \ . \tag{2}$$

Here, k denotes the two-dimensional, plane-strain bulk modulus, which is $\lambda + \mu$ in an isotropic material. Subscript T denotes deformation in the x_1–x_2 plane, perpendicular to the fibers. Subscript LT denotes shear deformation in any plane containing the x_3 axis, that is, the fiber axis. Equations (1) and (2) were also derived by Hill [10] for a single fiber placed concentrically in a cylindrical matrix. Hermans [19] obtained them also by considering Hill's assembly to be embedded in an unbounded solid having the effective elastic moduli of the composite. In this model, the fiber: matrix cylinder radius ratio is $r_1/r_2 = c^{1/2}$.

Knowing k_T, one can derive the Young modulus E_L (along x_3) and the Poisson's ratio $\nu_{LT} = -\epsilon_1/\epsilon_3$, where uniaxial stress is along x_3 and ϵ denotes strain. This is done by using the relationship given by Hill [10]:

$$\frac{\frac{1}{k_T} - \frac{1}{k_f}}{\nu_{LT} - \nu_f} = \frac{\frac{1}{k_T} - \frac{1}{k_m}}{\nu_{LT} - \nu_m} = \frac{\frac{1}{k_f} - \frac{1}{k_m}}{\nu_f - v_m} = \frac{4\nu_{LT} - \nu_m - c(\nu_f - \nu_m)}{E_L - E_m - c(E_f - E_m)} . \qquad (3)$$

Solving for E_L and ν_{LT}, using eqn (1), one finds

$$E_L = (1 - c)E_m + cE_f + \frac{4c(1 - c)(\nu_f - \nu_m)^2}{\frac{(1 - c)}{k_f} + \frac{c}{k_m} + \frac{1}{\mu_m}} \qquad (4)$$

and

$$\nu_{LT} = (1 - c)\nu_m + c\nu_f + \frac{c(1 - c)(\nu_f - \nu_m)\left(\frac{1}{k_m} - \frac{1}{k_f}\right)}{\frac{(1 - c)}{k_f} + \frac{c}{k_m} + \frac{1}{\mu_m}} . \qquad (5)$$

Of course, both of these relationships represent a simple, linear "rule of mixtures" plus a higher-order correction term. The advantages of eqns (1)–(2) are clear: they give simple, explicit relationships for four of the composite's elastic constants in terms of the isotropic elastic constants of the constituent materials, the fiber and the matrix. On the other hand, self-consistent approaches lead to implicit relationships.

Bose and Mal [7, 8] also obtained Eqs (1) and (2), but by a different approach: by considering the effective velocity for long-wavelength plane waves propagating perpendicular to the fibers, for both a longitudinal wave and for a shear wave polarized along x_3, the fiber axis. By a similar approach, examining a shear wave propagating and polarized in a plane transverse to the fibers, Bose and Mal [7] also derived an expression for the transverse shear modulus:

$$\mu_{TT} = \mu_m + \frac{2c(k_m + \mu_m)(\mu_f - \mu_m)}{k_m + \left(\frac{k_m}{\mu_m} + 2\right)[c\mu_m + (1 - c)\mu_f]} . \qquad (6)$$

Previous studies [10, 17] did not obtain this explicit expression, but bounds instead. In fact, Eq (6) corresponds to the lower bound. Equations (1), (2), (4) and (5) are also identical to the lower-bound results. Thus, the "quasi-crystalline" approximation used by Bose and Mal to derive Eqs (1), (2) and (5) leads to the lower-bound results. Equation (6) coincides also with Hermans' [19] result. From the above relationships, one obtains for the boron-aluminum composite, using results in Tables 1 and 2:

$$\begin{aligned} E_L &= 2.292 \cdot 10^{11}\text{N/m}^2, \\ k_T &= 1.267 \cdot 10^{11}\text{N/m}^2, \\ \mu_{LT} &= 0.559 \cdot 10^{11}\text{N/m}^2, \\ \mu_{TT} &= 0.523 \cdot 10^{11}\text{N/m}^2, \\ \nu_{LT} &= 0.230. \end{aligned}$$

Since the composite behaves transversely isotropic with the unique symmetry axis along x_3, the C_{ij} elastic-stiffness constants can be computed from

$$C_{11} = C_{22} = k_T + \mu_{TT}, \tag{7}$$
$$C_{33} = E_L + 2\nu_{LT}C_{13}, \tag{8}$$
$$C_{44} = C_{55} = \mu_{LT}, \tag{9}$$
$$C_{66} = \tfrac{1}{2}(C_{11} - C_{12}) = \mu_{TT}, \tag{10}$$
$$C_{12} = k_T - \mu_{TT}, \tag{11}$$
$$C_{13} = C_{23} = 2\nu_{LT}k_T. \tag{12}$$

These results are given in the final column of Table 3.

Turning now to the graphite fiber-reinforced composites, we note that the above model Eqs (1, 2, 4–6) can easily be generalized to the case when the transverse-isotropy properties of the graphite fibers are to be taken into account. This was presented in [6] (see also, [16] and [20]). If we solve these equations for the fiber elastic constants, we obtain

$$C^f_{44} = \mu^m + \frac{2\mu^m(C_{44} - \mu^m)}{2c\mu^m - (1 - c)(C_{44} - \mu^m)}, \tag{13}$$

$$C^f_{66} = \mu^m + \frac{2\mu^m(C_{66} - \mu^m)(k^m + \mu^m)}{2c\mu^m(k^m + \mu^m) - (1 - c)\ (C_{66} - \mu^m)\ (k^m + 2\mu^m)}, \tag{14}$$

$$C^f_{11} - C^f_{66} = k^m + \frac{(k^m + \mu^m)(K - k^m)}{c(K + \mu^m) - (K - k^m)}, \tag{15}$$

$$\nu^f_{31} = \frac{\left[\dfrac{1 - c}{K^f} + \dfrac{c}{k^m} + \dfrac{1}{\mu^m}\right]\nu_{31} - (1 - c)\left[\dfrac{1}{K^f} + \dfrac{1}{\mu^m}\right]\nu^m}{c\left[\dfrac{1}{k^m} + \dfrac{1}{\mu^m}\right]}, \tag{16}$$

$$E^f_3 = \frac{1}{c}\,[E_3 - (1 - c)E^m] - \frac{4(1 - c)(\nu^f_{31} - \nu^m)^2}{\dfrac{1 - c}{K^f} + \dfrac{c}{k^m} + \dfrac{1}{\mu^m}}. \tag{17}$$

DISCUSSION

For the boron-aluminum composite, we consider the correspondence between observed C_{ij}'s and their counterparts predicted by three models: square-array, hexagonal-array, and random-distribution.

C_{33} is predicted reasonably well by all three models, although all are slightly high, perhaps reflecting the slight uncertainty in Young's modulus of the boron fibers.

C_{11} is predicted best by the lattice models, and C_{22} is predicted best by the random model. As shown in Fig. 2, this probably reflects the different imperfections in fiber distributions along the x_1 and x_2 directions.

C_{44} and C_{55}, which represent shears with the force parallel to the fibers, are not predicted accurately by the square-array model; but they are predicted well by both the hexagonal-array and the random models. Thus, these elastic constants permit one to distinguish fiber arrays that are transversely anisotropic (tetragonal, orthorhombic) from those that are transversely isotropic (hexagonal, random).

C_{66}, which represents shears with a force perpendicular to the fibers, is predicted well only by the random model. Since C_{66} represents also the velocity of a plane wave both propagated and polarized in the transverse plane, of all elastic constants it should be most sensitive to the fiber distribution. Thus, the different predictions for the hexagonal and random models, both of which are transversely isotropic, are not too surprising. Furthermore, Fig. 2 shows little evidence of either three-fold or six-fold symmetry around the fiber axis.

C_{12}, C_{13}, and C_{23}, the so-called off-diagonal elastic constants, are predicted surprisingly well by the random model. Since these constants are always determined indirectly, whether experimentally or theoretically, one expects larger errors than for the diagonal elastic constants, the C_{ii}'s discussed above. Absence of large discrepancies between observation and theory for these three elastic constants gives one simultaneous confidences in the experimental measurements and in the random-distribution model for this particular composite.

The bulk modulus,

$$B = \frac{1}{9} \sum_{i,j=1}^{3} C_{iijj}, \tag{18}$$

predicted by either the hexagonal model (1.103) or the full-random model (1.107) agrees well with observation (1.120). Since the bulk modulus includes six out of nine of the C_{ij}'s, barring fortuitous error cancellations, this observation-theory agreement within 1% also tends to establish the simultaneous credibility of both measurements and theory.

Results in column 4 of Table 4 show that the studied graphite fiber composites show orthotropic elastic symmetry, which is approximately transversely isotropic, which requires four C_{ij} interrelationships:

$$C_{11} = C_{22};\ C_{13} = C_{23};\ C_{44} = C_{55};\ C_{66} = (C_{11} - C_{12})/2. \tag{19}$$

The microstructure in Fig. 2 also suggests transverse-isotropic symmetry.

Concerning the first-guess graphite-fiber elastic-constant calculations, we see good agreement for C_{11}, C_{22}, and C_{33}; fair agreement for C_{13} and C_{23}; and poor agreement for C_{44}, C_{55}, C_{66}, and

C_{12}. Thus, the criterion of choosing a graphite-elastic-constant set based on E_3^f, the axial Young modulus, succeeds partially.

One can obtain a better, complete graphite-fiber elastic-constant set by using Eqs (13)–(17). From these five equations, the graphite-fiber elastic-constant results in column 5 of Table 4 differ significantly from the first-guess values in column 2. E_3^f is 3 percent lower than the first-guess value and 5 percent less than the fiber-manufacturer's estimate (235 GPa). Among all the calculated fiber-elastic-constant values, we have most confidence in E_3^f, which is well known to follow a linear rule-of-mixture. For the fibers (columns 2 and 5 in Table 4), the notable differences occur in the shear moduli: C_{44}^f and C_{55}^f differ by 25 percent and C_{66}^f by 30 percent. For transverse-isotropic symmetry, C_{44} is the torsional modulus T_3 around the x_3 axis—for fibers, an easily measured elastic constant. Thus, measuring T_3 and E_3 for fibers should provide useful information on fiber structure. That T_3 differs while E_3 is approximately the same suggests a structural difference not related to the orientation of hexagonal graphite unit cells in the fiber. We can compute the bulk modulus from Eq (18). For the first fiber we find 35.6 GPa, for the second 33.9 GPa. Reported graphite B values range from 34 to 210 GPa; and, from monocrystal measurements, theory predicts a possible range of 37 to 163 GPa [10]. Probably, the low B values for the present fibers reflect porosity or cracks.

After matching the graphite elastic constants to the measured composite elastic constants and recalculating the composite's properties, we should observe which composite C_{ij} constants differ most from observation. From Table 2, we see three: C_{22}, C_{13}, and C_{23}. C_{13} and C_{23} hardly surprise us because these indirect, off-diagonal elastic constants almost always present problems for both the experimentalist and theorist. The other off-diagonal elastic constant presents little problem in the transverse-isotropic-symmetry case because of the relationship $C_{66} = (C_{11} - C_{12})/2$, where we can both measure and calculate C_{11} and C_{66} directly. The C_{22} disagreement arises because we assumed that an orthotropic-symmetry material was approximately transversely isotropic.

CONCLUSIONS

Boron-aluminum

1. The random-fiber-distribution model predicts successfully the elastic constants of a laminated material. For the six principal C_{ij} ($C_{ij} = C_{ii}$, i = 1–6), theory and observation differ on average 2%.
2. The C_{66} elastic shear stiffness provides the most discriminating test of various fiber-distribution models. Conversely, the observed C_{66} provides the best gage of fiber distribution (square, hexagonal, random).
3. By applying of Eqs (13)–(17) we find that the boron fibers are nearly isotropic.

Graphite-magnesium

1. Graphite-fiber elastic constants chosen on the basis of the axial Young modulus, E_3, the most measurable fiber elastic constant,

lead to wrong composite-elastic-constant predictions, especially for the shear moduli C_{ii} (i = 4,5,6).

2. Graphite fibers with the same axial Young modulus, E_3, can possess different elastic constants, especially the torsional modulus $T_3 = C_{44}$.

3. For all considered fibers, the bulk modulus computed from the C_{ij} lies near or below graphite's lower bound.

It is also found from the model studies of both boron-fiber and graphite-fiber reinforced composites that by knowing the matrix and composite elastic constants, and by using the model inversely, we can calculate the anisotropic fiber elastic constants.

ACKNOWLEDGMENT

Specimens for study of graphite-fiber composites originated at the Toray Industries Composite Materials Laboratory in Otsu, Japan, where we thank especially T. Kyono and A. Kitamura. Dr. R.D. Kriz provided the computer program. S.A. Kim and M.W. Austin made painstaking measurements. Ming Lei, guest worker from the Institute of Metal Research, Shenyang, P.R. China, provided some calculations and a critical reading. S.K. Datta received support from the Office of Naval Research, grant N00014-86-K-0280.

REFERENCES

[1] Hashin, Z., "Analysis of a Composite Materials - A Survey," Journal of Applied Mechanics, Vol. 50, 1983, pp. 481–505.
[2] Christensen, R.M., "Mechanical Properties of Composite Materials," in Mechanics of Composite Materials, Pergamon, New York, 1983, p. 1.
[3] Sendeckyj, G.P., "Elastic Behavior of Composites," in Composite Materials, Vol. 2, 1974, pp. 45–83. Academic Press, New York.
[4] Walpole, L.J., "Elastic Behavior of Composite Materials: Theoretical Fundamentals," in Advances in Applied Mechanics, Vol. 21, 1981, pp. 169–242. Academic Press, New York.
[5] Bert, C.W., "Experimental Characterization of Composites," in Composite Materials, Vol. 8, 1975, pp. 73–133. Academic Press, New York.
[6] Datta, S.K., Ledbetter, H.M., and Kriz, R.D., "Calculated Elastic Constants of Composites Containing Anisotropic Fibers," Int. J. Solids and Str., Vol. 20, 1984, pp. 429–438.
[7] Bose, S.K. and Mal, A.K., "Longitudinal Shear Waves in a Fiber-reinforced Composite," Int. J. Solids and Str., Vol. 9, 1973, pp. 1075–1085.
[8] Bose, S.K. and Mal, A.K., "Elastic Waves in a Fiber-reinforced Composite," J. Mech. Phys. Solids, Vol. 22, 1974, pp. 217–229.
[9] Datta, S.K. and Ledbetter, H.M., "Elastic Constants of Fiber-reinforced Boron-Aluminum: Observation and Theory," Int. J. Solids and Str., Vol. 19, 1983, pp. 885–894.
[10] Hill, R., "Theory of Mechanical Properties of Fiber-reinforced Materials: In Elastic Behavior," J. Mech. Phys. Solids, Vol. 12, 1964, pp. 199–212.
[11] Achenbach, J.D., "Generalized Continuum Theories for Directionally Reinforced Solids," Arch. Thch., Vol. 28, 1976, pp. 257–278.

[12] Hlavacek, M., "A Continuum Theory of Fiber-reinforced composite," Int. J. Solids and Str., Vol. 11, 1975, pp. 199–211.

[13] Kitamura, A. and Kataoka, S., in Proceedings, International Carbon Conference (Bordeaux, France, July 1984), p. 216. Toray Data Sheet TY-111A (June 1983).

[14] Ledbetter, H.M. and Read, D.T., "Orthorhombic Elastic Constants of an NbTi/Cu Composite Superconductor," J. Appl. Phys., Vol. 48, 1977, pp. 1874–1879.

[15] Ledbetter, H.M., Frederick, N.V., and Austin, M.W., "Elastic-constant Variability in Stainless-steel 304," J. Appl. Phys., Vol. 51, 1980, pp. 305–309.

[16] Kriz, R.D. and Stinchcomb, M.W., "Elastic Moduli of Transversely Isotropic Graphite Fibers and Their Composites," J. Exper. Mech., Vol. 19, 1979, pp. 41–49.

[17] Hashin, Z. and Rosen, B.W., "The Elastic Moduli of Fiber-reinforced Materials," J. Appl. Mech., Vol. 31, 1964, pp.223–232.

[18] Hashin, Z., "Theory of Composite Materials," in Mechanics of Composite Materials, 1970, pp. 201–242. Academic Press, New York.

[19] Hermans, J.J., "The Elastic Properties of Fiber-reinforced Materials When the Fibers are Aligned," Proc. K. Ned. Akad. Wet, Vol. B70, 1967, pp. 1–9.

[20] Hashin, Z., "Analysis of Properties of Fiber Composites with Anisotropic Constituents," J. Appl. Mech., Vol. 46, 1979, pp. 546–550.

Hassel Ledbetter

MONOCRYSTAL—POLYCRYSTAL ELASTIC-CONSTANT MODELS

REFERENCE: Ledbetter, Hassel, "Monocrystal—Polycrystal Elastic-Constant Models," Dynamic Elastic Modulus Measurements in Materials, ASTM STP 1045, Alan Wolfenden, editor, American Society for Testing and Materials, Philadelphia, 1990.

ABSTRACT: Considering only cubic symmetry (three independent monocrystal elastic-stiffness coefficients, C_{ij}), we review various models for converting the C_{ij} to the effective macroscopic quasiisotropic and homogeneous elastic constants, usually taken as B, the bulk modulus, and G, the shear modulus. To test the models, we consider a typical metal: copper, which possesses a moderate Zener elastic-anisotropy ratio, 3.19, and which was measured by pulse-echo dynamic (MHz) methods. We find that the Hershey—Kröner—Eshelby, and equivalent, models work best. We ignore models that lack a physical basis. Using the H-K-E model, we calculate the effective polycrystalline elastic constants of twenty-five cubic elements.

KEYWORDS: bulk modulus, elastic constants, monocrystal-polycrystal relationships, physical properties, Poisson ratio, shear modulus, Young modulus.

INTRODUCTION

The problem of averaging monocrystal elastic coefficients C_{ij} to obtain engineering elastic constants such as Young modulus, shear modulus, and Poisson ratio is important in science and in technology. Despite much work on the problem, no final solution exists. Historically, methods proposed by Voigt [1] and Reuss [2] are important. Practically, methods suggested by Hill [3] enjoy wide use because they offer computational simplicity and acceptable agreement with measurement. A 'best' averaging method is sought mainly because (i) we can calculate more reliable values of polycrystalline elastic constants from monocrystal results, and

Dr. Ledbetter is a research metallurgist at NIST (formerly NBS), Boulder, Colorado 80303.

(ii) we can better understand polycrystalline-aggregate stress-strain states. Some previous reviews on this subject include those by Hearmon [4], Watt and coworkers [5], and Hashin [6].

All the averaging methods described here share common assumptions: (i) small grain-to-specimen sizes; (ii) absence of voids, nonhomogeneities, and so on; (iii) cohesion of crystallites occurs through very thin grain-boundary regions that are deformed relative to the crystal interiors; (iv) randomly oriented grains; and (v) grains large enough so that interfaces remain nonimportant. In fact, for most purposes, these assumptions apply fairly well to many polycrystalline aggregates.

Tensors provide a natural, elegant way to describe a crystal's physical properties. Here, we shall consider a fourth-rank tensor, which represents the elastic stiffness C_{ijkl}, which relates a field tensor, stress σ_{ij}, to a matter tensor, strain ϵ_{kl}, through a generalized Hooke's law:

$$\sigma_{ij} = C_{ijkl}\ \epsilon_{kl}. \qquad (1)$$

Alternatively, we can invert Eq (1) to show the elastic-compliance tensor S_{ijkl}:

$$\epsilon_{ij} = S_{ijkl}\ \sigma_{kl}. \qquad (2)$$

Depending on crystal symmetry, the C_{ijkl} tensor contains up to twenty-one independent components. We shall limit the present discussion to cubic symmetry with only three independent components. Voigt [1] chose the following set:

$$C_{1111} = C_{11} \qquad (3)$$
$$C_{1122} = C_{12} \qquad (4)$$
$$C_{2323} = C_{44}. \qquad (5)$$

Here, the two-index C_{ij} represent the usual Voigt four-to-two contraction scheme, where the two-index C_{ij} are not tensor components [7]. We can choose other sets of cubic-symmetry C_{ij}.

For example, Zener [8] chose the following three:

$$C = C_{44} \qquad (6)$$
$$C' = 1/2\ (C_{11}-C_{12}) \qquad (7)$$
$$B = 1/3\ (C_{11}+2C_{12}). \qquad (8)$$

All of Zener's C_{ij} relate to simple stress-strain combinations. C_{44} represents resistance to shear on a (100) plane in a [100] direction. Similarly, C' represents (110) [$\bar{1}$10] shear resistance. B represents the bulk modulus, or reciprocal compressibility. We often define a dimensionless ratio

$$A = C/C'. \qquad (9)$$

This represents a cubic crystal's elastic-shear anisotropy. We can show that C and C' represent upper and lower bounds on a crystal's shear resistance. If a material is isotropic, the shear resistance depends neither on shear plane nor on shear direction; thus A = 1. For Zener's elastic constants, the stiffnesses and compliances are symmetrical:

$$C_{44} = S_{44}^{-1} \tag{10}$$
$$C_{11} - C_{12} = (S_{11} - S_{12})^{-1} \tag{11}$$
$$C_{11} + 2C_{12} = (S_{11} + 2S_{12})^{-1}. \tag{12}$$

There arises the following question: how do the monocrystal C_{ij} relate to the two independent elastic constants of a quasiisotropic material? The usual example is a nontextured polycrystal, which exhibits perfect disorder, as described by Kröner [9].

For cubic symmetry, Eqs 8 and 12 show that the bulk modulus is known unambiguously. All averaging methods must contain Eq 8 because B is a rotational invariant, independent of coordinate system. The remaining problem then is to estimate another quasiisotropic elastic constant, usually the shear modulus $G(C_{ij})$.

As emphasized first by Stokes [10], the natural choice for two random-polycrystal elastic constants is the bulk modulus B and the shear modulus G, which represent extreme deformation cases: volume change without shape change and, conversely, shape change without volume change. For pure dilatation, Hooke's law becomes

$$\sigma = -P = B(\Delta V/V). \tag{13}$$

Here, P denotes pressure and V volume. For pure shear, Hooke's law becomes

$$\tau = G\gamma. \tag{14}$$

Here, τ denotes shear stress and γ shear strain. For isotropic materials, the shear modulus equals the torsion modulus [11].

Thus, the problem is clear, how do B and G depend on the three C_{ij}: C_{11}, C_{12}, and C_{44}? Many famous physicists addressed this seemingly simple question. Despite intense, varied efforts, this crystal-physics problem retains high interest. Herein, we shall describe some of the solutions and compare them with observation. We shall not consider all models, but altogether a sufficient number: nine. We shall omit any model that contains questionable physics or resorts purely to calculation-measurement agreement (lacks a physical basis). We begin with a chronological order.

Voigt's Method

Voigt [1] gave the first solution to the $G(C_{ij})$ problem, and a good summary occurs in his famous Lehrbuch der Kristallphysik. Voigt assumed that in a polycrystal strain is constant and the effective stress is

$$\langle\sigma_{ij}\rangle = 1/8\pi^2 \int \sigma_{ij}(\Omega)\, d\Omega. \tag{15}$$

And that the effective elastic stiffness is

$$<C_{ijkl}> = 1/8\pi^2 \int C_{ijkl}(\Omega)\ d\Omega. \qquad (16)$$

Here, Ω denotes the solid angle subtended by the Euler angles θ, ϕ, ψ and $\int d\Omega = 8\pi^2$. From this view

$$G = <C_{44}> = <\tfrac{1}{2}\ (C_{11}-C_{12})>. \qquad (17)$$

And, we can calculate by using the usual coordinate transformation for a fourth-rank tensor:

$$C'_{ijkl} = a_{im}a_{jn}a_{ko}a_{lp}C_{mnop} \qquad (18)$$

$$C'_{2323} = C_{44} + (C_{11}-C_{12}-2C_{44})(a_{21}{}^2a_{31}{}^2+a_{22}{}^2a_{32}{}^2+a_{23}{}^2+a_{33}{}^2). \qquad (19)$$

Here, the a_{ij} denote direction cosines connecting "new" and "old" coordinate systems [12]. The a_{ij} relate to Euler coordinates according to

$$a_{21} = -\cos\theta\cos\phi\sin\psi - \sin\phi\cos\psi \qquad (20)$$
$$a_{22} = \cos\phi\cos\psi - \sin\phi\sin\psi\cos\theta \qquad (21)$$
$$a_{23} = \sin\theta\sin\psi \qquad (22)$$
$$a_{31} = \cos\phi\sin\theta \qquad (23)$$
$$a_{32} = \sin\phi\sin\theta \qquad (24)$$
$$a_{33} = \cos\theta. \qquad (25)$$

Thus,

$$G = <C_{44}> = <C_{44}'> = \int_0^{2\pi} \frac{d\psi}{2\pi} \int_0^{2\pi} \frac{d\phi}{2\pi} \int_0^{\pi} \frac{C_{44}'\sin\theta d\theta}{2} \qquad (26)$$

$$= C_{44} + \frac{(C_{11}-C_{12}) + 3C_{44}}{5} \qquad (27)$$

$$G^{(1)} = G_V = (1/5)(C_{11}-C_{12} + 3C_{44}). \qquad (28)$$

This represents a simple linear combination of Zener's C' and C: $\tfrac{1}{2}(C_{11}-C_{12})$ and C_{44}, favoring the latter by a ratio of 3:2. Equation 28 shows that for elastic isotropy

$$G^{(1)} = G_V = C_{44} = (\tfrac{1}{2})(C_{11}-C_{12}). \qquad (29)$$

The notation $G^{(1)}$ means a first-order upper bound. This bound is correct to the first order of the anisotropy constant, $C_{11}-C_{12}-2C_{44}$, which vanishes for isotropy.

Reuss Method

Voigt's solution remained unquestioned for forty years. In 1929, Reuss [2] suggested an obvious alternative: assume that stress is constant and effective strain is

$$<\epsilon_{ij}> = 1/8\pi^2 \int \epsilon_{ij}(\Omega)\ d\Omega. \qquad (30)$$

And that the effective elastic compliance is

$$\langle S_{ijkl}\rangle = 1/8\pi^2 \int S_{ijkl}(\Omega)\, d\Omega. \tag{31}$$

Similar to Voigt's approach, this leads to

$$\frac{5}{G_R} = \frac{4}{C_{11}-C_{12}} + \frac{3}{C_{44}} = \frac{5}{G_{(1)}} . \tag{32}$$

The notation $G_{(1)}$ means lower first-order bound. Also, this bound is correct to the first order of $C_{11}-C_{12}-2C_{44}$.

We call $G_V = G^{(1)}$ and $G_R = G_{(1)}$ first-order bounds. They improve considerably the zeroeth-order bounds: C_{44} and $\frac{1}{2}(C_{11}-C_{12})$. Comparing the Voigt and Reuss methods shows that an averaging procedure produces different results depending on whether we average a tensor or its inverse.

Huber-Schmid-Boas Method

In the 1930s Huber and Schmid [13] proposed a method elaborated by Boas [14–17]. Subsequently, researchers frequently refer to the Huber-Schmid-Boas method, failing to distinguish them. The Huber-Schmid method gives results between the Voigt and Reuss, in good agreement with observation for the few cases they considered. Owing probably to their computational complexity, and perhaps also to their limited access by English readers, these methods appear seldomly in recent research. Brief accounts of the Huber-Schmid method have been given in English by Schmid and Boas [18], Stadelmaier [19], and Hill [3]. The Boas method has been described briefly in English by Boas [18]. Kröner [20] commented on both these methods, among others.

In addition to the five assumptions listed in the introduction, Huber and Schmid made two additional assumptions: (i) individual crystallites behave completely independently of neighboring crystallites (crystallites respond only to external macroscopic forces); and (ii) the averaging problem proceeds independently of macroscopic specimen geometry (to solve the problem, Huber and Schmid assumed a circular cylinder).

Like Reuss, Huber and Schmid assumed constant stress, satisfying the mechanical-equilibrium conditions

$$\sum_j \partial\sigma_{ij}/\partial x_j = 0. \tag{33}$$

Here, σ_{ij} = stress tensor and x_j = spatial coordinate. However, they proposed that the spatial integration should be carried out for reciprocal strains, or, equivalently, for reciprocal elastic compliances. Thus,

$$G = \langle G\rangle = \frac{1}{N} \sum_{\alpha=1,N} G'_\alpha = \frac{1}{\Omega_0} \int G'_\alpha(S_{ij}, \Omega)\, d\Omega$$

$$= \frac{1}{\Omega_0} \int \frac{1}{S'_{44_\alpha}} (S_{ij}, \Omega)\, d\Omega. \tag{34}$$

Here, the index α indicates one of many of N orientations. Equation 34 represents only an alternative averaging scheme for the elastic compliances S_{ij} and possesses no unique physical basis.

To solve Eq 34, Huber and Schmid assumed a circular-cylinder specimen with forces acting only on the base faces. They obtained a converging series solution for cubic symmetry and a closed-form solution for hexagonal symmetry. Boas [15] obtained a series solution for tetragonal symmetry and applied the results to tin. Each case of interest requires complicated calculations.

As Hill [3] pointed out, the Huber-Schmid method amounts to assuming that within each crystallite the stress is pure tension or pure torsion acting along a direction fixed with respect to the specimen axis. One defines a general modulus for that direction, and averages that modulus over all possible crystal orientations.

In comparisons made below, we obtained the effective shear modulus by numerically averaging the reciprocal torsion modulus [16]:

$$\frac{1}{G} = \frac{1}{2}(S'_{44} + S'_{55}) - \frac{\frac{1}{2}(S'^{2}_{34} + S'^{2}_{35})}{S'_{33}} . \tag{35}$$

Equation 35 extends the Huber-Schmid approach by considering the restrained bending that tends to occur when we twist crystals along a general (nonsymmetry) direction.

Hill Methods

In 1952, Hill [3] published an important thermodynamic strain-energy study that established the Voigt and Reuss results as first-order bounds on the shear modulus. (Zeroeth-order bounds are C_{44} and C'.)

$$G_V \geq G \geq G_R . \tag{36}$$

Inequality 36 is valid for all symmetries. In the case of cubic symmetry,

$$G_V - G_R = \frac{3}{5} \frac{[2C_{44} - (C_{11}-C_{12})]^2}{[4C_{44} + 3(C_{11}-C_{12})]} = \frac{3(A-1)^2}{5A(2A+3)} C_{44} . \tag{37}$$

Here, $A = 2C_{44}/(C_{11}-C_{12})$ denotes Zener anisotropy. Hill concluded that, without further information, we should proceed by assuming either an arithmetic mean

$$G = (\tfrac{1}{2})\ (G_V + G_R) \tag{38}$$

or a geometric mean

$$G = (G_V G_R)^{\frac{1}{2}} . \tag{39}$$

We can show that the arithmetic mean always exceeds the geometric.

Kröner Method

In 1958, Kröner [20] reconsidered the averaging problem from the viewpoint of a self-consistent elastic-inclusion model. He used ideas developed by Eshelby [21] combined with the concept of elastic polarizability. Kröner obtained a quartic equation equivalent to the cubic equation:

$$G^3 + \alpha G^2 - \beta G - \gamma = 0 \tag{40}$$

Here,

$$\alpha = (45\kappa + 20\nu)/40 \tag{41}$$
$$\beta = 3\mu\ (\kappa + 4\nu)/8 \tag{42}$$
$$\mu = C_{44} \tag{43}$$
$$\nu = (C_{11}-C_{12})/2 = C' \tag{44}$$
$$\kappa = (1/3)(C_{11} + 2C_{12}) = B. \tag{45}$$

Later, Gairola and Kröner [22] showed that one can write the solution to Eq 40 as

$$G = \frac{a_2G_0^2+\beta_2G_0+\gamma}{G_0^2+a_1G_0+\beta_1}\ . \tag{46}$$

Here,

$$a_1 = (45\kappa+24\mu+36\nu)/40 \tag{47}$$
$$a_2 = (2\nu+3\mu)/5 = G_V \tag{48}$$
$$\beta_1 = 3\kappa(2\mu+3\nu)/20 \tag{49}$$
$$\beta_2 = 3(6\kappa\nu+9\kappa\mu+20\mu\nu)/40 \tag{50}$$
$$\gamma = 3\kappa\mu\nu/4. \tag{51}$$

We can solve Eq 46 iteratively by starting with almost any guess for G_0. Inserting $G_0 = \infty$ yields $G = G_V$. Inserting $G_0 = 0$ yields $G = G_R$.

Eshelby [23] discussed the quartic–cubic-equation relationship and the equivalence of Kröner's result to one obtained by Hershey [24]. (Eshelby's Eq 6.15 needs a 2 inserted as a multiplier in the last term.) Below, we call this average the Hershey–Kröner–Eshelby average.

Hashin-Shtrikman Method

Using variational principles, Hashin and Shtrikman [25] derived upper and lower bounds that improve those of Voigt and Reuss. Following Gairola and Kröner [22], we write these bounds as $(\mu>\nu)$

$$G_2^{(u)} = G_{HS}^{(u)} = \frac{\mu(48\kappa\nu+27\kappa\mu+76\mu\nu+24\mu^2)}{18\kappa\nu+57\kappa\mu+36\mu\nu+64\mu^2} \tag{52}$$

$$G_2(l) = G_{HS}(l) = \frac{\nu(57\kappa\mu+18\kappa\nu+84\mu\nu+16\nu^2)}{12\kappa\mu+63\kappa\nu+24\mu\nu+76\nu^2} \tag{53}$$

If $\nu > \mu$, then the upper and lower bounds interchange.

Kröner Bounds

Using variational principles, Kröner and Koch [26] derived improved third-order bounds. Again using expressions given by Gairola and Kröner [22], these bounds are

$$G^{(3)} = G_K^{(u)} = \frac{\mu\nu(258\kappa+396\mu+264\nu)+81\kappa\mu^2+108\mu^3+36\kappa\nu^2+32\nu^3}{252\mu\nu+195\kappa\mu+144\mu^2+180\kappa\nu+104\nu^2} \qquad (54)$$

$$G_{(3)} = G_{K(l)} = \frac{\mu\nu(540\kappa\nu^2+945\kappa\mu\nu+1300\mu\nu^2+390\kappa\mu^2+1200\mu^2\nu)}{\mu\nu(999\kappa\nu+540\nu^2+666\kappa\mu+1720\mu\nu+240\mu^2)+48\kappa\mu^3+162\kappa\nu^3}. \qquad (55)$$

Higher-Order Bounds

For most materials, for most practical purposes, bounds higher than third-order are unnecessary; third-order bounds are sufficiently close. For copper, for example, third-order shear moduli differ by only 48.54/47.61, or about 2%. (Using existing methods, we can measure shear moduli, with little difficulty, to about 0.2%.) For cubic symmetry, we can calculate bounds of arbitrarily high order by using the Gairola–Kröner formula [22].

Highly anisotropic materials can have very different third-order bounds. For example, Gairola and Ledbetter [27] calculated bounds for graphite. For the shear modulus, third-order bounds differ by 108.2/12.9, a factor of 8! But, graphite represents an extreme case: the most anisotropic material ever measured.

Aleksandrov Method

Aleksandrov [28] focused on the C_{ijkl} invariants. There exist two linear invariants:

$$I_1^{(1)} = \Sigma\, C_{iikk} = 9B \qquad (i,k = 1,3) \qquad (56)$$

and

$$I_1^{(2)} = \Sigma\, C_{iiii} + \Sigma_{i\neq k} C_{ikik} = 3(C_{11}+2C_{44}). \qquad (i,k = 1,3) \qquad (57)$$

The first linear invariant leads to the bulk modulus B, and the second linear invariant leads to the sum of the three ρv^2 values, where ρ denotes mass density and v sound velocity. However, the second linear invariant fails to produce an unambiguous expression for G: $(C_{11}+2C_{44})$ gives the Voigt result while $(S_{11}+2S_{44})$ gives the Reuss result, as noted by Leibfried [29].

Aleksandrov obtained an unambiguous solution by considering the sixth-order invariant obtained after converting the C_{ijkl} to the Voigt C_{ij} and finding the determinant:

$$I_6 = (C_{11}+2C_{12})\, C_{44}^3\, (C_{11}-C_{12})^2 \tag{58}$$

$$= 12B\, C_{44}^3 C'^2 = 12BA^5 C_{44}^5. \tag{59}$$

Here, C' and A are defined in Eqs 7 and 9.

For a quasiisotropic material

$$I_6^0 = 12BG^5. \tag{60}$$

Thus, equating I_6 and I_6^0 gives

$$G = C_{44}^{\frac{3}{5}}\, C'^{\frac{2}{5}} = C_{44} A^{-\frac{2}{5}}. \tag{61}$$

Whereas the Voigt result averages C_{44} and C' arithmetically with the weights $\frac{3}{5}$ and $\frac{2}{5}$, Alexandrov's result represents a geometric average with the same weights.

Ledbetter–Naimon Method

To obtain G, Ledbetter and Naimon [30] considered the acoustic Debye characteristic temperature Θ_D. They assumed that

$$\Theta_D(\text{polycrystal}) = \Theta_D(\text{monocrystal}). \tag{62}$$

This means that grain boundaries contribute nothing to elastic stiffness (softness) or to specific heat. We can calculate the acoustic Debye temperature from

$$\Theta = \frac{h}{k}\left[\frac{3}{4\pi V_a}\right]^{\frac{1}{3}} v_m. \tag{63}$$

Here, h and k denote the Planck and Boltzmann constants, V_a atomic volume, and v_m mean sound velocity:

$$\frac{3}{v_m^3} = \frac{1}{v_l^3} + \frac{2}{v_t^3}\ . \tag{64}$$

For the monocrystal, we obtain v_m from

$$v_m = \left[\frac{1}{12\pi}\int \sum_{i=1,3} v_i^{-3}\, d\Omega\right]^{-\frac{1}{3}}. \tag{65}$$

The v_i $(i = 1,2,3)$ represent the three roots of the Christoffel equations. Then we obtain G by solving iteratively the following equation:

$$v_m^{-3} = \frac{1}{3}\rho^{\frac{3}{2}}\left[(B+\tfrac{4}{3}G)^{-\frac{3}{2}} + 2G^{-\frac{3}{2}}\right]. \tag{66}$$

An Example Material: Copper

We consider copper because it represents a typical metal, exhibits moderate Zener anisotropy ($A = 3.19$), and possesses well-known elastic constants, both polycrystal and monocrystal. At $T = 295$ K, Ledbetter [31] reported $B = 138.9$ and $G = 47.9$ GPa. From a survey of eighteen monocrystal measurements, Ledbetter and Naimon [30] recommended $C_{11} = 169.6$, $C_{12} = 122.4$, and $C_{44} = 75.4$ GPa.

Table 1 shows the averaging results obtained by all the methods described above, including third-order bounds. We find a calculated bulk modulus of 138.1, within 0.6% of observation, not shown in the table.

The averaging method giving closest agreement with observation is the Hershey–Kröner–Eshelby method: 48.3 versus 47.9 GPa observed, a difference of 0.8%.

TABLE 1 – Copper's polycrystalline shear modulus (G) calculated with various models, units 10^{11} N/m^2.

Method	Shear Modulus
Voigt	0.5468
Hashin–Shtrikman$^{(u)}$	0.4951
Kröner$^{(u)}$	0.4862
Hershey–Kröner–Eshelby	0.4825
Kröner$_{(l)}$	0.4770
Hill (arithmetic)	0.4741
Hill (geometric)	0.4738
Aleksandrov	0.4682
Hashin–Shtrikman$_{(l)}$	0.4606
Huber–Schmid–Boas	0.4413
Reuss	0.4015
Observed	0.479

Cubic Elements

For twenty-five cubic elements, Table 2 gives elastic-constant-average results by the Hershey–Kröner–Eshelby method. The table includes the monocrystal elastic constants (C_{ij}), mass density (ρ), Zener elastic anisotropy (A), bulk modulus (B), Young modulus (E), shear modulus (G), Poisson ratio (ν), longitudinal sound velocity (v_l), and transverse sound velocity (v_t). At the far right, we show a source code for the C_{ij}; thus 66HG means that silver's C_{ij} were measured in 1966 by Hiki and Granato. Because the C_{ij} sources occur in many handbooks, for example [32,33], we omitted the twenty-five references.

. TABLE 2 - Monocrystal and polycrystal elastic constants of cubic elements.

Element	C_{11}	C_{12}	C_{44}	ρ	A	B	E	G	ν	v_ℓ	v_t	C_{ij} Source
		(10^{11}N/m^2)		(g/cm^3)			(10^{11}N/m^2)			(cm/μs)		
Ag	1.2220	0.9070	0.4540	10.500	2.88	1.0120	0.8249	0.3024	0.3641	0.3671	0.1697	66HG
Al	1.0675	0.6041	0.2834	2.697	1.22	0.7586	0.7038	0.2616	0.3454	0.6408	0.3114	68T
Au	1.9290	1.6380	0.4150	19.300	2.85	1.7350	0.7949	0.2792	0.4236	0.3304	0.1203	66HG
C	10.7600	1.2500	5.7580	3.512	1.21	4.4200	11.4095	5.3327	0.0698	1.8119	1.2322	57MB
Cr	3.5000	0.6780	1.0080	7.200	0.71	1.6187	2.7954	1.1530	0.2122	0.6621	0.4002	63BD
Cu	1.6960	1.2240	0.7540	8.930	3.20	1.3813	1.2965	0.4825	0.3436	0.4762	0.2324	74LN
Fe	2.3140	1.3470	1.1640	7.872	2.41	1.6693	2.1236	0.8244	0.2880	0.5930	0.3236	66RS
Ge	1.2853	0.4826	0.6680	5.323	1.66	0.7502	1.3166	0.5452	0.2075	0.5268	0.3200	63MA
Ir	5.9947	2.5582	2.6882	22.520	1.56	3.7037	5.6121	2.2494	0.2475	0.5456	0.3160	65PH
K	0.0370	0.0314	0.0188	0.851	6.71	0.0333	0.0260	0.0095	0.3698	0.2323	0.1056	65SS
Li	0.1350	0.1144	0.0878	0.533	8.52	0.1213	0.1107	0.0410	0.3479	0.5748	0.2776	61TS
Mo	4.6370	1.5780	1.0920	10.228	0.71	2.5977	3.2318	1.2501	0.2926	0.6457	0.3496	67DA
Na	0.0739	0.0622	0.0419	0.971	7.16	0.0661	0.0561	0.0207	0.3585	0.3106	0.1459	60D
Nb	2.4019	1.2558	0.2822	8.570	0.49	1.6378	1.0492	0.3765	0.3932	0.4997	0.2096	66A
Ni	2.4810	1.5490	1.2420	8.910	2.67	1.8597	2.2064	0.8471	0.3023	0.5792	0.3083	65EC
Pb	0.4966	0.4231	0.1498	11.344	4.08	0.4476	0.2506	0.0891	0.4067	0.2234	0.0886	69MS
Pd	2.2710	1.7604	0.7173	12.038	2.81	1.9306	1.3378	0.4831	0.3845	0.4625	0.2003	60R
Pt	3.4670	2.5070	0.7650	21.500	1.59	2.8270	1.7773	0.6369	0.3952	0.4135	0.1721	65M
Pu	0.3628	0.2673	0.3359	15.750	7.03	0.2991	0.4115	0.1619	0.2707	0.1808	0.1014	76LM
Rb	0.0289	0.0245	0.0164	1.560	7.45	0.0260	0.0218	0.0080	0.3603	0.1532	0.0716	67GT
Si	1.6578	0.6394	0.7962	2.331	1.56	0.9789	1.6291	0.6662	0.2226	0.8950	0.5346	64MA
Ta	2.6023	1.5446	0.8255	16.626	1.56	1.8972	1.8514	0.6922	0.3374	0.4118	0.2040	66S
Th	0.7530	0.4890	0.4780	11.694	3.62	0.5770	0.7463	0.2905	0.2844	0.2872	0.1576	66A
V	2.2870	1.1900	0.4315	6.022	0.79	1.5557	1.2939	0.4752	0.3614	0.6029	0.2809	61B
W	5.2239	2.0437	1.6083	19.257	1.01	3.1038	4.0983	1.6010	0.2799	0.5216	0.2883	67LG

Summary

1. The monocrystal–polycrystal physical-property problem remains of great interest in crystal physics.

2. Being a fourth-rank tensor, C_{ijkl}, the elastic stiffness presents a particularly difficult monocrystal–polycrystal problem.

3. Because elastic coefficients relate to a wide variety of solid-state-physics problems and stress-strain phenomena, many various averaging methods exist.

4. Among all methods considered, the Hershey–Kröner–Eshelby model agrees best with observation.

5. For cubic symmetry, the bulk modulus is given by $B = \frac{1}{3}(C_{11}+2C_{12})$. Neither theory nor observation dispute this relationship, which arises because $(C_{11}+2C_{12})$ is a rotational invariant.

6. Considering copper, a moderately anisotropic material, we find that third-order (Kröner) shear-modulus bounds differ by only about 2%, while the zeroeth-order bounds differ by a factor of 3.2.

7. For cubic symmetry, a simple formula given by Gairola and Kröner [22] allows us to calculate both even and odd bounds to any order, n. When n becomes large, the bounds converge to Kröner's [20] self-consistent solution.

8. For perfectly disordered aggregates, Kröner proved that the self-consistent method is exact. For other aggregates, there exist formally exact solutions [34]. However, these solutions are too complicated, even for modern computers.

Acknowledgments

The author profited from interactions with B. Gairola and especially E. Kröner, both at the University of Stuttgart. M. Lei, visiting scientist from Institute of Metal Research (Shenyang), helped with calculations.

References

[1a] Voigt, W., "Ueber die Beziehung zwischen den beiden Elasticitätsconstanten isotroper Körper," Annalen der Physik, Vol. 38, 1989, pp. 573–587.

[1b] Voigt, W., Lehrbuch der Kristallphysik, Teubner, Leipzig, 1928, pp. 954–964.

[2] Reuss, A., "Berechnung der Fliessgrenze von Mischkristallen auf Grund der Plastizitätsbedingung für Einkristalle," Zeitschrift für Angewandte und Mathematik und Mechanik, vol. 9, 1929, pp. 49–58.

[3] Hill, R., "The Elastic Behavior of a Crystalline Aggregate," Proceedings of the Physical Society, vol. A65, 1952, pp. 349–354.

[4] Hearmon, R.F.S., "The Elastic Constants of Polycrystalline Aggregates," in Physics of the Solid State, Academic, New York, 1969, pp. 401–414.

[5] Watt, J.P., Davies, G.F., and O'Connell, R.J., "The Elastic Properties of Composite Materials," Reviews of Geophysics and Space Physics, vol. 14, 1976, pp. 541–563.

[6] Hashin, Z., "Analysis of Composite Materials. A Survey", Transactions, American Society of Mechanical Engineers: Journal of Applied Mechanics, vol. 50, 1983, pp. 481–505.

[7] Nye, J.F., Physical Properties of Crystals: Their Representation by Tensors and Matrices, Oxford, London, 1960, p. 134.

[8] Zener, C., Elasticity and Anelasticity of Metals, U. Chicago Press, Chicago, 1948, p. 16.

[9] Kröner, E., "Self-consistent scheme and graded disorder in polycrystal elasticity," Journal of Physics F: Metal Physics, vol. 8, 1978, pp. 2261–2267.

[10] Stokes, G.G., Mathematical and Physical Papers, Volume 1, Cambridge U.P., Cambridge, 1880, p. 120. Presented to Cambridge Philosophical Society in 1845.

[11] Hearmon, R.F.S., An Introduction to Applied Anisotropic ELasticity, Oxford U.P., London, 1961, p. 51.

[12] Reference [7], pp. 9–14.

[13] Huber, A. and Schmid, E., "Bestimmung der elastischen Eigenschaften quasiisotroper Vielkristalle durch Mittelung," Helvetica Physica Acta, vol. 7, 1934, pp. 620–627.

[14] Boas, W. and Schmid, E., "Zur Berechnung physikalischer Konstanten quasiisotroper Vielkristalle," Helvetica Physica Acta, vol. 7, 1934, pp. 628–632.

[15] Boas, W., "Zum elastischen Verhalten von Zinn-Ein- und Vielkristallen," Helvetica Physica Acta, vol. 7, 1935, pp. 878–883.

[16] Boas, W., "Zur Berechnung des Torsionmoduls quasiisotroper Vielkristalle aus den Einkristallkonstanten," Helvetica Physica Acta, vol. 8, 1935, pp. 674–681.

[17] Boas, W., "Die Berechnung von Eigenschaften technischer Werkstücke aus Einkristallkonstanten und Kristallitordnung," Schweizer Archiv für Angewandte Wissenschaft und Technik, vol. 1, No. 12, 1935, pp. 257–264.

[18a] Schmid, E. and Boas, W., Kristallplastizität mit besonderer Berücksichtigung der Metalle, Springer, Berlin, 1935, section 81. English translation: Plasticity of Crystals, Hughes, London, 1950.

[18b] Boas, W., Physics of Metals and Alloys, Melbourne U.P., Victoria, 1947, pp. 94–100.

[19] Stadelmaier, H.H., "Some Notes on the Relation Between the Elastic Moduli of Anisotropic Cristallites and Quasiisotropic Polycrystalline Aggregates," Zeitschrift für Angewandte Mathematik und Physik, vol. 6, 1955, pp. 246–252.

[20] Kröner, E., "Berechnung der elastischen Konstanten der Vielkristalls aus den Konstanten des Einkristalls," Zeitschrift für Physik, vol. 151, 1958, p. 504–518.

[21] Eshelby, J.D., "The determination of the elastic field of an ellipsoidal inclusion, and related problems," Proceedings of the Royal Society (London), vol. A241, 1957, pp. 376–388.

[22] Gairola, B.K.D. and Kröner, E., "A Simple Formula for Calculating the Bounds and the Self-Consistent Value of the Shear Modulus of a Polycrystalline Aggregate of Cubic Crystals," International Journal of Engineering Science, vol. 19, 1981, pp. 865–869.

[23] Eshelby, J.D., "Elastic Inclusions and Inhomogeneities," in Progress in Solid Mechanics, Volume 2, North-Holland, Amsterdam, pp. 130–133.

[24] Hershey, A.V., "The Elasticity of an Isotropic Aggregate of Anisotropic Cubic Crystals," Journal of Applied Mechanics, vol. 21, 1954, pp. 236–240.

[25] Hashin, Z. and Shtrikman, S., "On Some Variational Principles in Anisotropic and Nonhomogeneous Elasticity," Journal of the Mechanics and Physics of Solids, vol. 10, 1962, pp. 335–342.

[26] Kröner, E. and Koch, H., "Effective Properties of Disordered Materials," SM Archives, vol. 1, 1976, pp. 183–238.

[27] Gairola, B.K.D. and Ledbetter, H.M., "Elastic constants of random polycrystalline graphite," nonpublished research, NIST, 1988.

[28] Aleksandrov, K.S., "Average Values of Tensor Quantities," Soviet Physics-Doklady, vol. 10, 1966, pp. 893–895.

[29] Leibfried, G., "Versetzungen in anisotropem Material," Zeitschrift für Physik, vol. 135, 1953, pp. 23–43.

[30] Ledbetter, H.M. and Naimon, E.R., "Relationship between single-crystal and polycrystal elastic constants," Journal of Applied Physics, vol. 45, 1974, pp. 66–69.

[31] Ledbetter, H.M., "Sound velocities and elastic-constant averaging for polycrystalline copper," Journal of Physics D: Applied Physics, vol. 13, 1980, pp. 1879–1884.

[32] Simmons, G. and Wang, H., Single Crystal Elastic Constants and Calculated Aggregate Properties: A Handbook, MIT Press, Cambridge, 1971.

[33] Hearmon, R.F.S., in Landolt-Börnstein Numerical Data and Functional Relationships in Science and Technology, New Series, Group III, Volumes 11 and 18, Springer, 1979.

[34] Dederichs, P.H. and Zeller, R., "Variational treatment of the elastic constants of disordered materials," Zeitschrift für Physik, vol. 259, 1973, pp. 103–116.

Steve H. Carpenter

DETECTION OF THE INITIATION AND GROWTH OF CRACKS USING PRECISION, CONTINUOUS MODULUS MEASUREMENTS

REFERENCE: Carpenter, S. H., "Detection of the Initiation and Growth of Cracks Using Precise, Continuous Modulus Measurements," Symposium on Dynamic Elastic Modulus Measurements in Materials, ASTM STP 1045, Alan Wolfenden, Editor, American Society for Testing and Materials, Philadelphia, 1990

ABSTRACT: The use of precision, continuous modulus measurements to detect the initiation and growth of cracks in a number of experimental conditions will be reported on. The nucleation of cracks in a material will cause a decrease in the elastic modulus of that material. Correlation between the initiation and growth of cracking with a simultaneous decrease in modulus have been obtained. Modulus measurements have been carried out using a modified composite Marx oscillator with specially designed samples. The modulus was calculated from the resonant frequency of the composite oscillator. Comparisons of experimental data with theoretical treatments given in the literature will be provided.

KEYWORDS: crack detection, crack growth, modulus measurements, stress corrosion cracking, cathodic charging, exfoliation

The purpose of this paper is to present results from a number of experiments which have been carried out to demonstrate the viability of using continuous modulus measurements to detect and study the nucleation and growth of cracks in test samples. Results from three separate experiments will be presented. Some information on two of the experiments has been previously published [1,2,3]. The three experiments are:

1.- The nucleation and growth of cracks in pure iron due to cathodic charging with hydrogen [1,2],
2.- The exfoliation of 7075 aluminum alloy,
3.- The stress corrosion cracking of 304 stainless steel [3].

The basic premise for all of the experiments is that a sample containing cracks should have a lower elastic modulus than an identical sample of the same material containing no cracks.

Dr. Carpenter is a Professor of Physics at the University of Denver, Physics Department, Denver, CO 80208

Bristow [4] investigated the dependence of the elastic moduli on the presence of cracks in some detail. He reported that for a material containing n randomly orientated penny-shaped microcracks per unit volume each having a radius of a, the Young's modulus and shear modulus would be given by

$$E_c = E_o[\ 1 - 16(1-v^2)(10-3v)na^3/45(2-v)] \qquad (1)$$

$$u_c = u_o[\ 1 - 32(1-v)(5-v)na^3/45(2-v)] \qquad (2)$$

where

E_c = Young's modulus in the cracked material,
u_c = the shear modulus in the cracked material,
E_o = Young's modulus in the non-cracked material,
u_o = the shear modulus in the non-cracked material,
v = Poisson's ratio.

Analysis of these equations clearly predict a lowering of the elastic moduli with the nucleation and increased growth of cracks within a material.

In all of the experiments reported on in this paper the modulus of the test specimens was continuously monitored by accurately measuring the resonant frequency of the specimen while driving it in a standing wave configuration. Standing waves in both the longitudinal and torsional mode were used depending on which best suited the experimental conditions. Modified Marx composite piezoelectric oscillators [5,6] were used to drive the different test specimens at their resonant frequency. A resonant frequency of approximately 50 kHz was used for longitudinal waves and approximately 40 kHz for torsional waves. The resonant frequency was easily measured to within one hertz. The elastic moduli was easily calculated from the resonant frequency of the sample. The samples and techniques used to cause crack nucleation and growth while simultaneously monitoring the resonant frequency will be discussed with the results from each experiment.

EXPERIMENTAL RESULTS

Cathodic Charging of Pure Iron

The experimental setup used to monitor crack initiation and growth in pure iron due to cathodic charging is shown schematically in Figure 1. Cylindrical samples were machined from billets of pure Armco iron to a diameter of 0.476 = 0.003 cm and to a length corresponding to one-half wave length. Since the assembly was driven in a standing wave pattern, the center of the quartz bars and the sample were displacement nodes, hence the necessary electrical and support connections could be made. The system could be used for either torsional or longitudinal quartz bars. The samples were annealed in a vacuum of better than 10^{-6} torr for 6 hours at 500°C after machining and before cathodic charging. Samples were electropolished in H_3PO_4 at a current density of 60 mA/cm^2 prior

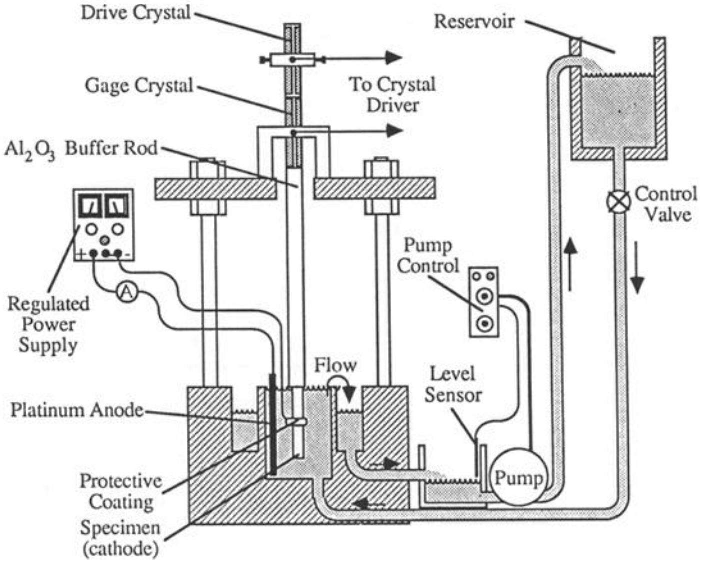

Figure 1.- Schematic of the experimental setup used to measure the resonant frequency and internal friction during cathodic charging.

to cathodic charging to provide uniform surface conditions. Cathodic charging was carried out at current densities ranging from 10 to 90 mA/cm^2 in a 1N H_2SO_4 solution with trace amounts of As_2O_3 and CS_2 added to enhance the hydrogen uptake. A 3/2 wavelength Al_2O_3 buffer rod was placed between the quartz bars and the sample to protect the silver contacts on the quartz crystals from the acid solution. The solution was circulated around the sample and the temperature of the solution was maintained constant by a heat exchanger placed in the solution reservoir. The charging conditions used were known to produce cracking in pure iron [7], which is localized to the surface. Figure 2 is a micrograph of a cross section of an iron sample after cathodic charging for 180 minutes at a current density of 30 mA/cm^2, while being vibrated at a constant strain amplitude of 5 x 10^{-6}.

The behavior of the resonant frequency and internal friction as a function of cathodic charging time for the sample shown in Figure 2 is given in Figure 3. Notice the decrease in resonant frequency which corresponds to a decrease in the elastic modulus. To demonstrate that the loss of frequency was due to the presence of cracks, two samples were vibrated in a longitudinal mode (to remove the radial dependence) during cathodic charging for 5 and 480 minutes. All experimental conditions were the same for both samples. After charging, the samples were removed from the buffer rod and were carefully machined to remove the cracked outer layer. The resonant frequency was measured:

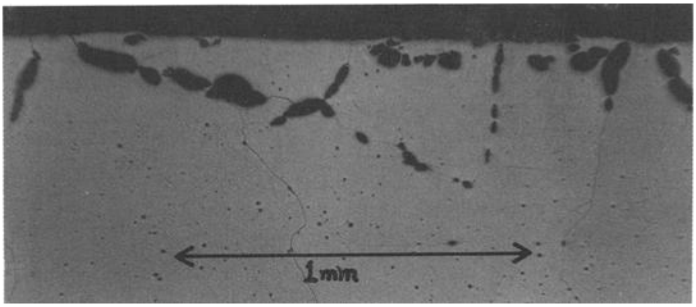

Figure 2.- Micrograph of a cross section of an iron sample after cathodic charging for 180 minutes at a current density of 30 mA/cm^2.

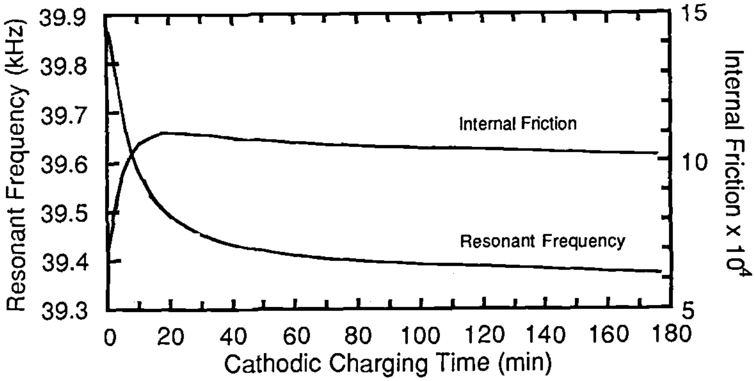

Figure 3.- Typical resonant frequency and internal friction data for the sample shown in Figure 2. (torsional vibration)

1.- before charging,
2.- after charging,
3.- after machining,
4.- after machining and reannealing.

The data are shown in Figure 4. As expected, the frequency loss is dependent on the charging time, a larger loss is observed for longer charging time. However, in both cases the frequency loss (modulus) was recovered when the cracked outer layer was removed. Clearly the decrease in the modulus was due to the cracked outer layer of material. The failure to return to exactly the resonant frequency before charging is most probably due to the necessary removal and regluing of the sample to the buffer rod.

Since the cracking is localized to the surface of the sample, one can model the sample as a composite with a thin cracked outer layer and an unaffected inner core. Using the effective modulus for a composite sample and Bristow's expression for the cracked layer it is possible to predict that the change in frequency should be given by the following expression [2]:

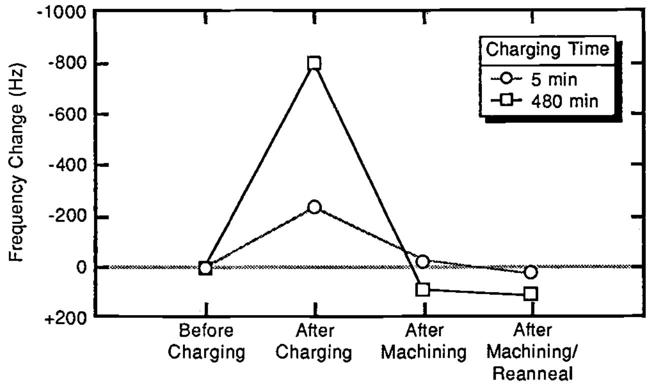

Figure 4.- Plot of the resonant frequency for samples before and after the removal of the cracked outer layer.

$$\Delta f = -\ f_o(C)na^3\,\Delta d/d \qquad (3)$$

where

f_o = the frequency before charging begins,
C = a constant depending on the material and mode of vibration,
Δd = the depth of cracking,
d = the diameter of the sample.

Since n, a and Δd can be determined by metallography it is possible to experimentally determine the validity of equation 3. Figure 5 gives the results of thirteen separate experiments where Δf is plotted against $na^3\,\Delta d/d$. Equation 3 predicts a straight line, a fairly good agreement is obtained (corr. coeff. 0.822). The good fit indicates that measurement of the change in frequency during cathodic charging gives a fairly accurate measure of the size, density and depth of cracking produced by the cathodic charging. For a more detailed description and further results see references 1 and 2.

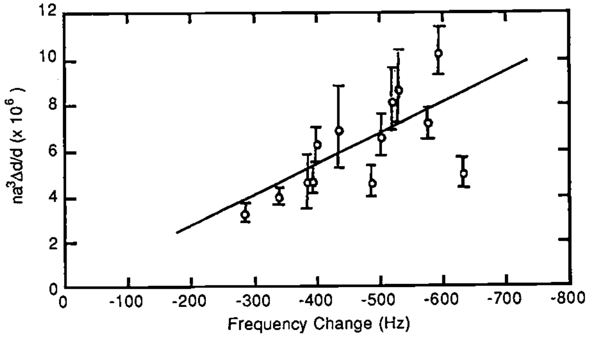

Figure 5.- Plot of the quanity $na^3\Delta d/d$ versus the loss of resonant frequency for various experimental conditions.

Exfoliation of 7075 Aluminum Alloy

Exfoliation corrosion, also known as layer or lamellar corrosion is a specific type of selective corrosion resulting from a rapid lateral attack along multiple narrow paths parallel to the metal surface. It is usually only observed in heavily rolled microstructures. In the tests reported in this paper the exfoliation was caused by the generation of corrosion products, originally from pitting, which forced the layers of metal apart along grain boundaries just below the surface causing the test specimen to swell and enlarge. The exfoliation causes flakes of the metal to be pushed up and peeled back from the surface as shown in Figure 6.

A system very similar to the one shown in Figure 1 was used to monitor the resonant frequency and internal friction during exfoliation. The test material used was a commericially available 2.54 cm thick plate of 7057-T651 aluminum alloy. Coupons 30.5 cm by 30.5 cm were cut from the plate and were annealed at 163 C for 1, 4, 6, 8, 10, 16, 32 and 64 hours. After annealing, damping samples 6.4 mm by 6.4 mm by 51 mm (one half-wavelength for a longitudinal wave at 50 kHz.) were machined from the coupons. The samples were symmetrical to the mid-plane of the plate with the long dimension in the rolling direction. All tests were conducted according to the ASTM Standard Method of Testing for Exfoliation, i.e. the EXCO test for the Exfoliation Susceptibility of 7xxx Series of Aluminum Alloys containing Copper [9] was used. The exfoliation test consists of exposing the test coupon to a solution of 4 molar NaCl, 0.5 molar $KNO_3$8, 0.1 molar HNO_4 in distilled water for 48 hours at room temperature. The solution must be in sufficient quantity to provide a volume to surface area ratio of at least 7.75 ml/cm^2.

At present, the most common method used to assess the degree of exfoliation is to compare the exposed or corroded surfaces with a set of standard photographs. Figure 7 shows the corroded surfaces for a complete set of larger samples after the EXCO test. Careful analysis of the photographs indicate that the degree or amount of exfoliation increases with prior annealing time up to the 8 hour anneal. Beyond the 8 hour anneal the amount of exfoliation decreases with the samples annealed for 32 and 64 hours showing only pitting.

Figures 8 and 9 give the resonant frequency and internal friction versus exposure time in the EXCO solution for the as received samples and for those annealed at 1, 4, 6 and 8 hours prior to testing. Similar data for samples annealed at longer times are shown in Figures 10 and 11. The test specimen was vibrated in the EXCO solution in a longitudinal standing wave at approximately 50 kHz. giving a continuous measurement of the resonant frequency and damping. The tests were carried out at a constant strain amplitude of approximately 5 x 10^{-5}. Analysis of the resonant frequency data reveals a gradual decrease over the first 6 hours to a semi-plateau after which there is a sudden downturn. The time at which the downturn occurs decreases with the prior anneal time. A proposed explaination, which is consistent with visual observations, of the frequency data is as follows.

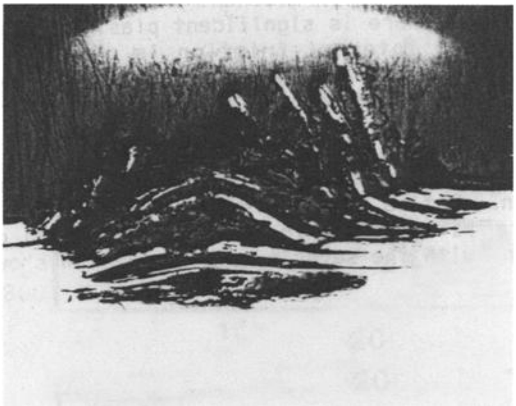

Figure 6.- Photograph of a corroded surface showing the characteristics of exfoliation. (x45) The sample was annealed for 8 hours and exposed for 48 hours.

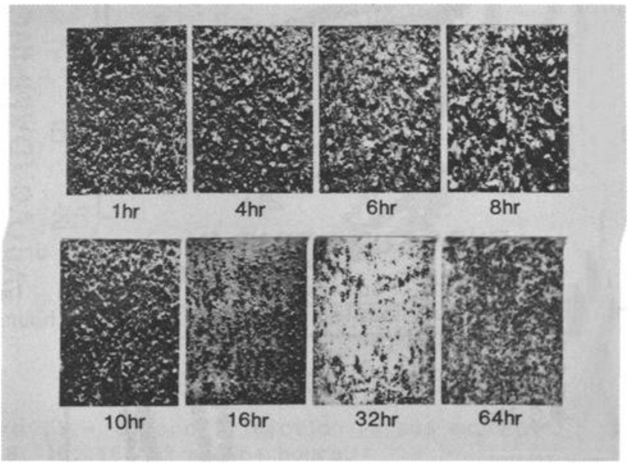

Figure 7.- Photograph of corroded samples which were annealed for the times shown. All samples were exposed for 48 hours.

The initial drop of the frequency appears to be related to the bubbling of hydrogen from the surface of the test specimen. Both the amount of the decrease and the rate of decrease were nearly constant for all of the samples even those which did not show signs of exfoliation. The second drop in frequency is believed to mark the onset of exfoliation and is due to the formation and growth of cracks in the surface layers of the specimen. Notice that an ordering of the times at which the second turn down occurs is consistent with the degree of exfoliation as shown in Figure 7. The internal friction data is somewhat different, but provides an even clearer measure of the onset of the exfoliation corrosion process.

The internal friction is not sensitive to the hydrogen bubble formation and no corresponding change in internal friction is observed when the first drop in resonant frequency occurs. However, as exfoliation begins there is significant plastic deformation and a rapid increase in the internal friction is observed. The rapid increase in damping correlates extremely well with the second drop in resonant frequency. Data for the sample annealed for 64 hours support the above explanation. The 64 hour sample showed only pitting with no exfoliation. The data for this sample show neither a second drop in resonant frequency nor a sudden increase in the internal friction. Notice that the systematic movement of the time at which the rapid increase in internal friction occurs is in complete agreement with the severity of exfoliation shown in Figure 7.

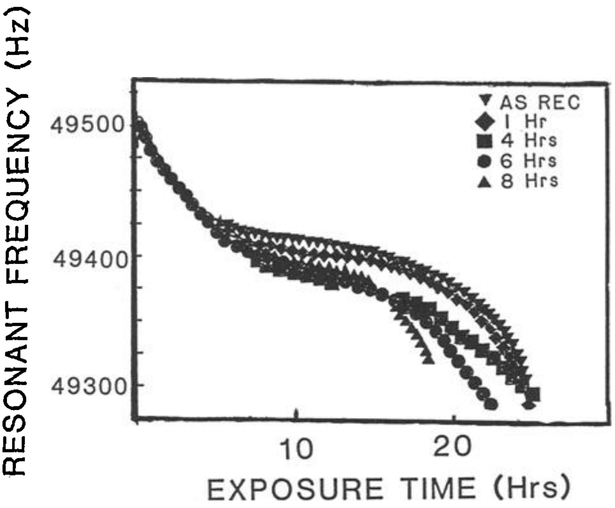

Figure 8.- Resonant frequency versus exposure time for as received samples and those annealed for 1, 4, 6, and 8 hours.

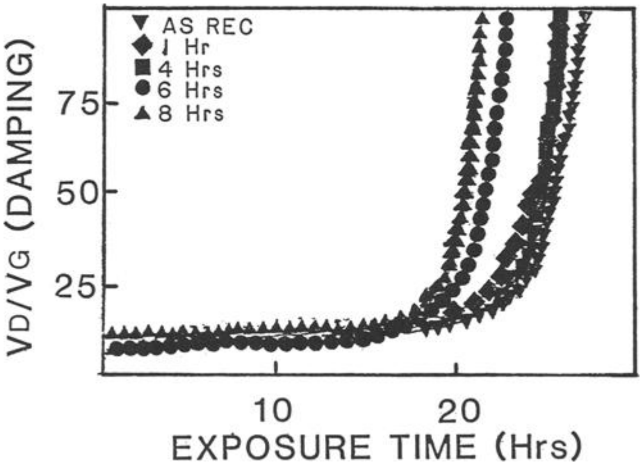

Figure 9.- Internal Friction versus exposure time for as received samples and those annealed for 1, 4, 6 and 8 hours.

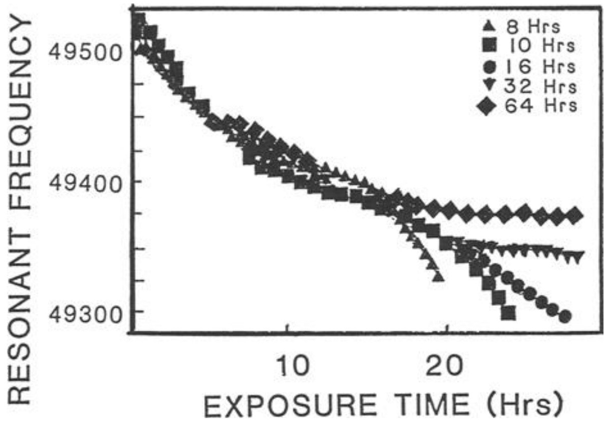

Figure 10.- Resonant frequency versus exposure time for samples annealed for 8, 10, 16, 32 and 64 hours.

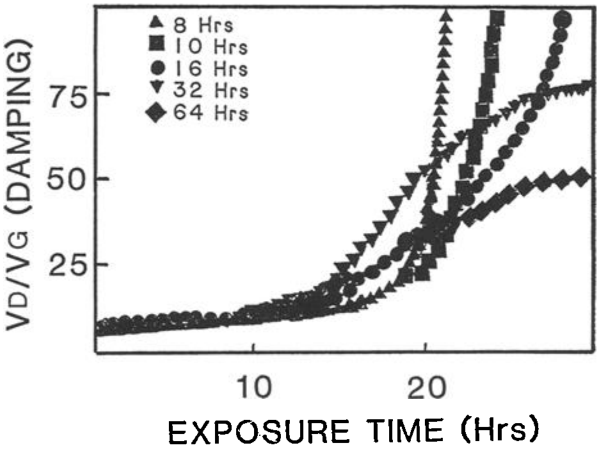

Figure 11.- Internal friction versus exposure time for samples annealed 8, 10, 16, 32 and 64 hours.

<u>Stress Corrosion Cracking of 304 Stainless Steel</u>

In order to use resonant frequency (modulus) measurements to monitor stress corrosion cracking it is necessary to have a sample design which allows for the application of a stress without disturbing the wavetrain. The schematic of a sample which meets these conditions is shown in Figure 12. The sample is three half wavelengths long, the gripping nodes and solution cup being located at displacement nodes. The solution cup was 316 stainless steel and was silver soldered to the 304 stainless test specimen. A schematic of the loading grips with the sample is shown in Figure 13. The behavior of 304 stainless steel when exposed under applied stress to three test solutions was investigated.

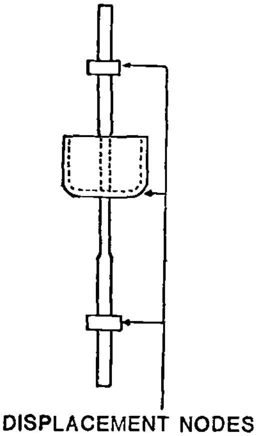

Figure 12.- Schematic of special sample used to measure the resonant frequency.

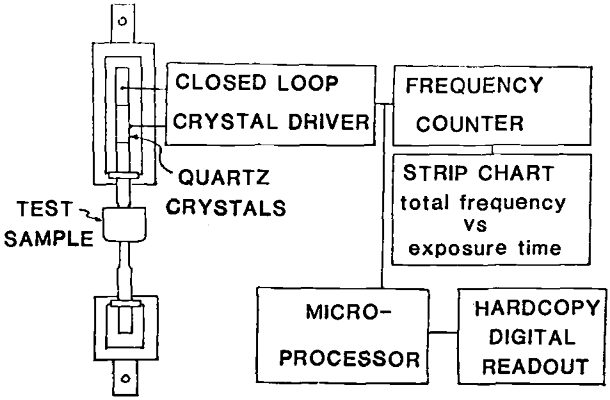

Figure 13.- Schematic of the experimental apparatus used to measure the resonant frequency.

The test solutions were chosen in the following way: (1) solution one was chosen because it was known to cause stress corrosion cracking in 304 stainless steel for the experimental conditions used [3], (5N H_2SO_4 + 0.5N NaCl); (2) solution two was chosen because it should not cause cracking, (5N Na_2SO_4) and (3) solution three was chosen because it was not known whether or not it would cause cracking, (5N Na_2SO_4 + 5N H_2SO_4). Experiments were conducted in the following manner:

1.- Test samples were deformed in tension to 7% total strain. The samples were designed and fabricated such that the 7% deformation produced a length giving a resonant frequency which matched that of the quartz crystals.

2.- After deformation, the samples were allowed to stress relax under load until there was no measureable change in either the load or resonant frequency during a time segment of one hour.

3.- After complete relaxation, the test solution was added to the cup at the center of the sample and the resonant frequency was monitored for an extended period of time, usually several hours.

4.- After a selected time period, the test solution was removed and the samples were examined for evidence of stress corrosion cracking. Some samples were simply unloaded and inspected while others were pulled to failure and then examined.

Experimental examination of samples exposed to solutions two and three gave no evidence of cracking of any kind. As expected no significant changes in the resonant frequency during testing with solutions two and three were observed. However, as expected, samples exposed to solution one showed extensive stress corrosion cracking. Figure 14 is a micrograph indicating the kind of cracking obtained. Little or no change in the resonant frequency was observed for a short incubation time (approximately 10^4 sec.), after which there was an almost linear decrease in the resonant frequency. Figure 15 provides an example of the experimental data. The magnitude of the change in resonant frequency was found to be directly related to the amount of cracking. While no model has been formulated to directly express the frequency loss in terms of crack parameters a number of tests were carried out where samples were tested until a predetermined frequency loss had occurred and then they were examined metallographically. Figure 16 shows the data for the change of resonant frequency as a function of the average depth of cracking. Figure 17 shows the change in resonant frequency as a function of the percentage of crack area to total area measured on a mid-plane longitudinal cross section. The data clearly demonstrate that the change in resonant frequency (elastic modulus) is a result of the cracking in the specimen.

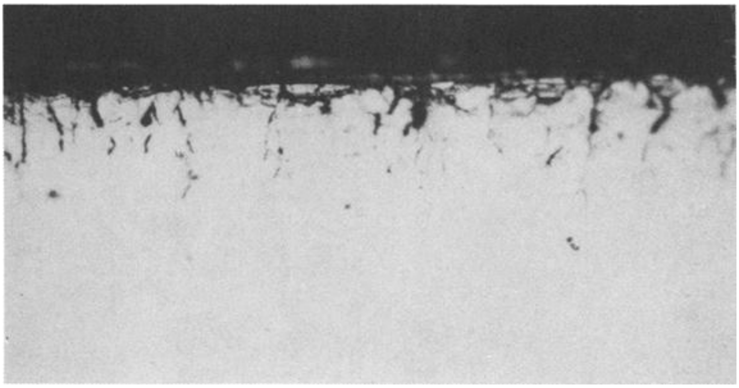

Figure 14.- Micrograph of stress corrosion cracking in 304 stainless steel. Change of resonant frequency = -258 Hz.

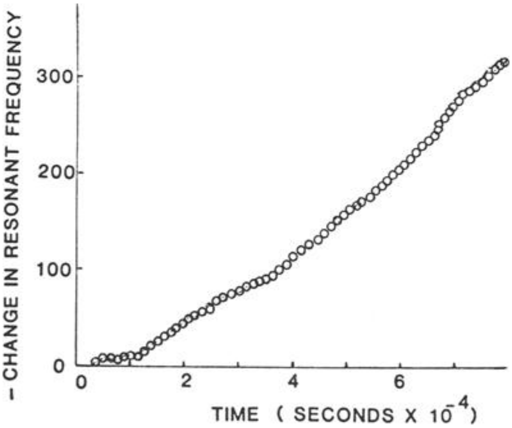

Figure 15.- Negative change in resonant frequency versus exposure time for a 304 stainless steel sample, strained 7% and exposed to 5N H_2SO_4/0.5N NaCl solution.

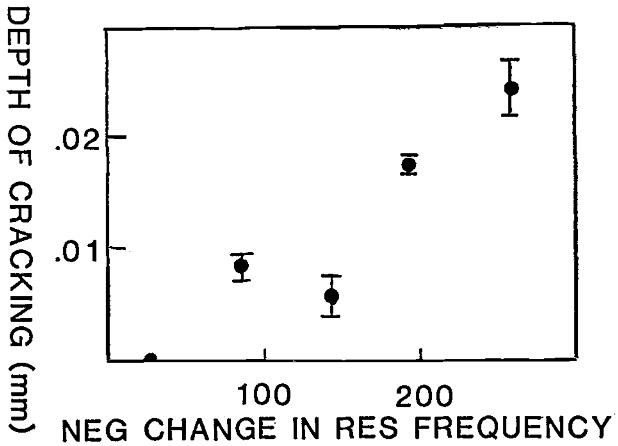

Figure 16.- Depth of cracking versus the negative change in resonant frequency for different 304 stainless steel samples.

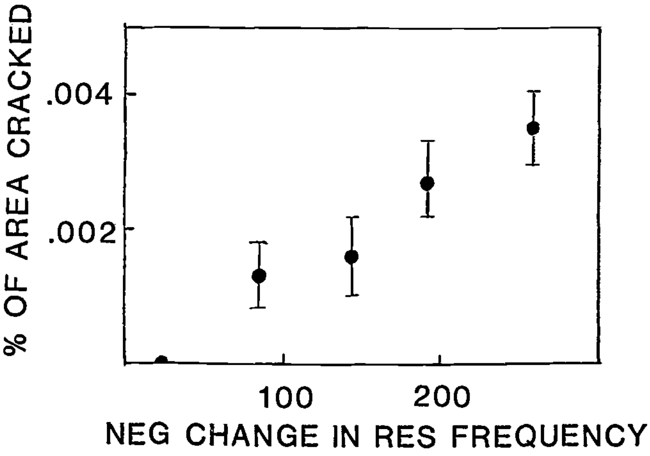

Figure 17.- Ratio of the area cracked to total area plotted versus the negative change in resonant frequency for different 304 stainless steel samples.

CONCLUSIONS

The results presented, for all three experiments, indicate that continuous precise modulus measurements can be used to detect and monitor the nucleation and growth of cracks. While in two of the experiments, no definitive relationship between the amount of cracking and the loss of resonant frequency have been developed, good correlation was obtained.

REFERENCES

[1] Armstrong, J.H. and Carpenter, S.H., Metallurgical Transactions A, Vol. 19A, 1988, p. 473.

[2] Armstrong, J.H., Ph.D. Dissertation, University of Denver, June 1985.

[3] Carpenter, S.H. and Siebert, O.W., Corrosion, Vol. 39, 1983, p. 103.

[4] Bristow, J.R., British Journal of Applied Physics, Vol. 11, 1960, p. 81.

[5] Marx, J., Review of Scientific Instruments, Vol. 22, 1951, p. 503.

[6] Robinson, W.H., Carpenter, S.H. and Tallon, J.L., Journal of Applied Physics, Vol. 45, 1974, p. 1975.

[7] Bernstein, I.M., Metallurgical Transactions, Vol. 1, 1970, p. 3143.

[8] ASTM Designation G 34, American Society for Testing and Materials, 1916 Race Street, Philadelphia, PA 19103.

Anthony N. Sinclair, Phineas A. Dickstein, Jan K. Spelt, Emanuel Segal, and Ytzhak Segal

ACOUSTIC RESONANCE METHODS FOR MEASURING DYNAMIC ELASTIC MODULUS OF ADHESIVE BONDS

REFERENCE: Sinclair, A. N., Dickstein, P. A., Spelt, J. K., Segal, E., and Segal, Y., "Acoustic Resonance Methods for Measuring Dynamic Elastic Modulus of Adhesive Bonds", Dynamic Elastic Modulus Measurements in Materials, ASTM STP 1045, Alan Wolfenden, editor, American Society for Testing and Materials, Philadelphia, 1990.

ABSTRACT: An investigation is made into acoustic resonance methods for measuring the dynamic elastic modulus of the adhesive layer in a bonded metal-to-metal joint. Empirical studies have indicated that this parameter may be used to infer the cohesive strength of the bond; in theory, an accurate measurement of two or more resonant frequencies should give both the elastic modulus and thickness of the adhesive layer. Verifying the accuracy of the technique was greatly hampered by the strong dependence of elastic properties in the adhesive on the test frequency.

The resonant frequencies of aluminum-to-aluminum adhesive joints were determined by both contact and immersion acoustic resonance techniques; receptance analysis was then used to determine the elastic modulus. Results were consistent with those achieved by time-of-flight measurements on bulk adhesive specimens. Based on these tests, inherent limitations of the Fokker Mark II Bondtester for assessing the cohesive strength of a bond were explored.

KEYWORDS: adhesives, elastic moduli, nondestructive evaluation, bondtester, ultrasonic testing, receptance model, cohesive failure

INTRODUCTION

Adhesive bonding holds many potential advantages over more traditional methods of joining engineering structures and components. When properly applied, adhesives spread the load evenly over a large area, thereby avoiding large stress concentration factors that could cause premature failure. The risk of damaging the material in the joint area during manufacture, as could be the case in riveting or welding, is largely eliminated. Adhesives are particularly useful in situations that involve the linking of unlike materials together, or the fabrication of structures from fiber reinforced composites. Further advantages of adhesive bonding include increased stiffness of the joint area, reduced machining requirements, a smoother external surface, sealing of the joint area, and reduced cost.

Drs. Sinclair and Spelt are assistant professors in the Mechanical Engineering Department, University of Toronto, Canada M5S 1A4; Dr. Dickstein is a research scientist in the same department. Drs. E. Segal and Y. Segal are professors in the Nuclear Engineering Department, Technion, Haifa, Israel 32000.

Although not subject to many of the problems facing riveting or welding, adhesives do bring their own set of challenges in the areas of bond failure and bond inspection. Earlier works have noted that a nondestructive method for measuring the bulk elastic modulus of the adhesive material in a joint would aid in estimating the bond strength [1-5]. This paper will explore acoustic resonance methods of measuring elastic moduli of the bond line in aluminum-to-aluminum adhesive bonds, and assess their relative merits and limitations. The implications of the results will be used in a look at the Fokker Mark II bondtester [5], widely used for estimating the cohesive strength of the adhesive material by correlations with the resonant frequencies of a bonded specimen.

DEFECTS AND FAILURE MODES IN ADHESIVE BONDS

Defects in adhesive joints can be categorized into three broad groups; for each group, efforts have been made to develop methods of nondestructive evaluation (NDE) to warn of inherent weakness or impending failure of the bond:

Voids and Disbonds: A void or disbond is a localized area in which there is an unfilled gap between the two adherends. Such a defect may be a result of poor procedures in the spreading of the adhesive in the manufacturing stage; another possibility is stress-induced damage, originating either during the curing cycle or in service. Gasses released during the curing cycle may also lead to voids within the adhesive layer.

Acoustic methods are the preferred nondestructive method for detecting such defects. The techniques take a number of different forms, depending on the accessibility of the specimen, expected geometry of the defect, and desired resolution. Pulse-echo, through-transmission, mechanical impedance measurement, resonant frequency determination, and attenuation methods have all been used with some degree of success [1,6,7]. This defect type is well-suited to automated inspection by a C-scan, provided geometry and accessibility will permit.

Low Strength of the Bond-Adhesive Interface: Separation of the bulk adhesive from one of the adherends is normally termed an "adhesive" failure, as it is due to a lack of adhesion between the adhesive and adherend. Low adhesive strength is usually a result of improper pretreatment of the adherends, or environmental degradation [8-11]. It is more commonly encountered in metal-to-metal bonds rather than with composities. Proper pretreatment of a metal adherend such as aluminum calls for careful cleaning, degreasing, removal of any oxide by an etching process, and then an anodizing treatment to produce a new uniform oxide layer [12,13]. This oxide should link to the bonding agent by a complex mechanism involving both mechanical keying and chemical interaction; details of this linking phenomenon are not yet well-understood [14].

Nondestructive testing of the adhesive strength of a bonded joint remains a very elusive goal. The oxide layer on each adherend is on the order of 1 μm thick, so that any direct method of characterizing the interface would need very fine resolution. Preliminary studies indicate that the reflection coefficient of sound from the adherend-bond interface could indicate conditions within the oxide layer, but this technique would require ultrasound frequencies on the order of tens of megahertz or even higher [1,15]. While such research continues, the industrial response is to guard against these failures by tight quality control checks of the surface pretreatment of the adherends during the manufacturing stage, and indirect checks for environmental damage of in-service components.

Weak Cohesive Strength of the Bulk Adhesive Layer: Failures within the bulk adhesive are termed "cohesive" in nature. Cohesive failure may be precipitated by localized defects as discussed earlier; such defects can usually be detected nondestructively. Alternatively, environmental factors, inadequate curing or poor mixing may cause the bulk properties of the adhesive to be perturbed from their nominal state, and lead to failure of the specimen [4]. A combination of these two effects is also possible. Assuming proper pretreatment of the adherends and no environmental degradation, the cohesive failure mode is expected if an external load is increased to the point of destruction of the specimens.

There is no direct method to nondestructively measure the cohesive strength of bulk adhesive material. However, factors that may cause a perturbation in cohesive strength can also lead to changes in Young's modulus E of the adhesive. Several studies have confirmed this connection, and semi-empirical relationships give cohesive strength as a function of E for certain types of adhesives, geometry, and loading pattern [6,16-18].

There are still many challenges that must be addressed when estimating bond strength from a measurement of the elastic modulus:

(a) Lateral Constraint: For most metal-to-metal adhesive bonds, the bond line is very thin (less than 0.3 *mm*), and the adherends typically have an elastic modulus far greater than that of the adhesive. Under these conditions, a tensile load exerted perpendicular to the bonded area puts the adhesive in an approximate state of uniaxial strain, i.e., there is a high degree of constraint in the plane of the bond. Assuming isotropic properties of the adhesive, Hooke's Law then gives the apparent modulus $\tilde{E}$, equal to the ratio of normal stress to strain:

$$\tilde{E} = \frac{\sigma}{\varepsilon} = \frac{E\,(1-\nu)}{(1+\nu)(1-2\nu)} \tag{1}$$

It is the value of $\tilde{E}$, rather than Young's modulus E, that is measured in a ultrasonic test of the bond. A second, independent measurement of elastic properties would be needed to determine individual values for E and ν.

(b) Variations in Bond Line Density or Thickness: Under some conditions, resonance techniques are incapable of distinguishing variations in $\tilde{E}$ from variations in density or thickness of the bond. Studies have shown that the cohesive strength of a bond does depend on each of these parameters, but the form of the dependence is different for each [2,3]. This greatly complicates the use of resonance techniques for estimating cohesive strength via correlations with the apparent adhesive modulus.

(c) Loading Mode: A high value of $\tilde{E}$ combined with a low value of failure strain indicates that an adhesive will show a larger value of cohesive strength in a tensile test (e.g., a butt joint) than in a peel test. This is because a peel test is characterized by relatively large values of stress concentration factor k_t at the edge of the bond; a high value of $\tilde{E}$ would accentuate the stress concentration and thereby promote failure [19]. By contrast, a large value of elastic modulus in a butt joint would tend to bring elasticity values of the adhesive and adherend closer together. This *reduces* the stress concentration for this configuration, and thereby leads to an apparent increase in yield stress. Although empirical relationships have been developed between measured values of E and cohesive strength, it is seen that such relationships must be applied with caution, and observed trends cannot be readily extrapolated to bonds of a different configuration.

(d) Modulus of Elasticity in a Viscoelastic Material: Several researchers have used acoustic techniques to estimate E for adhesive materials. In general, it was found that the result was highly dependent on the vibration frequency. This is due to the fact that the extent of material flow is frequency and amplitude dependent, and material flow affects the apparent modulus. In addition, Ramakrishnan et al [20] noted that the extent of dependence of E on frequency appears to be a function of thickness of the specimen. These factors pose grave complications in the verification of any method for measuring $\tilde{E}$, as two measurement methods can be legitimately compared only if they use specimens of comparable thickness, and stress the specimens at the same frequency.

(e) Dependence of $\tilde{E}$ on Bond Thickness: The thickness of an adhesive bond can affect the apparent modulus in several ways [20]. First, there is the question of lateral constraint, discussed in Section (a) above. A very thick adhesive layer would have less lateral constraint, and therefore a smaller value of $\tilde{E}$, than a thin layer.

Second, a complex tri-axial stress state is often present near the bond perimeter, which is usually the failure initiation site in a peel or shear loading mode. The thickness of the bond will influence this stress pattern, and can lead to perturbations in stress concentration factors. This can clearly affect the magnitude of the failure load, but may also influence the apparent modulus.

Third, the curing cycle will affect a thin adhesive layer differently from a thick one. The thick adhesive will be more prone to gas entrapment, which can cause variations in density and a drop in the measured value of E. The center of the thick adhesive layer is more insulated from the adherends than would be a thin layer; this will affect the temperature profile as a function of time. A complex temperature profile may also lead to residual stresses and stress concentrations that will distort $\tilde{E}$. Tests have shown deviations of several percent in values of elastic constants between samples of bulk adhesive, and adhesive material cured between two adherends [21].

(f) Breaking Strength: Failure of a bond can occur at the adhesive/adherend interface; failure can be precipitated at a localized flaw; failure can be due to an applied stress (shear or normal) that is greater than the yield stress of the bulk adhesive. An accurate evaluation of E will give no indication of the possibility of the first failure mode, perhaps some information on the second (e.g., significant porosity would cause an apparent decrease in $\tilde{E}$), and perhaps some on the third (via correlations between bulk values of E and cohesive strength). Under these conditions, it is clear that determination of $\tilde{E}$ alone will not serve as a universal indicator of bond strength. However, when combined with other tests and strict quality control standards on the pretreatment of adherend surfaces, the apparent modulus can be an important indicator of bond quality.

VIBRATIONS IN LAYERED MEDIA

Nondestructive inspection of the adhesive between two bonded metal components requires an inspection technique that can penetrate several millimeters through the adherend material. Limited access to the far side of the component often rules out the use of radiography; this leaves acoustic methods as the most popular method for characterizing the adhesive layer properties. Some of these, such as the low frequency impedance test, are suited to the detection of localized disbonds and voids. For evaluation of the elastic modulus, resonance techniques are the most appropriate.

This paper will be confined to the study of two aluminum adherends of equal thickness, bonded together by a uniform layer of adhesive as shown in Figures 1 and 2. Each material layer is represented by the material parameter set $\{E_i, l_i, \rho_i\}$, designating the layer effective modulus, thickness, and density respectively for $i = U$ (adherend), $i = V$ (adhesive), and $i = W$ (transducer crystal). It will be assumed that all waves are of compression mode (no shear component) and travel perpendicular to the plane of the bond at a speed c_i in material i:

$$c_i = \sqrt{\tilde{E}_i/\rho_i} \tag{2}$$

For the hypothetical case where the adherends and adhesive have the same values of $\tilde{E}$ and ρ, resonant frequencies ω_n of the isolated joint (Figure 1) are easily shown to occur at:

$$2(l_U + l_V + l_U) = 2\pi n \frac{c_U}{\omega_n}, \quad n = 1, 2, \ldots \tag{3}$$

Because adhesives typically have a far smaller modulus and density than metal adherends, the mathematics become somewhat more complicated.

Two well-known methods for measuring the resonant frequencies of a bonded component with piezoelectric crystals are contact and immersion (non-contact) testing. In an immersion test, the specimen is placed underwater, and ultrasonic signals are beamed at the specimen through the fluid (Figure 1). If the sound is at a resonant frequency of the test sample, the round-trip path of sound passing through the specimen will contain an integral number of wavelengths. The sound beam returning to the probe will then be a composite of the beam reflected from the front face, and sound beams that have made one or more passes through the sample. The sound beams that passed through the sample will be 180^0 degrees out of phase with the beam reflected from the front face, as the reflection coefficient is negative at the specimen backwall. The resonant frequencies will therefore be marked in the frequency domain by a pronounced *minimum* in the magnitude spectrum, due to the effects of destructive interference.

Strikingly different effects are found in contact measurements, illustrated in Figure 2. The

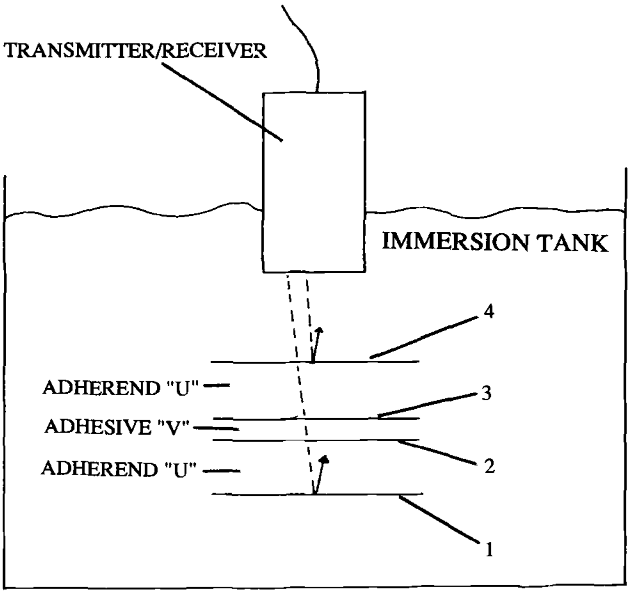

FIG. 1 -- Immersion ultrasonic test of adhesive bond.

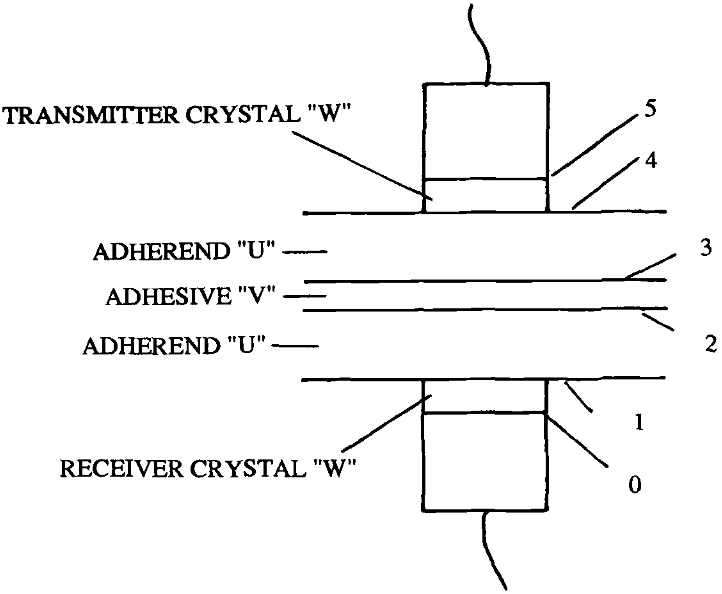

FIG. 2 -- Contact ultrasonic test of adhesive bond.

probes are acoustically coupled to the specimen by means of a coupling oil. As a result, one must now consider resonances not of the specimen by itself, but of the entire probe-specimen-probe system. If the probe is excited by an alternating voltage at the system's resonant frequency, the electrical impedance of the transmitter will drop. The piezoelectric crystal's oscillations will become large, and the crystal will deposit more power into the specimen. Resonant frequencies in this case are therefore identified by a pronounced *maximum* in the magnitude spectrum of both the transmitted and received waveform.

Together with the elastic modulus, the damping coefficient of the adhesive may also be of interest when characterizing bonded joints [6,14,22]. Usually the damping coefficient of the adherends is so much lower than that of the adhesive that the former can be neglected. Therefore, the amount of damping is indicative of the strain in the adhesive, and its viscous characteristics. As such, it can be interpreted as an imaginary component of the elastic modulus of the adhesive. Its value is an indicator of the condition of the bond material.

Damping manifests itself in many ways. For continuously forced excitation of a mode that involves appreciable strain in the adhesive, a large damping coefficient leads to relatively small amplitudes of vibration, appreciable energy loss, and a large phase difference between force and displacement. Measurement of any of these three parameters, then, can serve as an indicator of the damping coefficient [23,24].

RECEPTANCE MODEL

The natural frequencies of vibration for a multi-layered system may be determined through receptance analysis. The receptance $\alpha^A_{m,n}$ of a system "A" is defined as the steady-state amplitude of harmonic displacement $\psi(A,m)$ at point m caused by a sinusoidally varying force of amplitude $T(A,n)$ per unit area and frequency ω at point n [25]. In general, the receptance of "A" will be a function of the forcing frequency ω:

$$\alpha^A_{m,n}(\omega) = \frac{\psi(A,m)}{T(A,n)} \tag{4}$$

If m and n refer to the same point, then Eq 4 gives the direct receptance of "A"; for two different points m and n, the cross receptance is defined. Note that for an undamped system, $\psi(A,m)$ becomes infinite at resonant frequencies, indicating an infinite value for the system receptance. In practice, some damping is always present which tends to suppress the amplitude and broaden the width of the resonant peak. The magnitude of the damping coefficient is assumed to be sufficiently small that it does not cause a substantial shift in the frequencies of the resonances.

In the application of the receptance model to the study of an adhesively bonded joint, it is convenient to separate the joint into its constituent layers, with labeled boundary points as shown in Figures 1 and 2. The individual receptances of each layer are easily measured or calculated [25]. From such building blocks, a compound system may be modeled. The method is mathematically equivalent to solving the wave equation in each of the homogeneous layers of the system [26].

Derivation of the equations pertinent to the simple adhesive joint configuration of Figure 1, isolated from all other systems, was carried out by Adams and Coppendale [27]. They defined a parameter F in terms of the receptances of the individual joint components:

$$F = (\alpha^U_{2,2} + \alpha^V_{2,2})^2 - (\alpha^V_{2,3})^2 \tag{5}$$

where the direct and cross receptances of the joint components are given as functions of wavenumber $k_i = \omega/c_i$ in material i by:

$$\alpha^i_{m,m} = -cot\,(k_i l_i)/(\tilde{E}_i k_i) \qquad \text{and} \qquad \alpha^i_{m,m+1} = \frac{-1}{\tilde{E}_i\, k_i\, \sin\,(k_i l_i)} \tag{6}$$

for $i = U,\ V,\ W$, where component i has the boundaries $[m,\ m+1]$. Using receptance analysis, it has been shown that the resonant frequencies for acoustic waves traveling through an adhesively bonded joint correspond to values of k_i for which F equals zero [27]:

$$F(\tilde{E}_U, \tilde{E}_V, k_U, k_V, l_U, l_V) = 0 \tag{7}$$

Therefore, using Eqs 5-7, measurement of two natural frequencies of the bonded joint will give implicit expressions for the effective adhesive modulus $\tilde{E}_V$ and thickness l_V. Unfortunately, the solution of $\tilde{E}_V$ and l_V must be iterative in nature, and the sensitivity of results to errors in experimental measurements are in general difficult to quantify.

EXPERIMENT

A number of single lap shear specimens were made, each consisting of two identical Al-6061 adherends with properties listed in Table 1. The adhesive was the single-part epoxy CYBOND 4535A [28] with a nominal thickness ranging from 0.05 *mm* up to 0.60 *mm*, controlled by side shims during the manufacturing process. The adherends were pretreated per ASTM Standard D2651-79, bonded and cured according to manufacturer's directions.

TABLE 1 -- Bonded aluminum-to-aluminum test specimens.

Adherend thickness	1.62 *mm*
Adherend density	2700 kg/m^3
Adherend effective modulus	109 *GPa*
Adhesive density	1150 kg/m^3
Crystal[a] thickness	0.288 *mm*
Crystal density	7300 kg/m^3
Crystal effective modulus	147.4 *GPa*

[a] Parameters of lead zirconante titanate transducer crystals

In order to obtain reference values of elastic constants against which the results of the resonance tests could be compared, static tension tests were performed on bulk samples of adhesive. Sample thickness ranged from 2.1 *mm* to 3.2 *mm*. Specimens were strain gauged in the loading and transverse directions. A value of Poisson's ratio of 0.36 was obtained from the samples. Consistent, repeatable values of Young's modulus could not be obtained; the reason is believed to be permanent deformation of the samples during the test.

Due to the poor results of the static tension test, the sonic velocity in bulk adhesive specimens was measured in order to get reference values of $\tilde{E}_V$ based on Eq 2. The results of these measurements, performed on samples of thickness 2.65 *mm* and 3.04 *mm*, are plotted in Figure 3 as a function of frequency. At relatively high frequencies in the 15 *MHz* range, viscoelastic flow is inhibited, and therefore the apparent modulus approaches 9-10 *GPa*. The apparent modulus drops to about 5 *GPa* at low frequency. Note that this test method is well-suited to the characterization of relatively thick bulk specimens. However, extremely high ultrasonic frequencies would be required to achieve sufficient resolution for testing bonded specimens in this manner; the amplitude of such signals would be insufficient for reliable measurements. In addition, it would be impossible to ascertain whether a change in sonic velocity in the adhesive were due to a perturbation in E_V, ρ_V, or both.

Immersion Test

In the first set of ultrasound measurements, an immersion pulse-echo configuration was used. Echo signals from the adhesive layer were measured using a highly damped transducer with a frequency band extending from 5 to 15 *MHz*. The echo signals were digitized and transformed to the frequency domain, where dips in the frequency spectrum (Figure 4(a)) or discontinuities in the derivative of the phase spectrum (Figure 4(b)) indicate resonances. Figures 4(a) and 4(b) correspond to specimens with l_V=0.61 *mm*. Note that not all resonances are easily identified in Figure 4(a); the phase information in Figure 4(b) is useful in identifying some (but not all) of them. In addition, some of the resonances may be due to wave modes not included in the model.

TABLE 2 -- Measured resonant frequencies of bonded aluminum-to-aluminum test specimens

Resonant frequency #	Immersion Test (*MHz*)	Contact Test (*MHz*)
1	5.90	4.90
2	7.43	5.90
3	8.10	6.15
4	9.69	7.46
5	10.00	8.50
6	10.49	8.87
7	11.81	10.55
8	12.12	11.45
9	12.95	12.39
10	13.74	13.91

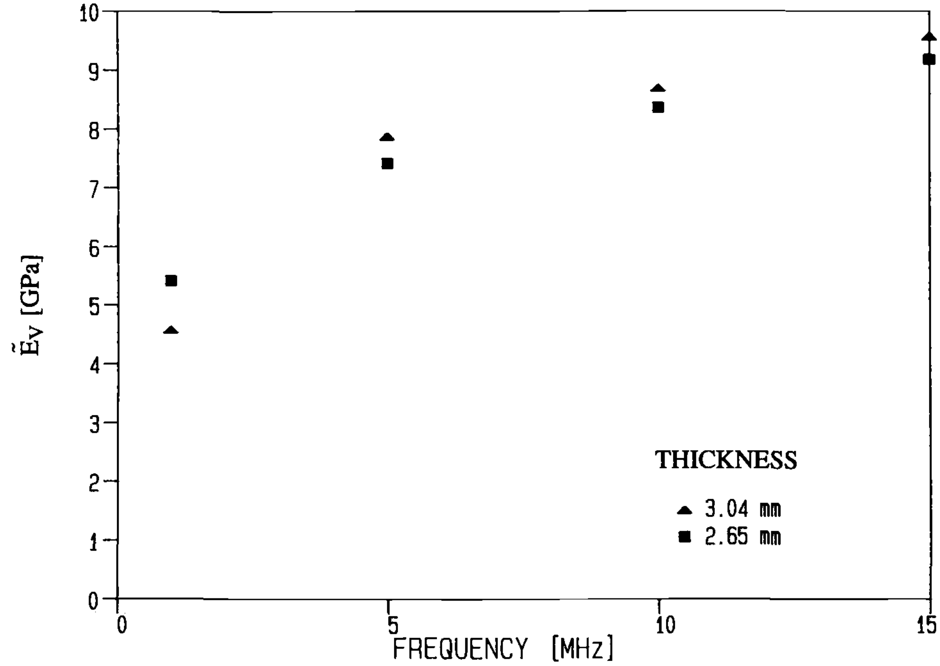

FIG. 3 -- $\tilde{E}$ for CYBOND 4535A based on ultrasonic time-of-flight tests.

Calculations were then made of the theoretical resonant frequencies by iterative solution of Eq 7. For the adhesive layer, a wide range of values were used for $\tilde{E}_V$ and l_V, in order to study the sensitivity of resonant frequencies to these parameters.

Figure 5 shows the calculated values of the first six resonances as a function of l_V, for a fixed value of $\tilde{E}_V$ equal to 7.2 *GPa*. Figure 6 shows the resonant frequencies for l_V fixed at 0.3 *mm*, and variable $\tilde{E}_V$. The Figures show that the values of the resonant frequencies are not highly sensitive to $\tilde{E}_V$ nor to l_V, for significant ranges of these parameters. It is preferable that use of Eq 7 to characterize the adhesive layer be confined to those resonances where the

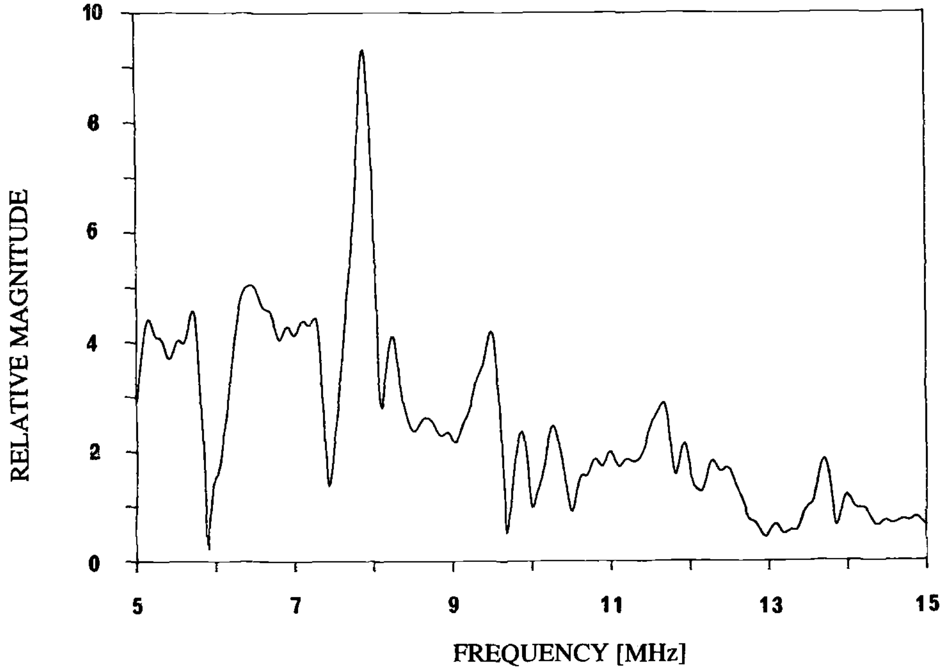

FIG. 4(a) -- Magnitude spectrum of echo signal in immersion test.

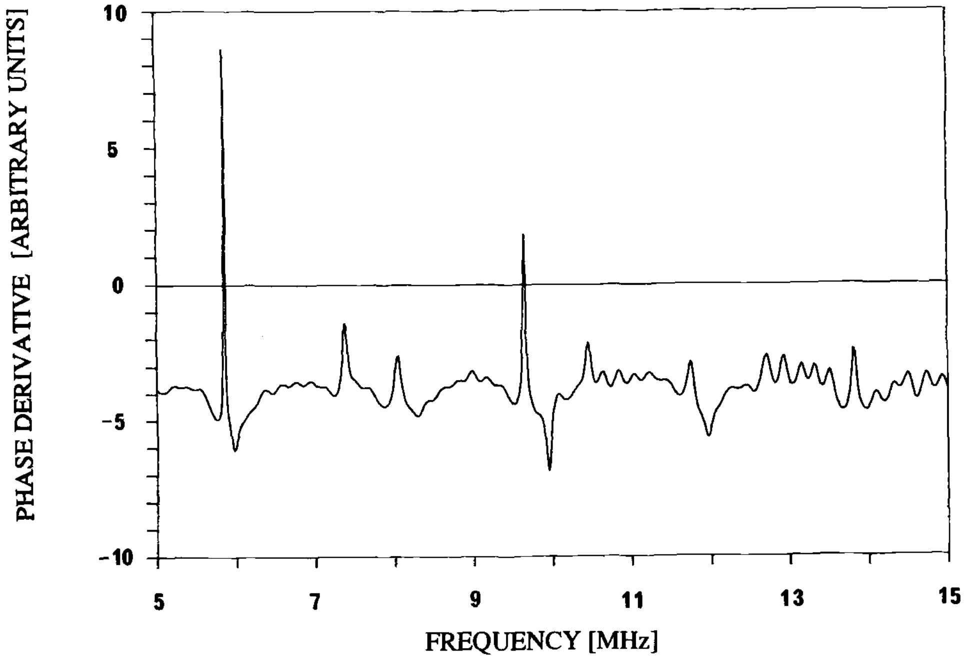

FIG. 4(b) -- Phase spectrum of echo signal in immersion test.

sensitivity is high. This is not always practical, particularly for adhesive bonds used in the aviation industry which are typified by high elastic modulus and small bond thickness; the lower resonant modes in this case are not going to give an accurate indication of the adhesive layer characteristics.

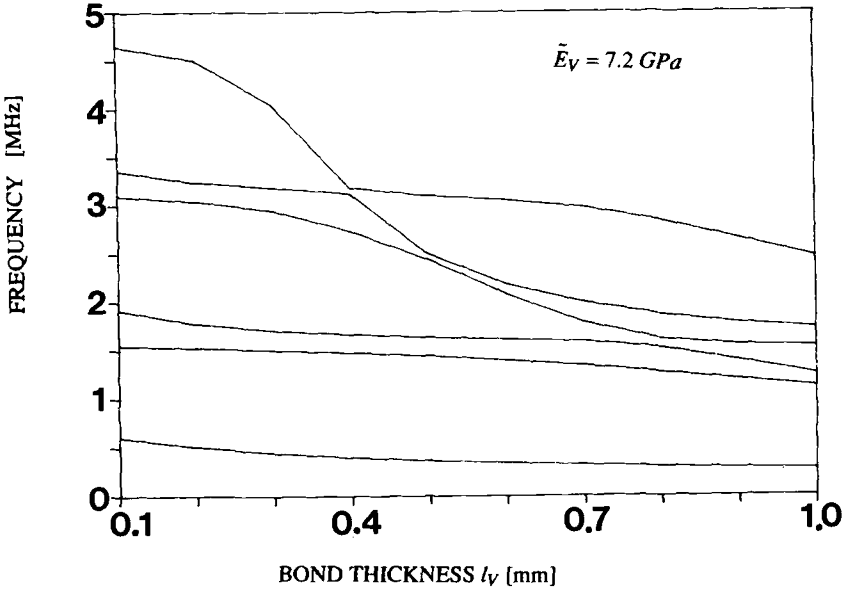

FIG. 5 -- Numerically calculated resonances in bonded specimens vs l_V.

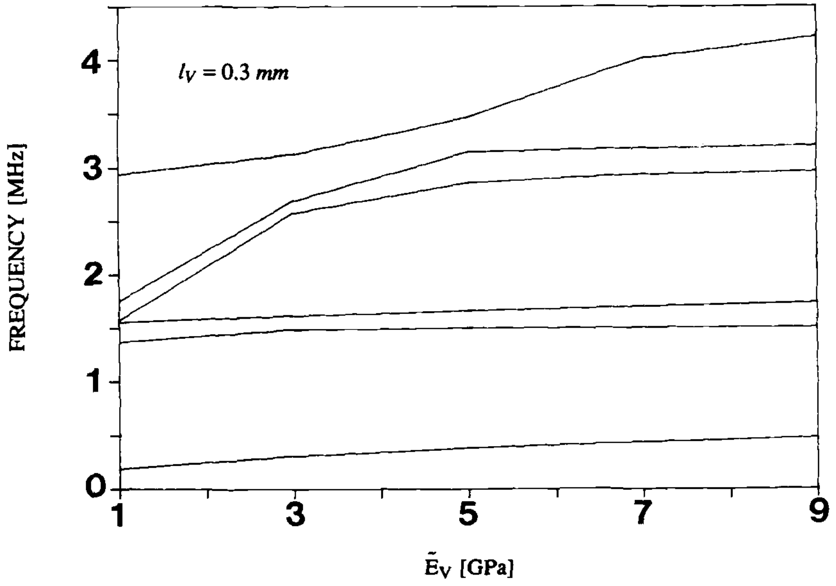

FIG. 6 -- Numerically calculated resonances in bonded specimens vs $\tilde{E}_V$.

If the receptance model were a perfect representation of the system, and all experimental measurements were exact, the data of Table 2 could be correlated with contours such as those shown in Figures 5 and 6 to yield exact values of $\tilde{E}_V$ and l_V. In the absence of such perfection, there is the potential for significant errors in calculated values of the adhesive parameters based on Eq 7 and measured values of two natural frequencies. Guyott and Cawley recognized this problem [16]; they suggested that a number q resonances, $q > 2$, be experimentally measured, and a decision function $D(\tilde{E}_V, l_V)$ be defined as follows:

$$D(\tilde{E}_V, l_V) = \sum_{i=1}^{q} \left[\frac{[\omega_i(\tilde{E}_V, l_V) - \omega_i^*]^2}{\omega_i(\tilde{E}_V, l_V)} \right] \tag{8}$$

where ω_i^* are the experimentally measured natural frequencies listed in Table 1, and $\omega_i(\tilde{E}_V, l_V)$ are the corresponding frequencies calculated from Eq 7. The value of D should approach zero for the true values of $\tilde{E}_V$ and l_V. Limitations of the receptance model and the frequency dependence of $\tilde{E}_V$, however, prevent this zero value from being reached. Instead, the iteratively determined set $(\tilde{E}_V, l_V)$ for which D is a minimum is assumed to characterize the adhesive layer. Limitations of this scheme are:

(a) The normalization factor on the right hand side of Eq 8 tends to unduly weight the lower resonant modes in determining the minimum value of D.

(b) The procedure demands a one-to-one match-up between each measured resonance and the corresponding harmonic calculated from Eq 7. This match-up may be difficult if the measured spectrum of natural frequencies does not contain any of the lower harmonics.

(c) The scheme cannot be used to find the precise frequency dependence of $\tilde{E}_V$, as the solution is dependent on data collected over a finite frequency range.

(d) The scheme requires a very large amount of computer time, in order to find the values of $\omega_i(\tilde{E}_V, l_V)$, $i = 1, .. q$.

For the spectrum shown in Figure 4, it was not possible to match up each measured resonant frequency ω_i^* with its numerically evaluated harmonic $\omega_i(\tilde{E}_V, l_V)$. Equation 8 could therefore not be used to determine adhesive layer parameters. A new algorithm was therefore devised to determine $\tilde{E}_V$ and l_V via the parameter G, defined as follows:

$$G(\tilde{E}_V, l_V) = \sum_{i=1}^{q} \left[F(\tilde{E}_V, l_V, \omega_i^*) \right]^2 \tag{9}$$

where the q values of F are determined from Eq. (5). Values of G were calculated for a wide range of $\tilde{E}_V$ and l_V. A minimum in G is used to indicate values of $\tilde{E}_V$ and l_V for the test specimens. Note that this scheme can produce erroneous results if a measured resonant frequency does not have a corresponding value ω_i predicted by the receptance model; the presence of shear mode resonances could create such a problem. Confining one's attention to the most prominent resonances in Figure 4 will minimize this danger.

The measured resonant frequencies listed in Table 2 were divided up into sets, and a minimum in G was sought for each set. Only two such sets were used for the immersion results; each set must contain resonances within a small frequency range, as $\tilde{E}_V$ is known to be frequency dependent. Results are given in Table 3. Calculated values of E_V were 7.04 *GPa* and 8.99 *GPa* at average frequencies of 7.1 *MHz* and 10.1 *MHz*, respectively. Within experimental error, these results are not inconsistent with the ultrasonic time-of-flight data shown in Figure 3; deviations between the two measurement methods are on the order of 10-15%. As discussed earlier, the ultrasonic measurements were made on bulk samples of adhesive, whose properties may differ somewhat from bond material within an adhesive joint.

Estimates of the bond thickness l_V from Eq 9 were 0.64 and 0.47 *mm*. Compared to the destructively measured value of 0.61 *mm*, it is seen that the errors are substantial, up to 23%; it is possible that one or more of the observed resonances did not correspond to those predicted by the receptance model.

Contact Measurements

A second set of measurements was taken for the same specimens, this time using a contact through-transmission technique with a matched pair of damped probes with a frequency band extending from 5 to 15 *MHz*. The two probes were mounted with a coupling oil on opposite sides of the joint, and held in place by a controlled, constant pressure. The transmitter was excited by a sweep generator, Wavetek model 166, sweeping from 4.5 *MHz* up to 15 *MHz*. The amplitude of the signal picked up by the receiver probe was measured and stored as a function of frequency. Any modulation of the amplitude-frequency relationship due to nonlinearity of the electronics was eliminated by deconvolution with a reference signal.

The signal spectrum amplitude after this deconvolution process is shown in Figure 7. Peaks in the spectrum indicate resonances of the entire probe-joint-probe system. These frequencies are listed in Table 2.

TABLE 3 -- Numerically estimated values of adhesive effective modulus and thickness

	Resonance Designation[a]	Average Frequency (*MHz*)	E_V (*GPa*)	l_V (*mm*)
Immersion:				
	1,2,3	7.1	7.04	0.64
	4,5,6	10.1	8.99	0.47
Contact:				
	2,3,4	6.5	8.22	0.40
	5,6,7	9.3	8.97	0.54
	8,9,10	12.6	8.20	0.73

[a] Refers to tabulated resonance designations of Table 1. Values of $\tilde{E}_V$ and l_V were calcualted using up to four adjacent resonances.

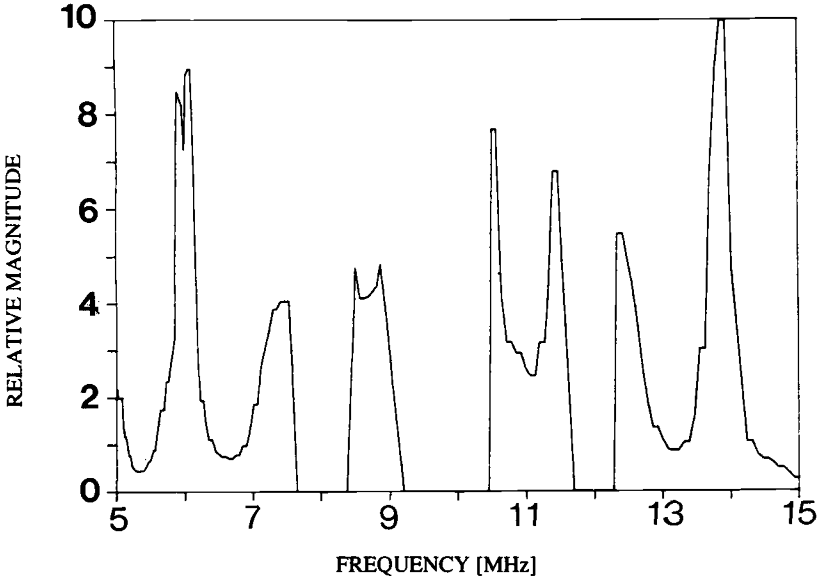

FIG. 7 -- Magnitude spectrum of ultrasonic signals in contact test

Because the contact testing configuration corresponds to a five-layer system (transmitter, adherend, adhesive, adherend, receiver), Eq 5 must be modified. The direct receptance of a five-layer system is derived in Appendix A under the assumption that the effects of damping can be neglected. This receptance, given by Eq A-5, must become infinite (i.e., its denominator F must go to zero) at the natural frequencies:

$$F(\tilde{E}_V, l_V) = \alpha^W_{1,1} + \alpha^U_{2,2} - c_3 \cdot \alpha^U_{1,2} \qquad (10)$$

where c_3 is defined by the recursive relation given in Eq A-6. Note that Eq. (10) has been somewhat simplified due to the symmetry of the system shown in Figure 2. The resonant frequencies for contact testing were divided into three groups, as was done for the immersion results. Application of Eqs 9 and 10 then gave values of E_V and l_V, listed in Table 3. Values for the elastic modulus are seen to be close to those obtained with immersion testing. Values for l_V again showed considerable spread, although their mean is within 10% of the destructively measured value of 0.61 *mm*.

The principle behind the contact and immersion schemes is the same, although there are advantages to each method. For the immersion method, there is not the concern related to contact pressure of the probe. Automation of a test program by the use of C-scans is also more amenable to an immersion environment. However, contact testing is more practical in many industrial situations, where the structure is very large or where immersion of the joint could lead to water damage of the structure. Contact measurements may also be more practical in very confined spaces, or where the surface is highly contoured. In addition, the resonant frequencies were easier to identify with contact testing.

The results reported for the immersion and contact tests correspond to specimens with relatively thick adhesive layers - on the order of 0.6 *mm*. Tests were also conducted on specimens with adhesive layers with l_V as small as 0.05 *mm*. However, as noted by Guyott and Cawley [2,22] and Curtis [3], the resonant frequencies of such specimens are highly insensitive to the characteristics of the adhesive layer, particularly for the lower harmonics. This is a quandary that has plagued commercial instruments that rely on measurements of natural frequencies to infer properties of the adhesive; an illustration is provided in the next section.

FOKKER BONDTESTER

The Fokker Mark II bondtester has seen widespread use for the inspection of adhesive joints in the aviation industry [2,5,18,29]. The purpose of the instrument is to evaluate the cohesive strength of the adhesive, and detect the presence of disbonds through measurement of resonance parameters. The assessment of cohesive strength is based on empirical relationships between strength and the resonant frequencies and amplitudes.

The instrument consists of a sweep frequency generator, which scans over a range of approximately 80 *kHz*, with a central frequency that can be set anywhere from 50 *kHz* to 500 *kHz*. The generator output is fed to a contact piezoelectric probe, in a pulse-echo configuration. An internal circuit monitors the apparent impedance of the probe as a function of frequency; the impedance drops to a minimum whenever the frequency is at a natural resonance of the probe. If the probe is linked via a coupling fluid to a plate or adhesive joint, then the internal circuit will detect resonances of the entire probe-joint system.

To start the test sequence, an initial signal is obtained by placing the bondtester on a single adherend; the bondtester stores the measured resonant frequency of the probe-adherend system as a reference. It has been demonstrated that the measured value of this resonant frequency corresponds well with that predicted by a 2-layer receptance model [2]. (Analysis has shown that there are actually several resonant modes and corresponding frequencies possible in the operating range of the instrument. In practice, only one of these modes is used, the selection depending on the thickness and stiffness of the adhesive.)

When placed on an adhesively bonded joint, the system resonance will shift from the resonance value, and this shift $\Delta\omega$ is indicated on the instrument readout. An assessment of the cohesive strength is then based on data charts supplied by the instrument manufacturer that correlate cohesive strength with $\Delta\omega$. A different chart is required for each joint configuration and type of adhesive.

An estimate of $\tilde{E}_V$ is never explicitly determined by the bondtester. In fact, for very thin (less than 0.2 *mm* thick), stiff adhesive layers, the sonically induced deformation takes place largely within the adherends. For such bonds, typical of those used in the aviation industry, there is little sensitivity of $\Delta\omega$ to the adhesive modulus, thickness, or density. In the limit of vanishingly small l_V, the specimen behaves like two adherends coupled together with no intervening adhesive layer, and the resonant frequencies are determined from Eq 3 with l_V set to zero.

For adhesive layers that are relatively thick and not so stiff, the adhesive acts as a spring with a stiffness constant $\tilde{E}_V/l_V$, linking two non-deformable masses together. Note that this model can be valid only for the fundamental mode. The resonant frequency will drop if the stiffness constant drops, but this does not uniquely indicate the perturbations in $\tilde{E}_V$ and l_V.

The data charts supplied by the bondtester manufacturer correlating the resonant frequency shift to cohesive strength are actually based on the assumption that the elastic modulus of the adhesive is a constant, and that any perturbation of resonant frequency must be caused by a shift in l_V. Several researchers have noted that, in general, the cohesive strength of a bond tends to drop if l_V is increased or $\tilde{E}_V$ is decreased. In either case, a drop in the fundamental resonant frequency may indeed be an indication of decreasing bond strength. However, the dependence of strength on $\tilde{E}_V$ is different from that on l_V so that the charts may not indicate the correct deviation in cohesive strength.

To help resolve ambiguous readings, the instrument has a second indicator that shows the strength of the resonance, which in turn is dependent on the amount of damping. This is particularly useful for the inspection of honeycomb structures, where the resonant frequency as measured by the instrument is only very weakly dependent on the honeycomb structure and the condition of honeycomb-to-adherend bonding. In such a case, the measured damping coefficient is a good indicator of flaws.

Experiment

A series "A" of single lap shear specimens was manufactured following the ASTM D1002-72 Standard for the strength properties of adhesives in shear by tension loading of metal-to-metal specimens. The adherends were Al-2043 T3, each 1.62 *mm* thick, and pretreated by a chromic-acid anodization process according to the MIL-A-8625D Standard. The purpose of this pretreatment is to place a uniform layer of oxide, approximately 1.5 μm thick, on the adherends to promote high adhesive strength across the adherend-bond interface. The adhesive was FM-73 [28]. Bondline thickness was controlled by side shims; a range of l_V from nominal 0 up to 0.5 *mm* was used. The curing cycle recommended by the manufacturer was employed.

For comparison, a second series "B" of specimens was made, but a chromic acid conversion process was used to pretreat the adherends. This treatment tends to leave a highly non-uniform oxide layer that is less well suited for adhesive bonding in this case than the anodization process. The curing cycle was identical to that for series "A".

A third series "C" of specimens was made, identical to series "A" except that a much higher curing temperature was used, resulting in a scorching effect. For this series, all specimens had l_V equal to 0.5 *mm*.

All specimens were inspected using the Fokker bondtester; results are shown in Figure 8. Figure 9 shows the destructively measured breaking load for the specimens. The following trends are noted:

(a) For series "A", which received the proper adherend pretreatment, failure was cohesive in nature. For $l_V < 0.3$ *mm*, breaking load was largely independent of l_V; breaking load dropped when l_V was raised beyond this limit. These results correlated well with those of the bondtester, except for l_V equal to nominal zero. This discrepancy may be due to a number of factors, but it is known that resonance techniques are highly insensitive to bond material characteristics for very thin bondlines.

(b) The series "B" specimens failed adhesively due to the non-optimum pretreatment. Because the interface between each adherend and the adhesive is so thin, the system resonances are totally insensitive to the interfacial condition. The bondtester is therefore seen

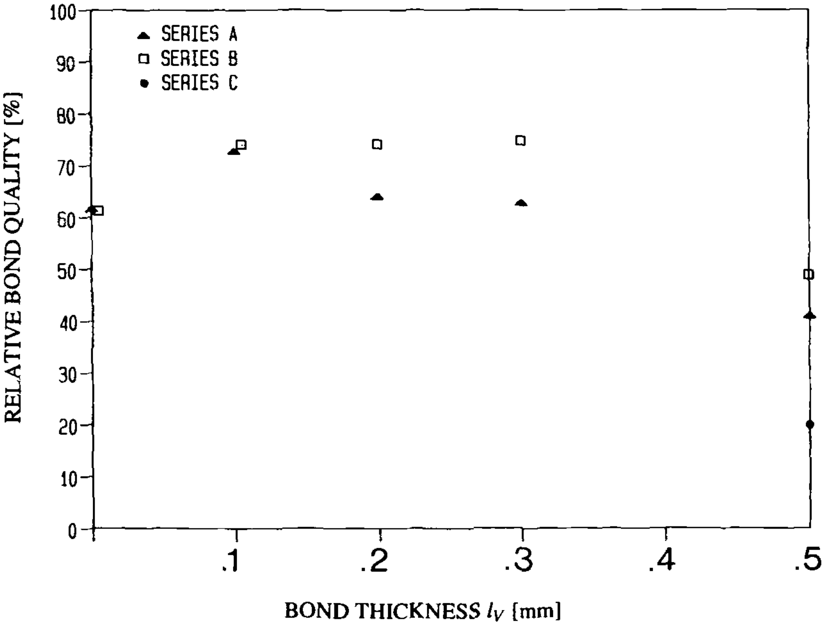

FIG. 8 -- Cohesive strength of adhesive joint, estimated by Fokker bondtester.

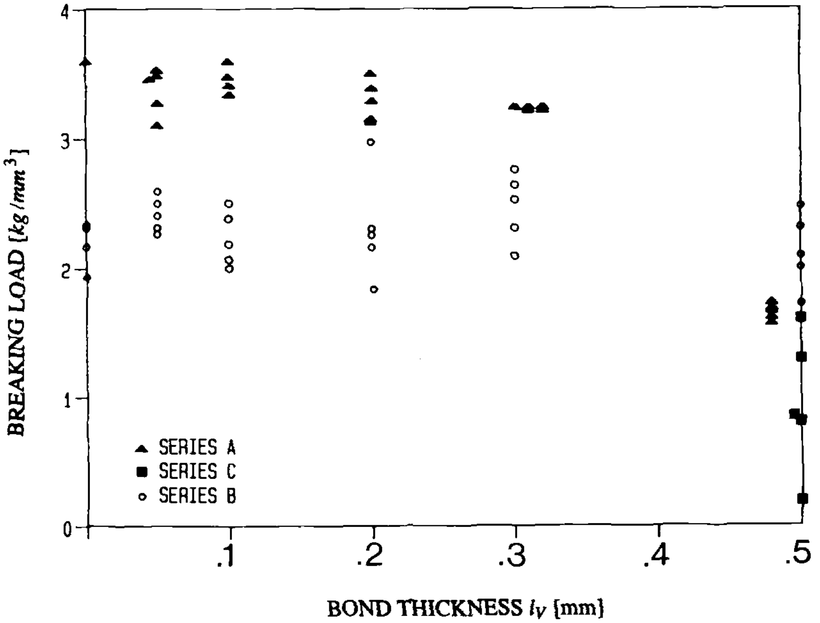

FIG. 9 -- Breaking loads of test specimens.

to be useless for identifying low interfacial strength. As expected, the bondtester indicates similar cohesive strength for series "A" and "B", as they had the same adhesive and curing process.

(c) The scorched specimens of series "C" suffered damage to the bulk adhesive from the excessive curing temperature. The low cohesive strength predicted by the bondtester was confirmed by destructive testing.

CONCLUSIONS

Receptance analysis can be used to determine the resonant frequencies of an adhesive joint as a function of the adhesive density, elastic modulus, and thickness. The bond's cohesive strength is in turn dependent on many factors, including the elastic modulus and stress distribution. Under certain conditions therefore, the bond strength can be inferred from a measurement of the resonant frequencies. There are, however, serious limitations to this scheme:

(1) Failure of an adhesive joint may be either adhesive or cohesive in nature. Resonant frequencies give no information as to the adhesive (interfacial) strength.

(2) Resonant frequencies of a bond are sensitive to the cohesive strength only for relatively thick bondlines. Such specimens are not representative of those required for certain high performance applications, such as the aircraft industry.

(3) The strong frequency dependence of the adhesive's elastic modulus seriously complicates the processing of resonant frequency data, and contributes to an uncertainty in the final results.

(4) The extent of lateral constraint on the adhesive affects the value of the apparent modulus E_V. This constraint is in turn dependent on the bondline thickness, specimen geometry and test frequency. These factors make it difficult to compare the results of two different methods for determining the apparent modulus of the adhesive.

APPENDIX A: RECEPTANCE MODEL FOR A MULTI-LAYERED BODY

Consider a one-dimensional body made up of N layers Y_i, $i = 1, \ldots N$ in intimate contact, as shown in Figure A-1.

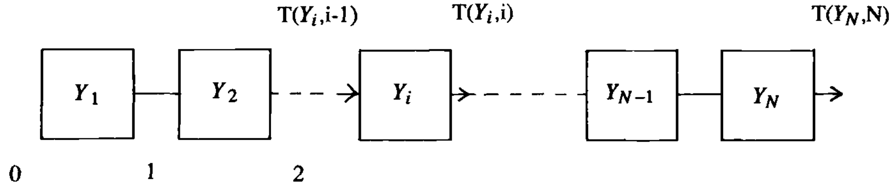

FIG. A-1 -- Model of multi-layered system for receptance analysis

The boundary to the right of Y_i is labeled point i. Each layer Y_i is subjected to two forces per unit area: $T(Y_i, i)$ acting on point i, and $T(Y_i, i-1)$ acting at point $i-1$. All forces are internal to the system except for $T(y_1, 0)$ which is set to zero, and $T(Y_N, N)$. By Newton's third law of motion,

$$T(Y_i, i) + T(Y_{i+1}, i) = 0 \tag{A-1}$$

Continuity of displacement $\psi(Y_i, i)$ of point i in layer Y_i can be expressed as:

$$\psi(Y_i, i) = \psi(Y_{i+1}, i) \tag{A-2}$$

From the definition of the receptance given in Eq 4, it is easily shown:

$$\psi(Y_{i+1}, i) = \alpha_{i,i}^{Y_{i+1}} \cdot T(Y_{i+1}, i) + \alpha_{i,i+1}^{Y_{i+1}} \cdot T(Y_{i+1}, i+1), \quad i=0, \ldots N-1 \tag{A-3}$$

$$\text{and} \quad \psi(Y_i, i) = \alpha_{i,i}^{A_i} \cdot T(Y_i, i) + \alpha_{i,i-1}^{A_i} \cdot T(Y_i, i-1), \quad i=1,\dots N \tag{A-4}$$

For the cases of the system for ultrasonic contact measurements shown in Figure 2, $N = 5$ and the system is symmetric: $Y_1 = Y_5 =$ "W", $Y_2 = Y_4 =$ "U", and $Y_3 =$ "V". Combination of Eqs A-1 to A-4 yields the direct receptance of the system $\psi(W, 5)/T(W, 5)$:

$$\frac{\psi(Y_5, 5)}{T(Y_5, 5)} = \alpha_{5,5}^{Y_5} - c_4 \cdot \alpha_{5,4}^{Y_5} \tag{A-5}$$

where c_i is defined by the recursive relation:

$$c_i = \begin{cases} \dfrac{\alpha_{i,i+1}^{Y_{i+1}}}{\alpha_{i,i}^{Y_i} + \alpha_{i+1,i+1}^{Y_{i+1}} - c_{i-1} \cdot \alpha_{i-1,i}^{Y_i}}, & i > 1 \\ \dfrac{\alpha_{1,2}^{Y_2}}{\alpha_{1,1}^{Y_1} + \alpha_{2,2}^{Y_2}}, & i=1 \end{cases} \tag{A-6}$$

Formulas for the direct and cross receptances of the individual layers, $\alpha_{m,m}^{Y}$ and $\alpha_{m,n}^{Y}$ are given in Eq 6.

The system is in resonance when the receptance at point 5, as given by Eq A-5, goes to infinity; this occurs when the denominator of Eq A-5, designated by the symbol F, goes to zero. This expression for F is used in Eq 10 to calculate the natural frequencies of the five-component system shown in Figure 2.

REFERENCES

[1] Stone, D. E. W.,"Nondestructive Methods of Characterising the Strength of Adhesive-Bonded Joints - A Review," Technical report 86058, Royal Aircraft Establishment, Ministry of Defence, Farnborough, Hants, UK, 1986.

[2] Guyott, C. C. H., and Cawley, P., "Use of the Fokker Bondtester on Joints with Varying Adhesive Thickness", presented at the International Conference on structural Adhesives in Engineering, 1988; available as paper C162/86 in Conference Publication 1986-86, Mechanical Engineering Publications Limited, London,

[3] Curtis, G. J., "A Critique of Acoustic Methods of Adhesive Bond Strength Determination", in Adhesion 4, Applied Science Publishers Limited, London, 1980, pp. 113-147.

[4] Adams, R. D., and Cawley, P., "A Review of Defect Types and Nondestructive Testing Techniques for Composites and Bonded Joints", NDT International, Vol. 21, No. 4, Aug. 1988, pp. 208-222.

[5] "Introduction to the Fokker Bondtester Model 80 L", operation manual, Fokker B.V., Amsterdam, The Netherlands, 1986.

[6] Segal, E., and Rose, J. L., "Nondestructive Testing Techniques for Adhesive Bond Joints," in Research Techniques in Nondestructive Testing, Vol. 4, Academic Press, London, 1980, pp. 275-316.

[7] Lange, Y. V., "The Local Method of Free Elastic Vibrations and its Applications to Testing in Industry," NDT International, Vol. 18, No. 5, Oct. 1985, pp. 256-260.

[8] Hartshorn, S. R., "The Durability of Structural Adhesive Joints", in Structural Adhesives, Chemistry, and Technology, Plenum Press, New York, 1986, pp. 347-406.

[9] Venables, J., D., "Adhesion and Durability of Metal/Polymer Bonds", Proceedings of the International Symposium on Adhesive Joints, Kansas City, Plenum Press, 1982 pp. 453-467.

[10] Venables, J. D., "Adhesion and Durability of Metal/Polymer Bonds," in Adhesion 7, Applied Science Publishers Limited, London, 1983, pp. 87-93.

[11] Minford, J. D., "Permanence of Adhesive-Bonded Aluminum Joints", in Adhesives in Manufacturing, Marcel Dekker Inc., New York, 1983, pp. 567-601.

[12] "Standard Practice for Preparation of Metal Surfaces for Adhesive Bonding," ASTM Standard D2651-79 (reapproved 1984), in 1988 Annual Book of ASTM Standards, Vol. 15.06, American Society for Testing and Materials, Philadelphia, year 1988, pp. 167-171.

[13] Brockerman, W., Hennemann, O. D., Kollek, H., and Matz, C., "Adhesion in Bonded Aluminum Joints for Aircraft Construction," International Journal of Adhesion and Adhesives, Vol. 6, No. 3, July 1986, pp. 115-143.

[14] Pocius, P., "Fundamentals of Structural Adhesive Bonding," in Structural Adhesives, Chemistry, and Technology, Plenum Press, New York, 1986, pp. 23-68.

[15] Sinclair, A. N., Graf, M., and Allen A. L., "Mechanical Wave Interaction at a Diffuse Interface," Research in Nondestructive Evaluation, Vol. 1, No 1, 1989, pp. 31-49.

[16] Guyott, C. C. H. and Cawley, P., "Evaluation of the Cohesive Properties of Adhesive Joints Using Ultrasonic Spectroscopy," NDT International, Vol. 21, No. 4, Aug. 1988, pp. 233-240.

[17] Adams, R. D., Coppendale, J., and Peppiatt, N. A., "Failure Analysis of Aluminum-Aluminum Bonded Joints," in Adhesion 1, Applied Science Publishers Limited, London, 1978, pp. 105-120.

[18] Lloyd, E. A., and Brown, A. F., "Recent Developments in Non-Destructive Testing of Adhesive-Bonded Joints," in Adhesion 1, Applied Science Publishers Limited, London, 1978, pp. 133-144.

[19] Bikerman, J. J., "Experimental Strength of Adhints," in The Science of Adhesive Joints, Second edition, Academic Press, New York, 1968 pp. 264-307.

[20] Ramakrishnan, N., De, A. K., and Suryanarayan, S., "Dynamic Effective Young's Modulus of Thin Adhesive Layers in Bonded Joints," Journal of Testing and Evaluation, JTEVA, Vol. 10, No. 5, Sept. 1982, pp. 192-198.

[21] Jangblad, D., Gradin, P., and Stenström, T., "Determination and Verification of Elastic Parameters for Adhesives," Adhesively Bonded Joints: Testing, Analysis, and Design, ASTM STP 981, American Society for testing and Materials, Philadelphia, 1988, pp. 54-68.

[22] Guyott, C. C. H. and Cawley, P., "The Ultrasonic Vibration Characteristics of Adhesive Joints," Journal of the Acoustical, Society of America, Vol. 83, No. 2, Feb. 1988, pp. 632-640.

[23] Mercier, N. and de Belleval, J. F., "Phase Information in Ultrasonic Spectroscopy," Proceedings of the IEEE 1983 Ultrasonic Symposium, Institute of Electrical and Electronic Engineers, New York, 1983, pp. 909-913.

[24] Meyer, P. A. and Rose, J. L., "Modeling Concepts for Studying Ultrasonic Wave Interaction with Adhesive Bonds," The Journal of Adhesion, Vol. 8, Oct. 1976, pp. 107-120.

[25] Bishop, R. E. D. and Johnson, D. C., "Torsional and Longitudinal Vibration of Uniform Shafts and Bars," in The Mechanics of Vibration, Cambridge University Press, London, 1960, pp. 245-281.

[26] Brekhovskikh, L. M., Waves in Layered Media, second edition, Academic Press, New York, 1980.

[27] Adams, R. D. and Coppendale, J., "Measurement of the Elastic Moduli of Structural Adhesives by a Resonant Bar Technique," Journal of Mechanical Engineering Science, Vol. 18, No. 3, June 1976, pp. 149-158.

[28] American Cyanamid, Havre de Grace, Maryland 21078.

[29] Guyott, C. C. H., Cawley, P. and Adams, R. D., "Vibration Characteristics of the Mk II Fokker Bond Tester Probe," Ultrasonics, Vol. 24, No. 6, Nov. 1986, pp. 318-324.

Peter L. Lovelady and Miguel Picornell

SAMPLE COUPLING IN RESONANT COLUMN TESTING OF CEMENTED SOILS

REFERENCE: Lovelady, P.L., and Picornell, M., "Sample Coupling in Resonant Column Testing of Cemented Soils," Dynamic Elastic Modulus Measurements in Materials, ASTM STP 1045, Alan Wolfenden, Ed., American Society for Testing and Materials, Philadelphia, 1990.

ABSTRACT: Low-strain shear moduli of lightly cemented sand can be obtained by testing specimens in a resonant column. In the literature a variety of techniques have been suggested for coupling the sample to the base and cap of the device. These studies' results suggest that the shear modulus of cemented sand changes with confining pressure. In this study, the specimens were coupled to the end platens with epoxy which was allowed to harden before testing. The results indicate that the low strain shear modulus of lightly cemented sand is nearly independent of confining pressure for pressures up to 500 kPa. The difference in the effect of confining pressure on the shear modulus, in this and other studies, is attributed to the different coupling techniques used. The results illustrate the need for a rigid connection between the specimen and the end platens.

KEYWORDS: resonant column, soil tests, soil dynamics, shear modulus, cemented soils, sample coupling, sand

INTRODUCTION

The shear modulus of soils at low strain amplitudes is commonly determined in a resonant column device. A cylindrical soil specimen is placed between a base plate and a cap and a torsional sinusoidal force excitation is applied by electromagnetic oscillators. Several types of imposed boundary conditions on the ends of the specimen are in use to perform this type of test, but perhaps the most common type is the fixed-free conditions; where one end of the specimen is held rigidly fixed, while the other end is subject to the force function. The vibratory response of the free end of the specimen is used to backfigure the shear modulus of the specimen at the strain amplitude imposed. The test consists of increasing the frequency of the force function until resonance is achieved in the fundamental mode of vibration of the specimen. The resonant frequency is then used to calculate the apparent shear modulus of the specimen.

P.L. Lovelady, research assistant, and Dr. M. Picornell, assistant professor, are affiliated with the Department of Civil Engineering, University of Texas at El Paso, El Paso, Texas 79968-0516.

A very critical aspect of this test is the coupling between the specimen and end platens. In routine torsional soil testing, porous stones are rigidly attached to the end platens and the friction between the porous stones and the soil is enough to develop an adequate coupling at low strain amplitudes. The effectiveness of this coupling technique at higher strain amplitudes is limited by the effective axial stress across the specimen-platen contacts, the shear modulus of the specimen, and the friction coefficient between end platens and specimen [1]. The coupling between specimen and platens increases with increasing confining pressure. Alternative coupling techniques are in use to transmit the shear stresses induced by the torsional excitation. One alternative consists of attaching radial teeth to the end platens, that are sunk into the ends of the specimen [2].

Techniques similar to those described have been used by some researchers [3, and 4] for dynamic testing of artificially cemented soils. This study questions the effectiveness of these coupling techniques for cemented sands. In this study, resonant column tests were performed on artificially cemented sands with a coupling technique that ensures binding between the specimen and the end platens. The results of this study are compared to the results obtained with other coupling techniques. This comparison provides a basis on which the capabilities of the different coupling methods can be evaluated.

ANTECEDENTS

The shear modulus of cohesionless soils is known to be affected by a number of parameters. The most important factors are the effective confining pressure (or the mean principal stress in triaxial loading) and the strain amplitude imposed on the specimen. The shear modulus is the largest at low-strain amplitudes. The maximum shear modulus of cohesive and cohesionless soils has been found to depend on the mean principal effective stress [5, and 6] through the following empirical equation:

$$G_{max} = K\,(\bar{\sigma}_o)^{0.5} \qquad (1)$$

where G_{max} is the low-strain shear modulus, K is a function of void ratio and overconsolidation ratio, and $\bar{\sigma}_o$ is the mean principal effective stress. The exponent, 0.5, of the confining pressure has been confirmed by the work of a number of researchers [2]. It has been suggested that this equation consistently predicts the variation of maximum shear modulus (of clean dry cohesionless soils) with void ratio and confining pressure within about ten percent [7]. Thus, there is overwhelming evidence that a log-log plot of the maximum shear modulus of clean dry cohesionless soils should be a straight line with a slope of 0.5.

The non linearities of the stress-strain equation for granular soils has been explained with a theoretical model of perfect spheres [8]. The deformation of the skeleton of spheres is elastic only at the very first stages of loading. As the stress increases, slip begins to take place around the edges of the contact area between the spheres. After the shear force at the contact exceeds the friction developed between spheres, gross sliding of the spheres starts to take place. In a real cohesionless soil, some contacts between grains are much less stable than others. Thus, gross sliding does not occur at all contact points at the same time but, rather, there is a gradual collapse of the structure. This results in a progressively more compact structure with an increase of the number of contact points per particle.

These considerations suggest that the stiffening of the granular soil skeleton with confining pressure is the result of two phenomena. One is the gross sliding of particles that results in a more compact grain skeleton with a larger number of contact points per particle. The second is the increase of the normal interparticle forces resulting in a stiffer binding between grains.

The relative importance of these effects has been illustrated in shear wave velocity measurements on a dry crushed quartz silt [9]. These measurements indicate that the exponent (power) of the confining pressure is 0.6 on first loading, which also causes a large change in void ratio of the specimen. By way of contrast, upon reloading of the specimen, negligible changes of void ratio occur and the power of the confining pressure is only 0.17.

These considerations helped to develop a working hypothesis of the behavior that is reasonable to expect from cemented sands. In this sense, the only modification to introduce in the sphere model discussed above is to include the effect of the cementation deposited at the contacts between particles. In a cemented granular soil, to cause gross sliding of the particles, it is necessary to exceed the friction between grains and the strength of the cement bond. Thus it seems reasonable to expect that the shear modulus of cemented sand will depend on a power of the confining pressure which should be small initially (ie., a flat slope of the maximum shear modulus log-log plot) until the cement bonds are broken, and, thereafter, would behave as uncemented sand. The magnitude of the change of the power of the confining pressure should be controlled by the extent of the cementation at the interparticle contacts and the strength of the cement itself.

There is some evidence in the existing literature that support this hypothesis. The initial tangent modulus of elasticity of concrete mixes has been shown to be independent of confining pressure [10]. Also, resonant column tests on frozen silts indicate that the shear modulus is independent of confining pressure [11] in the range of confining pressures tested (90-500 kPa). Furthermore, these tests show that the shear modulus increases two fold when the temperature of the specimen is decreased from -1°C to -10°C, thus indicating that the shear modulus is primarily determined by the rigidity of the cementation. These studies illustrate that, at low-strain amplitudes, the shear modulus of highly cemented granular media is determined by the cementation. Furthermore, the shear modulus is found to be independent of the applied effective confining pressure on the specimen.

In summary, the shear modulus of uncemented soils is a function of the power of 0.5 of the confining pressure, and the shear modulus of highly cemented soils is independent of confining pressure. It seems reasonable that these two extremes should bound the behavior for intermediate degrees of cementation or for lower strength cements. This appears to be the case for lime treated expansive clays [12], which exhibit a change in shear modulus to the 0.1 power of the confining pressure. The shear modulus of unsaturated silts and sands has been shown to be affected by the additional effective stress caused by the pore water menisci [7]. The shear modulus is maximum at some intermediate degree of saturation. At this point, the gross sliding of individual grains would have to occur by destroying the menisci and, thus, the pore water would act as some sort of weak cement. The results of this study [7] suggest that the shear modulus of unsaturated silts and clays changes with the power of 0.37 of confining pressure. Therefore, it appears that even very weak cements such as the pore water menisci can have a discernible effect on the power of the confining pressure.

PREVIOUS INVESTIGATIONS

Several researchers have published results of resonant column tests on cemented sand [3, 4, and 13]. In the first work known to the authors, [3], Type I Portland cement was used to stabilize a naturally occurring sand with particle sizes falling between sieves No. 10 and No. 200. The dry sand was mixed with the cement, and the appropriate amount of water to achieve the desired moisture content was added and mixed with the sand-cement. The specimens were formed by compacting the mix in five layers in a Harvard miniature compactor mold. After compaction, the specimens were extruded, wrapped in plastic, and cured for 28 days in a controlled environment at 21°C and at a relative humidity of 95%.

The cured specimens were tested in a fixed-free resonant column to determine the shear modulus at low strain amplitudes. There is no report that any special precaution had been adopted to ensure the coupling of the specimens to the base and cap of the device. The specimens were prepared at the optimum conditions identified in previously performed compaction tests. Specimens with three degrees of cementation (2, 4, and 6%) were tested, and the confining pressures used ranged from 20 kPa to 240 kPa.

The results reported by [3] on untreated sand specimens confirm the findings of earlier studies; that is, the shear modulus at low strain amplitudes changes with the power of 0.5 of the confining pressure. Regarding cemented specimens, the study's results indicate that the higher the cement content the higher the effect (the power) of confining pressure on the shear modulus of the specimen. While the shear modulus of uncemented sand increased with the 0.5 power, the shear modulus of the 6% cement specimens increased with the 0.86 power of confining pressure.

In another study of the shear modulus of artificially cemented sand [4], Monterrey No. 0/30 sand was cemented with Type I-II Portland cement. The specimens were prepared in lucite cylinders. A portion of the sand was first shaken with the cement and then the desired amount of water was added. The rest of sand was then added to the mix. The sand-cement-water mixture was pluviated into the mold with intermitting tapping on the sides of the mold to achieve the desired density. The specimens inside the mold were placed inside a water bath and cured for 14 days.

The specimens were removed from the mold by opening a lengthwise slit of the mold. This allowed the specimen to slide freely out of the mold. The specimens were placed in a fixed-free resonant column device and the coupling to the end platens was entrusted to eight radial teeth embedded in each of the porous stones. The testing program included uncemented specimens, and specimens with 1, 2, and 4% cement. The confining pressures used ranged from 10 kPa - 400 kPa.

The results of [4] indicate that the shear modulus of uncemented Monterrey No. 0/30 increases with the 0.43 power of confining pressure. The cementation causes a general increase of the shear modulus of the specimen, but the shear modulus of the cemented specimens is found to increase with the same power (0.43) of confining pressure.

In a third study [13], specimens of Monterrey No. 0 sand cemented with Type I Portland cement were tested in a longitudinal and torsional Drnevich resonant column device. The specimens were prepared by compacting a cement-sand-water mixture in eight layers in PVC molds. The mix for each layer was weighted and mixed separately. The specimens were cured underwater for variable lengths of time. Afterward, the specimens were extruded from the molds, and a gypsum cement was used to couple the specimen to the end platens. This cement prevented the saturation of the specimens in the resonant column. Specimens with cement contents of 1, 2, 5, and 8% were tested, and the confining pressures used ranged from 49 kPa to 588 kPa.

The results of [13] were presented as the increase of the low-strain shear modulus of the cemented specimen above the shear modulus of the uncemented specimen. The results indicate that, at low degrees of cementation, the shear modulus of cemented sand changes with confining pressure with the same trend as for uncemented sand. As the cementation degree increases, the gain in shear modulus due to confining pressure is progressively reduced.

All three of the previous studies agree that increasing the cement content results in an increase of the shear modulus of the mix. However, the rate of increase of the shear modulus at low-strain amplitudes with confining pressure is completely different for each study. The first study [3] found increasingly larger powers of confining pressure for increasing cement content in the specimen. The second study [4] found that the degree of cementation did not alter the power of the confining pressure. The third study [13] found that increasing cement contents causes a decrease in the power of confining pressure from a maximum value at low cement contents to a minimum value at large cement contents.

The disagreement between the three studies as to the change in power of the confining pressure with the degree of cementation indicates that some of the testing techniques used might not have been appropriate. As a matter of fact, none of the three studies support the working hypothesis of the expected behavior of cemented soils described in the previous section. Although the reason is not apparent, the main difference between the three studies is the coupling of the specimen to the end platens. Thus, a potential cause of the disagreement is that the specimens were not coupled to the platens appropriately. Some of the results presented in the third study [13] also point in this direction. In this sense, the published dynamic moduli at low-strain amplitudes of 2% cement specimens at several confining pressures are presented in Table 1.

TABLE 1 -- Low strain dynamic moduli of cemented sands

Confining* Pressure (kPa)	Shear* Modulus (GPa)	Elastic* Modulus (GPa)	Poisson's Ratio
49	0.107	0.800	2.72
98	0.166	0.867	1.61
196	0.235	0.916	0.94
392	0.341	1.034	0.52
588	0.439	1.147	0.31

* Values Taken from Figure 6 in [13].

Also shown in the Table 1 are the Poisson's ratio calculated using the following relationship:

$$\nu = \frac{E}{2G} - 1 \qquad (2)$$

where E is the elastic modulus, G the shear modulus, and ν is the Poisson's ratio. The high values of Poisson's ratio backfigured are clearly meaningless. It is relevant to note that for increasing confining pressure the backfigured Poisson's ratio decreases. At the highest pressure used in [13], the Poisson's ratio becomes more credible. If the shear modulus was underestimated while the elastic modulus was correctly determined, then Eq. 2 would yield Poisson's ratios larger than the actual ones. This is precisely what the results in Table 1 show. Thus the high Poisson's ratio at low confining pressure and the concurrent decrease of Poisson's ratio for increasing confining pressures suggest that the shear moduli were underestimated in this study, a very likely cause being a poor coupling between specimen and end platens. Similar data were not available for the other two studies; thus no such evaluation was possible.

TESTING PROGRAM

The discrepancies observed in the existing literature (described in the previous section) indicated the potential need of a better coupling of the specimen to the end platens. With this purpose in mind, a testing program on cemented sand specimens was undertaken with an alternative coupling technique to those used in previous studies.

For this purpose, Ottawa sand was sieved and the size fraction passing sieve No. 40 and retained on sieve No. 100 was used for the preparation of the specimens. Type I-II Portland cement was used as the stabilizing agent. The amount of sand and cement needed for one specimen were first mixed together by shaking them together in a jar. Next, water was added to the sand-cement and mixed with a spatula in a bowl. The amount of water used was the same for all specimens; the amount was chosen to prevent the loss of water-cement during the compaction process. The mix was split into six equal amounts. Each amount was then compacted separately with the same number of blows from a heavy, large diameter cylinder in a teflon coated PVC mold slit along its side and held together with hose clamps. The top of each layer was etched to loosen some of the mixture so that the next layer could adhere. The compacted specimens inside the molds were then left to cure for six days in a 100% relative humidity environment; afterward, they were placed underwater in an accelerated curing tank at 60° C. After seven days, the specimens were removed from the tank and left to air dry for a week. Then, the hose clamps were removed, the slit opened, the specimen removed from the mold, and stored in an airtight plastic bag.

The specimens were then tested in a torsional resonant column (Drnevich). The specimens were coupled to the end platens with epoxy (2-ton clear Epoxy, by Devcon). This entailed slight modifications of the device. The porous stones were substituted with solid aluminum discs, manufactured to the same sizes as the porous stones, and tightly screwed to the base and cap. The base of the device has two orifices provided to allow the saturation of the specimen. The lower aluminum disc was carved in such a way that two orifices on the base were connected to a single central pipe protruding above the disc. The pipe was intended to prevent the epoxy from clogging the opening. The presence of the pipe forced the need to carve into the specimen a depression to house it. Although, the specimen was not glued at the center, the shear strains are minimum in this area and, thus, did not affect significantly the stiffness of the connection. This pipe allowed the performance of tests on saturated specimens, and insured that the pore air was at atmospheric pressure in the tests on dry specimens.

The test proceeded in the following steps:

1. The membrane was rolled on the pedestal and secured with O-rings.
2. The epoxy was spread on the base with a spatula. Prior to this the screw head slots were covered with talc.
3. The specimen was cemented and aligned on the base.
4. The epoxy was spread over the cap and the cap was then placed over the specimen.
5. The driving magnets and coils were assembled and centered immediately and the epoxy was then allowed to harden 24 hours.
6. Prior to testing, the membrane was rolled over the specimen and secured to the cap. Next, the cell was assembled.
7. Testing started at atmospheric pressure and at low-strain amplitudes. The cell pressure was then increased in 69 kPa steps to a maximum of 483 kPa.
8. Then the pressure was reduced to the desired value and testing proceeded to increasingly higher strain amplitudes.

Specimens were prepared with cement contents of 2, 3, 4, and 5% and for various relative densities of the sand. For each combination of cement content and relative density, an average of seven specimens were tested. Most specimens were tested dry, but one batch of 5% cement specimens were saturated first, then consolidated under the confining pressure, and the torsional excitation was applied under undrained conditions. The saturation of the specimen was attempted with backpressure after a vacuum had been applied inside the specimen.

RESULTS AND DISCUSSION

The epoxy resin used for coupling has a setting time of thirty minutes and develops full strength in sixteen hours. Nevertheless, a resonant column test was performed on a specimen twenty four hours after gluing the specimen; the same specimen was kept glued to the platens for a week and the dependence of maximum shear modulus on confining pressure redetermined. The results showed no discernible differences in shear modulus. Thus, there was no need to wait more than 24 hours.

The sizes of a batch of specimens was monitored during the curing period, and it was observed that the specimens were experiencing some changes in length. These minor changes have, nevertheless, appreciable effect on the relative density of sand particles. In this sense, the relative densities of the specimens reported here were recalculated based on the unit weights of the specimens at the time of testing. This was accomplished by subtracting the weight of cement and moisture present. Control tests were performed to ensure that the cement was evenly distributed throughout the specimens. For this purpose, specimens were split into six discs and each individual disc was thoroughly ground with a mortar and pestle. The cement and the sand were separated by sieving the material through sieve No. 100. The weights of cement recovered were constant for all six discs, thus indicating that a fairly uniform distribution of the cement was achieved throughout the specimens. Therefore, the sand relative densities backfigured from actual unit weights are thought to be more accurate than those attempted in the preparation of the specimens. Nevertheless, this resulted in slight variations (less than 5 percentage points) of the relative density of the sand for the specimen of each degree of cementation.

The low-strain shear moduli of each batch of specimens of the various degrees of cementation exhibited some scatter. This scatter is attributed to the slight variation of the relative density of the sand, and is illustrated in Figure 1, where the average of seven tests for each degree of cementation (3% and 5%) are shown together with the extreme test results. Although some scatter is present, all the tests show that the shear modulus changes with confining pressure in a similar manner.

The effects of confining pressure on the maximum shear modulus of cemented specimens are shown in Figure 2. The line shown for each degree of cementation is the average of seven determinations. Also shown as dots, out of scale, are the shear modulus of the specimens at atmospheric pressure. Shear modulus at atmospheric pressure were not attempted, or least reported, in previous studies. This fact had also suggested to the authors that specimen coupling was a potential problem in the previous works.

These results indicate that cementation has a very significant effect on the slope of the line of maximum shear modulus vs. confining pressure, in the sense that even minor degrees of cementation significantly reduce the dependence of maximum shear modulus on confining pressure. The hypothesis advanced in the ANTECEDENTS section can explain these results; that is, with increasing cementation the slope of the line decreases from the slope corresponding to uncemented soil to a nearly horizontal line for highly cemented (5% in this study) sand.

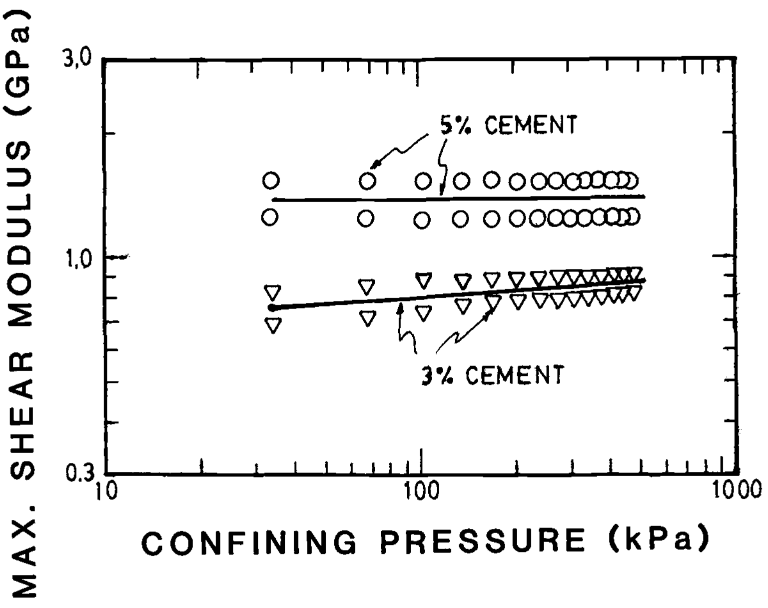

FIG. 1 -- Illustration of Typical Scatter in the Test Results.

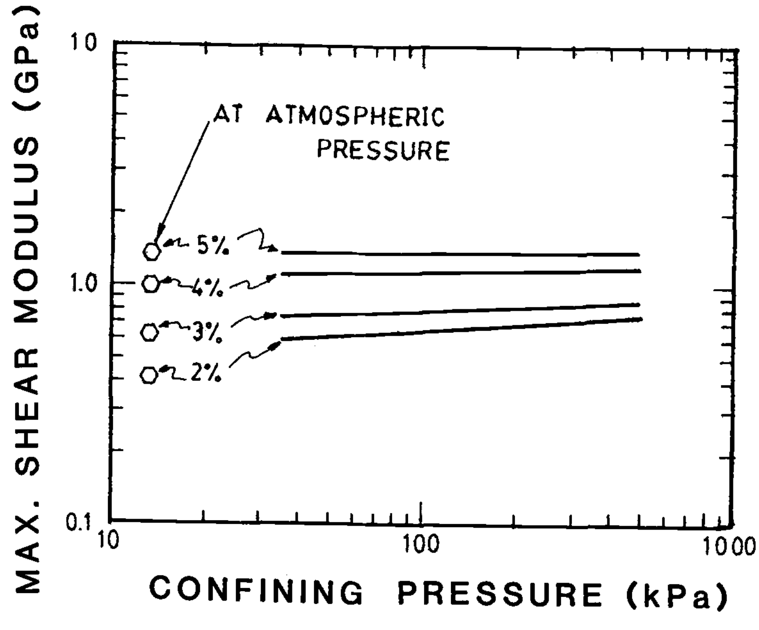

FIG. 2 -- Effects of Degree of Cementation on the Maximum Shear Modulus.

The results of the tests performed on saturated 5% cement specimens under undrained conditions are very close to the results obtained on the dry specimens. At low confining pressure, the results on dry specimens exceed by 1% the results on saturated specimens. At high confining pressures, the shear modulus of the saturated specimens exceeds by 5% the modulus of the dry specimens. For both lines the slopes are nearly zero: 0.005 and 0.026 for the dry and saturated specimens, respectively. Thus, these results indicate that saturation and undrained conditions during resonant column testing do not have a significant effect on the low-strain shear modulus of strongly cemented sands. A similar conclusion has been reached for silts and sands [7].

At higher strain amplitudes the behavior is markedly different for saturated or dry conditions. A comparison of the shear modulus versus strain amplitude for two specimens, one dry and the other saturated, is presented in Figure 3. Both curves show a wide range of low strains where the shear-modulus is at the maximum. After reaching a threshold strain, the shear modulus drops abruptly for both specimens; however, the saturated specimen started to experience the drop at lower strain levels than the dry specimen. Thus, the saturation of the specimen did not affect the shear modulus at low strain amplitudes; however, at high strain amplitudes, saturation has the effect of significantly reducing the shear modulus.

The degrees of cementation used in this study produce extremely fragile and brittle specimens. These specimens are very easily cracked at the time of placing them between the platens and of centering the oscillator. This required the assembly and centering of the driving mechanisms while the epoxy had not yet hardened. Almost invariably, if the centering was left until after the curing period of the epoxy, the specimens cracked just above the epoxy film on the pedestal. These were hairline cracks invisible to the naked eye, but were very apparent when the specimen was gently tilted. Specimens that had been cracked showed quite a different behavior: a much larger gain of shear modulus with confining pressure than for intact specimens. An example of two identical 2% cement specimens, one cracked and the other intact, are presented in Figure 4, which illustrates the large effect of the crack on the slope of the line (0.31). The large change in slope caused by a hairline crack of a very irregular surface clearly indicates that friction is not an effective coupling mechanism in cemented soils. If friction between portions of a cracked specimen is not effective in coupling the two portions of the specimen, the friction between the cemented sand and a metal surface, such as aluminum, cannot be relied on unless the confining pressures are very large. The epoxy resin used in this study adheres to metals and to the cemented sand, thus providing a coupling that does not allow relative displacements between platens and specimen. In this sense, for the removal of the specimen from the cell it was necessary to chisel the dried epoxy from the cap and the base. This technique, thus provides a stiff coupling and an efficient means of transmitting the torsional excitation to the specimen.

A comparison of the results of this study to the results of previous studies is presented in Figures 5, 6, and 7. These figures show that the low-strain shear modulus of cemented sand was underestimated in the previous works and the effect of the confining pressure was overestimated. Some of the differences observed might be attributed to this study having used slightly different sand,

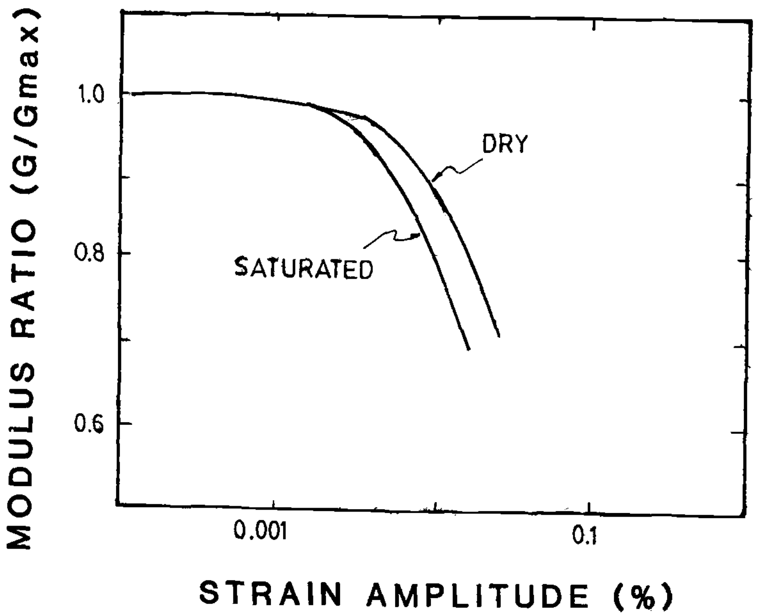

FIG. 3 -- Effects of Saturation and Undrained Conditions on the Modulus Ratio

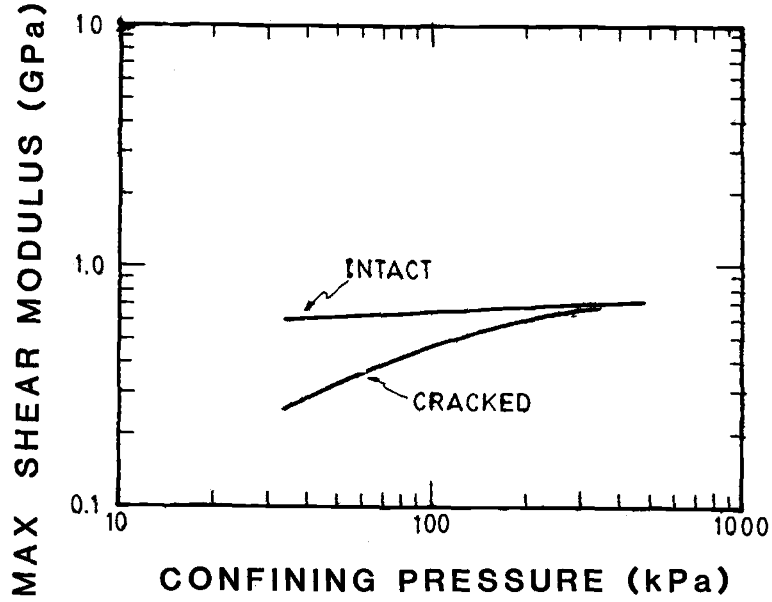

FIG. 4 -- Effects on the Maximum Shear Modulus of Cracks in the Specimen (2% cement)

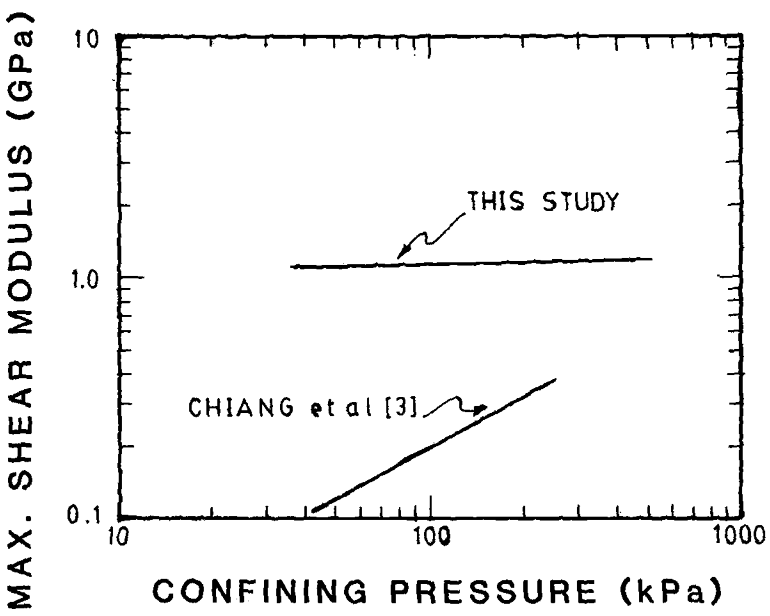

FIG. 5 — Comparison of the Results of this Study to the Results of Chiang & Chae [3], (4% cement, and 103.6 pounds per cubic foot)

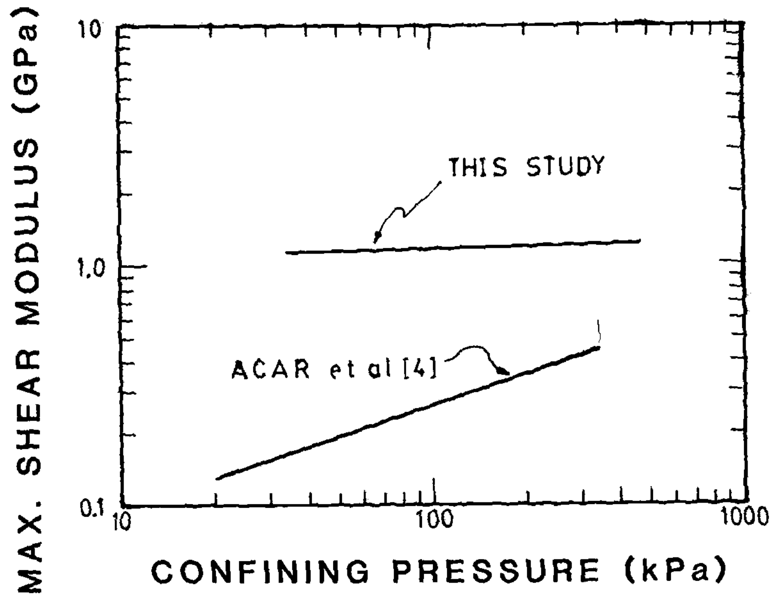

FIG. 6 — Comparison of the Results of this Study to the Results of Acar et al. [4] (4% cement, and 50% Relative Density)

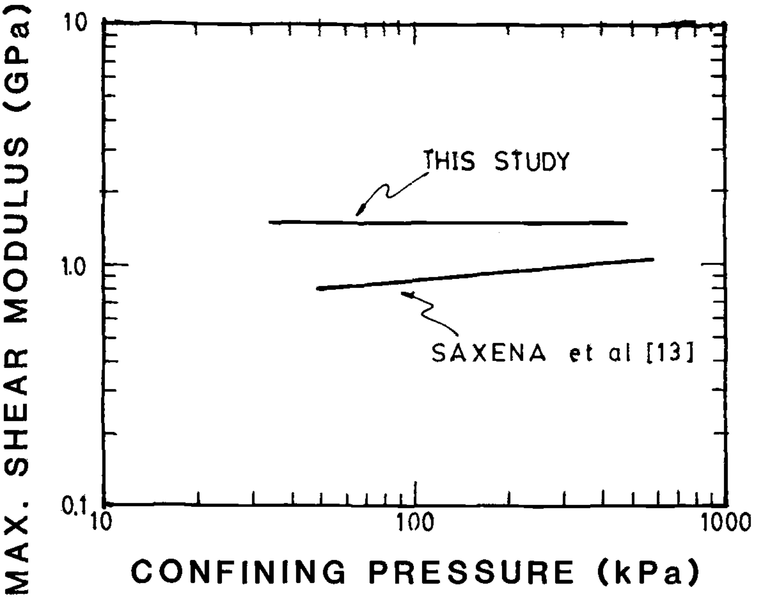

FIG. 7 — Comparison of the Results of this Study to the Results of Saxena et al. [13] (5% Cement, 43% Relative Density - Data Taken from Fig. 307 in [15])

cement, specimen preparation and curing procedures. However, the differences are so large that they can only be explained by an imperfect coupling between the specimen and the end platens. This contention is clearly suggested by the observed effect of hairline cracks illustrated in Figure 4.

When the coupling of the specimens is entrusted to friction or radial blades [3, 4], the results presented in Figures 5 and 6 indicate that comparable shear moduli are measured, although the effect of confining pressure is different. The results shown in Figure 7 show that (at high degrees of cementation) the coupling of the specimens with hydrostone gypsum cement [13] yields somewhat larger shear moduli than coupling with friction or blades. However, gypsum cement does not adhere to the metal surfaces of the base and the cap [14]; thus, the coupling between the gypsum cement and the platens is entrusted to friction. The comparison of these results to the results of this study manifest the need of a coupling material that adheres to the metal surfaces of the end platens.

CONCLUSIONS

From the results of this study, it is possible to draw the following conclusions:

1. To test cemented soils in a torsional resonant column, it is necessary to provide a rigid coupling between the specimen and the platens. The coupling compound should adhere to the metal surfaces of the end platens.

2. Relying on friction, radial blades or a coupling compound that does not adhere to metal results in an overall underestimation of the low-strain shear modulus in the range of confining pressures used. The underestimation is larger for smaller confining pressures. This causes a fictitious effect of showing large gains in shear modulus with confining pressure, which do not reflect the material behavior but rather the result of an increased coupling due to increased confining pressure.
3. Contrary to the findings of previous work, even small degrees of cementation cause very large changes of shear modulus at low strain amplitudes and almost completely eliminate the dependence of low-strain shear modulus on the confining pressure in the range of pressures used.
4. The maximum shear modulus of cemented sands is predominantly determined by the degree of cementation and the properties of the cementing agent.
5. Saturation of the specimen and testing under undrained conditions have a negligible effect on the low strain shear modulus. But, at high strain amplitudes, the saturated specimens are less rigid than the dry specimens.

ACKNOWLEDGEMENTS

The work reported has been conducted as part of the research funded by the National Science Foundation Grant No. RII-8604132. This support is gratefully acknowledged. Special thanks are extended to Teresa Limon, Margarita Arriaga, Horacio Fernandez, Elizabeth Gonzalez, and Stephen Greaber, who assisted in the testing program.

REFERENCES

[1] Drnevich, V.P., "Resonant-Column Testing-Problems and Solutions," Dynamic Geotechnical Testing, ASTM STP 654, American Society for Testing and Materials, 1978, pp. 384-398.

[2] Peji Yu, and F.E. Richart, "Stress Ratio Effects on Shear Modulus of Dry Sand," Journal of Geotechnical Engineering, ASCE, Vol. 110, No. 3, 1983, pp 331-345.

[3] Chiang, Y.C., and Y.S. Chae, "Dynamic Properties of Cement-Treated Soils, Highway Research Record, No. 379, Highway Research Board, National Academy of Sciences, 1972, pp. 39-51.

[4] Acar, Y.B., and E.A. El-Tahir, "Low Strain Dynamic Properties of Artificially Cemented Sand, "Journal of Geotechnical Engineering, ASCE, Vol. 112, No. 11, 1986, pp. 1001-1015.

[5] Hardin, B.O., and W.L. Black, "Vibration Modulus of Normally Consolidated Clay," Journal of the Soil Mechanics and Foundations Division, ASCE, Vol. 94, No. SM2, 1968, pp. 353-369.

[6] Hardin, B.O., and V.P. Drnevich, "Shear Modulus and Damping in Soils: Design Equations and Curves," Journal of the Soil Mechanics and Foundations Division, ASCE, Vol 98, No. SM7, 1972, pp. 667-692.

[7] Wu, S., D.H. Gray, and F.E. Richart, "Capillary Effects on Dynamic Modulus of Sands and Silts" Journal of Geotechnical Engineering, ASCE, Vol. 110, No. 9, 1984, pp. 1188-1203.

[8] Whitman, R.V., E.T. Miller, and P.J. Moore, "Yielding and Locking of Confined Sand," Journal of the Soil Mechanics and Foundations Division, ASCE, Vol. 90, SM4, 1964, pp. 57-84.

[9] Hardin, B.O., and F.E. Richart, "Elastic Wave Velocities in Granular Soils," Journal of the Soil Mechanics and Foundations Division, ASCE, Vol. 89, No. SM1, 1963, pp.33-65.
[10] Richart, F.E., A. Brandtzaeg, and R.L. Brown, "A Study of the Failure of Concrete Under Combined Compressive Stresses," University of Illinois Bulletin, University of Illinois, Urbana, Vol. 26, No. 12, 1928, pp. 42-67.
[11] Vinson, T.S., C.R., Wilson, and P. Bolander, "Dynamic Properties of Naturally Frozen Silt," Proceedings, Permafrost: Fifth International Conference, National Academy of Science, 1986, pp. 1315-1320.
[12] Au, W.C., and Y.S. Chae, "Dynamic Shear Modulus of Treated Expansive Soils," Journal of the Geotechnical Engineering Division, ASCE, Vol. 106, No. GT3, 1980, pp. 255-273.
[13] Saxena, S.K., A.S Avramidis, and K.R. Reddy, "Dynamic Moduli and Damping Ratios for Cemented Sands at Low Strains," Canadian Geotechnical Journal, 25 (2), 1988, pp. 353-368.
[14] United States Gypsum, Tooling and Casting Division, Personal Communication, Chicago, 1989.
[15] Avramidis, A.S., "Dynamic and Static Behavior of Cemented Sands," Ph.D. Dissertation, Illinois Institute of Technology, 1985, p. 576.

John S. Smith, Michael D. Wyrick, Jon M. Poole

AN EVALUATION OF THREE TECHNIQUES FOR DETERMINING THE YOUNG'S MODULUS OF MECHANICALLY ALLOYED MATERIALS

REFERENCE: Smith, J. S., Wyrick, M. D., and Poole, J. M., "An Evaluation of Three Techniques for Determining the Young's Modulus of Mechanically Alloyed Materials," Dynamic Elastic Modulus Measurements in Materials, ASTM STP 1045, Alan Wolfenden, editor, American Society for Testing and Materials, Philadelphia, 1990.

ABSTRACT: Two dynamic and one static technique for determining Young's modulus of mechanically alloyed (MA) materials were evaluated for their suitability for quality control testing and as a tool for development of new MA materials. The dynamic techniques included the commonly used continuously excited free - free beam technique tested in both longitudinal and flexural modes, and the relatively new impulse excitation technique tested in the flexural mode. The dynamic techniques showed a minor difference between the impulse and continuous techniques but still yielded results agreeing within ± 1%. The static technique yielded results differing from - 5% to + 7% of the dynamic results. The impulse excitation method is particularly well suited for quality control work, while the continuous method is best for elastic behavior characterization. It is conjectured that the static tensile method accuracy may be adversely affected if the tested material is non-isotropic.

KEYWORDS: modulus of elasticity, anisotropy, mechanical alloying, testing, reproducibility, texture

Oxide dispersion strengthened (ODS) alloys produced by the mechanical alloying process feature a high melting point, exceptional high temperature strength and microstructural stability. The predominant commercial example is INCONEL^{TM} alloy MA 754, a Ni-20%Cr alloy strengthened by a fine uniform yttrium oxide dispersoid. The alloy is typically specified for high performance gas turbine engine hot section parts, such as vanes, that utilize its excellent high temperature strength and thermal fatigue resistance [1].

J. S. Smith and J. M. Poole are Metallurgist-Advanced, and M. D. Wyrick is Project Specialist with Inco Alloys International, Inc., Research and Development, Huntington, WV 25720. ^{TM}INCONEL is a registered trademark of the Inco family of companies.

By design, MA superalloys have a preferred crystalline orientation. INCONEL alloy MA 754 properties are attained by exacting thermomechanical processes that simultaneously develop a high aspect ratio grain structure, strong <100> rod texture (alloy MA 754 is face centered cubic), low modulus in the working direction (typically ranging from 145 to 170 GPa), with thermal fatigue resistance and high strength in the working direction. Young's modulus is an accurate indicator of the texture and thermal fatigue resistance [2]. Being a much simpler and more economical test, modulus testing not only became a primary tool in the development of MA/ODS alloys, but is now a routinely specified quality control test.

The modulus determined here has been called the "free" or "complex" Young's modulus as opposed to the "pure" Young's modulus. The free modulus is determined from a specimen allowed to vibrate freely, and includes effects from bending and twisting. The pure modulus is determined when the specimen is prevented from twisting during vibration or strain. For isotropic homogenous materials the free and pure Young's modulus are equivalent [3].

The purpose of this study was to evaluate three different test techniques for determining Young's modulus of textured alloys. The criterion in view was the usefulness of test methods for quality control testing. The need is for rapid testing, good accuracy and reproducibility (within ± 2%, for example), and simple testing procedures and specimens. Many other good methods exist for elastic modulus testing [4,5], perhaps some with higher precision, but the three selected in this study seemed to offer the best probability of meeting the criterion.

In addition, concern had been expressed that the elastic modulus of textured MA alloys may vary with the test technique. Interlaboratory/technique reproducibility studies have been conducted on isotropic materials [4,5], but no technique reproducibility study has been conducted on orthotropic metallic materials to the authors' knowledge.

EXPERIMENTAL PLAN/PROCEDURE

Material and specimens. Thirteen cylindrical specimens were machined from hot rolled plates with varying thermomechanical process histories, which provided a fairly broad range of Young's elastic modulus. The plates were prepared from two heats with the compositions given in Table 1. While commercial INCONEL alloy MA 754 bars typically have a <100> rod texture, an analysis of some plates used in this study indicated the plate generally had a (110)[001] sheet texture. In general, the sharper the (110)[001] texture, the lower the modulus in the hot working direction.

Dynamic elastic modulus specimen dimensions, listed in Table 2, were selected to provide a diameter/length ratio of 0.10 to minimize Poisson's ratio effects due to the preferred orientations. After completion of the dynamic elastic tests, the specimens were machined into tensile bars with a nominal gage diameter of 6.35 mm and a gage length of 25.4 mm for static elastic modulus testing. The tensile bars were pulled to fracture after the static elastic modulus was determined. Table 3 gives the tensile properties at room temperature.

TABLE 1 -- Composition, w%

Heat No.	C	Ni	Cr	Al	Ti	Y	O
DT0616B	0.05	Bal	19.46	0.34	0.46	0.57	0.39
DT0931B	0.05	Bal	19.53	0.32	0.46	0.60	0.38

TABLE 2 -- Dimensions of dynamic elastic modulus test specimens

Specimen	d, mm	l, mm	d/L	eccentricity, mm
1	9.540	95.25	0.100	0.002
2	9.515	95.22	0.100	0.033
3	9.522	95.22	0.100	0.020
4	9.528	95.20	0.100	0.020
5	9.540	95.22	0.100	0.008
6	9.566	95.24	0.100	0.010
7	9.550	95.22	0.100	0.020
8	9.548	90.17	0.106	0.015
9	9.550	95.22	0.100	0.015
10	9.561	95.22	0.100	0.008
11	9.614	95.25	0.101	0.008
12	9.520	95.24	0.100	0.020
13	9.525	95.22	0.100	0.005

TABLE 3 -- Mechanical properties at room temperature

Specimen	Proportional Limit MPa	0.2% Yield Strength MPa	Tensile Strength MPa	EL[a] %	RA %
1	379	590	967	18	28
2	374	642	1003	20	24
3	325	559	940	20	27
4	334	614	998	21	25
5	337	545	934	19	28
6	290	545	914	18	18
7	328	572	943	18	27
8	398	614	969	19	25
9	325	545	925	19	20
10	371	548	909	16	18
11	344	598	940	21	28
12	381	547	897	16	15
13	314	592	911	25	30

([a] Gage length = 25.4 mm)

Test Techniques. One static and two dynamic elastic modulus test techniques were reviewed. The terms static and dynamic loosely refer to the strain rate and amplitude. Generally, static testing involves relatively large elastic strains and slow strain rates, while dynamic testing involves small strains (on the order of 10^{-6}) and high strain rates.

The static technique used here was conducted largely in accordance with ASTM E111-82. Tensile bars were tested on a 27000 kilogram Tinius-Olsen screw-type tensile machine. Elongation was measured using a Class B-1 averaging extensometer and recorded on an autographic load-elongation recorder over a single loading cycle. The strain rate to yield was 0.005 mm/mm. Elastic modulus was measured over strains less than 0.25%.

The two dynamic techniques may be described as continuous excitation (CE) and impulse excitation (IE), referring to the manner in which the specimens are vibrated or excited. The continuous excitation method has been described in detail in several references [6,7], and especially by Spinner and Tefft [8].

The cylindrical specimens were vibrated in both longitudinal and flexural modes. In the longitudinal mode, the specimens were driven sinusoidally on one end and the longitudinal wave was detected on the opposite end. Specimens were driven continuously using a scanning audio oscillator and Astatic model 12U phonograph cartridges. Displacement was detected using the same type cartridge connected to a sweep null detector, dual trace oscilloscope, and frequency counter. The fundamental resonant frequency was determined from resonant peaks on the null detector, oscilloscope Lissajou patterns, and nodal analysis of the specimen.

In the longitudinal mode, Young's modulus is calculated from the longitudinal fundamental resonant frequency (f_1), the specimen density (ρ), diameter (d), length (L), and a shape correction factor (K) by the following equation:

$$E_{CL} = \rho(2Lf_1)^2/K \qquad (1)$$

where, $K = 1 - 0.125(\pi\mu d/L)^2$, μ = Poisson's ratio, and $\rho = 8300\ \text{kg/m}^3$ for all specimens.

The Young's modulus (E_{CF}) for the CE flexural mode is determined from a specimen suspended by threads from the phonograph cartridges near its fundamental nodal points. One thread delivers the driving vibration to the specimen and the other thread returns the displacement to the detector cartridge. The looping suspension method described in [9] was used. The fundamental flexural resonant frequency is determined in a similar manner to that for the longitudinal resonance. Flexural Young's modulus is calculated from the flexural resonant frequency, specimen dimensions and density, and a shape correction factor (T) by the following:

$$E_{CF} = 1.2619\rho(L^2f/d)^2T \qquad (2)$$

The shape factor T is a function only of Poisson's ratio and d/L, and can be found in tables developed by Spinner and Tefft [8].

Both the longitudinal and flexural formulas were derived assuming isotropic and homogeneous materials. However, these formulas can apply to non-isotropic materials so long as one remembers that the determined elastic modulus is appropriate for the tested orientation only.

The impulse excitation technique is relatively new [5] and was accomplished here using an instrument called the GrindoSonic [10]. Only the impulse flexural Young's modulus (E_{IF}) was determined since the longitudinal period measurements of the specimens fell below the recommended range of the instrument for good resolution.

In the IE flexural method the specimen is supported at its fundamental nodal points centered over an acoustic microphone. The specimen was lightly tapped by hand with a thin alumina rod to initiate vibration which was detected by the microphone and transmitted to the instrument. The resultant transient vibration is electronically analyzed to yield the digitally displayed natural period. The flexural resonant frequency is calculated from the period, from which E_{IF} is calculated using the formula for continuous flexural excitation.

Poisson's ratio corrections. Ideally, the most accurate Young's modulus values will be obtained when Poisson's ratio is known so that more accurate shape correction factors can be determined. The best procedure is to determine also the shear modulus at the same time as the Young's modulus is determined. A value for Poisson's ratio can then be calculated which serves as a first estimate in an iterative process utilizing the basic equations relating E, G and μ.

In this evaluation, however, the accepted quality control practice for determining Young's modulus was followed which means the shear modulus was not determined and Poisson's ratio was assumed to be 0.30 in calculating the shape correction factors. The Poisson's ratio for INCONEL alloy MA 754 can range from 0.05 to 0.45, depending on the texture of the material and orientation of the specimen. Assessing the shape correction factors with a Poisson's ratio of 0.3 and d/L of 0.10, a maximum error of 0.2% for the longitudinal mode and 0.3% for the flexural mode may occur.

TABLE 4 -- Calibration results, dynamic techniques

	Frequency, Hz	Error
Impulse	2044.4	+ 0.05%
Continuous	2044.6	+ 0.06%
NIST	2043.3	...

RESULTS

Calibration of dynamic methods, flexural mode. Calibration of both the CE and IE flexural modes can be verified using NIST standards. Table 4 shows the results of the verification tests using NIST Standard Reference Material 718, polycrystalline alumina reference bar #C1 [11]. The results show no significant difference between the CE and IE flexural resonant frequencies and error of less than 0.06% with respect to the reference bar.

Rotational variation, dynamic flexural mode. Specimens tested in the dynamic flexural modes simultaneously vibrate in two directions oriented 90° from each other. Thus it is necessary to rotate the specimen and determine the highest and lowest flexural resonant frequencies, and calculate the mean Young's modulus from these.

Table 5 gives the flexural Young's modulus results as a function of specimen rotation for both the continuous and impulse techniques. The differences within each test technique are typical when compared to the literature [9]. Figure 1 shows that the rotational variation measured by the two techniques is very similar.

Figure 2 shows there was no correlation of rotational variation in elastic modulus with the mean flexural Young's modulus. A comparison of the specimen diametral eccentricities in Table 2 with the rotational elastic modulus variation shows no correlation, suggesting that the variation may be partly due to texturing.

The primary finding is that both the CE and IE methods will, for practical purposes, measure the same rotational elastic modulus variation in the flexural mode.

TABLE 5 -- Rotational variation in flexural modulus

Specimen	Continuous		Impulse	
	E_{CF_1} GPa	E_{CF_2} GPa	E_{IF_1} GPa	E_{IF_2} GPa
1	158.8	162.5	158.9	162.7
2	166.2	167.1	165.9	167.3
3	168.4	168.9	167.6	168.7
4	167.1	167.9	166.7	168.0
5	175.4	178.4	175.3	178.3
6	178.7	185.9	177.6	185.9
7	179.3	189.2	179.1	189.9
8	179.6	184.7	179.4	184.5
9	189.3	193.2	189.1	192.8
10	206.5	209.3	205.8	208.9
11	207.0	209.7	206.4	209.5
12	213.5	215.3	212.8	214.9
13	231.6	235.1	231.2	234.4

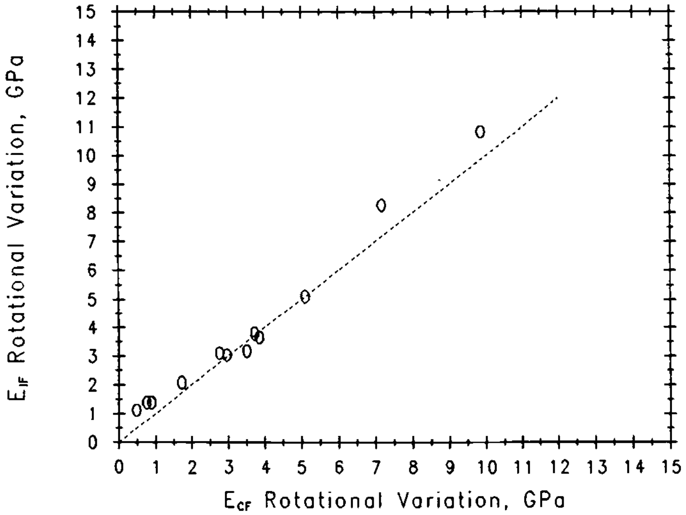

FIGURE 1 -- Variation in flexural Young's modulus due to specimen rotation, E_{IF} versus E_{CF}.

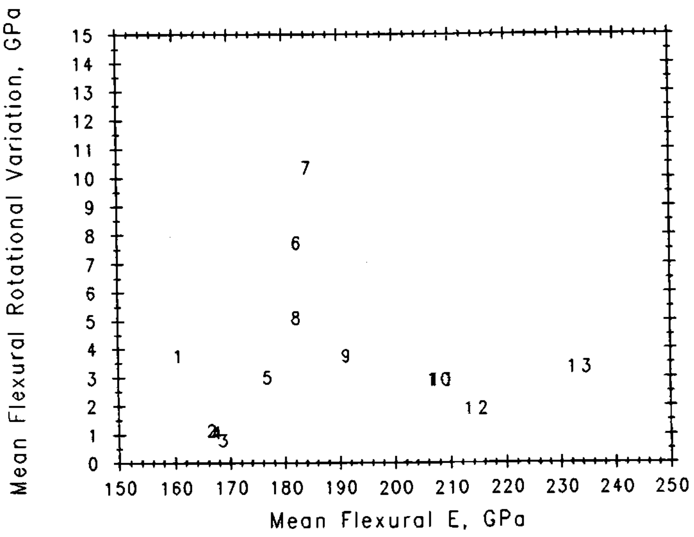

FIGURE 2 -- Mean flexural (both E_{IF} and E_{CF}) rotational variation in Young's modulus versus the mean flexural Young's modulus.

TABLE 6 -- Young's modulus results, GPa

Specimen	Static	Continuous Longitudinal	Continuous Flexural	Impulse Flexural
1	158.0	159.3	160.7	160.8
2	158.7	164.4	166.6	166.6
3	162.9	166.4	168.7	168.2
4	167.2	164.9	167.5	167.3
5	172.0	177.1	176.9	176.8
6	195.1	182.2	182.3	181.8
7	188.3	184.6	184.3	184.5
8	184.8	181.2	182.2	182.0
9	198.2	192.2	191.3	191.0
10	209.8	207.7	207.9	207.4
11	222.2	208.5	208.4	207.9
12	222.1	214.2	214.4	213.9
13	231.9	233.3	233.4	232.8

Young's modulus results. Table 6 gives the final Young's modulus results for the four techniques/modes tested. The flexural modulus was calculated from the mean of data presented in Table 5. The following difference plots are derived from this Table.

Flexural mode: E_{IF} versus E_{CF}. Figure 3 illustrates the difference in the flexural impulse versus continuous excitation techniques. E_{IF} averaged about 0.2% higher than E_{CF}. This difference is less than that of the CE flexural versus longitudinal modes.

Continuous technique: E_{CF} versus E_{CL}. Figure 4 shows the continuous flexural versus continuous longitudinal elastic modulus differences. The mean difference is about 0.4%, but the difference is greater below 180 GPa.

E_{IF} versus E_{CL}. The difference plot in Figure 5 is nearly identical to the E_{CF} versus E_{CL} difference plot. The mean difference is 0.2%, slightly less than the continuous flexural versus longitudinal difference. The same variation of difference with elastic modulus values exists for the IE flexural versus CE longitudinal techniques.

Static versus dynamic. The difference plots between the static and dynamic modulus techniques are all very similar, and only the E_S versus E_{CL} differences are shown in Figure 6. Where the dynamic techniques and modes varied at most 1.5%, the static elastic modulus varies from - 5% to + 7% from the dynamic elastic modulus.

Paired differences statistical summary. Table 7 contains the results of a paired difference statistical analysis of the various methods. The only mean differences showing any significance (at the 5% level) were the IE versus CE paired differences. The IE technique resulted in Young's modulus values about 0.3 GPa higher than those of the CE technique. While statistically significant, this is not considered significant in a practical sense.

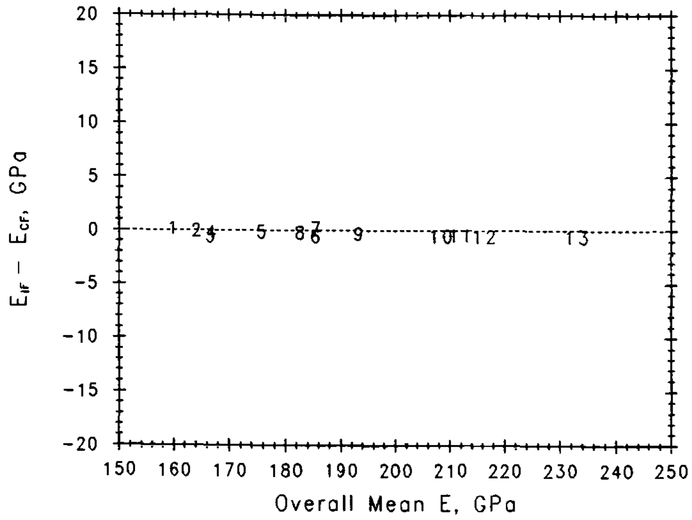

FIGURE 3 -- (E_{IF} - E_{CF}) differences versus overall mean Young's modulus. Mean difference = -0.3 GPa.

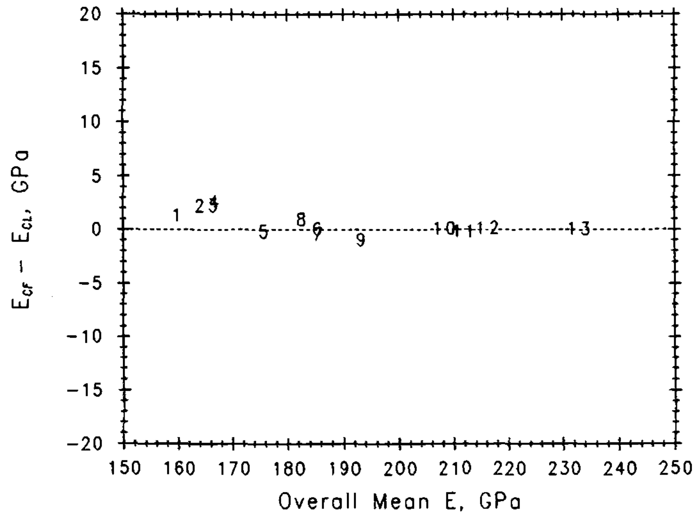

FIGURE 4 -- (E_{CF} - E_{CL}) differences versus overall mean Young's modulus. Mean difference = 0.6 GPa.

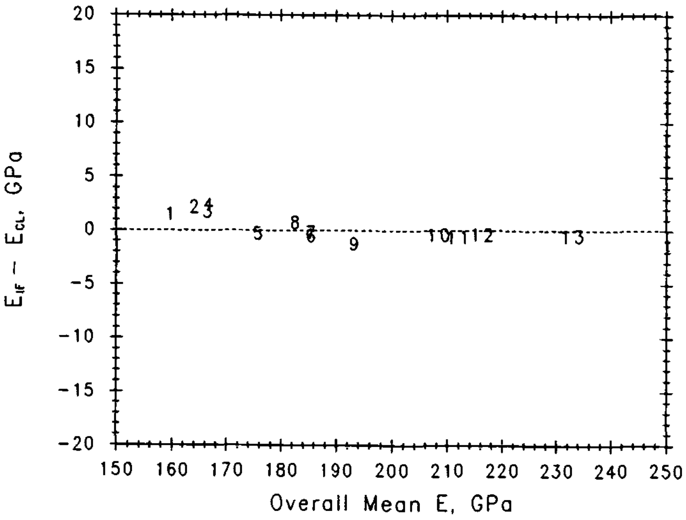

FIGURE 5 -- (E_{IF} - E_{CL}) differences versus overall mean Young's modulus. Mean difference = 0.4 GPa.

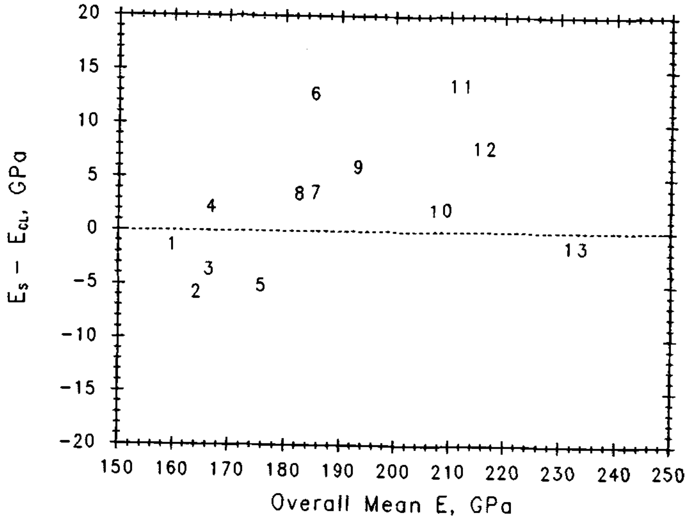

FIGURE 6 -- (E_S - E_{CL}) differences versus overall mean Young's modulus. Mean difference = 2.7 GPa.

TABLE 7 -- Paired differences (in GPa) statistical summary

	E_S-E_{CL}	$E_{CF}-E_{CL}$	$E_{IF}-E_{CL}$	E_S-E_{CF}	E_S-E_{IF}	$E_{IF}-E_{CF}$
mean	2.7	0.6	0.4	2.1	2.3	-0.3
standard dev.	6.2	1.1	1.2	6.8	7.0	0.3
npcc[a]	0.98	0.95	0.93	0.99	0.99	0.96
significant?[b]	no	no	no	no	no	yes

[a] npcc = normal probability correlation coefficient
[b] Significant at the 5% level.

The other major item to note is the large variance of the differences when comparing the statically determined elastic modulus with the elastic moduli from the dynamic methods.

DISCUSSION

Static methods. The static methods have been used successfully for decades. Some argue that these methods provide a more appropriate elastic modulus at engineering stress - strain amplitudes. In addition, one may obtain the proportional and elastic limits, directly observe anelasticity, and if the test is continued to fracture, determine the mechanical tensile properties of the specimen.

The variability of the static versus dynamic Young's modulus results in this study are greater than expected. The primary sources of error include specimen and extensometer misalignment during loading, and a lack of precision in measuring the load - elongation slope from the autographic recorder chart.

It is conjectured that the preferred orientation in the specimens exaggerated errors introduced by the static technique problems of misalignment and imprecision, thus explaining the comparatively large variability. Specimens with preferred orientations will deform in a non-uniform manner under load. If this is the case, then it seems that static methods may be susceptible to excessive error when used for anisotropic materials.

Static techniques have other drawbacks. These techniques are time consuming in contrast with dynamic techniques (particularly the impulse technique), are restricted by specimen configurations and sizes, and are destructive in nature. Unless strain gaging is used, neither Poisson's ratio nor shear modulus can be measured. At elevated temperatures the static techniques are very difficult to perform accurately, especially when the material is prone to creep.

Dynamic methods. For engineering purposes, the CE and IE dynamic methods and modes produced equivalent results despite the textured nature of INCONEL alloy MA 754. Reproducibility was good between the methods, averaging less than 1% deviation. This reproduction of Young's modulus is impressive considering the different modes of wave propagation, the different means of vibrational excitation, and the assumption of 0.30 for Poisson's ratio.

These methods have many advantages for Young's modulus testing. They are non-destructive, utilize readily obtainable low cost instrumentation, are adaptable to environmental testing and to elevated temperatures, and accomodate a wide variety of specimen configurations and sizes. Testing by the impulse excitation technique is exceptionally simple and fast, does not require highly trained personnel for routine work, and is portable as well.

An important consideration for anisotropic materials is that dynamic techniques can allow elastic moduli testing in several orientations, provide shear moduli and Poisson's ratio estimates, and thus permit the development of directional elastic stiffnesses and/or compliances. The elastic behavior of a material can be defined, even if it is anisotropic.

On the other hand, most dynamic methods operate only at micro-strain levels, a fact which occasionally draws criticism that these are not typical engineering strains, and may give overly high engineering moduli. Nevertheless, on balance, the dynamic methods, and especially the impulse method, appear best suited for elastic moduli determinations.

SUMMARY

The best Young's modulus test technique for routine quality control work appears to be the impulse excitation technique, closely followed by the continuous excitation technique. The impulse excitation method combines rapid testing, high accuracy, and simplicity when using appropriate test specimens. A major advantage is that specimen nodal analysis is not required to identify the fundamental resonant frequencies if the specimen is configured, supported and tapped properly.

The continuous excitation method requires more operator skill and knowledge, is a more time consuming test, and requires nodal analysis to determine the resonance of a material with unknown modulus. However, this method can be used to determine the shear frequencies and overtones if desired. For conducting complete elastic characterization studies, the continuous excitation method is recommended.

The static tensile loading method seems undesirable for quality control work. Improvements in accuracy can be achieved by using digital data collection that can be mathematically reduced instead of autographic charting with subjective analysis. Multiple load cycling in the elastic range would minimize the opportunity for gross errors. Careful attention to specimen machining and extensometer alignment would reduce mis-alignment errors. However, even when all this is done, the static test is still laborious and relatively time consuming.

REFERENCES

[1] INCONEL alloy MA 754 Technical Data Handbook, Inco Alloys International, Inc., Huntington, W. V.

[2] Gilman, P. S., "Mechanical Alloying of Aluminum and Nickel Base Alloys," Progress in Powder Metallurgy 1985, Vol. 41, 1985, pp. 455-469.

[3] Wachtman, J. B., Tefft, W. E., Lam, Jr., D. G., and Stinchfield, R. P., "Elastic Constants of Synthetic Single Crystal Corundum," Journal of Research of the NBS - A. Physics and Chemistry, Vol. 64A, No. 3, May - June 1960, pp. 213-228.

[4] Richards, J. T., "An Evaluation of Several Static and Dynamic Methods for Determining Elastic Moduli," Symposium on Determination of Elastic Constants, ASTM STP No. 129, June 25, 1952, pp. 71-100.

[5] Wolfenden, A., Harmouche, M. R., Blessing, G. V., Chen, Y. T., Terranova, P., Dayal, V., Kinra, V. K., Lemmons, J. W., Phillips, R. R., Smith, J. S., Mahmoodi, P., and Wann, R. J., "Dynamic Young's Modulus Measurements in Metallic Materials: Results of an Interlaboratory Testing Program," Journal of Testing and Evaluation, Vol. 17, no. 1, January 1989, pp. 2-13.

[6] Fine, M. E., "Dynamic Methods for Determining the Elastic Constants and their Temperature Variation in Metals," Symposium on Determination of Elastic Constants, ASTM STP No. 129, June 25, 1952, pp. 43-67.

[7] ASTM C 848, "Standard Test Method for Young's Modulus, Shear Modulus, and Poisson's Ratio for Ceramic Whitewares by Resonance,"

[8] Spinner, S., and Tefft, W. E., "A Method for Determining Mechanical Resonance Frequencies and for Calculating Elastic Moduli from these Frequencies," ASTM Proceedings , Vol. 61, 1961, pp. 1221-1238.

[9] Dickson, R. W., and Spinner, S., "An Improved Method for the Determination of Torsional and Flexural Resonance Frequencies of Cylindrical Specimens," Journal of Materials, JMLSA, Vol. 3, No. 3, Sept. 1968, pp. 716-724.

[10] GrindoSonic is a trademark of J. W. Lemmons-Electronika, N. V., Leuven, Belgium.

[11] Dickson, R. W., and Wachtman, J. B., "An Alumina Standard Reference Material for Resonance Frequency and Dynamic Elastic Moduli Measurement, I. For Use at 25°C," Journal of Research of the National Bureau of Standards - A. Physics and Chemistry, Vol. 75a, No. 3, May - June 1971, pp. 155-162.

Bryce L. Fowler

INTERACTIVE PROCESSING OF COMPLEX MODULUS DATA

REFERENCE: Fowler, B. L., "Interactive Processing of Complex Modulus Data," Dynamic Elastic Modulus Measurements in Materials, ASTM STP 1045, Alan Wolfenden, editor, American Society for Testing and Materials, Philadelphia, 1990.

ABSTRACT: A methodology for processing damping material complex modulus data and presenting it in a manner that is meaningful to the damping designer is discussed. Initial parameter values for characterization equations are derived. The use of a computer program for characterization of complex modulus data is described.

KEYWORDS: complex modulus, characterization, viscoelastic materials, VEM, temperature shift function

Successful design of passive damping treatments using viscoelastic materials (VEM's) such as elastomers depends upon several factors. One important factor is accurate knowledge of the sensitivity of VEM properties to variations in temperature and frequency. Since it is impossible to test a viscoelastic material at every combination of temperature and frequency, the material is tested at discrete temperatures and frequencies and a relationship is developed that characterizes the material at all other combinations of temperature and frequency. This process is referred to as characterization.

The equations used in characterization are all of a parametric nature, often easily represented on computers. The hard part of characterization is to choose the equation parameters so that they accurately represent the VEM's properties. Interactive computer graphics have greatly improved the process of choosing and adjusting the correct parametric values.

Mr. Fowler is an engineer at CSA Engineering, 560 San Antonio Road, Suite 101, Palo Alto, CA 94306

This paper dicusses viscoelastic material characterization and provides a methodology for obtaining the parametric values used in the equations to represent the complex modulus of VEM's analytically.

THEORY

Viscoelastic materials are generally more difficult to characterize than are structural materials such as metals. This occurs for two basic reasons:

1. When an elastomer is dynamically loaded, even at levels well within its linear range, it converts a much larger fraction of the input energy into heat than does a metal. It is therefore necessary to measure both the energy storage property (stiffness) and energy dissipation property (damping).
2. Both stiffness and damping of elastomers tend to vary significantly with frequency and temperature. Generally, the more dissipative a material, the greater the variation.

Both problems are accommodated by describing the mechanical properties of the material in terms of a frequency- and temperature-dependent complex modulus (G^*). The stress-to-strain ratio for the material is treated as a complex quantity. Complex arithmetic provides a convenient means for keeping track of the phase angle by which an imposed cyclic stress leads the resulting cyclic strain. The complex shear modulus, for example, is usually expressed in the form

$$G^*(f,T) = G_0(f,T)[1 + j\eta(f,T)] \tag{1}$$

The real and imaginary parts of the modulus, which are commonly called the storage modulus and loss modulus, are given by $G_0(f,T)$ and $G_0(f,T)\eta(f,T)$, respectively. Fourier transform theory and the correspondence principle of viscoelasticity allow complex moduli to be used for calculating response to arbitrary dynamic inputs. Material properties are most often specified and measured in terms of their complex shear modulus because it allows greater flexibility in choosing the size and shape of the test specimen.

For infinitesimal strain and rate of strain, the time-dependent stress-strain relations for a viscoelastic material can be described by linear differential equations with constant coefficients. This linear behavior requires

$$\beta \equiv \left.\frac{d\log G_M}{d\log f_R}\right|_{transition} = \left.\frac{d\log G_R}{d\log f_R}\right|_{transition} = \left.\frac{d\log G_I}{d\log f_R}\right|_{transition} \tag{2}$$

and

$$\eta_{max} \cong \tan \frac{\pi\beta}{2} \tag{3}$$

where

G_M = magnitude of the complex modulus
G_R = real (storage) part of the complex modulus
G_I = imaginary (loss) part of the complex modulus
f_R = reduced frequency = $f_i \alpha_T (T_i)$
f_i = experimental frequency
T_i = experimental temperature
α_T = temperature shift function
η = G_I/G_R (also known as the loss factor or tan δ)

It has been shown by Rogers [1] that a solution to this requirement is given by the fractional complex modulus equation

$$G^*(f_R) = \frac{G_e + G_g z^\beta}{1 + z^\beta} \tag{4}$$

where

z = $j f_R / f_{R_0}$
f_{R_0} = reference reduced frequency
G_e = storage modulus rubbery asymptote
G_g = storage modulus glassy asymptote

The parameters G_e, G_g and f_{R_0} as well as parameters for α_T must be found such that the curve described by Eq 4 fits the data within the error bounds of the material test. Initial values for the parameters are first determined graphically and are then iterated and regressed for the best mathematical fit.

INITIAL PARAMETERS

Values for G_e and G_g may be obtained directly by drawing a plot of η versus G_M, as shown in Fig 1. Note that this plot is a useful indicator of data quality. Qualitative errors will often appear as data points that do not follow the overall inverted "U" shape from G_e to G_g. To evaluate β, the equation

$$\eta_{max} = \frac{\left(1 - \frac{1}{A}\right) \tan \frac{\pi\beta}{2}}{1 + \frac{1}{A} + \sqrt{\frac{2}{A}} \cos \frac{\pi\beta}{2}}, \qquad A = \frac{G_g}{G_e} \tag{5}$$

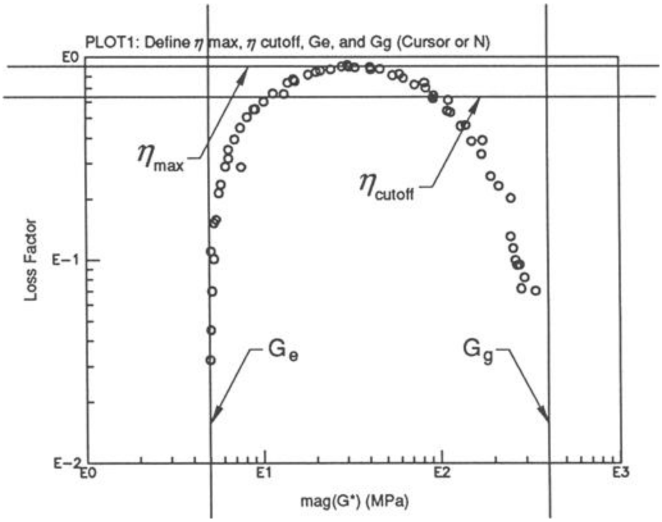

Figure 1. Obtain $\eta_{max}, \eta_{cutoff}, G_e$, and G_g

is derived from Eq 4. A value for η_{max} is obtained from the plot in Fig 1. Iteration is then used to calculate β. The transition region is defined by choosing an η_{cutoff} value from the plot in Fig 1. The use of η_{cutoff} to define the transition region is shown in Fig 2.

TEMPERATURE SHIFT FUNCTION

In the typical explanation of frequency-temperature equivalence, the temperature shift function, a function of temperature only, is constructed. The real part, the imaginary part, and the material loss factor of the complex modulus data are plotted as functions of reduced frequency. Historically, the temperature shift function for a particular damping material has been defined empirically by the experimental complex modulus data. The value of α_T at each experimental temperature is selected such that it simultaneously shifts horizontally the three complex modulus data points (G_R,G_I,η) to define curves and minimize scatter.

Computerized characterization and subsequent database storage has made it more efficient to represent the empirical temperature shift function as an analytic function. A widely used analytical representation for α_T is the WLF [2] equation. Unfortunately, this equation has not always been able to shift viscoelastic material data correctly outside the transition region. Other equations for α_T [3] have been formulated and have met with roughly equal success. A new approach is to use

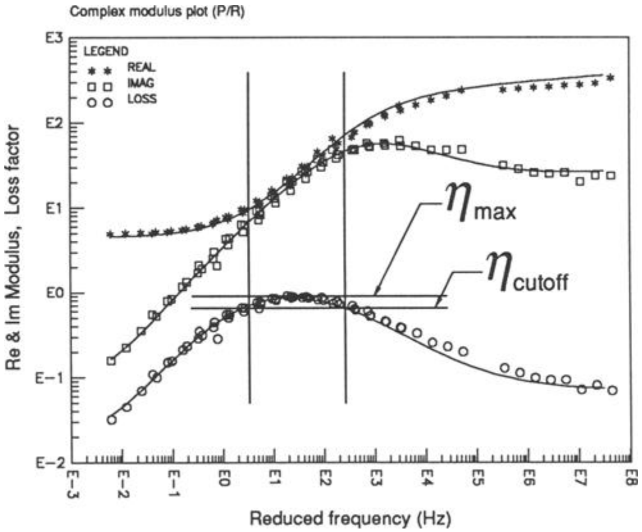

Figure 2. Transition region defined

a spline fit of the slopes of α_T for a relatively small number of equally spaced temperature points (e.g., 5 points) to define α_T. The reference temperature, T_Z, is obtained by fitting a quadratic function through the data points of $\log \eta$ versus T, solving for zero slope, and rounding to the nearest evenly spaced temperature point.

Initial values for the reference slope, S_{AZ}, and for the reference reduced frequency, f_{R_0}, are obtained by solving Eq 4 for α_T/f_{R_0}

$$\frac{\alpha_T(T_i)}{f_{R_0}} = \frac{1}{jf_i}\left[\frac{G_i^* - G_e}{G_g - G_i^*}\right]^{\frac{1}{\beta}} \tag{6}$$

Since Eq 6 is valid in the transition region, a quadratic is fit through the data points defined within the transition by $\eta \geq \eta_{cutoff}$ for α_T/f_{R_0} as a function of temperature. Defining $\alpha_T \equiv 1.0$ at T_Z, f_{R_0} is obtained from the reciprocal of the quadratic at T_Z. S_{AZ} is obtained as the slope of the quadratic at T_Z multiplied by the initial f_{R_0}.

A modified version of the WLF equation is then used

$$\log \alpha_T = -\frac{S_{AZ}(T - T_Z)(T_Z - T_\infty)}{(T - T_\infty)} \tag{7}$$

with T_∞ set equal to 10.0 to generate initial values of slope at all the other temperature-slope points. Finally, α_T is calculated as the integral of the spline of the slopes where the constant of integration is given by $\alpha_T \equiv 1.0$ at T_Z.

The accuracy of the α_T slope parameters is checked by looking at a plot of the complex modulus data versus the reduced frequency. The parameters (which represent spline knots) must be adjusted iteratively to remove any isotherm "shingles" (Figs 3 and 4).

COMPLEX MODULUS

Improvements to Eq 4 which add adjustment factors to provide a better curve fit in the glassy and rubbery regions have been offered by Bagley [4], Rogers [5], Nashif [6], and others. All equations work for some damping materials. None can adequately fit all sets of VEM data. Present methods use a piecemeal approach. An equation that has successfully fit the type of material of interest (e.g., adhesive) in the past or that is the most general is used and parameters are adjusted using regression and trial-and-error to get the best fit. If the equation's best fit is not adequate (i.e., the generated curve does not approximate the data over the entire reduced frequency domain) a different equation is tried. This approach has been implemented on a computer [7] with nine different complex modulus equations available.

Initial estimates of parameters vary for each model. For example, if the series fractional Maxwell equation, given by

$$G^* = G_e + \sum_{k=1}^{n} \frac{G_k}{1 + z_k{}^{-\beta_k} + \Delta_k z_k{}^{-\rho_k}}, \qquad z_k = j\left(\frac{f_R}{f_{R0}}\right)_k \tag{8}$$

where

$G_e < G_k < G_g$ stepping logarithmically

β_k = slope of storage modulus corresponding to G_k

Δ_k = pole multiplier

ρ_k = pole exponent

is chosen, β_k is set equal to the previously calculated β, Δ_k is the slope of the glassy intercept with the abscissa on a Cole-Cole plot [8] (i.e. G_I versus G_R), and ρ_k is set to 0.1 for all k.

The parameters are then adjusted iteratvely to give the best overall curve fit. Often, regression is used to somewhat automate these adjustments.

GRAPHICAL PRESENTATION

Jones [9] and, more recently, Jones and Rao [10] have developed methods to present complex modulus data graphically. These are the reduced-temperature nomogram

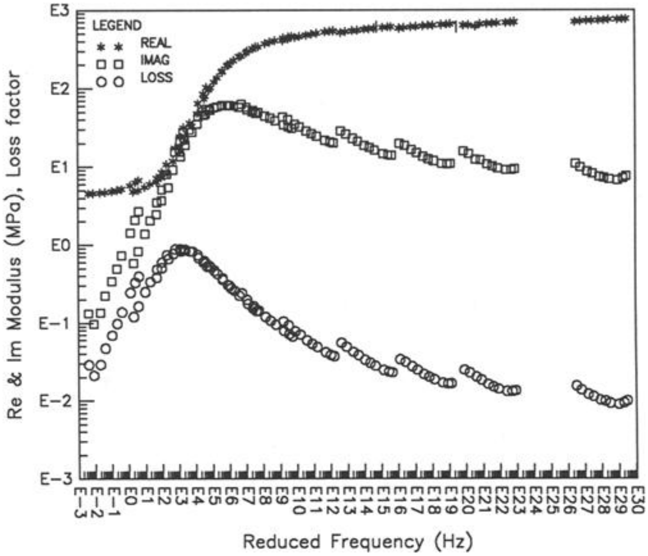

Figure 3. Isotherm shingles indicate incorrect α_T

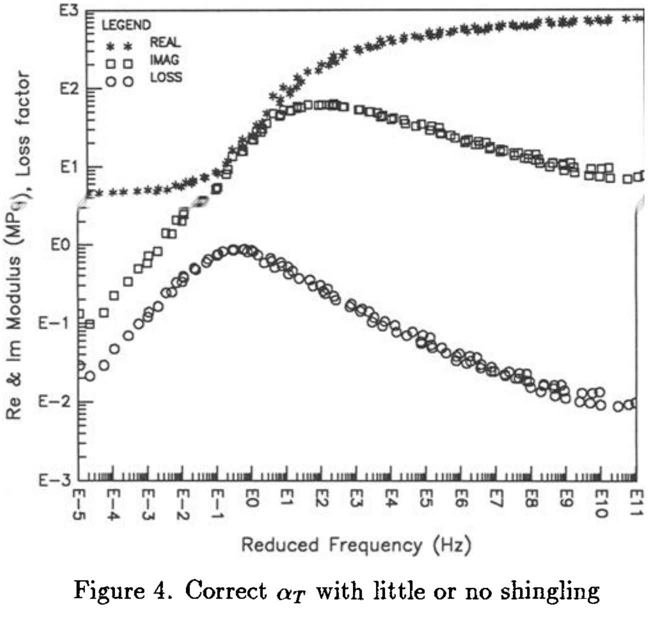

Figure 4. Correct α_T with little or no shingling

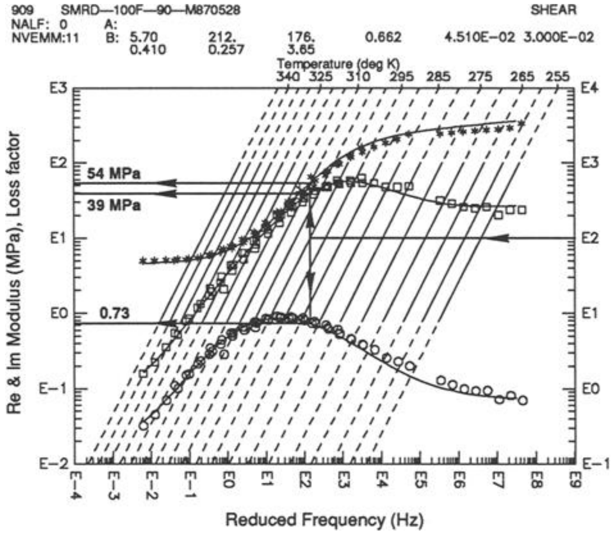

Figure 5. Reduced-temperature nomogram (international plot)

(also known as the international plot) and inverted "U" plot, respectively (Figs 5 and 6).

The international plot consists of the real and imaginary moduli displayed logarithmically on the left vertical axis along with the dimensionless loss factor. The horizontal scale is the reduced frequency defined in Eq 4. The right vertical axis is cyclic frequency displayed logarithmically in Hertz (Hz). Lines of constant temperature are superimposed on the plot from the relationship

$$\log f_R = \log f_i + \log \alpha_T\,(T_i) \tag{9}$$

These isotherm lines are usually calculated for steps of five degrees Kelvin and range from T_L to T_H to preclude extrapolation of temperature for which viscoelastic materials are highly sensitive. The range of experimental frequency is indicated by the solid region of the isotherm lines. In the area of extrapolated frequency, the isotherms are dashed. The use of the international plot to read interpolated values of modulus and loss factor is demonstrated in Fig 5. To get modulus and loss factor values corresponding to 100 Hz and 300°K, one reads the 100 Hz frequency on the right-hand scale and proceeds horizontally to the 300°K temperature line. Then proceed vertically to intersect the curves along a line of reduced frequency. Finally, proceed horizontally from these intersections to the left-hand scale to read the values of 54 MPa for the real modulus, 39 MPa for the imaginary modulus, and 0.73 for the loss factor.

The inverted "U" plot utilizes similar methodology, but removes the reduced frequency scale and directly superimposes constant temperature lines onto a plot

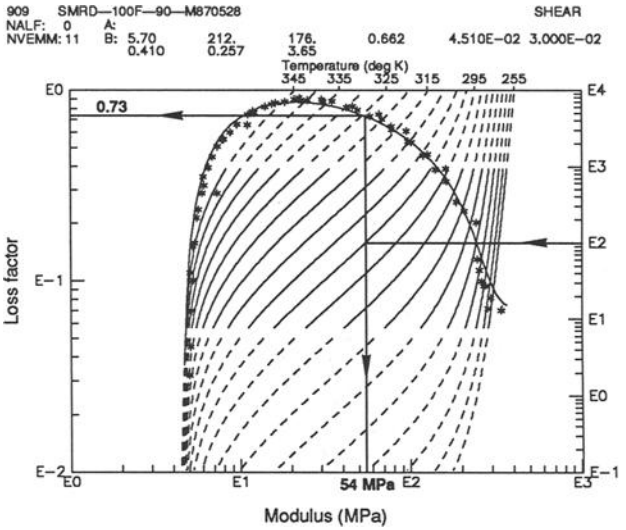

Figure 6. Inverted "U" plot

of loss factor versus the real part of the complex modulus with cyclic frequency still displayed on the right-hand axis. To follow the same example as above, start at the 100 Hz frequency value on the right-hand scale and move horizontally to the 300°K temperature line. Drop vertically downward to read 54 MPa off the horizontal axis, and proceed upward to the curve and then horizontally to read 0.73 off the left-hand vertical scale for the loss factor.

Other plots of interest include

1. $\log \alpha_T, d \log \alpha_T / dT$, and the apparent activation energy versus temperature
2. $\log f_i$ versus temperature
3. real and imaginary components of G^*, and η versus temperature

SUMMARY

Most viscoelastic materials data are for engineering applications and justifiably do not provide extensive coverage of temperature and frequency. The challenge of characterization is to make the data useful to the damping designer and simultaneously indicate limitations.

Using the methodology and graphical presentation outlined in this paper, this challenge can be met. Care must always be taken, however, to insure that the appropriate analytical representation of the complex modulus has been chosen. This caution indicates the pressing need to find a representation for complex modulus that may be used to fit all VEM data.

REFERENCES

[1] Rogers, L. C., "Operators and Fractional Derivatives for Viscoelastic Constitutive Equations," J. Rheology, Vol. 27, No. 4, 1983, pp. 351-372.

[2] Ferry, John D., Viscoelastic Properties of Polymers, John Wiley and Sons, 3rd ed., 1980.

[3] Rogers, L. C., "Graphical Presentation of Damping Material Complex Modulus," ISO/TC108/WG13, 1985.

[4] Bagley, R. L., "Applications of Generalized Derivatives to Viscoelasticity," AF Materials Lab TR-79-4103, November 1979 (Available from Defense Technical Information Center as ADA 081131.)

[5] Rogers, L. C., "DAMPING: On Modeling Viscoelastic Behavior," Shock and Vibration Bulletin, No. 51, 1981.

[6] Nashif, Ahid D., David I. G. Jones, John P. Henderson, Vibration Damping, John Wiley and Sons, 1985.

[7] Fowler, B. L., "Interactive Viscoelastic Material Properties Program," CSA Engineering Report No. 88-05-02, May 1988.

[8] Cole, K. S. and Cole, R. H., J. Chemistry and Physics, No. 9, 1941, pp. 341-351.

[9] Jones, D. I. G., "A Reduced-Temperature Nomogram for Characterization of Damping Material Behavior," 48th Shock and Vibration Symposium, October 1977.

[10] Jones, D. I. G., D. K. Rao, "A New Method for Representing Damping Material Properties," ASME Vibrations Conference, Boston, September 1987.

Author Index

Subject Index

ISBN 0-8031-1291-2